Institut für Physik und Astronomie der Universität Potsdam
Physik weicher Materie

Morphology, charge transport properties, and molecular doping of thiophene-based organic semiconducting thin films

Kumulative Dissertation
zur Erlangung des akademischen Grades
doctor rerum naturalium (Dr. rer. nat.)
in der Wissenschaftsdisziplin *Experimentalphysik*

eingereicht an der
Mathematisch-Naturwissenschaftlichen Fakultät
der Universität Potsdam

von

Patrick Pingel

Potsdam, im Juni 2013

Published online at the
Institutional Repository of the University of Potsdam:
URL http://opus.kobv.de/ubp/volltexte/2014/6980/
URN urn:nbn:de:kobv:517-opus-69805
http://nbn-resolving.de/urn:nbn:de:kobv:517-opus-69805

Abstract

Organic semiconductors combine the benefits of organic materials, i.e., low-cost production, mechanical flexibility, lightweight, and robustness, with the fundamental semiconductor properties light absorption, emission, and electrical conductivity. This class of material has several advantages over conventional inorganic semiconductors that have led, for instance, to the commercialization of organic light-emitting diodes which can nowadays be found in the displays of TVs and smartphones. Moreover, organic semiconductors will possibly lead to new electronic applications which rely on the unique mechanical and electrical properties of these materials.

In order to push the development and the success of organic semiconductors forward, it is essential to understand the fundamental processes in these materials. This thesis concentrates on understanding how the charge transport in thiophene-based semiconductor layers depends on the layer morphology and how the charge transport properties can be intentionally modified by doping these layers with a strong electron acceptor.

By means of optical spectroscopy, the layer morphologies of poly(3-hexylthiophene), P3HT, P3HT-fullerene bulk heterojunction blends, and oligomeric polyquaterthiophene, oligo-PQT-12, are studied as a function of temperature, molecular weight, and processing conditions. The analyses rely on the decomposition of the absorption contributions from the ordered and the disordered parts of the layers. The ordered-phase spectra are analyzed using Spano's model. It is figured out that the fraction of aggregated chains and the interconnectivity of these domains is fundamental to a high charge carrier mobility. In P3HT layers, such structures can be grown with high-molecular weight, long P3HT chains. Low and medium molecular weight P3HT layers do also contain a significant amount of chain aggregates with high intragrain mobility; however, intergranular connectivity and, therefore, efficient macroscopic charge transport are absent. In P3HT-fullerene blend layers, a highly crystalline morphology that favors the hole transport and the solar cell efficiency can be induced by annealing procedures and the choice of a high-boiling point processing solvent. Based on scanning near-field and polarization optical microscopy, the morphology of oligo-PQT-12 layers is found to be highly crystalline which explains the rather high field-effect mobility in this material as compared to low molecular weight polythiophene fractions. On the other hand, crystalline

dislocations and grain boundaries are identified which clearly limit the charge carrier mobility in oligo-PQT-12 layers.

The charge transport properties of organic semiconductors can be widely tuned by molecular doping. Indeed, molecular doping is a key to highly efficient organic light-emitting diodes and solar cells. Despite this vital role, it is still not understood how mobile charge carriers are induced into the bulk semiconductor upon the doping process. This thesis contains a detailed study of the doping mechanism and the electrical properties of P3HT layers which have been p-doped by the strong molecular acceptor tetrafluorotetracyanoquinodimethane, F_4TCNQ. The density of doping-induced mobile holes, their mobility, and the electrical conductivity are characterized in a broad range of acceptor concentrations. A long-standing debate on the nature of the charge transfer between P3HT and F_4TCNQ is resolved by showing that almost every F_4TCNQ acceptor undergoes a full-electron charge transfer with a P3HT site. However, only 5% of these charge transfer pairs can dissociate and induce a mobile hole into P3HT which contributes electrical conduction. Moreover, it is shown that the left-behind F_4TCNQ ions broaden the density-of-states distribution for the doping-induced mobile holes, which is due to the long-range Coulomb attraction in the low-permittivity organic semiconductors.

Contents

1 Introduction

Organic semiconductors have gained much attention during the last decades driven by the ambition to realize electronic devices such as organic solar cells, organic light-emitting diodes, and organic field-effect transistors with novel properties* or at low costs that are not attainable using conventional inorganic semiconductors. Typically, such devices comprise one or several layers of molecular, oligomeric, and/or polymeric organic semiconductors that have been prepared by evaporation or by a solution-based process. Especially the deposition of soluble compounds promises low-cost mass production via printing, blading, or spraying techniques.[1]

One major obstacle in the understanding and physical description of organic semiconductor layers is their complexity with regard to the layer morphology. Many solution-cast organic semiconductors, in particular the alkyl-substituted poly- and oligothiophenes that are dealt with within this thesis, form layers with a heterogeneous morphology which is made up of more or less defined domains with different qualities of molecular order. The heterogeneity, i.e., the variation of molecular constitution and conformation, the variety of intermolecular interactions, and the occurrence of spatial disruptions (grain boundaries) in these layers, has dramatic impact on the fundamental semiconductor properties.[2–18]

A plain example of how layer morphology determines the behavior of an organic semiconductor is the molecular weight dependence of the charge carrier mobility in organic field-effect transistor (OFET) devices made from poly(3-hexylthiophene), P3HT. Experimentally, it has been found that the mobility typically increases by four orders of magnitude from 10^{-6} to $10^{-2}\,\mathrm{cm}^2/(\mathrm{Vs})$ upon an increase of the polymer's molecular weight from 3 000 g/mol (referred to as low molecular weight) to 30 000 g/mol (high molecular weight).[14–16,18] Atomic force microscopy and X-ray diffraction studies revealed that the layer morphology changes drastically within this regime.[12,14–25] As seen in Fig. 1.1a-d, crystallization of low molecular weight P3HT chains leads to the formation of well-defined needle-like nanocrystallites, while high molecular weight layers

* Such novel properties include, for instance, the potential mechanical flexibility and robustness of devices and the versatile adjustability of the optical and electronic properties of the organic semiconductors by synthetic chemistry.

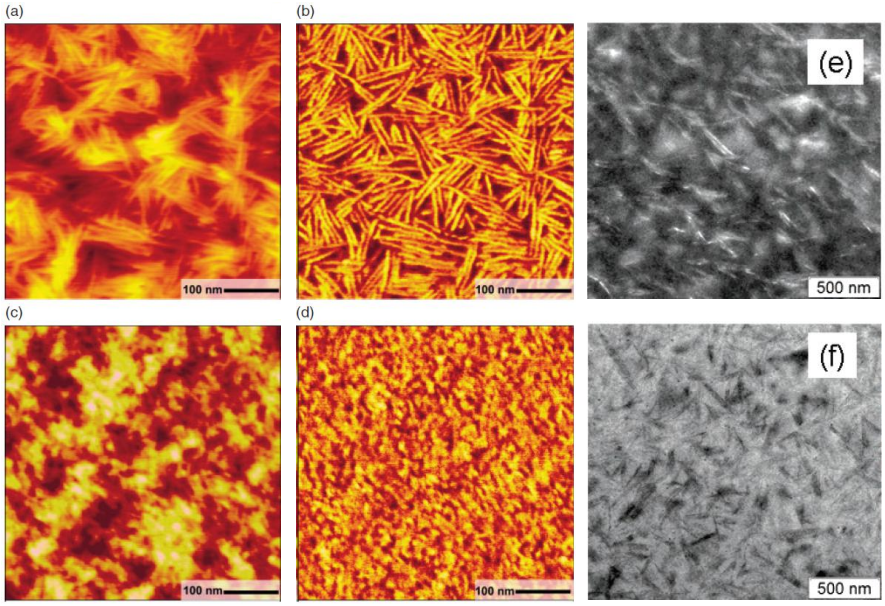

Figure 1.1: Atomic force microscopy topography and phase images of (a,b) low molecular weight and (c,d) high molecular weight P3HT layers by Kline et al.[14] (e,f) Transmission electron microscopy dark- and bright-field images of a low molecular weight P3HT layer by Zen et al.[17] Reprinted with permissions from Ref. [14] (a-d, Copyright 2003 Wiley-VCH Verlag GmbH & Co. KGaA, Weinheim) and Ref. [17] (e-f, Copyright 2006 American Chemical Society).

have, depending on the preparation conditions, a granular or lamellar structure which implies an intimate mixture of ordered and disordered domains.

Ambiguity arises in the interpretation of these data, in particular because the detailed layer structures are generally not experimentally accessible on a molecular scale. Kline et al. attributed the low field-effect mobility in low molecular weight samples to charge carrier trapping at the grain boundaries of the needle-like crystallites.[14] In high molecular weight P3HT, ordered domains might be interconnected by long P3HT chains which act as pathways for efficient charge transport.[15] On the contrary, Zen et al. pointed out that low molecular weight P3HT layers consist of highly ordered domains (the crystalline needles) which are actually embedded into a disordered matrix of non-planarized, coiled chains (see transmission electron microscopy images, Fig. 1.1e,f) and that these layers have a lower overall crystallinity than their high molecular weight counterparts.[16,17] Consequently, it has been proposed that the charge transport in P3HT and related polymer semiconductor layers is not determined by the perfection of the molecular packing, but by the overall degree of crystallinity of these samples.

Higher field-effect mobilities in the range of 0.1 to $1\,\mathrm{cm}^2/(\mathrm{Vs})$, which is on the order of the mobility in technologically relevant hydrogenated amorphous silicon, have been observed in α-oligothiophene-based layers deposited by evaporation.[26,27] Unlike the heterogeneous multi-phase morphologies of P3HT films, the structure of these layers

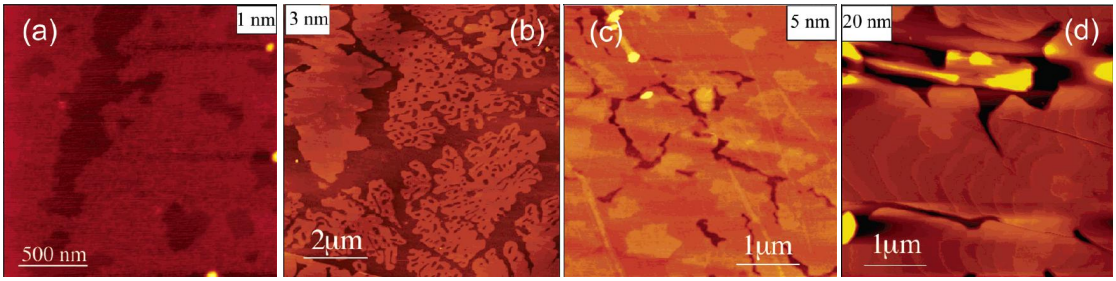

Figure 1.2: AFM topography images of α-6T layers with various nominal thicknesses on mica deposited from the vapor phase. Reprinted with permission from Ref. [29]. Copyright 2004 American Chemical Society.

exhibits high polycrystalline order (Fig. 1.2).[28,29] Crystallization is presumably facilitated by the chemical homogeneity of oligomer-based materials, in contrast to the typical distribution of molecular chain lengths in polymer samples. Structural studies on α-oligothiophene samples show that the molecules are almost planar and oriented perpendicularly to the substrate which is advantageous for the fast motion of charge carriers in a typical field-effect transistor geometry.[9,26,27,29] However, even in layers with very high crystallinity, macroscopic charge transport across the channel of an OFET might ultimately be determined by the presence of grain boundaries and packing defects. The typically lower mobilities (10^{-2} to 10^{-1} $\mathrm{cm}^2/(\mathrm{Vs})$) of solution-processed oligothiophenes such as α,ω-dihexylsexithiophene, for instance, have been attributed to imperfections in the chain packing quality, although the crystallinity of such layers is generally high.[30–33] In line with this interpretation, it has been shown computationally that paracrystalline disorder, i.e., fluctuations in the lattice spacing, leads to trap states in the band gap of the semiconductor which are detrimental to charge carrier transport.[34,35]

A common way to modify the charge carrier transport properties of organic semiconductors is to apply doping. Being widespread in the field of inorganic semiconductors, the concept of doping organic materials is very similar: By introducing appropriate electron-accepting (for p-type doping) or -donating (for n-type doping) species, additional charge carriers (holes or electrons, respectively) are created in the bulk semiconductor. These charge carriers relax in the energetic landscape and will eventually fill deep trap states and increase the charge carrier mobility. Correspondingly, doping has been successfully applied to enhance the field-effect mobility of transistors as compared to undoped devices.[36–39] Moreover, doped layers with high electrical conductivities are frequently used as hole- or electron-injecting layers in proximity to the electric contacts of organic light-emitting diodes.[40,41] Due to the doping-induced charge carrier density, the width of the Schottky depletion zone at the electrodes is reduced which results in better injection of charges and, consequently, leads to an increase of the luminance of these devices.

Reasonably stable p-type doping of solution-processed organic semiconductors has been achieved by using strong, soluble molecular acceptors such as tetrafluorotetracyanoquinodimethane (F_4TCNQ).[36–38,42–49] To date, the combination of F_4TCNQ and P3HT has resulted in the highest conductivities of up to 100 S/cm.[42] On the other hand, systematic studies of the doping mechanism and its effects on the charge carrier density and transport are rare.

Typical doping-related phenomena such as the often-reported low doping efficiency, which means that the charge carrier density induced by doping is much less than the dopant density,[46,50–53] and the nonlinear dopant density dependence of the conductivity[54] are not well addressed in literature.

In the first part of this thesis, which includes the work presented in sections 4.1 and 4.2, we clarify the quality and size of the aggregates in pure P3HT films and P3HT:fullerene bulk heterojunction layers by means of optical absorption spectroscopy. By applying the linear H-aggregate absorption model of Spano,[55] spectra recorded at various temperatures or after different annealing procedures are analyzed in terms of the aggregate width and the molecular order. These results are then linked to the local and macroscopic charge transport properties obtained from microwave conductivity measurements, organic field-effect transistors, and solar cells.

In the second part of this thesis, which includes the work presented in section 4.3, we investigate the highly ordered morphology of an oligomeric didodecyl-substituted polyquaterthiophene (oligo-PQT-12) sample, which has been fractionated from a polymer batch with a wide molecular weight distribution. We have recently shown that oligo-PQT-12 layers exhibit a field-effect mobility of typically $\sim 10^{-3}\,\mathrm{cm}^2/(\mathrm{Vs})$, which is unusually high for a low molecular weight polythiophene fraction.[56,57] Using scanning near-field and polarized optical microscopy, we characterize the molecular order in the ten-to-sub-micrometer range by taking advantage of the distinct optical properties of planarized and distorted molecules in ordered and less ordered (or disordered) environments. Although the crystallinity of oligo-PQT-12 layers is very high, we reveal local fluctuations of the quality and direction of molecular order, as well as the presence of grain boundaries which are otherwise not resolved by common topography-mapping techniques and which are probably adverse to charge carrier transport.

In the third part of this thesis, which includes the work presented in sections 4.4-4.7, we aim at understanding the process of doping P3HT with F_4TCNQ and the electrical characteristics of such doped layers. Using infrared and optical spectroscopy, we study the localized nature and the efficiency of the charge transfer. These results are compared to the density of doping-induced mobile holes which we have measured in a broad

range of doping ratios from the ppm to the per cent regime by means of admittance spectroscopy and surface potential measurements. Moreover, we elucidate the effect that ionized dopant molecules supposedly have on the charge transport by analyzing conductivity and mobility data using a model of Arkhipov et al.[58–60] These results are compared to absorption and charge transport data of F_4TCNQ-doped layers of poly(2-methoxy-5-(2'-ethylhexyloxy)-p-phenylene vinylene), MEH-PPV.

In what follows, we continue with an explanation of the principal concepts and models that are used in the present studies (Chapter 2). Chemical compounds and experimental procedures are subsequently described (Chapter 3). After that, a concise summary of the results and the interpretations of the present studies is given in Chapter 4. In Chapter 5, the main conclusions from this work are emphasized. Finally, Chapter 6 contains the list of publications related to this thesis and a detailed declaration of the authors' contributions. The publications and supplemental information are reprinted in the Appendix.

2 Theoretical background

2.1 Basic principles of organic molecular and polymeric semiconductors

Generally, organic molecular and polymeric semiconductors are hydrocarbon-based compounds with a conjugated binding pattern, i.e., with an alternating single and double bond sequence between the carbon atoms which make up the molecular backbone. In this configuration, the carbon atoms feature sp^2 hybridization, where the one p_z orbital is perpendicular to the three sp^2 orbitals in a common plane, see Fig. 2.1. At a carbon-carbon double bond, e.g., in ethylene, σ and π molecular orbitals are formed due to sp^2-sp^2 and p_z-p_z overlap of the two involved carbon atoms, respectively. Along a conjugated chain, p_z orbital overlap is not only across the double bonds, but occurs along the length of the conjugated segment, which gives single bonds a π-character as well. Consequently, extended π molecular orbitals are formed, where the ground-state electron-occupied π orbital with the highest energy (highest occupied molecular orbital, HOMO) and the unoccupied π orbital with the lowest energy (lowest unoccupied molecular orbital, LUMO) are of special importance for the semiconductor properties of these materials. In particular, the energy difference between HOMO- and LUMO-derived states, called band gap, is in the range of the energy of visible light which enables optical light absorption and emission.

A charge carrier, i.e., a hole or an electron, can reside in the HOMO or the LUMO of an organic semiconductor, respectively. Unlike in inorganic crystalline semiconductors, where charge carriers move rather freely in delocalized bands, strong electron-phonon coupling in organic semiconductors leads to the formation of polarons which become localized on individual molecules or chain segments. The strong binding of charges to the molecular backbone is particularly evident from the fact that a change of the charge distribution of a molecule, e.g., by optical absorption or ionization, will cause a change of the molecule's geometry in concomitance. Vice versa, molecular geometry variations, for instance in terms of a distribution of different conformations and constitutions in a thin film, cause a distribution of energetic states. Commonly, the density-of-states (DOS) distributions of the HOMO- and LUMO-derived states in semiconducting polymers are assumed to have a Gaussian shape. Charge transport within

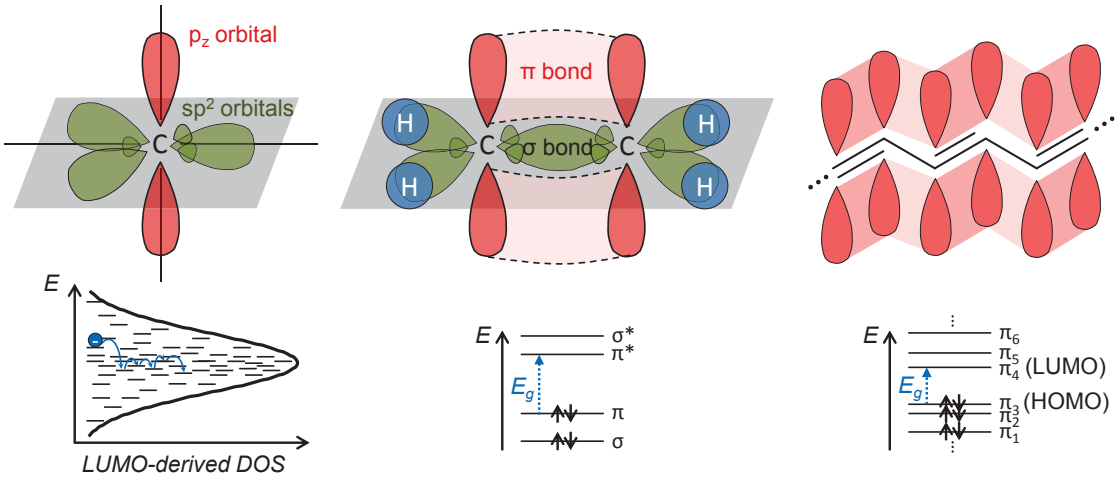

Figure 2.1: Scheme of the formation of the molecular π-orbitals in organic conjugated semiconductors. Involved sp^2-hybridized carbon atoms feature three sp^2 atomic orbitals in a common plane and one perpendicular p_z orbital (upper left). In ethylene, $H_2C{=}CH_2$, two sp^2 orbitals and two p_z orbitals form the sp^2-sp^2-σ- and the p-p-π-bond, respectively, with molecular σ- and π-orbitals ('*' denotes the antibonding character of some orbitals) (center). Along a conjugated chain, p_z orbitals overlap and result in an extended electronic π-system. The energetic distance between the highest-energy π-orbital which is occupied with two electrons in the ground state (HOMO) and the lowest-energy unoccupied π-orbital is the band gap E_g (right). Due to the strong localization of charge carriers to the molecular backbones, hole and electron transport proceeds via hopping in energetically distributed manifolds of HOMO- and LUMO-derived states, respectively (lower left).

this energetic landscape proceeds via consecutive hopping from one localized state to the next, see Fig. 2.1 and the explanations in section 2.4.

2.2 Crystallization of polyalkylthiophenes

Thiophene-containing polymers are among the most studied soluble organic semiconductors due to their good performance in organic field-effect transistors and organic solar cells. In particular, regioregular hexyl-substituted polythiophene, i.e., P3HT, was widely used in the past due to its high field-effect mobility and the high solar cell efficiency in combination with fullerene acceptors. A P3HT polymer chain is made up of thiophene repeat units, where each thiophene unit has a hexyl side chain in the 3-position which makes the polymer soluble in organic solvents such as chloroform and toluene. The chemical structure of P3HT is depicted in Fig. 2.2c. Regioregularity refers to the strict head-to-tail coupling of the thiophene units along the chain, which avoids steric hindrances between the side chains and allows the polythiophene backbone to planarize upon film formation.

Typically, thin films of alkyl-substituted polythiophenes are prepared by, e.g., spin-coating from a polymer solution, for instance in chloroform, where the polymer chains

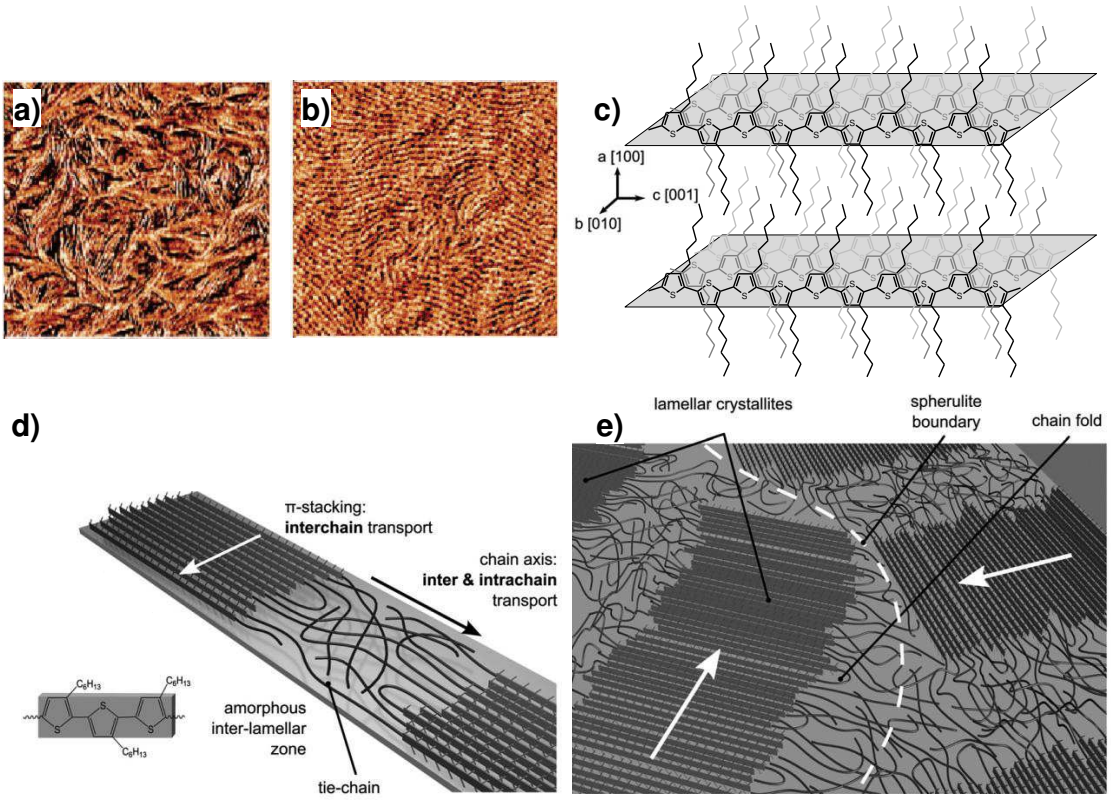

Figure 2.2: (a,b) Atomic force microscopy phase images (1 µm×1 µm) of P3HT layers drop-cast from toluene with molecular weights $M_w = 2.4$ and 7.0 kg/mol, respectively. (c) Schematic drawing of the molecular packing of P3HT chains. (d,e) Scheme of the morphology of a semicrystalline P3HT layer with ordered lamellae and disordered zones. Subfigures reprinted with permissions from Ref. [18] (a-b, Copyright 2006 American Chemical Society) and Ref. [61] (d-e, Copyright 2012 Wiley-VCH Verlag GmbH & Co. KGaA, Weinheim).

adopt a coiled conformation. In general, these layers are semicrystalline with disordered and ordered domains, whose fractions depend largely on the preparation conditions. Disordered domains contain polymer chains which did not planarize upon solvent evaporation. Ring-to-ring torsion and kinks within these chains interrupt the π-conjugation. As a result, the conjugation lengths in the disordered domains are widely distributed. Ordered domains, in contrast, are formed due to the interchain alignment of planarized polymer chains. High-resolution structural measurements reveal that ordered domains often correspond to needle-like or fibrillar structures, see Fig. 2.2a,b. Based on transmission electron and atomic force microscopy of P3HT layers, it was shown that the polymer chains crystallize in a lamellar fashion, where the planarized thiophene backbones are essentially oriented perpendicularly to the fibril long axis.[18,21] Thus, the fibril width correlates linearly with the contour length of the polythiophene chains for low and medium molecular weight samples.[18]

Fig. 2.2c shows the crystalline packing of P3HT chains on a molecular scale. In the a- or [100]-direction, sheets that incorporate the alkyl side chains are alternating with sheets

that comprise the thiophene backbones. In this direction, intermolecular coupling of the π-systems is absent due to the insulating nature of the alkyl substituents. In the b- or [010]-direction, planarized thiophene chains are cofacially stacked, such that electronic intermolecular π-π-interactions occur, which alter the optical and charge transport properties in comparison to disordered, noninteracting chains. Finally, the c- or [001]-direction points along the polythiophene chains' long axes.

Fig. 2.2d,e shows the current notion of P3HT layer morphology.[61] Due to the polydispersity, i.e., the distribution of polymer chain lengths, and constitutional, conformal or chemical defects of the polymer sample, many chain ends protrude beyond the edges of the crystalline fibrils, which results in disordered regions in between the fibrils. The disordered zones may also be made up of polymer chains which were not able to planarize during film formation. For a low molecular weight P3HT fraction, it has been suggested that the amorphous phase is primarily formed by the short chains of the chain length-distributed polymer sample.[17] Occasionally, chains that have been expelled from a fibril may fold back and re-enter the same fibril again. Back-folding of P3HT chains has indeed been observed on highly oriented pyrolytic graphite substrates.[62] Moreover, some chains can also bridge two different fibrils, especially in high molecular weight P3HT samples, which has beneficial consequences for the efficiency of interfibrillar, macroscopic charge transport, as we show in the course of this thesis. Indeed, back-folding of chains and the presence of tie chains are phenomena which are common to many high molecular weight polymers with fibrillar structures.[63,64]

2.3 Optical absorption of π-stacked linear polyalkylthiophene aggregates

The strength of an electronic-vibrational (vibronic) absorption is generally given by the square of the quantum mechanical transition dipole moment, i.e.,

$$A \propto \left| \langle \Psi_e \left| \tilde{\mu} \right| \Psi_g \rangle \right|^2, \tag{2.1}$$

where Ψ_g and Ψ_e are the electronic-nuclear wave functions of the ground and excited state, respectively, and $\tilde{\mu}$ is the dipole moment operator. Within the Born-Oppenheimer approximation, the wave functions can be separated as $\Psi(\vec{r},\vec{R}) = \phi(\vec{r},\vec{R})\chi(\vec{R})$, where ϕ and χ denote the electronic and nuclear wave functions, and $\vec{r}$ and $\vec{R}$ are the electronic and nuclear coordinates, respectively. Moreover, the dipole moment operator can be written as a sum of the electronic and nuclear dipole moment operators, $\tilde{\mu} = \tilde{\mu}_{\mathrm{el}} + \tilde{\mu}_{\mathrm{nuc}}$. For electronic transitions between two electronic states Ψ_g and Ψ_e, Eq. 2.1

can be transformed to[65]

$$A \propto \left|\overline{\langle \phi_e \left|\tilde{\mu}_{\mathrm{el}}\right| \phi_g \rangle}\right|^2 \left|\langle \chi_e | \chi_g \rangle\right|^2, \tag{2.2}$$

where the squared electronic transition dipole moment (first factor, averaged over the nuclear displacement during the transition) and the squared nuclear overlap integral (second factor) are separated. $\left|\langle \chi_e | \chi_g \rangle\right|^2$ is also called Franck-Condon factor. Often, the absorption spectra of amorphous organic semiconductors, where interchain π-π-interactions are insubstantial, can be assigned to a single electronic excitation in conjunction with the excitation of the first and higher excited states of essentially one vibrational mode starting from the ground-state, see Fig. 2.3. Based on modeling the nuclear wave functions with Hermite polynomials, the intensity series of such vibronic transitions from the ground-state to the m-th excited vibrational state (0-m transition) can be described by

$$|\langle \chi_m | \chi_0 \rangle|^2 = \frac{S^m \exp(-S)}{m!}, \tag{2.3}$$

where the Huang-Rhys factor S measures the mean level of vibrational excitation concomitant with the electronic transition.

If intermolecular π-π-interactions between two or more molecules are present, such as in polythiophene aggregates, the system Hamiltonian includes an interaction term $\tilde{H}'$, which accounts for the electrostatic interaction between the π orbitals of each two molecules n and m. In the simplest case of a dimer with identical molecules 1 and 2, the ground-state wave function can be expressed by $\Psi_g = \Psi_1 \Psi_2$ and has an energy of $E_g = 2E_{\mathrm{g,iso}} + W_g$, where $E_{\mathrm{g,iso}}$ is the ground-state energy of an isolated molecule and W_g is the Coulomb binding energy for the pair ($W_g < 0$) given by $\langle \Psi_g | \tilde{H}' | \Psi_g \rangle$. Upon electronic excitation, the coupling term $\tilde{H}'$ leads to a mixing of the states described by $\Psi_1^* \Psi_2$ and $\Psi_1 \Psi_2^*$ and, thus, two dimer states

$$\Psi_e^{\pm} = (\Psi_1^* \Psi_2 \pm \Psi_1 \Psi_2^*)/\sqrt{2} \tag{2.4}$$

with different energies

$$E^{\pm} = E_{\mathrm{e,iso}} + E_{\mathrm{g,iso}} + W_e \pm |\beta| \tag{2.5}$$

emerge. Here, $E_{\mathrm{e,iso}}$ is the excited-state energy of an isolated molecule and W_e is the Coulomb interaction energy between the charge distributions of the excited and the unexcited molecule, $W_e = \langle \Psi_1^* \Psi_2 | \tilde{H}' | \Psi_1^* \Psi_2 \rangle = \langle \Psi_1 \Psi_2^* | \tilde{H}' | \Psi_1 \Psi_2^* \rangle < 0$. $|\beta|$ denotes the resonance interaction energy, which stems from the terms $\pm| \langle \Psi_1^* \Psi_2 | \tilde{H}' | \Psi_1 \Psi_2^* \rangle | = \pm| \langle \Psi_1 \Psi_2^* | \tilde{H}' | \Psi_1^* \Psi_2 \rangle |$, and is equal to half of the energetic distance between E^+ and E^-. Fig. 2.3 depicts the split-up of the excited states in a dimer. Note that in H-aggregates,

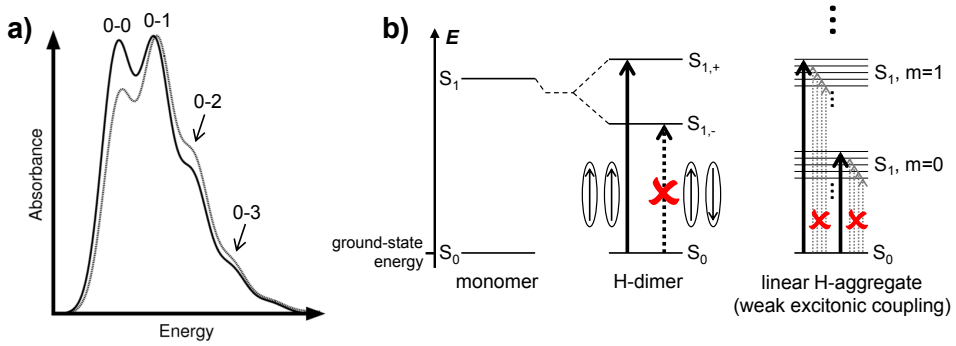

Figure 2.3: (a) Optical absorption spectra of planarized non-interacting (solid line) and weakly excitonically coupled molecules (dashed line), modeled with Eqns. 2.2, 2.3, and 2.6, assuming a Huang-Rhys factor of $S = 1$, a vibrational energy of $E_p = 0.3\,\mathrm{eV}$, and a linewidth of $\sigma = 0.12\,\mathrm{eV}$ for both spectra; additionally a free exciton bandwidth of $W = 0.1\,\mathrm{eV}$ is assumed for the aggregate spectrum. The labeled bands refer to the 0-m vibrational transitions starting from the vibrational ground-state, where m is the quantum number of the target vibrational state. (b) In excitonically coupled dimers, excited states split up. In weakly coupled linear H-aggregates, where the transition dipole moments of the individual molecules are perfectly parallel, the excited-state split-up leads to the formation of vibrational bands, labeled by m, where only transitions to the top of these bands are optically allowed.

where the transition dipole moments of both molecules are parallel, only transitions to the high-energy state are optically allowed, which leads to a spectral blue-shift of the absorption as compared to non-interacting molecules.[66]

In his model, Spano treated the far more complicated case of N weakly excitonically coupled polythiophene chains.[55,67] Due to the strong electron-phonon coupling, i.e., weak excitonic coupling, vibronic excitations are considered to be located on one molecular chain in the π-stack, while all other molecules remain electronically and vibrationally unexcited. As a consequence of the weak intermolecular interaction, Spano shows that the vibronic states split up into N states with an energetic distance which is lower than the vibrational energy. As a result, narrow vibrational bands are formed, see Fig. 2.3. Due to the H-aggregate nature of the parallel aligned planarized polythiophene chains in an ordered domain, i.e., the parallel orientation of the individual transition dipole moments, transitions to the top of the bands carry the oscillator strength, while all other transitions are optically forbidden. According to Spano's model and assuming a Gaussian line shape with a width of σ, the absorption spectrum of aggregated P3HT chains can be described by

$$A \propto \sum_{m=0} \left(\frac{S^m}{m!} \right) \left(1 - \frac{We^{-S}}{2E_p} \sum_{n \neq m} \frac{S^n}{n!\,(n-m)} \right)^2 \exp \left(\frac{\left(E - E_0 - mE_p - \frac{1}{2} \frac{WS^m e^{-S}}{m!} \right)^2}{2\sigma^2} \right), \quad (2.6)$$

where E_0 is the 0-0 transition energy of the aggregated species, E_p is the vibrational en-

ergy (fixed to 0.179 eV)*, m counts the vibrational excitations, the Huang-Rhys factor is fixed to $S = 1$ [55,68,69], and W is the free exciton bandwidth which is related to the electronic interaction energy and the energy difference between the top and the bottom of the vibrational bands. In Eq. 2.6, the bracketed weight factors correspond to the Franck-Condon factor of the aggregate absorption. Compared to Eq. 2.3, the Franck-Condon factor of non-interacting molecules, it can be seen that aggregation causes a modification of the vibronic intensity series. In particular, the intermolecular electronic coupling causes a reduction of the 0-0 band intensity relative to higher transitions, see Fig. 2.3. The correction of the transition energy by half of the bandwidth, i.e., by $\frac{1}{2}WS^m e^{-S}/m!$,† considers that only transitions to the top of the bands are optically allowed. Excitations to lower states of the bands become allowed if disorder is present; however, these transitions have very weak oscillator strengths and are, therefore, neglected.

As was shown by Beljonne et al. [72] and Gierschner et al. [73], the free exciton bandwidth W is related to the length of the cofacially stacked, planarized chain segments. We use the data from Ref. [73], assuming infinitely long linear polythiophene aggregates and including screening due to the polarizability of the surrounding molecules, to determine the width of the polythiophene fibrils, which shall be equivalent to the results from structural studies.

2.4 Charge carrier transport in semicrystalline polyalkylthiophene layers

In organic semiconductors, charge carriers are strongly bound to the molecular backbones. Therefore, charge transport is governed by a thermally activated hopping process from one site to another. The hopping rate ν is usually assumed to be Miller-Abrahams-like, [74,75] i.e.,

$$\nu \propto \exp(-2\gamma r) \begin{cases} \exp\left(-\frac{E_t - E_s}{k_B T}\right) & \text{if} \quad E_t > E_s \\ 1 & \text{else} \end{cases}, \tag{2.7}$$

where the first factor introduces the distance dependence along the coordinate r and the second factor is a weight that accounts for the temperature activation of a jump from a site with energy E_s to a site with energy E_t. γ is the inverse localization radius which is related to the electronic coupling of the two sites; $k_B T$ is the thermal energy.

* This corresponds to the C=C symmetric stretch, which is the vibrational mode that is the most coupled to the UV/Vis electronic transition of P3HT. [68]

† Note that the transition energy correction term in Eq. 2.6 erroneously lacks the '$m!$' in Refs. [70] and [71]. This has, however, no practical consequences, because the fit bounds cover only the 0-0 and 0-1 band range where $m! = 0! = 1! = 1$.

The hopping rate can be alternatively expressed, according to Marcus,[76] as

$$\nu \propto |J|^2 \frac{1}{k_B T} \exp\left(-\frac{\Delta G}{k_B T}\right) \quad \text{with} \quad \Delta G = \frac{\lambda}{4}\left(1 + \frac{G_{\text{free}}}{\lambda}\right)^2, \tag{2.8}$$

where J is the electronic coupling or transfer integral. In this model, charge carrier hopping requires that the energy barrier ΔG is overcome. G_{free} is the resulting Gibb's free reaction energy, and λ is the reorganization energy which stems from a relaxation of the molecular geometries and the change of polarization of the surrounding. Based on these hopping rates, several models have been developed by, for instance, Bässler et al.,[77] Vissenberg and Matters,[78] and Arkhipov et al.,[79] that describe the mobility of charge carriers in organic matter where the localized sites are energetically distributed. Practically, the relevant charge carrier densities in organic electronic devices are far lower than the total density of states (DOS). Therefore, charge transport is mainly located in the tail of the DOS distribution. Typically, DOS distributions of organic semiconductors are assumed to have a Gaussian or exponential dependence on energy.

All of the above-mentioned models have in common that they inherently assume that the charge transport properties and parameters are constant throughout the semiconductor under consideration. On the other hand, it has been pointed out in section 2.2 that polyalkylthiophene layers have a rather inhomogeneous structure with ordered and disordered regions. Clearly, the charge carrier mobility is higher in ordered domains than in disordered material due to the extended intermolecular π-stacking. Moreover, it has been pointed out by Sirringhaus et al.[9] that charge transport within a polyalkylthiophene stack is anisotropic. These authors found that the charge carrier mobility in field-effect transistors depends on the orientation of the π-stacking direction with respect to the direction of charge transport. In the b- and c-direction, i.e., parallel to the π-stacking direction and parallel to the conjugated molecules' long axes, respectively, charge transport is very efficient (see Fig. 2.2c for a visualization of the crystal packing). Street et al. estimated the hole mobility to be on the order of $10\,\text{cm}^2/(\text{Vs})$ and $300\,\text{cm}^2/(\text{Vs})$ or less in the b- and c-direction, respectively.[80] Charge transport along the a-direction is, in contrast, much less efficient due to the insulating nature of the alkyl side chains.

Street et al.[80] discuss a charge transport model for polymer layers with heterogeneous layer structure, which can explain the peculiarity that the field-effect mobility in such layers features a temperature-dependent activation energy. In particular, the DOS distribution is chosen to be a superposition of a DOS distribution with a sharp band edge which corresponds to the ordered portions of the layer, and an exponential DOS distribution which is contributed by the disordered domains. In addition, the mobility in the exponential band tail is chosen to depend on the position of the Fermi energy.

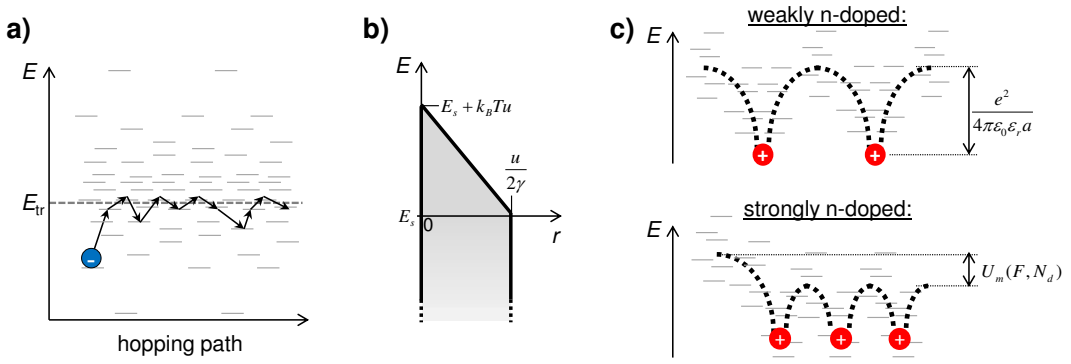

Figure 2.4: (a) Hopping transport of localized charge carriers in the tail of a DOS distribution is mainly between sites close to the transport energy E_{tr}. (b) Starting from a site with energy E_s, the positional and energetic distance of a hop is controlled by the hopping parameter u. Given a particular u, the shaded region shows the accessible range of target sites in terms of their energy and spatial distance. This region is used for the integration in Eq. 2.10. (c) Scheme of the overlap of the dopant ions' Coulomb potentials with the DOS distribution in the weak and strong doping regime according to Arkhipov et al.[59,60] The dopant ions constitute traps for the mobile charge carriers with a depth given by the Coulomb energy $e^2/(4\pi\epsilon_0\epsilon_r a)$. e is the elementary charge, $\epsilon_0\epsilon_r$ is the absolute permittivity of the semiconductor, and a corresponds to the distance between dopant ion and the nearest semiconductor site. Upon strong doping, neighboring Coulomb potentials overlap such that the trap depth is essentially reduced by $U_m(F, N_d)$.

This study is an example of how the heterogeneous properties are usually satisfactorily treated: Since there is no means of modeling the exact, and partially unknown, local electrical properties of such layers, effective values of the DOS distribution, the mobility, and other quantities are used in conjunction with the charge transport models which were originally derived for disordered matter.

2.5 Arkhipov's mobility model in doped disordered media

The model of Arkhipov and coworkers provides a concept to calculate the charge carrier mobility in arbitrary DOS distributions $g(E)$ at low electric field, where diffusion dominates the motion of charges.[58,79,81,82] Based on Miller-Abrahams-type hopping rates, see section 2.4, it is assumed that charge carrier transport comprises mainly sites that are close to a certain transport energy, as is shown in Fig. 2.4a. This assumption was motivated by earlier numerical studies of the hopping conduction in exponential band tails.[83] Here, following Arkhipov et al., we consider the transport of electrons; modification of the following equations to account for hole transport is, however, straightforward.

In an energetic distribution of states, the hopping rate is given by

$$\nu = \nu_0 \exp(-u) \quad \text{with} \quad u = 2\gamma r + \begin{cases} -\frac{E_t - E_s}{k_B T} & \text{if} \quad E_t > E_s \\ 0 & \text{else} \end{cases}, \tag{2.9}$$

where ν_0 is the attempt-to-hop frequency, u is the hopping parameter, γ is the inverse localization radius, E_t and E_s are the energy of the target and start site, respectively, and $k_B T$ is the thermal energy. For a given u, the number of available target sites in a spherical volume with radius r around a start site with energy E_s is

$$n(u, E_s) = 4\pi \int_0^{\frac{u}{2\gamma}} \int_{-\infty}^{E_s} g(E_t) r^2 \mathrm{d}r\mathrm{d}E_t + 4\pi \int_0^{\frac{u}{2\gamma} - \frac{E_t - E_s}{2\gamma k_B T}} \int_{E_s}^{E_s + k_B T u} g(E_t) r^2 \mathrm{d}r\mathrm{d}E_t. \tag{2.10}$$

The integration range corresponds to the shaded area in Fig. 2.4b. The first term in Eq. 2.10 accounts for hops that are downward in energy, and the second term accounts for upward jumps. In a relaxed system, i.e., under thermal equilibrium conditions, and at sufficiently low charge carrier concentration, most charge carriers reside in the tail of the DOS distribution. Within an acceptable distance around these states, vacant high-energy sites are far more numerous than states that are deeper in energy. Therefore, jumps that are downward in energy, i.e., the first term in Eq. 2.10, will be neglected. Substituting $E_{\mathrm{tr}} = E_s + k_B T u$ in the second term and evaluating the integral over r, Eq. 2.10 turns into

$$n(E_{\mathrm{tr}}, E_s) = \frac{\pi}{6} (\gamma k_B T)^{-3} \int_{E_s}^{E_{\mathrm{tr}}} g\left(E_t\right) \left(E_{\mathrm{tr}} - E_t\right)^3 \mathrm{d}E_t. \tag{2.11}$$

As a further simplification, the lower integration bound E_s can be replaced by $-\infty$ if the DOS function $g(E)$ has a tail that drops faster than $|E^{-4}|$. This is indeed the case for the tails of exponential- or Gaussian-shaped DOS functions that are commonly assumed for organic semiconductors. As hopping from one site to another becomes probable starting from $n(E_{\mathrm{tr}}, E_s) \approx 1$, the transcendent equation

$$\frac{6}{\pi} (\gamma k_B T)^3 = \int_{-\infty}^{E_{\mathrm{tr}}} g\left(E_t\right) \left(E_{\mathrm{tr}} - E_t\right)^3 \mathrm{d}E_t \tag{2.12}$$

defines the effective transport energy E_{tr} at low charge density. In order to account for the fact that some states in the DOS distribution are occupied and, thus, not available as target sites, the DOS function is replaced by the density distribution of vacant sites,

i.e., by $g(E)[1-(1+\exp[(E-E_F)/(k_BT)])^{-1}]$.[58] Thus, Eq. 2.12 turns into

$$\frac{6}{\pi}(\gamma k_B T)^3 = \int_{-\infty}^{E_{\mathrm{tr}}} \frac{g(E_t)}{1+\exp(-(E_t-E_F)/k_BT)}(E_{\mathrm{tr}}-E_t)^3 \mathrm{d}E_t, \tag{2.13}$$

where E_F is the Fermi energy. Note that E_{tr} is not necessarily the true transport energy, since downward jumps and, therefore, also back jumps to the start site, are neglected.

In order to calculate the charge carrier mobility, it is assumed that charge transport is governed by diffusion. According to the classical Einstein relationship, the mobility is related to the diffusion coefficient D via

$$\mu = \frac{eD}{k_BT} = \frac{e\bar{\nu}\bar{r}^2}{k_BT}, \tag{2.14}$$

where D is the product of the mean square jump distance $\bar{r}^2$ and the average jump rate $\bar{\nu}$. Since the previous assumptions about the DOS function include that most of the available sites are close to E_{tr}, the average hopping distance is, according to Ref. [58],

$$\bar{r} = \left(\int_{-\infty}^{E_{\mathrm{tr}}} g(E)\mathrm{d}E\right)^{-1/3}, \tag{2.15}$$

where, interestingly, the correction of $g(E)$ in terms of unavailable occupied states is not considered. Averaging of the hopping rates of all present charge carriers yields

$$\bar{\nu} = \frac{\int_{-\infty}^{E_{\mathrm{tr}}} f(E)\exp\left(\frac{E-E_{\mathrm{tr}}}{k_BT}\right)\mathrm{d}E}{\int_{-\infty}^{E_{\mathrm{tr}}} f(E)\mathrm{d}E}, \tag{2.16}$$

where $f(E) = g(E)/(1+\exp((E-E_F)/k_BT))$ is the density distribution of the occupied states. Interestingly, in Eq. 2.16 Arkhipov et al. omit the distance dependency of the hopping rate, which is given by Eq. 2.9. The denominator of Eq. 2.16 is roughly equal to the charge carrier density n, which is related to the Fermi energy and the DOS function via

$$n = \int_{-\infty}^{\infty} \frac{g(E)}{1+\exp((E-E_F)/k_BT)}\mathrm{d}E. \tag{2.17}$$

Finally, combining Eqns. 2.14-2.17 gives the charge carrier mobility

$$\mu = \frac{e\nu_0}{k_BTn}\left[\int_{-\infty}^{E_{\mathrm{tr}}} g(E)\mathrm{d}E\right]^{-2/3} \times \int_{-\infty}^{E_{\mathrm{tr}}} \frac{g(E)}{1+\exp((E-E_F)/k_BT)}\exp\left(\frac{E-E_{\mathrm{tr}}}{k_BT}\right)\mathrm{d}E. \tag{2.18}$$

Computationally, the closed set of Eqns. 2.13, 2.17, and 2.18 is solved numerically for a given DOS function $g(E)$ and given values of the parameters ν_0, γ, n, and T.

Usually, it is assumed that the DOS functions of organic semiconductors are exponential- or Gaussian-type. On the other hand, a broadening of the DOS distribution upon doping has been repeatedly suggested.[84–87] Arkhipov and coworkers point out that this broadening is probably caused by the Coulomb potentials of the ionized dopants which overlap with the DOS distribution of the undoped organic semiconductor,[59,60] see Fig. 2.4c. In other words, the dopant ions exert a rather long-range Coulomb attraction which leads to trapping of the majority charge carriers. Therefore, in their model, Arkhipov et al. replace the transport site closest to each dopant ion by a single trap, shifted in energy by the energy of the Coulomb attraction. The resulting DOS function, for mobile electrons and dopant cations, reads[59]

$$g(E) = \frac{N - N_d}{N} g_i(E) + \frac{N_d}{N} g_i \left(E + \frac{e^2}{4\pi\epsilon_0\epsilon_r a} - U_m(F, N_d) \right), \tag{2.19}$$

where N_d is the density of dopant ions, N is the total density of states in the intrinsic semiconductor, $g_i(E)$ is the intrinsic DOS function, ϵ_r is the relative permittivity, and a is the distance between a trapped charge carrier and a dopant ion, which should correspond physically to the distance of the dopant ion and the next semiconductor site. The non-trivial term $U_m(F, N_d)$ accounts for the overlap of neighboring Coulomb potentials at high dopant ion densities, where F is the electric field due to the externally applied bias. In this case, the effective trap depth is reduced, see Fig. 2.4c.

Using Eq. 2.19 as a DOS function for the calculation of mobilities can lead to a rather complex behavior of the mobility as a function of dopant ion concentration, i.e., doping ratio. Arkhipov et al. have observed that, especially for intrinsic DOS functions with a low energetic breadth, the mobility can decrease with increasing doping ratios in the regime of weak doping.[60] This is against the common notion that doping-induced charge carriers fill up the tail of the (intrinsic) DOS distribution and, thus, lead to an increase of the mobility. Arkhipov et al. show that the mobility decrease is due to the effect of Coulomb trapping which overcompensates for the fill-up of the DOS distribution. At high doping ratios, where neighboring Coulomb potentials overlap and trap depth is reduced, this imbalance is reversed and, accordingly, mobility increases.[59]

Although Arkhipov's model is widely used and established, it shall not be concealed that criticism of this model has been raised by other authors.[88] In particular, in the derivation of the trap depth, Arkhipov et al. treat the doped layers such as if they are depleted from the charge carriers and, thus, electrically charged. Generally, however, charge carriers are present and their electrical field should also be considered. The over-

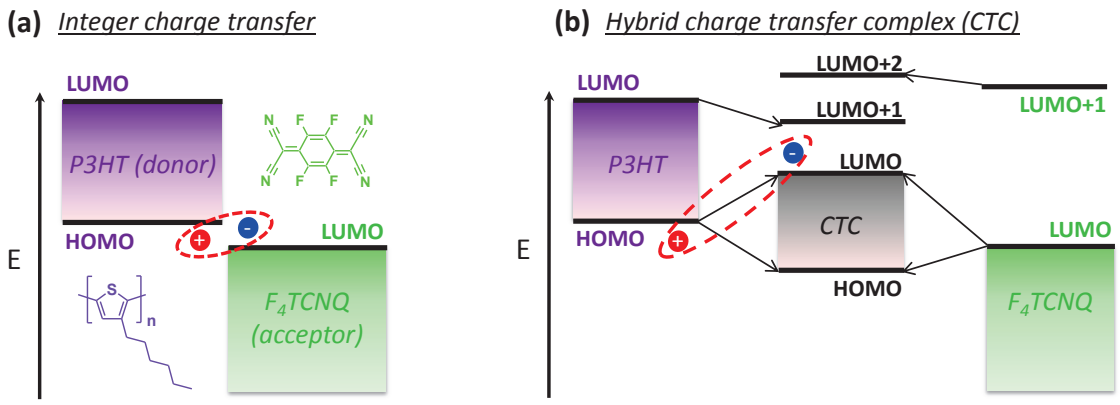

Figure 2.5: Contradictory models of the charge transfer between P3HT and F_4TCNQ. (a) Integer charge transfer model that presumes full ionization of donor and acceptor, resulting in a hole-F_4TCNQ anion pair that is bound or can split up. (b) Hybrid charge transfer model which presumes the formation of hybrid supramolecular orbitals upon electronic interaction of P3HT and F_4TCNQ. Free charge generation might occur by intermolecular excitation involving the HOMO of unreacted P3HT and the LUMO of a nearby CTC.

lap of neighboring dopant ions' Coulomb potentials is considered only in one direction, whereas it should be accounted for in three dimensions.

On the other hand, in this thesis, Arkhipov's mobility and DOS model for doped organic semiconductors is successfully used to explain quantitatively both the experimental work function data and the relationship between mobility or conductivity and doping ratio. We note that, avoiding Arkhipov's notion of a superposition of the DOS distribution and the spatially extended Coulomb potentials, the doped-layer DOS distribution can be essentially justified based on the argument that the (occupied) sites which are closest to the F_4TCNQ anions are lowered in energy by the Coulomb binding energy as compared to their original energetic position in the undoped (intrinsic) layer. Of course, then the notion of the overlap of the neighboring ions' Coulomb potentials becomes redundant, but, on the other hand, this term has little relevance ($U_m \leq 0.1\,\mathrm{eV}$) in the doping ratio range which we investigate here.

2.6 Models of the donor-acceptor ground-state charge transfer

It is well established that the doping effect in organic semiconductor thin films, i.e., the increase of the majority charge carrier density, is based on a charge transfer reaction involving an appropriate donor and acceptor. Two contradictory models that are commonly used to explain the donor-acceptor ground-state interaction are sketched in Fig. 2.5. Here, motivated by the aims of this thesis, we use the example of P3HT as a donor being p-doped with F_4TCNQ as a molecular acceptor.

In the integer charge transfer model (Fig. 2.5a), an electron is completely transferred from P3HT to the F_4TCNQ acceptor. Due to the typically low dopant concentration, the transferred electron remains fixed at the F_4TCNQ molecule. The associated hole on P3HT can either be Coulombically bound by the F_4TCNQ anion, or may move freely within the bulk matrix of P3HT. The notion of a strong Coulomb binding is in line with the common observation that the free charge carrier density is often far lower than the dopant concentration.[46,50] Charge carrier dissociation might be favored by dissociation pathways in the energetic landscape of the transport sites.[89] The exact mechanism that leads to the split-up of doping-induced charge pairs is, however, yet unknown.

Fig. 2.5b pictures an alternative model of molecular doping which relies on the formation of hybrid charge transfer complexes upon the interaction of the donor and acceptor. For the interaction between P3HT and F_4TCNQ, hybridization of the donor's HOMO and the acceptor's LUMO was suggested by density functional theory calculations.[42,90] Accordingly, a supramolecular charge transfer complex (CTC) is formed, whose HOMO and LUMO are distributed across both the donor and acceptor moiety.

Following the explanations in section 2.3, the electronic interaction term $\tilde{H}'$ between donor and acceptor leads to a mixing of wave functions which results in states that generally differ in energy from the states of the neutral, non-interacting donor-acceptor couple. Note that in contrast to the electronic interaction in molecular and polymer aggregates described in section 2.3, where wave function mixing is between the one-exciton states $\Psi_1^*\Psi_2$ and $\Psi_1\Psi_2^*$ (in case of a dimer; '*' denotes the electronic excitation of one of the molecules), the donor-acceptor interaction considers the mixing of the wave functions of the donor's HOMO (Ψ_D) and the acceptor's LUMO (Ψ_A). In the present case that (Ψ_D) and (Ψ_A) are not identical, the mixed-state wave functions are[65]

$$\Psi^{\pm} = \sqrt{\frac{1 \pm s}{2}}\Psi_D \pm \sqrt{\frac{1 \mp s}{2}}\Psi_A \tag{2.20}$$

and have energies of

$$E^{\pm} = E_0 \pm \frac{1}{2}\sqrt{\delta^2 + 4H_{AD}^2}, \tag{2.21}$$

where $s = \delta/\sqrt{\delta^2 + 4H_{AD}^2}$, E_0 is the average of the energy of the precursor states ($E_0 = 1/2[E_D + E_A + \langle\Psi_D|\tilde{H}'|\Psi_D\rangle + \langle\Psi_A|\tilde{H}'|\Psi_A\rangle]$), where the last two terms are usually small, and δ is the energy difference between these states ($\delta = E_0 = E_D - E_A + \langle\Psi_D|\tilde{H}'|\Psi_D\rangle - \langle\Psi_A|\tilde{H}'|\Psi_A\rangle$), where the last two terms are usually small. H_{AD} refers to the resonance interaction energy terms $\langle\Psi_A|\tilde{H}'|\Psi_D\rangle$ and $\langle\Psi_D|\tilde{H}'|\Psi_A\rangle$ which are equal. Accordingly, mixing of states becomes efficient if the energies of the precursor states are close in

energy ($\delta \to 0$, $s \to 1$). On the other hand, mixing becomes less probable if this energy difference is high.

In the hybrid CTC model, holes are created due to the electron deoccupation of P3HT HOMOs (and electron occupation of CTC LUMOs) as a consequence of Fermi-Dirac statistics. Whether these holes are free or Coulombically bound to charged CTCs is open to question.

3 Experimental methods

3.1 General sample preparation

The chemical structures of the herein used organic semiconductors are drawn in Fig. 3.1. Layers of regioregular poly(3-hexylthiophene), P3HT, poly(3,3‴-didodecyl-[2,2′:5′,2″: 5″,2‴]-quaterthiophene), oligo-PQT-12, and poly(2-methoxy-5-(2′-ethylhexyloxy)-p-phenylene vinylene), MEH-PPV, have typically been prepared by spin-coating from chloroform solutions on cleaned substrates in a N_2-filled glovebox at low contaminant level (O_2, H_2O < 1 ppm). The P3HT and oligo-PQT-12 fractions were provided by Prof. U. Scherf, Universität Wuppertal, and by Dr. S. Janietz, Fraunhofer IAP, Potsdam. The MEH-PPV sample was provided by Prof. H.-H. Hörhold, Universität Jena. Substrate cleaning was done by consecutive ultrasonication in various organic solvents (acetone, Hellmanex® cleaning solution, deionized water, and isopropanol). The semiconductors' solution concentrations and spin-coating speed were chosen according to the desired layer thickness. Note that some of the P3HT samples have deuterated side chains. Deuteration was chosen to enable neutron scattering experiments which are not subject of this thesis. Our extensive investigations show that the structural and electronic properties are not altered by the deuteration and that the performance of these P3HT fractions is comparable to non-deuterated P3HT in field-effect devices. For simplicity, usage of deuterated variants of P3HT is not explicitly mentioned in the following presentation.*

Bulk heterojunction samples of regioregular Sepiolid P200 P3HT, purchased from BASF, and [6,6]-phenyl-C_{61}-butyric acid methyl ester, PCBM, purchased from Solenne, were spin-coated from a mixed P3HT:PCBM weight ratio mixture in either chloroform or *o*-dichlorobenzene to give ca. 100 nm-thick layers. Some of these samples were thermally annealed at a selected temperature for 10 min. DCB-cast samples were stored in a Petri dish for 30 min (solvent annealing) prior to heating. As a reference for the PCBM optical absorption in a polymer matrix, a molar 1:1 mixed film of PCBM and polystyrene, PS, has been spin-coated from chloroform. PS was purchased from Fluka AG.

* Where applicable, deuteration of P3HT is, of course, indicated in the original articles.

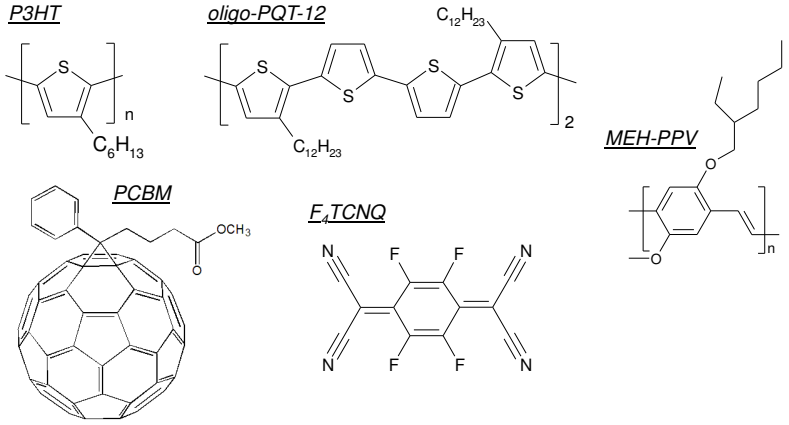

Figure 3.1: Chemical structures of the investigated semiconductors poly(3-hexylthiophene)(**P3HT**), poly(3,3'''-didodecyl-[2,2':5',2'':5'',2''']-quaterthiophene) (**oligo-PQT-12**), poly(2-methoxy-5-(2'-ethylhexyloxy)-p-phenylene vinylene) (**MEH-PPV**), [6,6]-phenyl-C_{61}-butyric acid methyl ester (**PCBM**), and tetrafluorotetracyanoquinodimethane (**F_4TCNQ**).

P-doping of P3HT and MEH-PPV was realized with the strong molecular acceptor tetrafluorotetracyanoquinodimethane, F_4TCNQ, purchased from Sigma-Aldrich. Layers with various thicknesses and mixing ratios have been prepared by spin-coating from common solutions of the polymer and F_4TCNQ in chloroform. Heat treatment of these samples has been avoided in order to prevent the volatilization of F_4TCNQ.

Note that all electrical measurements have been performed in the inert glovebox atmosphere or on encapsulated samples. Encapsulation was done using Araldite 2011 epoxy resin. Optical measurements were typically done directly after sample preparation in air. For exemplary samples, short-term stability of these samples with respect to ambient exposure was ensured by repeated measurements.

3.2 Optical absorption spectroscopy

UV-Vis-NIR absorption measurements have been performed on polymer solutions and thin films on glass substrates using a Cary 5000 photospectrometer. Typically, solution spectra have been recorded by averaging five consecutive scans in order to improve the signal-to-noise ratio. Thin film spectra have typically been measured using an integrating sphere. In the study of the optical properties of undoped and doped P3HT and MEH-PPV layers, ten consecutive transmission/reflection scans have been averaged. From the transmission and reflection spectra, the optical absorbance can be calculated by

$$\mathrm{OD} = \lg \frac{100 - \%R}{\%T}, \tag{3.1}$$

where $\%R$ and $\%T$ are the percentage reflectance and transmittance spectra.

Optical absorption spectra of P3HT and P3HT:PCBM layers have been analyzed with respect to the absorption of P3HT aggregates. Typically, the absorption of P3HT layers consists of a low-energy vibronic progression with a 0–0 peak at ca. 600 nm (2.05 eV) which originates from the absorption of the planarized chains in the ordered domains, and a rather unstructured high-energy part which stems from the twisted chains in disordered domains.[68] In order to analyze the aggregate part of the absorption, Eq. 2.6 was fitted to the low-energy part of the spectra, essentially covering the 0-0 and 0-1 absorption features. In this procedure, the parameters 0-0 transition energy E_0, linewidth σ, free exciton bandwidth W, and a global factor were varied according to nonlinear least squares Marquardt-Levenberg algorithm implemented by `gnuplot`. The sums in Eq. 2.6 have been truncated after the summands which correspond to $m = 6$ and $n = 10$, respectively. Confidence in the fitting range has been achieved by varying the upper and lower fit bounds around the 0-0 and 0-1 features which resulted in only little variation of the best-fit parameters.

3.3 Admittance measurements

Admittance measurements were performed on a sample geometry which corresponds to the traditional metal-insulator-semiconductor (MIS) structure. From these measurements, the charge carrier densities and bulk conductivities of undoped and p-doped P3HT and MEH-PPV have been extracted.

Fig. 3.2 shows the organic semiconductor MIS structure. Samples were prepared on cleaned glass substrates with a prepatterned indium-tin-oxide (ITO) electrode. First, a butanone solution of 90%/10% phenyl-/methyl-substituted polysilsesquioxane (PSQ), purchased from Gelest Inc., was spin-coated and cured at 350°C to give a ca. 160 nm-thick insoluble insulator layer. Then, the undoped or doped polymer solutions were spin-coated in inert atmosphere to give layer thicknesses in the range of 300-1200 nm. As an ohmic back contact, 5 nm MoO_3 and 100 nm Al were thermally evaporated in high vacuum through a shadow mask in order to prepare an electrode which partially overlaps the ITO contact. The resulting sample area was 16 mm^2. The samples were finally encapsulated.

The home-built admittance spectroscopy setup consists of a lock-in and a current-voltage amplifier. The lock-in oscillator supplies an AC voltage with selectable frequency to the circuit of the MIS sample and the current-voltage amplifier. The amplitude of the oscillator signal was typically $V_{\mathrm{rms}} = 25\,\mathrm{mV}$ in order to measure the small-signal

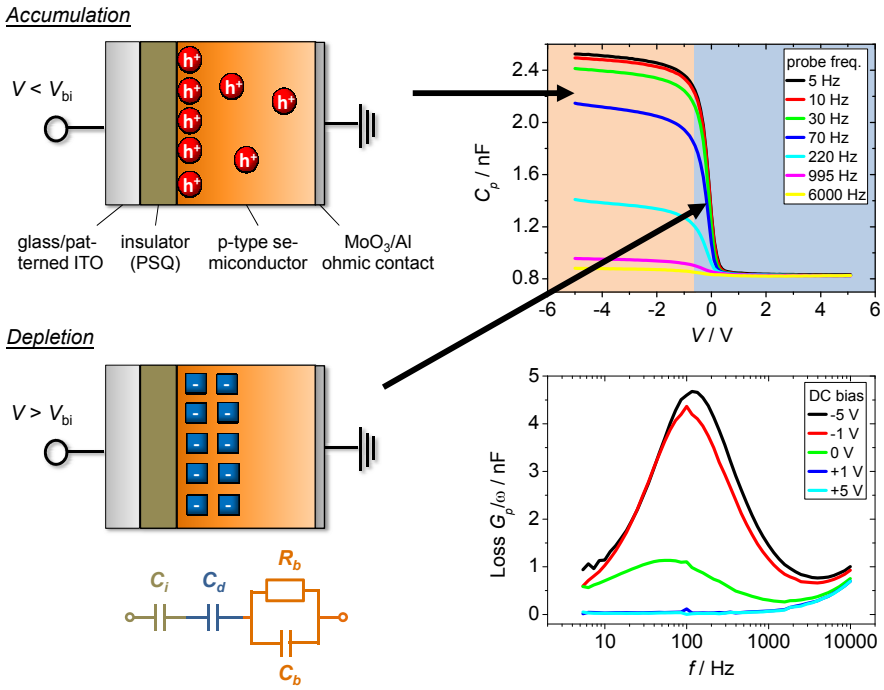

Figure 3.2: Left: Scheme of the MIS sample structure and the formation of an accumulation or depletion zone at the semiconductor-insulator interface depending on the DC bias V at the ITO contact. V_{bi} is the built-in voltage. The MIS sample can be modeled by the equivalent R-C circuit shown at the bottom. Top right: Exemplary C_p-V curves at different frequencies. Mott-Schottky analysis of the depletion region is used to determine the ionized dopant density. Bottom right: Exemplary G_p/ω-f curves show a characteristic maximum f_{max} when the sample is biased in accumulation, which is used to calculate the bulk conductivity.

response of the sample. The current-voltage amplifier translates the resulting AC current into a voltage signal which is passed back to the lock-in amplifier. The lock-in amplifier detects the 0°- and 90°-components of this signal with respect to the oscillator signal. For convenience, this output is translated into the parallel conductance and capacitance, G_p and C_p, respectively, i.e., the real and imaginary components of the admittance, $Y = G_p + i\omega C_p$. Upon applying a DC bias V to the ITO electrode, accumulation ($V < V_{bi}$ for a p-type semiconductor, where V_{bi} is the built-in voltage) or depletion ($V > V_{bi}$) of charge carriers occurs at the insulator-semiconductor interface. The DC voltage is provided by the current-voltage amplifier.

The MIS sample structure can be described by the equivalent circuit shown in Fig. 3.2. In principle, each layer is represented by a parallel R-C element. In practice, the resistances of the insulator and of the depletion zone are infinite and therefore neglected. C_i, C_d, and C_b are the capacitances of the insulator, depletion zone, and bulk layer, respectively. R_b is the bulk resistance. The equivalent circuit relates to the parallel con-

ductance and capacitance as follows:

$$G_p = \frac{\omega^2 R_b C_i^2 C_d^2}{\omega^2 R_b^2 [C_i^2 (C_d + C_i)^2 + C_i (2 C_d C_b^2 + C_d^2 C_b) + C_d^2 C_b^2] + (C_i + C_d)^2} \tag{3.2}$$

$$C_p = \frac{\omega^2 R_b^2 [C_i^2 (C_d C_b^2 + C_d^2 C_b) + C_i C_d^2 C_b^2] + C_i C_d^2 + C_i^2 C_d}{\omega^2 R_b^2 [C_i^2 (C_d + C_i)^2 + C_i (2 C_d C_b^2 + C_d^2 C_b) + C_d^2 C_b^2] + (C_i + C_d)^2} \tag{3.3}$$

Thereby, C_d, C_b, and R_b depend on the width of the depletion zone W according to $C_d = \epsilon_0 \epsilon_0 A / W$, $C_b = \epsilon_0 \epsilon_0 A / (L - W)$, and $R_b = (L - W) / (\sigma A)$, where ϵ_r is the relative permittivity (assumed to be 3.5 and 3.0 for P3HT and MEH-PPV, respectively), A is the sample area, L is the semiconductor layer thickness, and σ is the low-field bulk conductivity. Turning to accumulation, W vanishes, which means that C_d approaches infinity mathematically or, equivalently, C_d cancels from the equivalent circuit.

For measuring the charge carrier density in the semiconductor, we consider the depletion region of the C_p versus V curves at low frequency. Under this condition, the voltage-dependent width of the depletion zone is able to follow the small perturbation of V by the oscillating voltage V_{rms} instantaneously, i.e., the charge carriers in the bulk layer redistribute in phase with the AC voltage. At low frequency, $\omega \to 0$, Eq. 3.3 simplifies to

$$C_p = \left(\frac{1}{C_i} + \frac{1}{C_d} \right)^{-1}, \tag{3.4}$$

i.e., a connection of C_i and C_d in series. In accumulation ($C_d \to \infty$), the parallel capacitance is equal to the insulator capacitance, see Fig. 3.2. When depletion occurs, C_d becomes finite and the total sample capacitance drops. If inversion layer formation is absent, the depletion zone will grow until the whole semiconductor layer is depleted. Then, C_p yields the geometric capacitance of the MIS stack. In the depletion range, C_i and C_d carry equal charge $enAW$, where n is the number density of ionized dopants in the depletion zone, which is equivalent to the density of mobile holes in p-type P3HT and MEH-PPV. The applied external bias drops across C_i and C_d according to $V = V_i + V_d - V_{\mathrm{bi}}$, where V_{bi} is the built-in voltage. It can be shown that V_i and V_d relate to the depletion zone width as $V_d = \frac{en}{2\epsilon_0 \epsilon_r} W^2$ and $V_i = \frac{enA}{C_i} W$. Solving for W and using the definition of the depletion capacitance and Eq. 3.4, the Mott-Schottky relation

$$\frac{1}{C_i^2} = \frac{2}{\epsilon_0 \epsilon_r enA^2} (V - V_{\mathrm{bi}}) + \frac{1}{C_i^2} \tag{3.5}$$

can be derived which is conveniently used to determine the mobile charge carrier density n from the linear region of a $1/C_p^2$-V plot.

For determining the bulk conductivity of the organic semiconductor layers, we consider the G_p frequency spectra under accumulation conditions, i.e., $C_d \to \infty$ (for our samples, V is typically chosen to be -5 V). Eq. 3.2, expressed in terms of the loss function G_p/ω, simplifies to

$$G_p/\omega = \frac{\omega R_b C_i^2}{\omega^2 R_b^2 (C_i + C_b)^2 + 1}, \tag{3.6}$$

which describes a Gaussian bell shape in a G_p/ω-$\log\omega$ plot with a maximum at $\omega_{\max} = 1/(R_b(C_i + C_b))$. Indeed, such a curve is experimentally observed for our samples, see Fig. 3.2 (the frequency in the graph is expressed in terms of $f = \omega/(2\pi)$). Physically, the accumulation zone charge and discharge during the AC cycles starts to lag behind the voltage signal at frequencies around $\omega_{\max}$. Concomitantly, the accumulation capacitance drops toward the geometric capacitance. Considering the bulk resistance and capacitance in accumulation, $R_b = L/(\sigma A)$ and $C_b = \epsilon_0 \epsilon_r A/L$, the frequency maximum can be used to determine the bulk conductivity according to

$$\sigma = 2\pi f_{\max} (\epsilon_0 \epsilon_r + L C_i / A) . \tag{3.7}$$

Note that these values represent the conductivity at low electric field, because the DC voltage drops entirely across the insulator capacitance.

3.4 Surface potential (Kelvin probe) measurements

Surface potential measurements with the Kelvin probe method have been performed in order to gather information about the electronic structure and mobile hole density in the bulk of formally undoped and doped P3HT layers. Generally, the deposition of an organic semiconductor on a substrate with sufficiently low or high work function leads to the injection of electrons or holes into the semiconductor's manifold of LUMOs or HOMOs, respectively, which is driven by the formation of a constant Fermi level throughout the sample (see Fig. 3.3). As a result, band bending occurs, i.e., the semiconductor work function becomes layer thickness dependent. In case the semiconductor is p-doped, a classical Schottky contact forms on a low-work function electrode. In addition to minor electron injection into the LUMO manifold, Fermi level alignment is achieved here by the formation of a negative space charge zone at the semiconductor-metal interface, which is due to the depletion of mobile holes. As a consequence, a homogeneous distribution of negatively charged dopant ions is left behind which yields a characteristic parabolic shape of the work function versus layer thickness curve within the depletion width (see bottom right panel in Fig. 3.3).

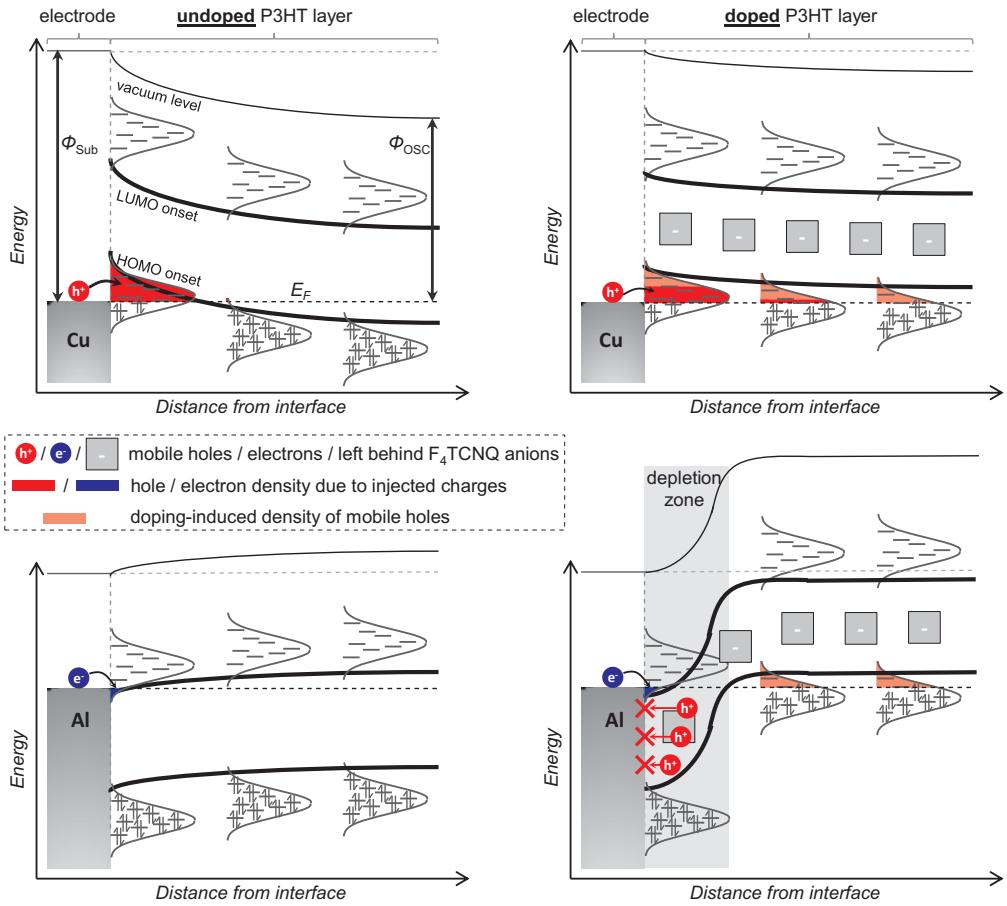

Figure 3.3: Scheme of the electron and hole transfer of undoped (left panels) and doped (right panels) P3HT layers on a high (Cu, upper panels) and a low work function (Al, lower panels) metal substrate.

Experimentally, undoped and doped P3HT layers were deposited from chloroform solutions by spin-coating on metal substrates. The solution concentrations were varied in order to prepare layers with different thicknesses in the range of ca. 5-200 nm. As low- and high-work function electrodes aluminum and copper, respectively, have been evaporated under high-vacuum conditions. The surface potential is measured using the capacitor-like configuration of a Kelvin probe setup.* The potential difference between the sample and a reference tip is adjusted such that the gap in between those is field-free. The work function of the sample is then calculated by

$$\Phi_{OSC}(L) = \Phi_{Sub} - \phi(L), \tag{3.8}$$

where Φ_{Sub} is the work function of the metal substrate, L is the semiconductor layer thickness, and $\phi(L)$ is the surface potential, referenced to $\phi = 0$ at the metal electrode.

* The instrument is a SKM KP 4.5 from KP Technologies Ltd. with 2-mm-diameter gold probe, calibrated against a highly ordered pyrolytic graphite reference sample with a work function of 4.6 eV.

In order to extract information on the density of mobile holes and the DOS distributions, the work function curves have been reconstructed by solving the following set of equations. The electrical potential $\phi(x)$ in a p-doped semiconductor layer follows the Poisson equation

$$\frac{\mathrm{d}^2\phi(x)}{\mathrm{d}x^2} = -\frac{\mathrm{d}F(x)}{\mathrm{d}x} = \frac{e}{\epsilon_0\epsilon_r}\left(n(x) - p(x) + N_a\right), \tag{3.9}$$

with the boundary condition $\frac{\mathrm{d}\phi}{\mathrm{d}x}(L) = F(L) = 0$, which is given by the measurement conditions of the Kelvin probe experiment (i.e., the electric field F vanishes between the sample surface and the Kelvin probe tip). In Eq. 3.9 $n(x)$ and $p(x)$ are the electron and hole densities in the LUMO and HOMO manifolds, respectively, N_a is the density of ionized acceptors which is equal to the density of mobile majority charge carriers in the semiconductor bulk, x is the distance from the electrode, and ϵ_r is the relative permittivity. Integration of Eq. 3.9 with respect to x is not feasible, because the position dependencies of n and p are not known. Therefore, we use the substitution $\frac{\mathrm{d}F}{\mathrm{d}x} = \frac{\mathrm{d}F}{\mathrm{d}\phi}\frac{\mathrm{d}\phi}{\mathrm{d}x} = \frac{\mathrm{d}\phi}{\mathrm{d}x}\frac{\mathrm{d}}{\mathrm{d}\phi}\left(-\frac{\mathrm{d}\phi}{\mathrm{d}x}\right)$ such that the left-and right-hand sides of Eq. 3.9 can be integrated with respect to $\frac{\mathrm{d}\phi}{\mathrm{d}x}$ and ϕ, respectively. The integration bounds are from a position x within the semiconductor towards the semiconductor surface at $x = L$:[91,92]

$$\int_{\frac{\mathrm{d}\phi}{\mathrm{d}x}}^{0}\left(\frac{\mathrm{d}\phi}{\mathrm{d}x}\right)'\mathrm{d}\left(\frac{\mathrm{d}\phi}{\mathrm{d}x}\right)' = \int_{\phi}^{\phi_L}\frac{e}{\epsilon_0\epsilon_r}\left(n(\phi') - p(\phi') + N_a\right)\mathrm{d}\phi' \tag{3.10}$$

$$\frac{\mathrm{d}\phi}{\mathrm{d}x}(\phi_L, \phi) = \left(-\frac{2e}{\epsilon_0\epsilon_r}\int_{\phi}^{\phi_L}\left(n(\phi') - p(\phi') + N_a\right)\mathrm{d}\phi'\right)^{1/2}, \tag{3.11}$$

where the primes indicate the integration variables and $\phi_L = \phi(L)$ is the surface potential. The equilibrium local charge densities are related to the HOMO- and LUMO-derived DOS distributions g_{HOMO} and g_{LUMO}, the Fermi level E_F, and the local potential according to

$$n(\phi) = \int_{-\infty}^{\infty}\frac{g_{\mathrm{LUMO}}(E + e\phi)}{1 + \exp\left(\frac{E - E_F}{k_B T}\right)}\mathrm{d}E \quad \text{and} \tag{3.12}$$

$$p(\phi) = \int_{-\infty}^{\infty}\frac{g_{\mathrm{HOMO}}(E + e\phi)}{1 + \exp\left(\frac{E_F - E}{k_B T}\right)}\mathrm{d}E. \tag{3.13}$$

The surface potential ϕ_L is related to the layer thickness L and Eq. 3.11 according to

$$0 = L - \int_{0}^{\phi_L}\left(\frac{\mathrm{d}\phi}{\mathrm{d}x}\right)^{-1}\mathrm{d}\phi. \tag{3.14}$$

The set of Eqns. 3.11-3.14 are solved at given values of N_a and T and given DOS functions g_{HOMO} and g_{LUMO} using numerical procedures. Surface potentials are translated into work function values using Eq. 3.8.

4 Summarized presentation

4.1 Quantitative analysis of the temperature-dependent optical absorption of P3HT layers with respect to layer morphology and the local and macroscopic charge transport properties*

The molecular weight dependence of the morphology and charge carrier mobility of P3HT layers has been pointed out in the Introduction. In this section, we make use of the analytical model of Spano[55] to evaluate the optical absorption of layers prepared from two different P3HT molecular weight fractions and measured at various temperatures. By this, information about the size, number, and packing quality of molecularly ordered domains in these layers are gained. These insights into layer morphology are then linked to the local (intragrain) and macroscopic charge transport properties.

Optical absorption spectra and local and macroscopic charge carrier mobilities of P3HT layers have been previously investigated in the course of the author's diploma thesis.[56] Fig. 4.1 shows the absorption spectra of two different P3HT batches with high and medium molecular weight, $M_w = 35\,800\,\mathrm{g/mol}$ and $M_w = 9\,200\,\mathrm{g/mol}$, respectively. Molecular weights have been determined by gel permeation chromatography. It has been found that significant spectral changes are induced upon heating the medium molecular weight P3HT layers at temperatures far below the melting range.† In particular, a pronounced blue-shift and the loss of vibronic structure is exhibited which implies that the P3HT chains adopt a less planarized backbone conformation. After cooling, the initial absorption spectrum is almost recovered, i.e., the modification of the nanomorphology is mostly reversible. For comparison, the absorption spectrum of high molecular weight P3HT is much less affected by heating and recovers completely upon cooling.

Local and macroscopic charge transport in P3HT has been previously investigated by

* This section is based on P. Pingel, A. Zen, R. D. Abellón, F. C. Grozema, L. D. A. Siebbeles, and D. Neher, "Temperature-Resolved Local and Macroscopic Charge Carrier Transport in Thin P3HT Layers", Adv. Funct. Mater. 20, 2286-2295 (2010).

† The onset temperature of melting can be read off from the calorimetry thermograms shown in the inset of Fig. 4.1. For medium and high molecular weight P3HT T_m is ca. 150°C and 220°C, respectively.

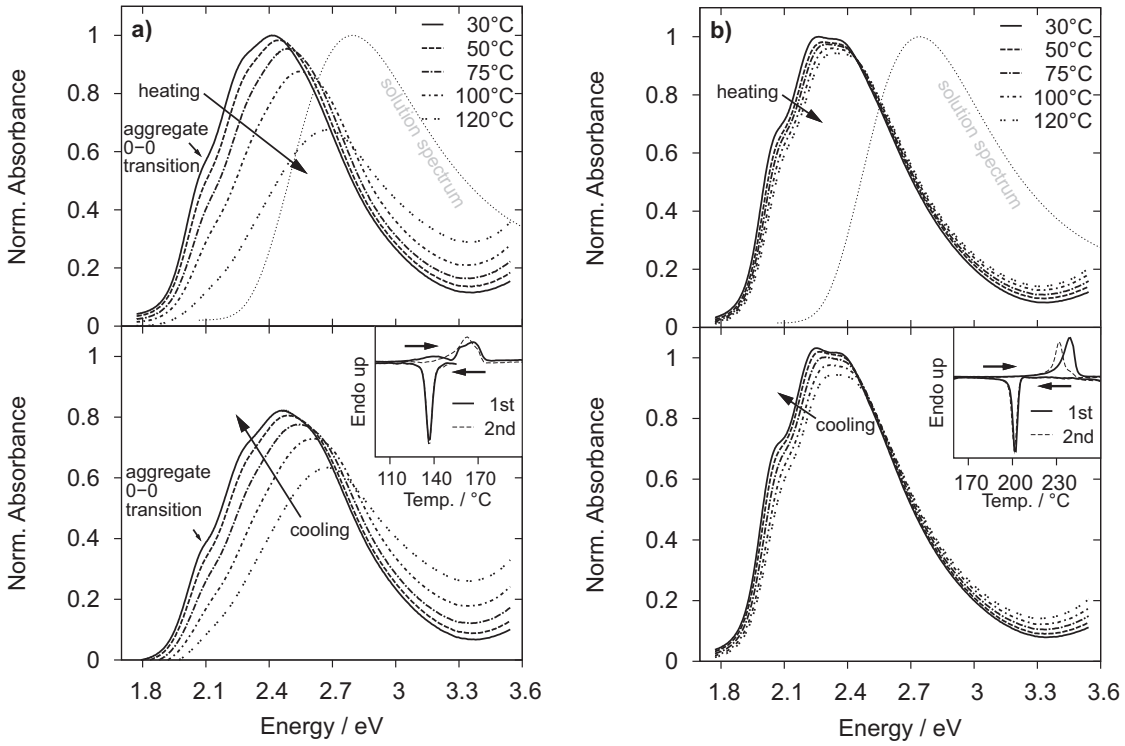

Figure 4.1: In-situ temperature dependence of the optical absorption of (a) medium and (b) high molecular weight P3HT layers upon a cycle of heating (upper panels) and subsequent cooling (lower panels). The absorption of P3HT in chloroform solution is shown for comparison. The insets show DSC thermograms of the solution-crystallized samples.

pulse-radiolysis time-resolved microwave conductivity (PR-TRMC) and organic field-effect transistor (OFET) measurements, see Fig. 4.2. The PR-TRMC technique induces a back-and-forth movement of charge carriers within the individual ordered domains of the sample. In contrast, charge transport in the channel of an OFET typically requires that charge carriers have to cross various morphological phases and grain boundaries. While the local PR-TRMC mobilities of medium and high molecular weight P3HT are rather similar and show both an increase upon heating, the macroscopic OFET mobilities are very different and show contrary temperature dependencies. In particular, we found that the macroscopic charge transport is thermally activated in high molecular weight P3HT while the macroscopic mobility drops strongly upon heating in medium molecular weight P3HT. Based on the changes of the optical absorption, we have qualitatively concluded that macroscopic charge transport is limited by the presence of disordered domains in the pathway of the charge carriers in medium molecular weight P3HT.

Extending the previous qualitative arguing, we now performed a precise quantitative analysis of the absorption spectra of the P3HT layers using the Spano model. Spano's analytic model describes the optical absorption of linear H-aggregates, which are formed in the ordered domains of P3HT layers due to the lamellar cofacial pack-

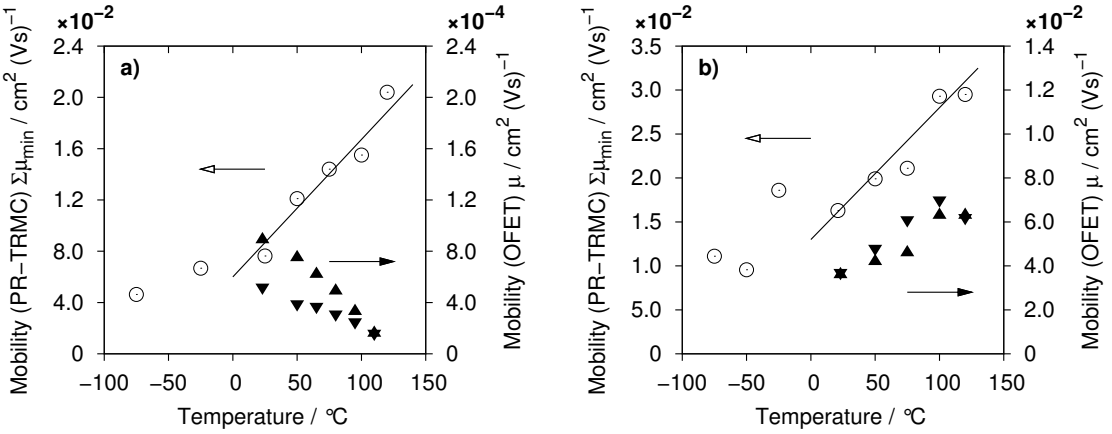

Figure 4.2: In-situ temperature dependence of local (PR-TRMC) and macroscopic (OFET) charge carrier mobilities in (a) medium and (b) high molecular weight P3HT. OFET mobilities were recorded in a cycle of heating and subsequent cooling. The lines are guides to the eyes.

ing of the planarized thiophene chains. A detailed review of the molecular packing of P3HT chains and the Spano model are given in sections 2.2 and 2.3, respectively.

The absorption spectrum of P3HT in chloroform solution, where the polymer chains adopt a non-planar conformation, suggests that the absorption of the solid disordered P3HT phase is insignificant at energies below 2.3 eV, see Fig. 4.3a. Therefore, in order to decompose the absorption spectra of P3HT layers into the contributions which stem from the aggregated and the disordered phases, Eq. 2.6 (the equation of the Spano model that describes the absorption of the H-aggregates) was fitted to the low-energy parts of the spectra, covering the 0-0 and 0-1 transition features. In this procedure, the 0-0 transition energy E_0, the Gaussian linewidth parameter σ, the free exciton bandwidth W, and a global scaling parameter were varied. An example of a fit is shown in Fig. 4.3a, and the resulting best-fit parameters for the medium and high molecular weight P3HT fractions are plotted in Fig. 4.3b,c as a function of the temperature. Note that the residual, i.e., the difference of the experimental and the modeled aggregate spectrum which should correspond to the disordered-phase spectrum, exhibits weak vibronic features while the absorption spectrum of a completely amorphous phase should be featureless. This suggests that the assumption of single values for E_0, σ, and W (instead of distributions) and the choice of Gaussian line shapes may be too simplistic. However, based on the coincidence of the energetic positions of the residual with the absorption of coiled P3HT chains in chloroform, we assume that the modeled absorption curve is representative for the aggregate absorption and covers most of this species present in the investigated layers.

Noticeably, the values for the 0-0 transition energy E_0 and for the linewidth σ are very similar for both P3HT fractions and their temperature dependence is weak. This sug-

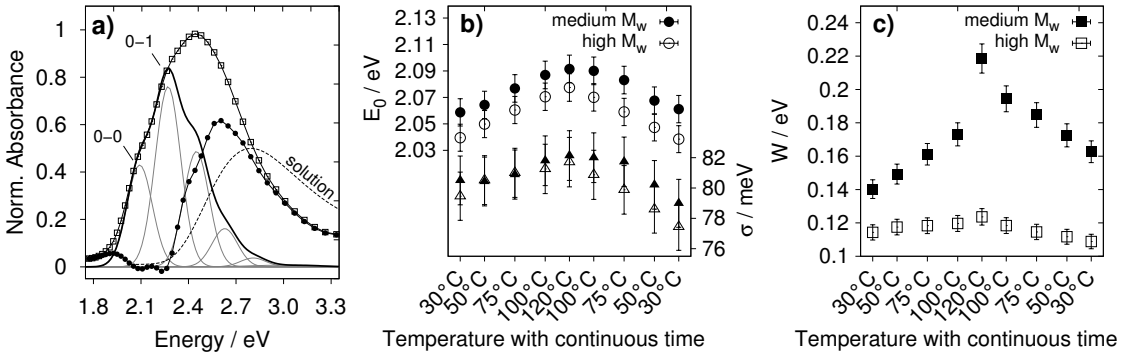

Figure 4.3: (a) Example fit of Eq. 2.6 (bold line) to the region of aggregate absorption (2.0-2.3 eV, comprising the 0-0 and 0-1 features) of a medium molecular weight P3HT layer at 50°C. The disordered-phase spectrum (line with closed symbols) is calculated by subtracting the fitted curve from the experimental data (line with open symbols). This spectrum has an energetic position similar to the solution spectrum of P3HT dissolved in chloroform (dashed line) (b,c) Best-fit parameters E_0, σ, and W, being the 0-0 transition energy of the aggregates' absorption, the width of the Gaussian line shape, and the free exciton bandwidth, respectively.

gests that the local electronic properties of the aggregated chains in the ordered domains are only weakly affected by molecular weight and temperature. The large spectral changes upon heating of medium molecular weight P3HT can, however, be explained by an overall decrease of aggregate absorption and a significant redistribution of oscillator strength among the vibronic transitions. This is expressed in terms of a strong increase of the free exciton bandwidth W in the medium molecular weight sample, while W remains almost constant and is generally lower in high molecular weight P3HT.

The behavior of the free exciton bandwidth W gives insight into the changes of the domain size and interchain distances of aggregated thiophene chains during the heating/cooling cycle. According to theoretical studies, an increase of W can be caused by three reasons:[72,73]* a decrease of the intermolecular π-stacking distance, a growth of the aggregate with respect to the number of interacting thiophene chains, and/or a smaller length of the interacting planarized chain segments (correlation length). Based on earlier studies,[22] we can exclude that a shrinkage of the π-stacking distance can cause the observed dependency of W.† A growth of aggregate size by an increase of the number of chains can be likewise discarded, because despite that crystal growth is a known effect upon annealing, the subsequent shrinkage of aggregate size, which would be required to explain the decrease of W upon cooling, is unlikely. Consequently, we attribute the increase and decrease of W during the cycle of heating and cooling to a reversible shortening of the interacting planarized chain segments at high temperature,

* In fact, Gierschner et al.[73] report the behavior of the excitonic coupling V_{AB} which is $W/2$ in aggregates with a large number (> 10) of thiophene chains.

† In particular, we have observed an abrupt decrease of the π-π lattice spacing of only 3% at 50°C and not a continuous change with temperature as is seen for W.

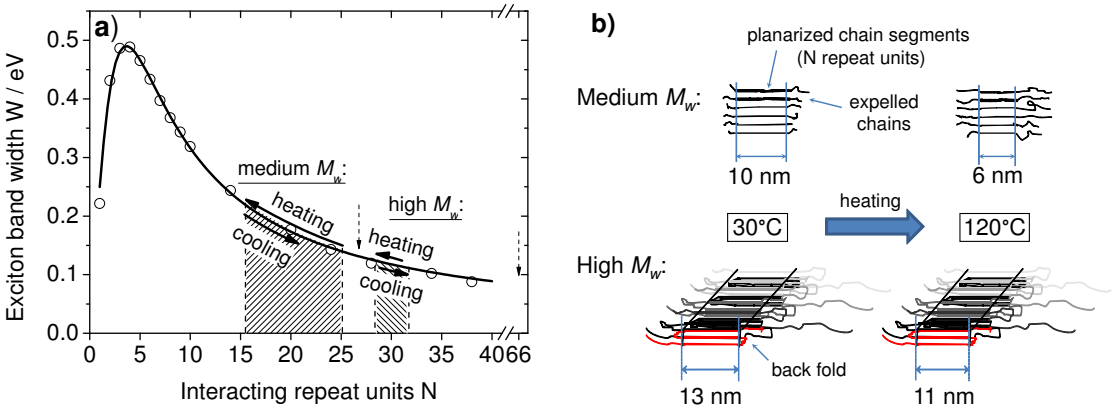

Figure 4.4: (a) Evolution of the free exciton bandwidth and the coherence length of intermolecularly interacting P3HT chains upon a cycle of heating and subsequent cooling. The dashed arrows indicate the contour length of the P3HT chains based on their number-averaged molecular weights, which have been corrected according to Liu et al.[93] Open-symbol data points have been adapted from Gierschner et al.[73] using $W = 2V_{AB}$. (b) Visualization of the decrease of coherence length upon heating in both P3HT fractions.

as is shown in Fig. 4.4.

A quantitative relationship between the free exciton bandwidth and the length of the interacting chain segments is available due to Gierschner et al.[73], see Fig. 4.4a. Translating the temperature dependence of W accordingly, we find that the number of interacting repeat units decreases from ~ 25 at room temperature to ~ 16 at 120°C in medium molecular weight P3HT (corresponding to a shortening of these segments from 10 nm to 6 nm). A comparison to the contour length of this P3HT fraction, which is 27 repeat units on average,* suggests that the medium molecular weight chains are fully elongated within the aggregates at room temperature. Upon heating to 120°C, which is well below the melting temperature, the aggregates undergo a "pre-melting", probably starting from the edges. This process is visualized in Fig. 4.4b.

The effect of heating is much weaker in high molecular weight P3HT. Within the same temperature regime, the number of interacting repeat units changes only slightly from ~ 31 to ~ 28 upon heating (corresponding to a change of segment length from 13 nm to 10 nm), which might be due to the higher melting temperature of this P3HT fraction. Taking into account that the contour length of high molecular weight P3HT is much longer (66 repeat units), it is likely that some chains fold back into the same aggregate. Back-folding possibly stabilizes the aggregates as has been suggested by Brinkmann et al.[21], and, therefore, pre-melting from the edges of the crystallites might be impeded.

* The number-average molecular weights of the P3HT batches have been corrected as suggested by Liu et al.[93] in order to account for the typical error of gel permeation chromatography which is due to the larger stiffness of the P3HT chains as compared to the polystyrene standards.

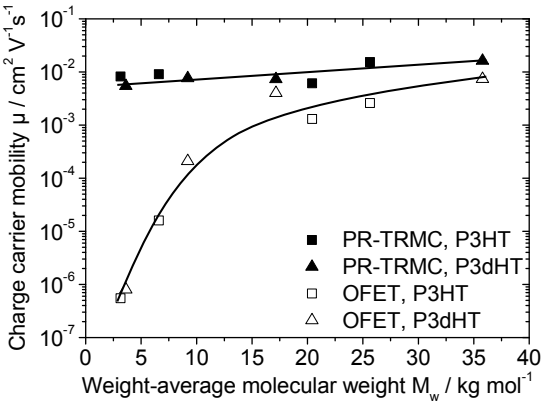

Figure 4.5: Local and macroscopic charge carrier mobilities from PR-TRMC and OFET measurements, respectively, against the weight-average molecular weight of the deuterated (P3dHT) and non-deuterated molecular weight fractions of P3HT. The lines are guides to the eyes.

From the previously measured charge transport data, we compiled the local and macroscopic charge carrier mobilities at room temperature of a number of P3HT samples with varied molecular weights, see Fig. 4.5. It can be seen that the local mobility is almost independent of molecular weight, which seems to be in opposition to the markedly different aggregate widths in medium and high molecular weight P3HT. However, it has been shown that changes of the aggregate width (within the range which is present here) have almost no effect on the transfer integral which determines the intragrain charge transport.[73] On the other hand, the values of the 0-0 transition energy E_0 and of the linewidth parameter σ, which are indicative for the degree of intra- and intermolecular energetic disorder, are very similar in medium and high molecular weight P3HT layers. We, therefore, conclude that the intragrain charge transport is rather unaffected by molecular weight, which is presumably due to a similar energetic disorder in the aggregates of the different P3HT fractions.

The decrease of the macroscopic mobility in medium molecular weight P3HT upon heating, see Fig. 4.2a, can be conclusively explained by the decrease of the aggregate width, which goes along with the widening of the disordered zones between the crystalline nanoribbons. Concomitantly, the disorder in the noncrystalline regions of the P3HT layers (in terms of a wider distribution of conjugation lengths due to torsion and kinks along the P3HT chains) is likely increasing as is suggested by the blue-shift of the absorption of this phase. Therefore, we conclude that the presence of the low-mobility disordered phase limits the macroscopic charge transport in low and medium molecular weight P3HT, which is in contradiction to the interpretation of Kline et al.[14,15] that charge transport is mainly limited by charge carrier trapping at grain boundaries in these samples. In high molecular weight P3HT, in contrast, crystalline domains are probably interconnected by long chains that by-pass the disordered regions. Therefore, the macroscopic mobility is much higher than in samples with lower molecular weight.

Circumventing charge transport through the disordered phase may also be the reason

why the local and macroscopic mobilities exhibit similar temperature dependencies in high molecular weight P3HT, as is evident from Fig. 4.2b. Interconnection of the ordered domains renders the macroscopic charge carrier mobility less susceptible to changes of the morphological heterogeneity. As a more general conclusion, we point out that efficient charge transport in organic semicrystalline semiconductors requires a high overall crystallinity with good interconnection of the ordered domains in these layers.

4.2 Quantitative analysis of the optical absorption of P3HT:PCBM layers with respect to morphology and the charge transport in solar cells*

The properties and performance of organic bulk heterojunction solar cells made from the prototypical donor-acceptor blend of P3HT and [6,6]-phenyl-C_{61}-butyric acid methyl ester (PCBM) vary largely with the preparation conditions, e.g., the annealing time and temperature, and the solvent used for casting these layers. In particular, spin-coating from chloroform (CF) or other low-boiling point solvents is known to produce layers with rather disordered P3HT domains and a fine dispersion of PCBM due to the fast drying time, which is non-optimal with regard to the solar cell efficiency.[94] Annealing procedures are then conventionally applied to induce a morphology change towards larger molecular order and purer domains.[3] Recent structural studies have shown that thermal annealing of P3HT:PCBM blend layers stimulates the crystallization of the P3HT chains and allows for the diffusion and aggregation of PCBM.[95] As a result of P3HT crystallization, percolation pathways for the hole transport are formed which lead to a higher hole mobility, a reduced charge carrier recombination, and, consequently, to a better solar cell efficiency.[96,97]

Despite that numerous studies on the relationship between morphology and solar cell performance of P3HT:PCBM blend layers exist, exact knowledge of the evolution of the morphology during processing, for instance, about the degree of aggregation and the intragrain disorder, is lacking. From X-ray diffraction data it is commonly hard to discriminate the intensity contributions of aggregated and disordered material, which is owing to the poorly resolved crystalline peaks for these layers. Moreover, determination of the absolute crystallinity of such samples would require a reference sample with 100% polymer crystallinity, which is not available. More sophisticated techniques, such as electron tomography, offer impressive insights into the three-dimensional layer morphology.[98] However, these techniques are usually very demanding in terms of

* This section is based on S. T. Turner, P. Pingel, R. Steyrleuthner, E. J. W. Crossland, S. Ludwigs, and D. Neher, "Quantitative Analysis of Bulk Heterojunction Films Using Linear Absorption Spectroscopy and Solar Cell Performance", Adv. Funct. Mater. 21, 4640-4652 (2011).

the measurement procedure, data evaluation and/or sample preparation. On the other hand, we have shown in section 4.1 that analyzing the optical absorption of the P3HT part of the spectra using Spano's model provides a simple means to access the aggregate content, size, and intragrain disorder of the P3HT phase.

Here, we use Spano's model to analyze the optical absorption of 1:1-weight ratio P3HT:PCBM bulk heterojunction layers, spin-cast from a solution in either CF or *o*-dichlorobenzene (DCB).* In contrast to spin-coating from CF, DCB-casting usually results in a highly crystalline, near-optimized layer structure due to the long drying time of the film.[4] The layers were either used as-prepared or underwent 10-min annealing at different temperatures well below the melting points of P3HT and PCBM. The results from the optical analyzes are used to explain the origin of the efficiency increase of CF-cast solar cells upon thermal annealing.

For a meaningful analysis of the P3HT absorption in the P3HT:PCBM blend layers, it is essential to subtract the contribution of the PCBM phase. Fortunately, the absorption bands of P3HT and PCBM are rather distinct, i.e., PCBM exhibits a single but broad absorption peak at 336 nm. A proper reference spectrum was obtained from a PCBM:polystyrene (PCBM:PS) sample which has been spin-coated from CF. After normalization of all spectra to 336 nm, 90% of the reference spectrum was subtracted from the P3HT:PCBM spectra. In this case, the resulting spectra of the P3HT phase closely resemble the short-wavelength absorption of a pristine P3HT layer. These spectra have been analyzed as has been described in section 4.1 by fitting Spano's absorption model to match the low-energy aggregate absorption.

The best-fit values for the free exciton bandwidth W and the linewidth parameter σ obtained from the analysis are shown in Fig. 4.6a,b along with results from as-prepared, non-annealed P3HT layers. Additionally, the percentages of P3HT chains contained in aggregates were deduced by a comparison of the integrated aggregate- and disordered-phase absorption spectra (Fig. 4.6c). Almost no change occurs in any of the values of E_0 (not shown), σ, W, and the percentage of aggregated chains upon annealing of the DCB-cast P3HT:PCBM samples and these parameters are nearly identical to those of corresponding pristine P3HT layers. This suggests that the PCBM component plays little to no role in the formation of the P3HT morphology in the slowly drying DCB-cast samples. Using the aforementioned relationship between the free exciton bandwidth W and the length of the interacting thiophene segments by Gierschner et al., the narrow range of W translates into approximately 40 planarized repeat units (i.e., 15 nm) which is comparable to the width of P3HT nanorods in similarly prepared blend samples found by electron tomography.[98] The low values of W and the line shape param-

* The herein used P3HT sample has an average molecular weight of M_w = 20-30 kg/mol, similar to the high molecular weight P3HT sample used in section 4.1.

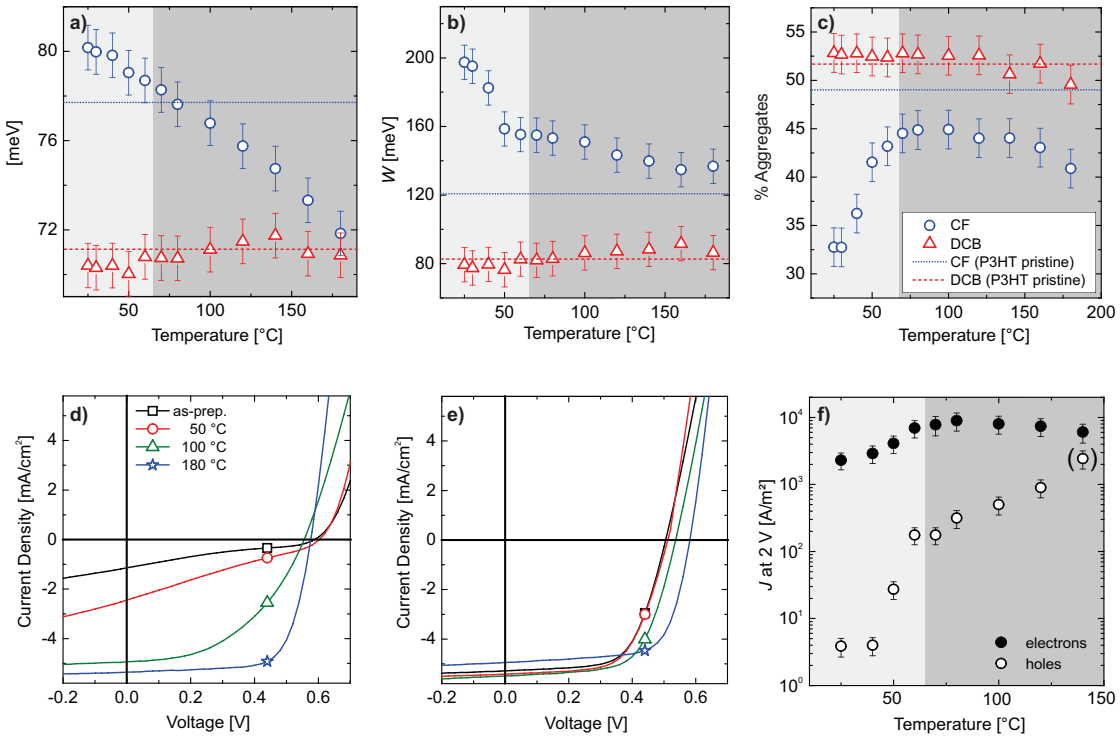

Figure 4.6: (a,b) Free exciton bandwidth W and Gaussian linewidth σ, respectively, stemming from the analysis of the absorption spectra of CF- and DCB-cast P3HT:PCBM films with the Spano model. (c) Percentage of P3HT chains contained in aggregates, determined by a comparison of the integrated aggregate and disordered-phase absorption spectra. (d,e) Solar cell characteristics of CF- and DCB-cast P3HT:PCBM films, as-prepared and annealed at various temperatures. (f) Electron- and hole-only currents at 2 V in P3HT:PCBM unipolar devices spin-cast from CF. Light-gray areas correspond to the glass transition regime. The temperatures beyond this range are highlighted in dark gray.

eter σ in DCB-cast samples suggest that casting from a high-boiling point solvent and subsequent solvent annealing leads to large aggregates with a low degree of intra- and interchain disorder.

In contrast, a marked decrease of the free exciton bandwidth W (i.e., an increase of the number of interacting planarized thiophene repeat units from ca. 17 to 26), and an increase of the percentage of aggregated chains is observed upon annealing of the CF-cast blend layers. These changes occur mainly at annealing temperatures up to 70°C which is apparently related to the glass transition regime of the amorphous intermixed P3HT:PCBM phase. Therefore, the onset of segmental chain motion within the glass transition range seems to be sufficient to allow for the rearrangement of P3HT chains which is required for the growth of the number and length of P3HT segments contained in the aggregates. Annealing above the glass transition temperature does not lead to further overall aggregation, but mainly improves the local order as is expressed by a steady decrease of σ. However, even at the highest annealing temperature the length of the aggregated chains and the crystallinity remain lower than in the DCB-cast samples

and in the pristine P3HT samples cast from CF, i.e., the disordered morphology of the as-prepared CF-cast layers is not completely equilibrated upon thermal annealing during the chosen time interval. Apparently, the presence of PCBM substantially disrupts the crystallization of P3HT in these samples.

The *j-V* characteristics of as-prepared and thermally annealed solar cells are shown in Fig. 4.6d,e. While the characteristics are rather unaffected by annealing for the DCB-cast samples, thermal annealing of the CF-cast devices leads to substantial increases of the short-circuit current, the fill factor, and, therefore, of the power conversion efficiency. Most interestingly, the solar cell efficiency of CF-cast samples increases with increasing annealing temperature up to 180°C, which is far above the glass transition range of the amorphous phase and in a regime where aggregate growth has been finished (as is expressed by the constant values of W and the percentage of aggregates above 70°C). Data on the hole and electron currents in single-carrier devices show that the solar cell efficiency goes along with an increase of the hole current, see Fig. 4.6f. In CF-cast layers which have not been subject to 180°C-annealing, the hole current density is much lower than the electron current density, suggesting a small hole mobility. Consequently, space-charge build-up leads to a high bimolecular recombination and, therefore, to a low power conversion efficiency in these devices.[5]

The low hole current density in the as-prepared CF-cast samples, being conducted by the P3HT phase, is likely a consequence of the small P3HT aggregates and the overall low crystallinity in these layers. Within the investigated range of annealing temperatures, the hole current density increase shows to regimes; a steep rise up to the end of the glass transition regime at ca. 70°C, followed by a less steep rise at higher temperatures. The initial steep rise coincides with a strong growth of the aggregate width and an increase of the percentage of aggregated chains. At higher annealing temperatures, where aggregate growth is essentially completed, the hole current density increase can be explained by the continued reduction of the energetic disorder in the aggregated domains of the P3HT phase (as is expressed by the steady decrease of the linewidth parameter σ). This interpretation is in line with the decrease of the power law order of the hole-only *j-V* characteristics with increasing annealing temperature, which means that hole trapping becomes less significant after thermal annealing.

Rivnay and coworkers[35] have shown that energetic disorder is typically present in aggregates of a thiophene-based polymer as a consequence of fluctuations of the π-π crystal lattice spacing (paracrystallinity). Such fluctuations can be caused by stacking defects and conformational changes and show up as diffraction order dependent peak broadening in X-ray diffractograms. Using a model aggregate where the spatial distances between isoenergetic sites are chosen from a Gaussian distribution, Rivnay et al. have shown that an exponentially shaped sub-band gap tail emerges, whose energetic

breadth increases with increasing paracrystallinity.

Based on the observed decrease of the intragrain energetic disorder, we infer that thermal annealing of the non-optimized, CF-cast P3HT:PCBM layers reduces the paracrystallinity of the P3HT aggregates. Probably, structural defects within the aggregates can be healed at elevated temperatures due to the increased segmental motion or due to recrystallization upon cooling. A low degree of intra- and interchain disorder and, within the observed range, a high content and size of aggregated chains in the P3HT phase, which can be reached by spin-coating from a solution in DCB or thermal annealing of CF-cast layers, is most favorable for hole transport and, therefore, for the efficient extraction of photogenerated charge carriers in P3HT:PCBM bulk heterojunction solar cells.

4.3 Molecular order and orientation of highly crystalline oligomeric PQT-12 layers probed by polarization and scanning near-field optical microscopy*

Typically, layers of low molecular weight polyalkylthiophene fractions exhibit a rather low charge carrier mobility in field-effect transistors, which is due to the low overall crystallinity and the poor interconnection of the ordered domains, see section 4.1. In low molecular weight P3HT layers, it has been suggested that especially the short polymer chains of the molecular weight distribution are not able to crystallize and, consequently, form a disordered phase.[17] On the other hand, it has been shown that oligothiophenes, i.e., molecular compounds with chemical homogeneity, form polycrystalline layers with a high field-effect mobility which often exceeds $0.1\,\mathrm{cm}^2/(\mathrm{Vs})$. These small molecules are almost planar and stand up-right on the substrate, which is particularly advantageous for the fast motion of charge carriers along the π-stacking direction, i.e., parallel to the substrate plane, in a typical transistor geometry.

In our earlier work (particularly including the author's diploma thesis),[56,57] we investigated the layer morphology of an oligomeric low molecular weight fraction of the polythiophene derivative poly(3,3‴-didodecyl-[2,2′:5′,2″:5″,2‴]-quaterthiophene), oligo-PQT-12. In contrast to low molecular weight P3HT films, these layers were highly crystalline, which we attributed to the specific synthesis scheme of this polymer that resulted in a very narrow molecular weight distribution. As a result of the polymerization from quaterthiophene monomers and appropriate solvent extraction, the oligo-PQT-12

* This section is based on S. Kühn, P. Pingel, M. Breusing, Th. Fischer, J. Stumpe, D. Neher, and Th. Elsässer, "High-Resolution Near-Field Optical Investigation of Crystalline Domains in Oligomeric PQT-12 Thin Films", Adv. Funct. Mater. 21, 860-868 (2011).

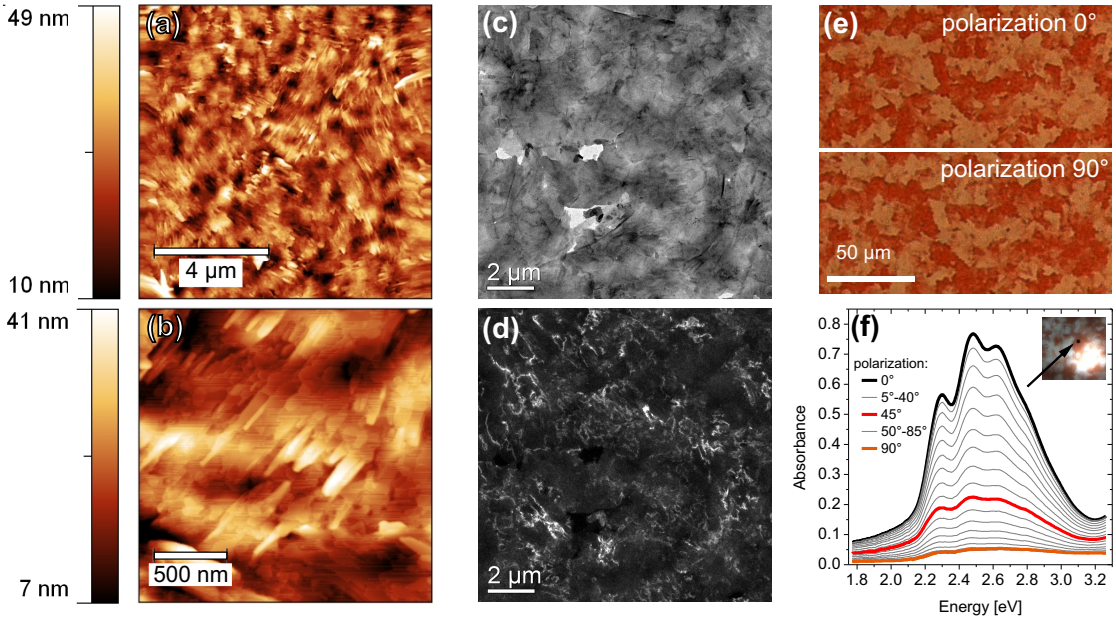

Figure 4.7: Microscopy images of thin oligo-PQT-12 layers: (a,b) AFM topographies on two length scales, (c,d) TEM bright- and dark-field images, (e) white-light polarization microscopy images with perpendicular polarizations (0° and 90°), and (f) polarized-light absorption spectra of a selected 6 µm × 6 µm domain (indicated in the inset) as a function of the polarizer angle.

sample consists of mainly quaterthiophene dimers (8 thiophene units), except for traces of trimers (12 thiophene units) and tetramers (16 thiophene units). Due to the high crystallinity of the oligo-PQT-12 layers, field-effect transistor measurements yielded a rather high charge carrier mobility ($\sim 10^{-3}\,\mathrm{cm}^2/(\mathrm{Vs})$) as compared to the typical field-effect mobility of low molecular weight P3HT fractions ($\sim 10^{-6}\,\mathrm{cm}^2/(\mathrm{Vs})$).[16,56,57] However, inspection of the atomic-force microscopy (AFM) and transmission electron microscopy (TEM) images of oligo-PQT-12 layers has lead to an indefinite picture of the layer structure. The AFM images show elongated crystalline needles with some degree of orientation correlation at the layer surface (Fig. 4.7a,b), while the TEM images display a plate-like crystalline texture with domains on the micrometer scale (Fig. 4.7c,d). In order to obtain a conclusive picture of the molecular chain packing and the degree of order in the oligo-PQT-12 layers, here, we extend our structural studies by using polarized far- and scanning near-field optical microscopy measurements.

Fig. 4.7e displays far-field optical microscopy images for two polarization directions of the transmitted light. To our surprise, these images reveal domains with homogeneous in-plane dichroism on the length scale of up to ten micrometers, which is much larger than the domains seen in the TEM images. The in-plane dichroism is caused by the strong orientation correlation of the molecules' transition dipole moments within the domains. Due to this anisotropy, light transmission is maximal or minimal, depending on whether the incident light is polarized perpendicularly or parallel, respectively, to

the transition dipole moment direction. The dichroic ratio of the transmission through a single domain is ca. 16, which suggests that the intragrain molecular orientation is highly uniform, see Fig. 4.7f. Moreover, the high in-plane dichroism observed here requires that the oligo-PQT-12 chains lie parallel to the substrate surface, because the transition dipole moment in oligo-PQT-12 is essentially oriented along the molecular backbone.[55]

Up to this point, we have observed, using three different methods, that molecular order is present in oligo-PQT-12 layers on three different length scales. Namely, topographical AFM images show elongated crystalline needles at the layer surface, TEM images show plate-like crystalline domains on the micrometer scale, and far-field polarized microscopy images reveal dichroic domains on the ten-micrometer scale. We, now, use scanning near-field optical microscopy (SNOM) as a tool which can resolve details of the layer morphology on a scale ranging from the sub-micrometer to the tens-of-micrometer regime. Thereby, we make use of the dichroic optical properties of the thin films and of the different optical spectra of ordered (planarized) and disordered (non-planarized) polythiophene chains, see section 4.1.

Firstly, using white-light and essentially unpolarized illumination,* local absorption spectra were recorded during the scan of the SNOM tip. These spectra were decomposed with respect to the absorption spectra of a prototypically perfectly ordered and a disordered phase. The ordered reference spectrum has been obtained on a sample with distinct isolated microcrystals by recording and averaging local spectra at various positions of these crystals. The disordered reference spectrum was obtained by measuring the far-field absorption spectrum of an oligo-PQT-12 film in the melted state, which, eventually, represents the most disordered, isotropic state of the molecular arrangement. During melting, the evolution of the absorption spectra exhibits an isosbestic point (IBP), which implies that the local absorption spectra can be reconstructed as a sum of the two reference spectra. The amount of ordered molecules relative to the total amount of molecules is introduced as an order parameter

$$\xi = \frac{A_{\text{ordered}}\left(\nu_{\text{IBP}}\right)}{A_{\text{ordered}}\left(\nu_{\text{IBP}}\right) + A_{\text{disordered}}\left(\nu_{\text{IBP}}\right)}, \tag{4.1}$$

where A and $\nu_{\text{IBP}} = 2.77\,\text{eV}$ are the absorbance and the energy at the IBP, respectively.

The order parameter ξ obtained from a portion of an oligo-PQT-12 layer is mapped in Fig. 4.8a. It is seen that ξ varies from 60% to 100%. The finite lower limit implies that well-ordered, crystalline material is present throughout the entire scan area

* Polarization control over a broad spectral range is illusive, mainly due to asymmetries in the fiber tip shape. Therefore, a specific linear polarization has been selected from the transmitted light for the absorption measurement.

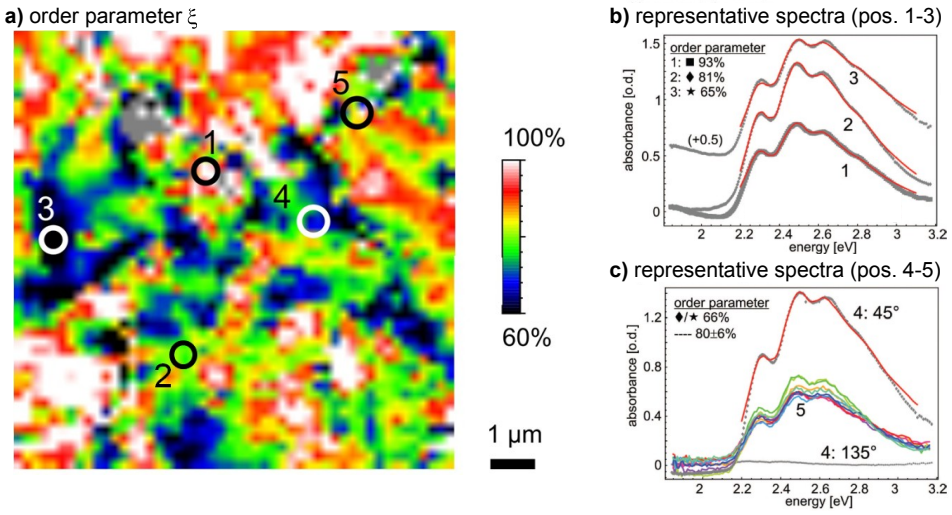

Figure 4.8: (a) Molecular order parameter ξ within a section of an oligo-PQT-12 layer, determined from the decomposition of the local absorption spectra. (b) Local absorption spectra at the representative positions 1-3 marked in (a). (c) Absorption spectra at the positions 4 and 5, based on various polarization angles of the transmitted light.

which is consistent with the vibronic peak structure seen in each of the sample spectra (Fig. 4.8b,c). Additionally, pronounced dichroism, exemplary shown for position 4 in Fig. 4.8c, is exhibited throughout the entire film except at physical defects and domain boundaries (such as position 5, see below).

As a second approach to study the molecular packing of the oligo-PQT-12 layers, we performed SNOM measurements using a polarization dependent detection of the transmitted light, in order to map the local dichroism. For that, the output at the SNOM probe was adjusted such that the sample was illuminated by monochromatic, circularly polarized light. Using a revolving polarizer (analyzer) in the detection path and a phase-sensitive detector locked in the same position as the angle of the polarizer, the amplitude and the phase of the detector signal are related to the local dichroism and molecular orientation, respectively. These data are shown in Fig. 4.9a,b.

Distinct 5-20 µm-sized domains with only little variations of the dichroism are seen. Apparently, these domains correspond to the features seen in the far-field microscopy images, see Fig. 4.7f. Moreover, domain boundaries and defects can be easily identified. At such locations (e.g., position 5 in Figs. 4.8a and 4.9a), the dichroism vanishes and, often, a sudden change of the molecular orientation occurs. We conclude that such defects and grain boundaries make up ca. 5% of the film area.* The grain boundaries have a width on the order of 100 nm or less and are not visible in the topography data (not shown). Within the domains with high dichroism, the molecular orientation is not

* The domain size and area-density of defects have been estimated from measurements of larger areas of the oligo-PQT-12 films.

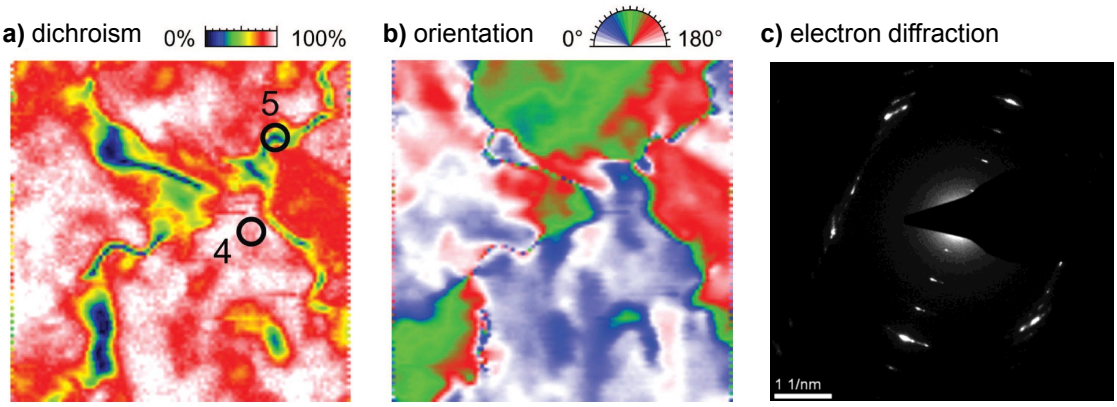

Figure 4.9: (a) Local dichroism and (b) molecular orientation within a section of an oligo-PQT-12 layer. Local dichroism has been measured based on the maximum and minimum transmission of monochromatic light (2.7 eV) which passed through a revolving polarizer (analyzer). The molecular orientation is with respect to the angular position of the analyzer. (c) TEM selected-area diffraction pattern of a portion of an oligo-PQT-12 layer.

strictly constant over an entire domain, but shows continuous variations on the order of tens of degrees on the micrometer scale. Such an orientational variety has also been observed in TEM selected-area diffraction patterns of oligo-PQT-12 films (Fig. 4.9c),[56,70] where the diffraction spots are smeared out over small circular segments. The lateral size of the sub-domains with a constant orientation corresponds roughly to the features previously seen in the TEM data, see Fig. 4.7c,d. Probably, these domains serve as a template for the orientation of the needle-like structures at the layer surface seen in the AFM data in Fig. 4.7a,b. In a similar manner, three-dimensional crystal growth upon film formation starts probably from a dense nucleation layer with very homogeneous molecular orientations at the substrate surface, as is typical for the crystallization of small molecules upon evaporation or solution processing.[99]

Based on the overall high order parameter, dichroism, and large orientational coherence, we hypothesize that there are different degrees of crystalline order in the oligo-PQT-12 films, rather than a binary mixture of distinct ordered and disordered phases co-existing side-by-side. This is in contrast to the typical morphology of low molecular weight polyalkylthiophene fractions, where crystalline domains are clearly separated and surrounded by disordered material. The reasons for the finite orientational correlation length and for the variations of the local spectra in oligo-PQT-12 layers may be sought in the structural imperfections of the molecular crystal order that affords some flexibility of the in-plane lattice spacings. As is evident from the polarization dependent transmission data, the formation of hard grain boundaries seems to be avoided if the molecular orientations of neighboring crystalline domains are not too different. This requires that the crystal axes are allowed to bend slightly. Finally, the overall high crystallinity of oligo-PQT-12 layers may cause the good charge transport properties in OFET devices based on this material.

4.4 Electrical characteristics of F_4TCNQ-doped P3HT layers in a broad range of dopant concentrations*

Molecular doping has been successfully used to overcome efficiency limitations of organic electronic devices. In this context, doping is commonly applied to evaporated small-molecule semiconductors in proximity to the electrodes of organic light-emitting diodes in order to promote charge carrier injection, transport, and, finally, luminance.[40,41] Molecular doping has also been frequently used in polymeric field-effect transistors, where effects on the charge carrier mobility, the threshold voltage and the hysteresis were reported.[36–38] Generally, an increase of field-effect mobility and a reduction of hysteresis was observed and attributed to the filling of deep traps in the channel region by doping-induced charge carriers.

Despite the emerging importance of doped organic semiconductors, studies of the effect that molecular doping has on the electrical characteristics are rare and usually cover only a very limited range of dopant concentrations. Particularly, the mechanism of doping (see section 2.6) and the doping efficiency, i.e., the fraction of dopants which lead to fully mobile charge carriers, are controversially discussed. Often, it is observed that the density of mobile charge carriers is far lower than the dopant concentration.[46,50–53] This has been explained by suggesting significant formation of isolated clusters of neutral dopants,[44,45] or in terms of a strong Coulomb interaction of the charge carriers with the ionized dopants[50,54]. In contrast, it has been reported that the charge carrier density does not depend on temperature in some F_4TCNQ-doped small-molecule organic semiconductors.[100–102] These authors argue that all acceptors are ionized and, if at all, only shallow trapping of the doping-induced charge carriers occurs.

Studies on p-type doping of various polymeric semiconductors focus mainly on using tetrafluorotetracyanoquinodimethane (F_4TCNQ) as an electron acceptor[36–38,42,44,46,49] due to its solubility in organic solvents and its high electron affinity (5.24 eV).[103] High electric conductivities of up to 100 S/m have been reported in F_4TCNQ-doped P3HT layers.[42] Here, we systematically investigate the electrical characteristics of p-type F_4TCNQ doped P3HT layers with respect to charge carrier density, mobility, and conductivity in a wide range of dopant concentrations from the ppm to the percent regime.

The density of mobile holes in undoped and F_4TCNQ-doped P3HT layers has been determined by measuring the admittance, i.e., the frequency-dependent complex sum

* This section is based on P. Pingel, R. Schwarzl, and D. Neher, "Effect of molecular p-doping on hole density and mobility in poly(3-hexylthiophene)", Appl. Phys. Lett. 100, 143303 (2012), and P. Pingel and D. Neher, "Comprehensive picture of p-type doping of P3HT with the molecular acceptor F_4TCNQ", Phys. Rev. B 87, 115209 (2013).

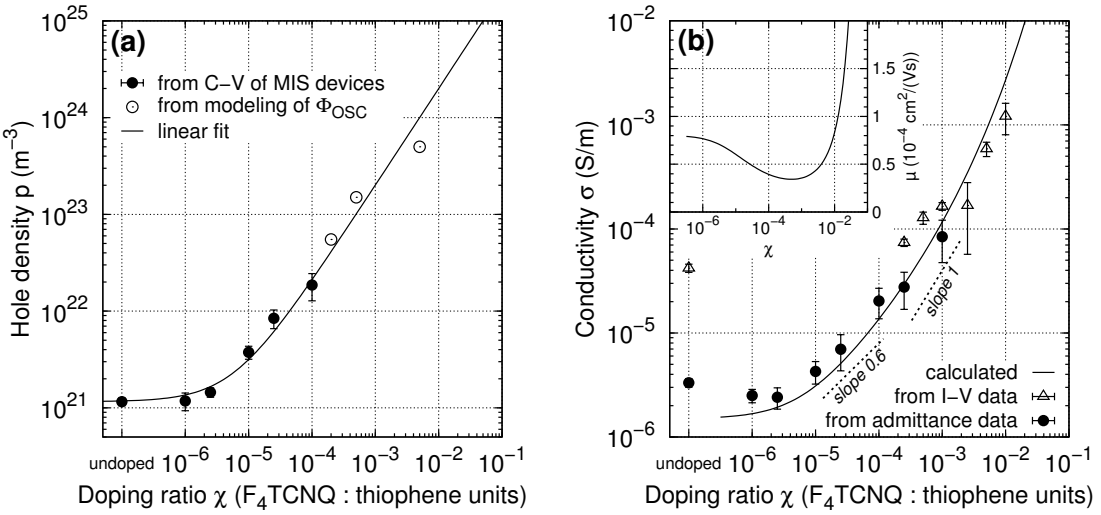

Figure 4.10: (a) Density of mobile holes in F_4TCNQ-doped P3HT layers as a function of doping ratio. Data have been obtained from admittance spectroscopy measurements on MIS samples and from numerical modeling of the work function curves of doped layers with varied thickness on metal substrates. The line corresponds to the linear function $p = 2.0 \times 10^{26}\,\mathrm{m}^{-3}\chi + 10^{21}\,\mathrm{m}^{-3}$. (b) Conductivity determined from admittance spectroscopy measurements on MIS samples and from I-V characteristics of hole-only devices. The line is the predicted conductivity based on the mobile hole densities and the mobility model of Arkhipov et al.[58–60] using the parameters given in Table 4.1. The inset shows the calculated mobility values.

of capacitance and conductance, of samples in a metal (oxide)–insulator–semiconductor (MIS) geometry, where the metal (oxide) electrode is indium-tin-oxide (ITO) and the insulator is a spin-coated and cured layer of a polysilsesquioxane derivative. Details on the sample preparation and measurement method can be found in section 3.3. In practice, the p-type semiconductor layer is depleted starting at the insulator surface by applying a positive DC voltage to the ITO electrode. The growth of the depletion zone depends on the number of ionized, left-behind acceptor molecules, i.e., those acceptors which contribute mobile holes to the bulk of the P3HT layer. The according dependence of the capacitance on the DC bias can hence be evaluated in terms of the mobile hole density which is induced by doping. Note that this procedure is not feasible at doping ratios higher than 10^{-4} due to the coincidence of depletion and inversion features in the capacitance data. In addition, the frequency dependence of the conductance of the MIS samples contains information on the bulk conductivity of the doped layers which is discussed further below.

The doping-induced mobile hole densities are shown in Fig. 4.10a. A doping ratio of $\chi = 10^{-4}$, or equivalently 1:10 000, means that one F_4TCNQ molecule is added per 10 000 thiophene repeat units of P3HT. A significant increase of the mobile hole density is seen at doping ratios χ exceeding 10^{-6}. The data can be well described by a linear function of the form $p = D\chi + p_0$, considering a background density of

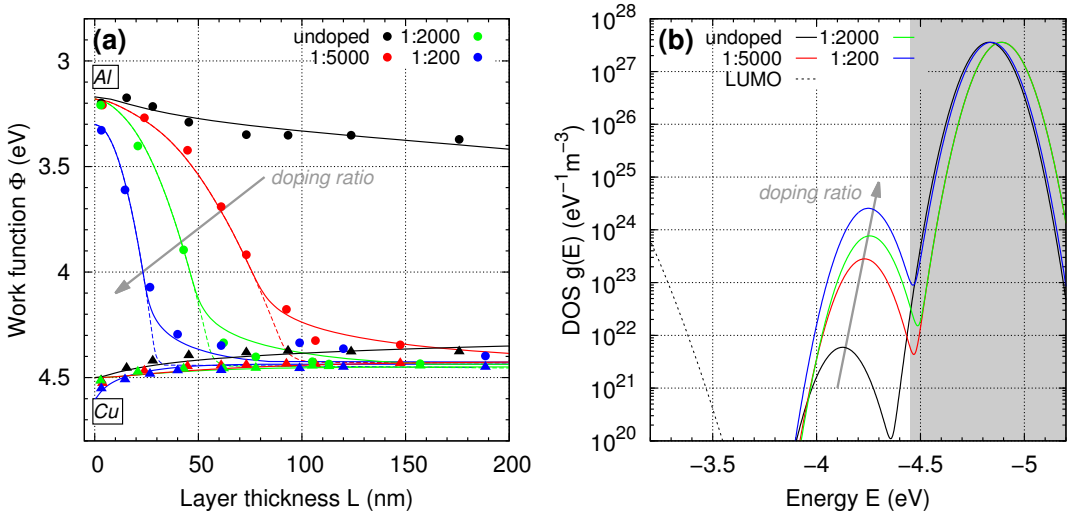

Figure 4.11: (a) Experimental data (symbols) and numerical calculated work functions (lines) of undoped and F_4TCNQ-doped P3HT layers on aluminum and copper. Numerical calculations assume Arkhipov's DOS distribution including doping-induced tail states (solid lines) or a single-Gaussian DOS shape (dashed lines). (b) Corresponding HOMO DOS distributions based on Arkhipov's model. The unshaded energy range is probed in the Kelvin probe experiment. A minor contribution of LUMO levels (dotted line) is inferred from the work function curve of undoped P3HT on aluminum.

$p_0 = 1.2 \times 10^{21}\,\mathrm{m}^{-3}$ and a slope parameter of $D = 2.0 \times 10^{26}\,\mathrm{m}^{-3}$. The linear increase of the amount of doping-induced mobile holes with increasing concentration of dopants is in accordance with previous reports on F_4TCNQ-doped P3HT and poly(2-methoxy-5-(2'-ethylhexyloxy)-p-phenylene vinylene) (MEH-PPV).[45,46] We can estimate, taken the mass density of P3HT[104] of 1.1 g/cm^3 and the molar mass of a thiophene unit, that the number density of thiophene units per volume is $4.0 \times 10^{27}\,\mathrm{m}^{-3}$. Hence, the doping efficiency amounts to ca. 5%, i.e., every twentieth applied F_4TCNQ dopant contributes a mobile hole which takes part in electrical conduction.

At high doping ratios ($\chi > 10^{-4}$), the mobile hole density data stem from the analysis of surface potential (Kelvin probe) measurements of F_4TCNQ-doped P3HT layers on copper and aluminum. Moreover, this methods yields information on the electronic DOS distribution of the polymer bulk.[105] The surface potential ϕ of the semiconductor is related to the sample's thickness-dependent work function via

$$\Phi_{\mathrm{OSC}}(L) = \Phi_{\mathrm{Sub}} - \phi(L), \tag{4.2}$$

where Φ_{Sub} is the work function of the metal substrate and L is the thickness of the semiconductor layer. Work function curves as a function of L are shown in Fig. 4.11a. Electrical contact of a metal and a semiconductor leads, if feasible, to Fermi level alignment through the formation of a space charge in the semiconductor layer. For the undoped and doped P3HT layers on copper this means that holes are injected from the metal into the HOMO manifold of P3HT. Consequently, the positive surface potential

leads to a decrease of the work function with increasing layer thickness, as is seen in Fig. 4.11a. Analogue to this, weak electron injection occurs from aluminum into the tail of the LUMO manifold of P3HT, which leads to a negative surface potential and, for an undoped layer, to a slow increase of the work function with increasing layer thickness.

In the p-doped layers on aluminum, on the other hand, a space charge is formed mainly by depletion of the contact-near region. As in a classical Schottky contact, the mobile doping-induced holes drift towards the aluminum electrode and get neutralized at the metal interface. The immobile F_4TCNQ anions are left behind and form a negative depletion zone. For a homogeneous spatial distribution of the anions, the work function curves have a parabolic shape for layer thicknesses smaller than the depletion width. From the depletion width, the anion density, and, therefore, the mobile hole density can be calculated. These data are shown in Fig. 4.10a and connect well to the mobile hole densities at lower doping ratios which were determined from the admittance measurements. Note that the Kelvin probe and the admittance measurements have been performed on different sample geometries including various metal electrodes, which substantiates that the mobile hole densities are characteristic for the bulk of the doped layers.

Aiming for a more quantitative analysis of the work function data, we attempt to model the work function-layer thickness curves numerically. As has been discussed in section 3.4, the curvature of $\phi(L)$ on a high or low work function electrode includes information about the DOS distributions of the HOMO- and LUMO-derived states of the semiconductor. At first, we assume a single Gaussian-shaped DOS distribution for the HOMO-derived states. While the calculated work functions for layers with different thicknesses on copper (not shown) are in satisfactory agreement with the experimental data, there are distinct discrepancies for the doped P3HT layers on aluminum (dashed lines in Fig. 4.11).* Most strikingly, the assumption of a simple Gaussian DOS shape is not in line with the long tail of the work function curves towards saturation which indicates that a proper description must account for doping-induced states at the tail of the DOS distribution.

Indeed, a broadening of the DOS distribution due to ionized dopants has been repeatedly suggested.[84–87] Arkhipov et al. discussed a model that accounts for the Coulomb interaction of the doping-induced charge carriers with the left-behind ionized dopants.[59,60] The foundations of this model are explained in section 2.5. Briefly, the superposition of the original Gaussian-shaped DOS distribution $g_i(E)$ and the binding energies caused by the Coulomb binding between the charge carriers and the dopant

* Note that for a proper description of the undoped-P3HT work function data a minor injection from aluminum into the tail of the P3HT LUMO distribution has been taken into account in all calculations.

ions leads effectively to a broadened DOS distribution

$$g_{\text{doped}}(E) = \frac{N - N_d}{N} g_i(E) + \frac{N_d}{N} g_i\left(E - \frac{e^2}{4\pi\epsilon_0\epsilon_r a} - U_m(N_d)\right), \tag{4.3}$$

where the density of ionized dopants N_d shall be equal to the mobile hole density, a shall correspond to the distance of a dopant ion and the closest semiconductor site, and, according to Arkhipov et al.,[59] the nontrivial value of $U_m(N_d)$ accounts for the overlap of neighboring dopant ions' Coulomb potentials at high doping ratios.

Using the DOS function from Eq. 4.3, numerical calculations of work function curves at the different doping ratios have been performed as is described in section 3.4. With the parameter set N, σ, and a given in Table 4.1 and the hole densities from Fig. 4.10a, a good agreement between the calculated and the experimental work functions is obtained (see solid lines in Fig. 4.11a). The according DOS distributions are plotted in Fig. 4.11b. As a result of the good reproduction of the work function curves using Arkhipov's DOS function Eq. 4.3, we infer that F_4TCNQ-doping introduces deep states in the tail of the distribution of HOMO-derived states in P3HT caused by the Coulomb potentials of left-behind ionized F_4TCNQ molecules. This is substantiated by the good agreement between the density of these tail states and the density of ionized acceptors which has been extracted from the initial parabolic shape of the work function curves at small film thicknesses.

Electrical conductivities of the F_4TCNQ-doped P3HT layers in the MIS geometry have been determined by analysis of the frequency dependence of the admittance, see section 3.3, and are shown in Fig. 4.10b. For consolidation, conductivities at high doping ratios have also been extracted from the linear regime of the I-V characteristics of hole-only devices. The conductivities exhibit a monotonous and nonlinear increase with increasing doping ratio.* This implies, in conjunction with the strictly linear increase of the mobile hole density upon doping, a rather complicated relationship between the doping ratio and the mobility of the mobile holes. In particular, we find a sublinear increase of the conductivity at low to moderate doping ratios ($\chi < 10^{-4}$) which means that the mobility decreases in this regime. At higher doping ratios the conductivity increase is superlinear and, thus, linked with an increase of the mobile hole mobility.

The observed doping ratio-dependence of the conductivity and mobility can be explained with the closed-form mobility model by Arkhipov et al.,[58–60] see section 2.5. Arkhipov's model provides a scheme to calculate the charge carrier mobility in the

* Note that the undoped hole-only device suffers from an increased conductivity which is probably due to the degradation of the polymer sample during the more-than-one-year delay between the I-V and the previous admittance measurements. This is supported by repeated admittance measurements on a freshly prepared undoped P3HT MIS device which yielded an increased mobile hole density and bulk conductivity.

total density of states N	$7 \times 10^{26}\,\mathrm{m}^{-3}$
DOS width parameter σ	78 meV
anion-trapped hole distance a	0.57 nm
inv. hole localization radius γ	$2.9\,\mathrm{nm}^{-1}$
attempt-to-hop frequency ν_0	$3 \times 10^{12}\,\mathrm{s}^{-1}$
electric field F	$2 \times 10^{4}\,\mathrm{Vm}^{-1}$
temperature T	300 K

Table 4.1: Parameters used in the numerical calculations of the work function curves (upper part of the Table) and of the mobile hole mobility and conductivity (upper and lower part of the Table) of F_4TCNQ-doped P3HT layers, see Fig. 4.10.

broadened DOS distribution given by Eq. 4.3. Using the parameter set given in Table 4.1, the calculated curves reproduce the experimental conductivity and mobility data well, see the solid lines in Fig. 4.10b. Among these seven parameters, the DOS distribution parameters N, σ, and a are already known from the analysis of the work function data. The values of the electric field F (being roughly estimated based on the effective AC voltage) and the temperature T are given by the experimental condition of the admittance measurements.

Following Arkhipov et al.,[59,60] we infer that the reduction of the mobile hole mobility at low to moderate doping ratios, i.e., the sublinear increase of conductivity with increasing doping ratio, is most likely caused by the broadening of the DOS distribution due to the Coulomb interaction of the charge carriers with the ionized left-behind F_4TCNQ molecules. The broadening counteracts the fill-up of the low-mobility tail of the DOS distribution upon doping. This prediction is in contrast to the usual presumption that the mobility is always increased upon doping due to the filling of traps by the doping-induced charge carriers.[54,106] On the other hand, a reduced mobility has also been observed at low doping ratios in electrochemically doped P3HT.[107] At higher doping ratios, the Coulomb potentials of individual ionized F_4TCNQ dopants may overlap such that the effective barrier for the release of trapped holes is lowered. As a consequence, the mobility becomes increasingly controlled by the fill-up of the DOS distribution in the strong doping regime and, hence, increases.

4.5 Localized nature of the charge transfer in F_4TCNQ-doped thiophene-based donor polymers*

It is well established that the doping effect, i.e., the increase of the majority charge carrier density, is based on a charge transfer reaction involving an appropriate donor and acceptor. However, our previous investigation of the efficiency of doping P3HT with F_4TCNQ has shown that the fraction of F_4TCNQ which induces mobile holes to the

* This section is based on P. Pingel, L. Zhu, K. S. Park, J.-O. Vogel, S. Janietz, E.-G. Kim, J. P. Rabe, J.-L. Brédas, and N. Koch, "Charge-Transfer Localization in Molecularly Doped Thiophene-Based Donor Polymers", J. Phys. Chem. Lett. 1, 2037-2041 (2010).

P3HT bulk is as low as 5%. Inevitably, this observation puts the physical character of the charge transfer reaction between these compounds into question. Two contradictory models that are commonly used to explain the donor-acceptor ground-state interaction are introduced in section 2.6.

Here, we make use of the distinct infra-red (IR) spectroscopic signatures of neutral and ionized F_4TCNQ to monitor if all F_4TCNQ acceptors undergo charge transfer and to estimate the degree of this charge transfer, i.e., the amount of (partial or onefold) negative charge which is transferred to a F_4TCNQ unit. This idea is inspired by the observation that F_4TCNQ undergoes a significant conformational change from a quinoidal, planar to a more aromatic, bent structure upon ionization.[42,108] In conjunction, the IR bands that are assigned to the asymmetric stretching vibrations of the C≡N groups of F_4TCNQ shift to lower wave numbers. This red shift was found to increase linearly with increasing degree of charge transfer.[109,110]

We study F_4TCNQ-doping of P3HT and of a series of P3HT-related statistical copolymers in which the 3-hexylthiophene (3HT) repeat unit sequence is interrupted by a varied content of 1,4-dithienyl-2,3,5,6-tetrafluorobenzene (TFB) units. The electron accepting character of the TFB units leads to a systematic variation of the polymers' ionization potentials with varied TFB content.[111] In particular, the ionization potential increases from 4.8 eV for P3HT to 5.1 eV for the copolymer with the maximum TFB molar content of 9.5%. Charge transfer upon doping is nevertheless expected for all (co)polymers due to the large electron affinity (5.24 eV) of F_4TCNQ.[103] However, differences in the degree of charge transfer and the fraction of reacted F_4TCNQ molecules might occur due to different charge distributions along the thiophene main chains caused by the varied amount of TFB units.

IR spectra in the C≡N stretching modes region of F_4TCNQ and F_4TCNQ:(co)polymer films at 1:10 and 1:3 F_4TCNQ:(thiophene unit) molar ratio are shown in Fig. 4.12. In neutral F_4TCNQ films, two bands (labeled *A* and *B*) are seen, which, following Meneghetti et al.[108] and the results of our supporting density functional theory (DFT) calculations, can be assigned to the b_{1u}- and b_{2u}-symmetry vibration modes shown aside in Fig. 4.12. The b_{3g}- and a_g-symmetry modes are IR-forbidden in the planar neutral F_4TCNQ molecule. Note that the strong intensity of feature *A* as compared to feature *B* points to a high crystallinity of the pure F_4TCNQ layers. Upon charge transfer, i.e., upon ionization of the F_4TCNQ acceptors, the bands are considerably red-shifted. Features *C* and *E* can now be assigned to the b_{1u} and b_{2u} modes, respectively. According to the DFT calculations, feature *D* is due to the formerly IR-forbidden a_g-symmetry mode. In addition, feature *E* contains a contribution of the b_{3g}-labeled mode. The occurrence of formerly IR-inactive modes upon charge transfer points to a strong geometry change of the ionized F_4TCNQ molecule towards a non-planar conformation.

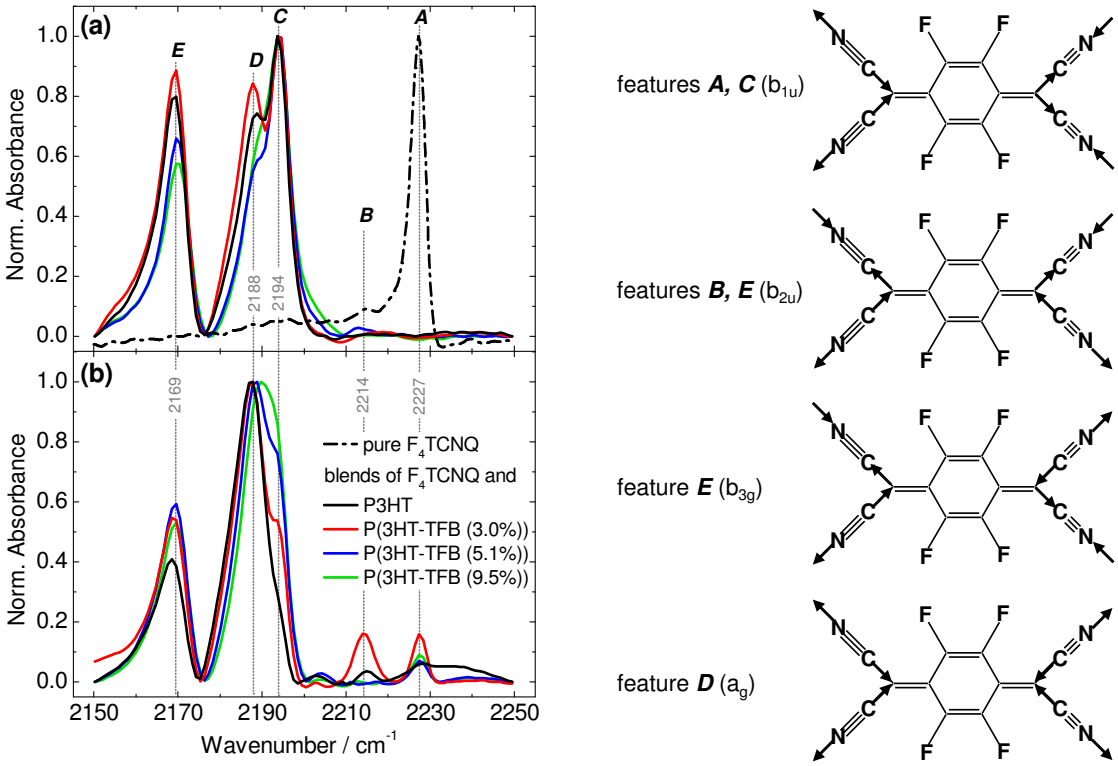

Figure 4.12: IR spectra and assigned C≡N stretching modes of neutral F_4TCNQ and F_4TCNQ blended with P3HT and the 3HT-TFB copolymers. (a) shows 1:10 and (b) shows 1:3 F_4TCNQ:(thiophene unit) molar ratio.

The red shift of the C≡N vibration modes is commonly used to determine the degree of charge transfer.[109,110] In fact, the present red shift points to a full onefold ionization of F_4TCNQ upon charge transfer with each of the tested (co)polymers. This result is, however, not shared by the accompanying DFT calculations which predict partial charge transfer between F_4TCNQ and a series of model donors, including quaterthiophene (4T), quinquethiophene (5T), and a block of thiophene and TFB units. Thereby, the amount of transferred charge depends highly on the exact position of the acceptor with respect to the donor. Based on the position and linewidth of the measured IR bands, such a variety of local conformations is, however, not observed in our experiments. As a consequence, it appears that, even at high doping ratios of 1:10 and 1:3, only one single charge transfer species is predominantly formed in which F_4TCNQ is fully onefold ionized.

Note that essentially no neutral F_4TCNQ is present at 1:10 doping ratio (features *A* and *B* are absent for these samples). At 1:3 doping concentration, a weak signature of neutral F_4TCNQ occurs in the IR spectra, indicative of the full occupation of all available donor sites by F_4TCNQ. Hence, the low doping efficiency of doping P3HT with F_4TCNQ, which has been found in section 4.4, cannot be explained by phase separation into domains of rather pure P3HT and pure (partly neutral) F_4TCNQ.

Our finding that only one specific charge transfer species is formed in the F_4TCNQ-doped layers is particularly remarkable for the copolymers that incorporate TFB units. Upon increasing the TFB content, the average length of uninterrupted thiophene blocks decreases.* Thus, deduced from the absence of a significant amount of neutral F_4TCNQ, adjacent charge transfer donor-acceptor pairs form along the same uninterrupted thiophene segment. Despite this close proximity, a shift or broadening of the IR bands at 1:3 doping concentration is not observed. If neighboring donor-acceptor pairs were to interact, a decrease of the amount of charge transfer or a rejection of charge transfer with further F_4TCNQ acceptors may have been expected, because a single thiophene donor would have had to donate charge to multiple acceptors. Thus, we point out that the charge transfer interaction with F_4TCNQ is a highly localized phenomenon, approximately limited to the spatial extend of F_4TCNQ, or, equivalently, a quaterthiophene unit. This also implies that the charge transfer interaction is governed by the local electronic properties of quaterthiophene, i.e., the 'local ionization potential' of the 4T segment, rather than depending on macroscopic parameters such as the ionization potential obtained from photoemission methods.

4.6 Comprehensive picture of p-doping P3HT with F_4TCNQ†

In order to gather a conclusive picture of the mechanism of doping P3HT with F_4TCNQ, we performed UV-Vis-NIR absorption spectroscopy to monitor the spectroscopic signature of neutral and ionized F_4TCNQ, and P3HT polarons in the near infra-red. From these data, we will finally conclude that, despite the low doping efficiency, almost every F_4TCNQ dopant that is added to the P3HT solution will be present as an ionized molecule in the blend layers.

Fig. 4.13a shows the optical absorbance normalized by layer thickness of undoped and F_4TCNQ-doped P3HT layers. Upon doping, pronounced sub-band absorption occurs in addition to the absorption of undoped P3HT. A qualitative comparison of the NIR region with literature data allows a clear assignment of the doping-induced features to P3HT polarons (rectangular-shaped absorption band at 1.2-1.8 eV and increasing absorption below 1 eV)[113,114] and singly negatively charged F_4TCNQ (peaks at 1.43 and 1.62 eV)[112,115]. According reference spectra of ionized F_4TCNQ and of iodine-doped P3HT in chloroform solution are shown in Fig. 4.13b. In order to quantify the absolute concentration of ionized acceptors, we seek to decompose the NIR absorption into the

* The average length of uninterrupted thiophene blocks is roughly 10 in case of the 3HT-TFB sample with 9.5% TFB content (including the unsubstituted thiophene units of the TFB monomer).

† This section is based on P. Pingel and D. Neher, "Comprehensive picture of p-type doping of P3HT with the molecular acceptor F_4TCNQ", Phys. Rev. B 87, 115209 (2013).

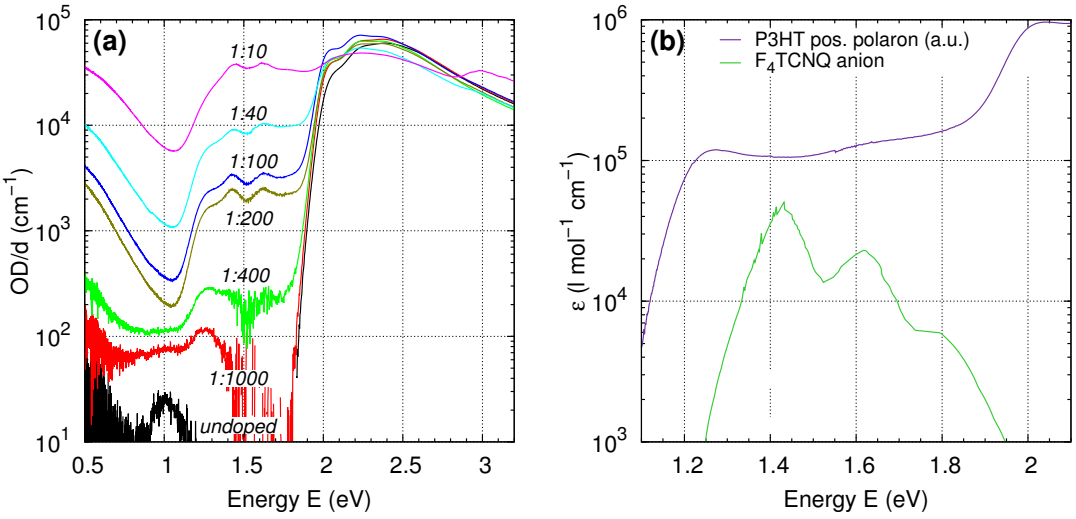

Figure 4.13: (a) Thickness-normalized absorbance spectra of undoped and F_4TCNQ-doped P3HT layers. (b) P3HT polaron and F_4TCNQ anion reference spectra. The F_4TCNQ anion spectrum is reprinted with permission from Ref. [112]. Copyright 1989 American Chemical Society.

P3HT polaron and F_4TCNQ anion parts. However, because consistent spectra of the extinction coefficient of polarons in a P3HT layer are not available, we start by analyzing the absorption spectra of F_4TCNQ-P3HT blends in chloroform solution.

The spectra of F_4TCNQ-P3HT chloroform solutions with varied doping ratios are displayed in Fig. 4.14a. Qualitatively, these spectra coincide with the spectra of the doped layers, meaning that the charge transfer takes place already in solution upon the admixture of F_4TCNQ and P3HT. Next, we reconstruct the NIR absorption of the doped solution spectra by weighted sums of a F_4TCNQ anion and a P3HT polaron reference spectrum. An example of the reconstruction of the 1:100-doped sample is plotted in Fig. 4.14b. The F_4TCNQ anion reference spectrum stems from published absorption data of a charge transfer salt, in which F_4TCNQ is singly ionized.[112] The P3HT polaron reference has been prepared by doping the P3HT powder by exposure to iodine vapor and subsequent dissolution of the doped compound into chloroform.

The algebraic reconstruction of the F_4TCNQ-P3HT solution spectra yields concentrations of ionized F_4TCNQ which are in the range of 50-70% of the actually applied F_4TCNQ dopant concentrations upon blending with P3HT. Assuming that the F_4TCNQ anion and donor-acceptor charge transfer pair concentrations are equal, we can calculate the molar extinction coefficient of the charge transfer pairs. At 1.52 eV, the notable minimum in between the two major F_4TCNQ anion peaks, the molar extinction coefficient amounts to ca. 8.3×10^4 l/mol/cm. Using this value, and assuming that the molar extinction coefficient is similar in the doped layers, we can estimate the concentration of donor-acceptor pairs that have undergone charge transfer in the F_4TCNQ-doped

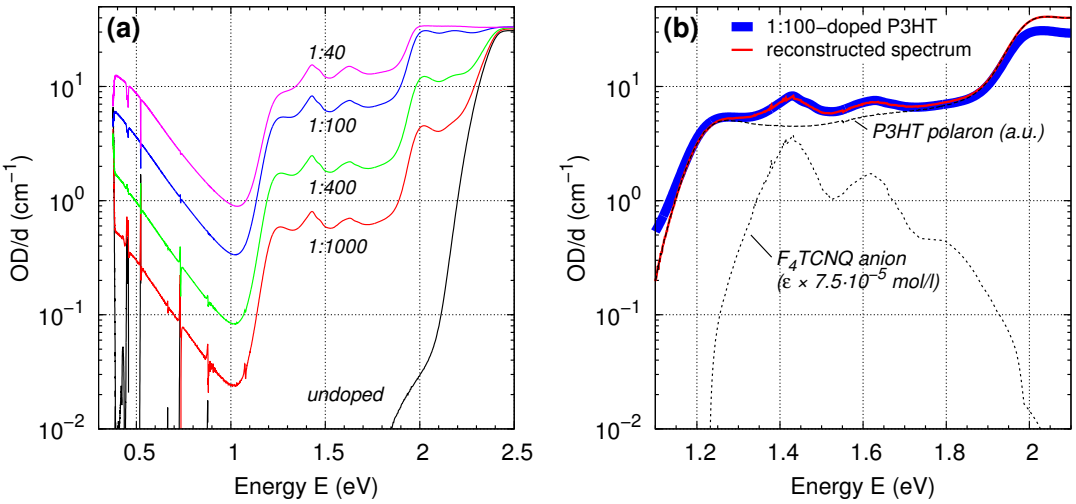

Figure 4.14: (a) UV-Vis-NIR absorbances normalized by the cuvette length (1 mm) of P3HT solutions in chloroform doped with various amounts of F_4TCNQ. The undoped sample had a concentration of 2 g/l. (b) Exemplary reconstruction of the P3HT polaron/F_4TCNQ anion absorption of the 1:100-doped P3HT sample from reference spectra.

P3HT film samples. It turns out that the concentration of ionized F_4TCNQ in these layers is only little lower (50-80%) than the molar concentration of intentionally applied F_4TCNQ upon preparation (assuming a mass density of 1.1 g/cm^3 of the solid film [104]). This means that the majority of applied F_4TCNQ acceptor molecules undergo charge transfer with P3HT.

Recalling the two models of molecular doping introduced in section 2.6, we can now confirm that doping P3HT with F_4TCNQ proceeds via a very efficient one-electron transfer from P3HT to the F_4TCNQ acceptor, which results in the formation of a P3HT polaron and a F_4TCNQ anion. A significant formation of isolated domains of neutral F_4TCNQ is thus ruled out. However, most of the donor-acceptor charge carrier pairs remain strongly bound and are not available for electrical conduction. This strong binding may be explained by the low permittivity of hydrocarbon-based semiconductors. On the other hand, 5% of these pairs are able to dissociate. The origin of the dissociation remains, however, unclear. According to the simulations of Mityashin et al., the split-up is favored by dissociation pathways within the energetic landscape of transport sites. [89] However, these pathways are due to the electrostatic interaction of neighboring charge pairs which implies a doping ratio dependent dissociation efficiency and, in particular, that almost no dissociation occurs at low doping ratios. Both of these predictions disagree with our experimental observations.

Note also, considering the model of hybrid charge transfer complex formation, that a significant amount of LUMO-derived states that could stem from these charge transfer species, would be detectable in the Kelvin probe measurements presented in section 4.4.

If such species were formed between P3HT and F_4TCNQ in the samples on aluminum, we should observe a rather sudden increase of the work function from the work function of aluminum to the level of those charge transfer complex-related states according to the density of applied F_4TCNQ acceptor molecules. This is clearly not the case for the charge transfer interaction between P3HT and F_4TCNQ.

4.7 Molecular p-doping of MEH-PPV with F_4TCNQ*

In addition to the studies of doping P3HT with F_4TCNQ, we investigate F_4TCNQ-doping of MEH-PPV layers, with respect to the mobile hole density, conductivity, and optical absorption. Note that MEH-PPV has a lower ionization potential (typically $\sim 5.1\,\mathrm{eV}$[116]) than P3HT, which is yet higher than the electron affinity of F_4TCNQ ($5.24\,\mathrm{eV}$[103]). Previous studies of F_4TCNQ-doped MEH-PPV layers by Zhang et al.[44,46] focused on modeling of the *j-V* characteristics of space-charge limited hole-only devices. From these analyses, it was concluded that the doping efficiency is about 1% and that the hole density increases linearly with the doping ratio (however, this was shown only for the narrow range of 0.11-0.17 mol% doping). Furthermore, it was proposed that the dissociation of the hole-anion charge transfer pairs is assisted by the electric field. This conclusion was based on the analysis of temperature-dependent *j-V* data and capacitance-voltage measurements on metal-semiconductor junctions.

The mobile hole density and bulk conductivity are extracted from admittance spectroscopy measurements of MIS samples and are shown in Fig. 4.15a,b. Low-field conductivities have also been determined from the *I-V* characteristics of hole-only devices. A significant and strictly linear rise of the density of mobile holes in the MEH-PPV bulk can be observed for doping ratios exceeding 10^{-4}. Thus, considering that the background charge carrier density in undoped MEH-PPV layers is similar to that of P3HT layers, it turns out that the efficiency of doping MEH-PPV with F_4TCNQ is considerably lower than for F_4TCNQ-doping of P3HT. Assuming a mass density of the undoped and doped MEH-PPV layers of $1\,\mathrm{g/cm^3}$, we can estimate the doping efficiency in these samples to be ca. 0.14%. Note that this value is one order of magnitude lower than the doping efficiency reported by Zhang et al.[46]

Upon F_4TCNQ-doping at moderate dopant concentrations ($\chi \sim 10^{-4}$), the bulk conductivity of these layers is notably lower than that of the undoped MEH-PPV samples, despite the significantly higher density of mobile charge carriers. This is probably due to the trap nature of ionized F_4TCNQ acceptor molecules, as has been pointed out for doped P3HT samples above, see section 4.4. Accordingly, for increasing doping ratios

* These results are currently unpublished.

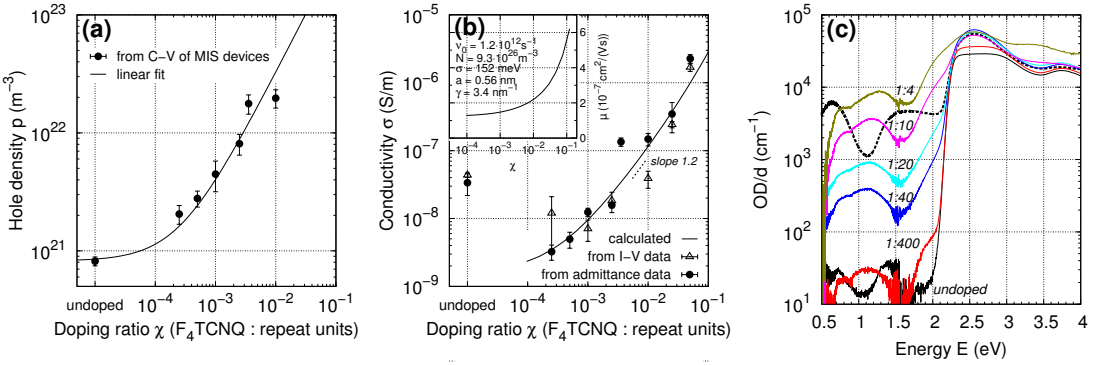

Figure 4.15: (a) Mobile hole density in F_4TCNQ-doped MEH-PPV layers. The line corresponds to the linear function $p = 3.2 \times 10^{24}\,\mathrm{m}^{-3}\chi + 8.2 \times 10^{20}\,\mathrm{m}^{-3}$. (b) Experimental and simulated conductivity of the doped layers. The inset shows the calculated mobility function and the simulation parameters. The meaning of these parameters is the same as in Table 4.1. (c) Absorption normalized by layer thickness of F_4TCNQ-doped MEH-PPV samples (solid lines, doping ratios given in the figure) and of an I_2 vapor-doped MEH-PPV layer (dashed line).

the conductivity increases linearly at moderate doping ratios until 10^{-3} and superlinearly at higher doping ratios. Note that the experimental conductivities are well reproduced by the mobility model of Arkhipov et al.[58–60] using the parameters given in Fig. 4.15b.

Although the electrical properties of F_4TCNQ-doped P3HT and MEH-PPV layers have close similarities – in particular, the linear increase of the mobile hole density, and the drop and increase of mobility at low and high doping ratios, respectively – the optical absorption spectra of F_4TCNQ-doped MEH-PPV layers indicate that the doping mechanism might be very different. Fig. 4.15c shows the UV-Vis-NIR spectra of undoped and doped MEH-PPV layers. As for doped P3HT, near infra-red absorption bands emerge upon increasing doping ratio. However, for the F_4TCNQ-doped MEH-PPV samples these features cannot be related to the ionized form of the donor or acceptor. In particular, the double-peak feature which is typical for singly ionized F_4TCNQ is absent. Comparison with the NIR spectrum of an I_2-doped MEH-PPV layer, which is presumably prototypical for the absorption of MEH-PPV polarons, yields no similarity with the F_4TCNQ-doped samples. Thus, we presume that the notion of an integer charge transfer, which does occur between P3HT and F_4TCNQ, may not be valid for the charge transfer between MEH-PPV and F_4TCNQ. Instead, partial charge transfer and the formation of hybrid charge transfer complexes, which has also been experimentally observed for other donor-acceptor pairs,[90] might occur upon F_4TCNQ-doping of MEH-PPV. Unlike for F_4TCNQ-doped P3HT, charge transfer complex formation between F_4TCNQ and MEH-PPV might be favored by the closer energies of the F_4TCNQ LUMO and the MEH-PPV HOMO, as has been outlined in section 2.6. Proof of the existence of such complexes and their related electronic states may be subject to ongoing research.

5 Conclusions

This thesis focuses on the structural and electrical characteristics of polyalkylthiophene layers. We have investigated the morphology of such layers by analyzing the local and far-field optical absorption, which includes information about the ratio of aggregated and disordered polymer chains, the intra- and interchain disorder, molecular orientation and the size of aggregates. These structural characteristics are used to explain the charge transport properties of the layers, which is a key to understand the device behavior of, for instance, organic field-effect transistors and solar cells. Moreover, we have investigated how the charge transport properties can be controlled and altered by molecular doping. We have presented a detailed study of the electrical properties of p-doped P3HT and MEH-PPV layers. Electrical measurements and optical spectroscopy were used to gain a conclusive picture about the mechanism of charge transfer between P3HT and the strong electron acceptor F_4TCNQ.

In the first part of this thesis, we have shown that detailed information about the amount, size, and disorder of P3HT aggregates can be extracted from optical absorption spectra of pure P3HT layers and P3HT:PCBM mixed layers. We have used the aggregate absorption model of Spano to separate the absorption contributions of aggregated and non-aggregated P3HT chains. The parameters obtained from this analysis are related to the intragrain disorder, the percentage of aggregates in the films, and the aggregate width, which were well in accordance with published data determined from other methods. Thus, Spano's model provides an unelaborate tool to study the morphology of layers that feature molecular or chain aggregation.

Comparing the properties of medium and high molecular weight P3HT, we have seen that the disorder in the P3HT aggregates of both layers is almost equal. This is most probably the reason why the intragrain charge carrier mobilities in these layers, as measured with microwave conductivity methods, are very similar. Furthermore, we have observed that the aggregate width in medium molecular weight P3HT corresponds to the length of the fully planarized P3HT chains. This is in contrast to the width of high molecular weight P3HT aggregates, which is much less than the contour length of the P3HT chains. Therefore, we presume that tie chains interconnect the ordered domains in high molecular weight P3HT, which explains the high macroscopic charge carrier

mobility in these layers. In contrast, intergrain connections are not possible in medium and low molecular weight P3HT samples. Therefore, the macroscopic charge transport must involve charge carrier motion through the disordered P3HT phase in these layers, which is the reason for the typically observed low field-effect mobilities in the low-to-medium molecular weight range.

Furthermore, we have analyzed the absorption spectra of P3HT:PCBM bulk heterojunction layers with respect to the Spano model. We have seen that thermal annealing of fast-drying chloroform-cast layers, which have a rather non-optimized and disperse morphology, causes both an increase of the size and number of P3HT aggregates and a reduction of the intragrain disorder if the annealing temperature is within the glass transition range. This is in accordance with the increase of the solar cell power conversion efficiency upon annealing. In addition, we have pointed out that the efficiency increase continues at higher annealing temperatures above the glass transition regime where aggregate formation and growth have been finished. In this regime, the improvement of the solar cell performance can be attributed to the continuous reduction of the disorder in the P3HT aggregates which leads to an increase of the hole current density and, therefore, to a balanced electron and hole transport at high annealing temperatures. On the other hand, spin-coating and solvent annealing using slowly evaporating dichlorobenzene as a solvent leads to a rather optimized morphology and solar cell performance of the P3HT:PCBM layers which is not improved further by thermal annealing.

In the second part of this thesis, we have investigated the layer morphology of an oligomeric polyquaterthiophene molecular weight fraction using far-field and scanning near-field optical microscopy. These layers are highly crystalline with domain sizes on the micrometer to tens-of-micrometer scale, which is probably due to the near-monodispersity of the oligo-PQT-12 sample. This is in contrast to the usual layer morphology of low molecular weight polythiophene fractions which contain a significant portion of disordered material. We have observed that the crystalline oligo-PQT-12 domains exhibit a strong in-plane dichroism which points to a high correlation of the molecular orientation. Investigating the molecular order and orientation in detail, we have found that the tens-of-micrometer-sized domains, which are separated by hard grain boundaries, consist of sub-domains with molecular orientations which differ slightly by not more than a few ten degrees. It appears that due to a certain flexibility in the crystalline lattice parameter and crystal axes, the formation of grain boundaries is avoided between these sub-domains. The exceptionally high crystallinity of the oligo-PQT-12 layers is probably the reason for the rather high field-effect mobility in these films.

In the third part of this thesis, we have derived a conclusive picture of the p-type dop-

ing of P3HT with the strong molecular acceptor F_4TCNQ with respect to the mechanism of charge transfer and the electrical characteristics of such doped layers. We have shown that the doping-induced concentration of mobile holes increases linearly with the dopant concentration; however, only 5% of the F_4TCNQ molecules create mobile holes. On the other hand, by quantitative analysis of the sub-band absorption of the doped P3HT layers we have proven that almost every F_4TCNQ that is introduced into the P3HT chloroform solution is present in the spin-coated layer as an anion. That means that the charge transfer mechanism between P3HT and F_4TCNQ is a full-electron charge transfer, ruling out the formation of a charge transfer complex via the hybridization of the donor's HOMO and the acceptor's LUMO. The finding that the density of mobile holes is much less than the concentration of ionized F_4TCNQ molecules must mean that the majority of the charge transfer pairs does not dissociate and remains strongly bound. We emphasize that the full-charge transfer mechanism present between P3HT and F_4TCNQ may, however, not be generally valid for all donor-acceptor ground-state interactions, as is indicated by the absorption spectra of F_4TCNQ-doped MEH-PPV layers.

Moreover, we have pointed out that the presence of the F_4TCNQ anions in the doped layers of P3HT and MEH-PPV strongly affects the charge transport properties as compared to the undoped polymer layers. In contrast to the common rash notion of a mobility increase upon doping due to trap filling, we have observed that the hole mobility is lower in weakly doped layers than in undoped samples. According to an established model of Arkhipov et al., this behavior is attributed to the rather long-range Coulomb attraction between the mobile, dissociated holes and the remaining F_4TCNQ anions. The doping ratio dependence of the mobility and conductivity is successfully modeled using Arkhipov's closed-form mobility model, which describes the mobile hole-anion attraction in terms of an effective broadening of the DOS distribution by deep trap states. Indeed, we have shown independently by using Kelvin probe measurements that a broadened DOS distribution is present in the F_4TCNQ-doped P3HT layers. Thus, the ionization of the dopants introduces additional tail states into the energetic landscape of the polymer layer, which serve as hole traps. The emergence of these traps counteracts the fill-up of the DOS tail by the doping-induced charge carriers and, in sum, a mobility decrease is seen at low doping ratios. At high doping ratios (in the mol% regime), the energetic landscape might flatten due to the high density of F_4TCNQ anions and, therefore, the mobility increases in this regime.

6 Publications

6.1 Publications discussed within this thesis and declaration of contributions

- Patrick Pingel, Achmad Zen, Ruben D. Abellón, Ferdinand C. Grozema, Laurens D. A. Siebbeles, and Dieter Neher, *Temperature-Resolved Local and Macroscopic Charge Carrier Transport in Thin P3HT Layers*, Adv. Funct. Mater. **20**, 2286-2295 (2010), DOI: 10.1002/adfm.200902273
  Contributions: PP performed the quantitative analysis of the optical spectra using the Spano model and the numerical evaluation of the transient microwave data. PP drafted the initial manuscript and took part in editing. OFET mobility data with respect to the molecular weight and temperature-resolved absorption data were measured by AZ during the course of his PhD studies. PR-TRMC mobilities were measured by RDA, FCG, and LDAS at the Delft University of Technology. Parts of these data were discussed, however solely qualitatively, in the diploma thesis of PP. DN supervised the project. FCG and DN co-edited the manuscript.

- Sarah T. Turner, Patrick Pingel, Robert Steyrleuthner, Edward J. W. Crossland, Sabine Ludwigs, and Dieter Neher, *Quantitative Analysis of Bulk Heterojunction Films Using Linear Absorption Spectroscopy and Solar Cell Performance*, Adv. Funct. Mater. **21**, 4640-4652 (2011), DOI: 10.1002/adfm.201101583
  Contributions: STT drafted and edited the initial manuscript. Experimental data were obtained by STT during the course of her MSc studies. PP initiated these measurements, provided the software script for data evaluation, and gave advice to the optical analysis. The single-carrier device studies were supported by RSt. DN supervised the project. PP, RSt, SL, DN co-edited the manuscript.

- Sergei Kühn, Patrick Pingel, Markus Breusing, Thomas Fischer, Joachim Stumpe, Dieter Neher, and Thomas Elsässer, *High-Resolution Near-Field Optical Investigation of Crystalline Domains in Oligomeric PQT-12 Thin Films*, Adv. Funct. Mater. **21**, 860-868 (2011), DOI: 10.1002/adfm.201001978
  Contributions: PP conducted the AFM measurements and the far-field microscopy.

Polarization microscopy at selected domains was done at the Fraunhofer IAP Golm in cooperation with ThF. Near-field optical measurements were performed by MB and SK at the Max-Born-Institut Berlin. Sample preparation was done by PP. SK drafted the initial manuscript. PP, ThF, DN, and ThE co-edited the manuscript. DN and ThE supervised the project.

- Patrick Pingel, Richard Schwarzl, and Dieter Neher, *Effect of molecular p-doping on hole density and mobility in poly(3-hexylthiophene)*, Appl. Phys. Lett. **100**, 143303 (2012), DOI: 10.1063/1.3701729
  Contributions: Experimental data were collected by RS during his research internship under the supervision by PP. Quantitative data analysis, and drafting and editing of the manuscript was done by PP. DN supervised the project and co-edited the manuscript.

- Patrick Pingel, Lingyun Zhu, Kue Surk Park, Jörn-Oliver Vogel, Silvia Janietz, Eung-Gun Kim, Jürgen P. Rabe, Jean-Luc Brédas, and Norbert Koch, *Charge-Transfer Localization in Molecularly Doped Thiophene-Based Donor Polymers*, J. Phys. Chem. Lett. **1**, 2037-2041 (2010), DOI: 10.1021/jz100492c
  Contributions: Experimental data were obtained by KSP during his master's thesis course. This project was supervised by J-OV, JPR, and NK. LZ, E-GK, and J-LB contributed the theoretical computations. SJ contributed the polymer samples. PP drafted and edited the manuscript. The manuscript was co-edited by LZ, E-GK, J-LB, SJ, JPR, and NK.

- Patrick Pingel and Dieter Neher, *Comprehensive picture of p-type doping of P3HT with the molecular acceptor F_4TCNQ*, Phys. Rev. B **87**, 115209 (2013), DOI: 10.1103/PhysRevB.87.115209
  Contributions: Unless otherwise stated in the article, sample preparation, measurements, and data analysis have been performed by PP. PP drafted and edited the manuscript. DN supervised the project and co-edited the manuscript.

6.2 Further publications

- G. Lu, J. Blakesley, S. Himmelberger, P. Pingel, J. Frisch, I. Lieberwirth, I. Salzmann, M. Oehzelt, R. di Pietro, A. Salleo, N. Koch, and D. Neher, *Moderate doping leads to high performance of semiconductor/insulator polymer blend transistors*, Nature Commun. **4**, 1588 (2013), DOI: 10.1038/ncomms2587

- M. Schubert, E. Preis, J. C. Blakesley, P. Pingel, U. Scherf, and D. Neher, *Mobility*

relaxation and electron trapping in a donor/acceptor copolymer, Phys. Rev. B **87**, 024203 (2013), DOI: 10.1103/PhysRevB.87.024203

- S. Albrecht, S. Janietz, W. Schindler, J. Frisch, J. Kurpiers, J. Kniepert, S. Inal, P. Pingel, K. Fostiropoulos, N. Koch, and D. Neher, *Fluorinated Copolymer PCPDTBT with Enhanced Open-Circuit Voltage and Reduced Recombination for Highly Efficient Polymer Solar Cells*, J. Am. Chem. Soc. **134**, 14932-14944 (2012), DOI: 10.1021/ja305039j

- I. Salzmann, G. Heimel, S. Duhm, M. Oehzelt, P. Pingel, B. M. George, A. Schnegg, K. Lips, R.-P. Blum, A. Vollmer, and N. Koch, *Intermolecular Hybridization Governs Molecular Electrical Doping*, Phys. Rev. Lett. **108**, 035502 (2012), DOI: 10.1103/Phys.Rev.Lett.108.035502

- S. Käbisch, P. Pingel, J. P. Rabe, and N. Koch, *Substrate- and oxidation-induced roughness of individual terraces of pentacene thin films*, Thin Solid Films **519**, 1857-1860 (2011), DOI: 10.1016/j.tsf.2010.10.032

- S. Joshi, P. Pingel, S. Grigorian, T. Panzner, U. Pietsch, D. Neher, M. Forster, and U. Scherf, *Bimodal Temperature Behavior of Structure and Mobility in High Molecular Weight P3HT Thin Films*, Macromolecules **42**, 4651-4660 (2009), DOI: 10.1021/ma900021w

- P. Pingel, A. Zen, D. Neher, I. Lieberwirth, G. Wegner, S. Allard, and U. Scherf, *Unexpectedly high field-effect mobility of a soluble, low molecular weight oligoquaterthiophene fraction with low polydispersity*, Appl. Phys. A **95**, 67-72 (2009), DOI: 10.1007/s00339-008-4994-0

- S. Joshi, S. Grigorian, U. Pietsch, P. Pingel, A. Zen, D. Neher, and U. Scherf, *Thickness Dependence of the Crystalline Structure and Hole Mobility in Thin Films of Low Molecular Weight Poly(3-hexylthiophene)*, Macromolecules **41**, 6800-6808 (2008), DOI: 10.1021/ma702802x

- A. Zen, P. Pingel, D. Neher, and U. Scherf, *Organic transistors utilising highly soluble swivel-cruciform oligothiophenes*, phys. stat. sol. (a) **205**, 440-448 (2008), DOI: 10.1002/pssa.200723504

- E. F. Aziz, A. Vollmer, S. Eisebitt, W. Eberhardt, P. Pingel, D. Neher, and N. Koch, *Localized Charge Transfer in a Molecularly Doped Conducting Polymer*, Adv. Mater. **19**, 3257-3260 (2007), DOI: 10.1002/adma.200700926

- A. Zen, P. Pingel, F. Jaiser, D. Neher, J. Grenzer, W. Zhuang, J. P. Rabe, A. Bilge, F. Galbrecht, B. S. Nehls, T. Farrell, U. Scherf, R. D. Abellón, F. C. Grozema, and L. D. A. Siebbeles, *Organic field-effect transistors utilizing solution-deposited oligothiophene-based swivel cruciforms*, Chem. Mater. **19**, 1267-1276 (2007), DOI: 10.1021/cm062000p

6.3 Select conference contributions

- P. Pingel and D. Neher, "A comprehensive picture of p-doping P3HT with the molecular acceptor F_4TCNQ", contributed talk at the DPG Spring Meeting, March 10^{th}–15^{th}, 2013, Regensburg

- P. Pingel and D. Neher, "Impedance Spectroscopy on Molecularly Doped MEH-PPV: Hole Density and Carrier Mobility", poster at the European Conference on Molecular Electronics, September 7^{th}–10^{th}, 2011, Barcelona

- P. Pingel, L. Zhu, K. S. Park, J.-O. Vogel, S. Janietz, E.-G. Kim, J. P. Rabe, J.-L. Brédas, and N. Koch, "The Localized Nature of Charge Transfer in F_4TCNQ-Doped Thiophene-Based Donor Polymers", poster at the Polydays, October 3^{rd}–5^{th} 2010, Berlin

- P. Pingel, A. Zen, R. D. Abellón, F. C. Grozema, L. D. A. Siebbeles, and D. Neher, "Temperature-Resolved Local and Macroscopic Charge Carrier Transport and Optical Absorption in Thin P3HT layers", poster at the MRS Spring Meeting, April 5^{th}–9^{th}, 2010, San Francisco

- P. Pingel, L. Zhu, K. S. Park, J.-O. Vogel, S. Janietz, E.-G. Kim, J. P. Rabe, J.-L. Brédas, and N. Koch, "The Localized Nature of Charge Transfer in F_4TCNQ-Doped Thiophene-Based Donor Polymers", contributed talk at the DPG Spring Meeting, March 21^{st}–26^{th}, 2010, Regensburg

- P. Pingel, A. Zen, F. C. Grozema, L. D. A. Siebbeles, and D. Neher, "A Consistent Picture of the Effect of Molecular Weight and Temperature on the Charge Transport in P3HT layers", poster at the International Workshop on Self-organized Materials for Optoelectronics, August 24^{th}–25^{th}, 2009, Mainz

Bibliography

[1] K. Hecker (Ed.) *Organic and Printed Electronics*. VDMA Verlag GmbH, Germany, 4th edn. (2011).

[2] I. A. Howard, R. Mauer, M. Meister, and F. Laquai. J. Am. Chem. Soc. **132**, 14866–14876 (2010).

[3] J. Jo, S.-S. Kim, S.-I. Na, B.-K. Yu, and D.-Y. Kim. Adv. Funct. Mater. **19**, 866–874 (2009).

[4] G. Li, V. Shrotriya, J. S. Huang, Y. Yao, T. Moriarty, K. Emery, and Y. Yang. Nat. Mater. **4**, 864–868 (2005).

[5] V. D. Mihailetchi, H. X. Xie, B. de Boer, L. J. A. Koster, and P. W. M. Blom. Adv. Funct. Mater. **16**, 699–708 (2006).

[6] H. C. Yang, T. J. Shin, L. Yang, K. Cho, C. Y. Ryu, and Z. N. Bao. Adv. Funct. Mater. **15**, 671–676 (2005).

[7] A. Facchetti. Mater. Today **10**, 28–37 (2007).

[8] G. M. Wang, J. Swensen, D. Moses, and A. J. Heeger. J. Appl. Phys. **93**, 6137–6141 (2003).

[9] H. Sirringhaus, P. J. Brown, R. H. Friend, M. M. Nielsen, K. Bechgaard, B. M. W. Langeveld-Voss, A. J. H. Spiering, R. A. J. Janssen, E. W. Meijer, P. Herwig, and D. M. de Leeuw. Nature **401**, 685–688 (1999).

[10] D. M. DeLongchamp, B. M. Vogel, Y. Jung, M. C. Gurau, C. A. Richter, O. A. Kirillov, J. Obrzut, D. A. Fischer, S. Sambasivan, L. J. Richter, and E. K. Lin. Chem. Mater. **17**, 5610–5612 (2005).

[11] C. Goh, R. J. Kline, M. D. McGehee, E. N. Kadnikova, and J. M. J. Fréchet. Appl. Phys. Lett. **86**, 122110 (2005).

[12] R. J. Kline, D. M. DeLongchamp, D. A. Fischer, E. K. Lin, L. J. Richter, M. L. Chabinyc, M. F. Toney, M. Heeney, and I. McCulloch. Macromolecules **40**, 7960–7965 (2007).

[13] J. F. Chang, B. Q. Sun, D. W. Breiby, M. M. Nielsen, T. I. Sölling, M. Giles, I. McCulloch, and H. Sirringhaus. Chem. Mater. **16**, 4772–4776 (2004).

[14] R. J. Kline, M. D. McGehee, E. N. Kadnikova, J. S. Liu, and J. M. J. Fréchet. Adv. Mater. **15**, 1519–1522 (2003).

[15] R. J. Kline, M. D. McGehee, E. N. Kadnikova, J. S. Liu, J. M. J. Fréchet, and M. F. Toney. Macromolecules **38**, 3312–3319 (2005).

[16] A. Zen, J. Pflaum, S. Hirschmann, W. Zhuang, F. Jaiser, U. Asawapirom, J. P. Rabe, U. Scherf, and D. Neher. Adv. Funct. Mater. **14**, 757–764 (2004).

[17] A. Zen, M. Saphiannikova, D. Neher, J. Grenzer, S. Grigorian, U. Pietsch, U. Asawapirom, S. Janietz, U. Scherf, I. Lieberwirth, and G. Wegner. Macromolecules **39**, 2162–2171 (2006).

[18] R. Zhang, B. Li, M. C. Iovu, M. Jeffries-EL, G. Sauvé, J. Cooper, S. J. Jia, S. Tristram-Nagle, D. M. Smilgies, D. N. Lambeth, R. D. McCullough, and T. Kowalewski. J. Am. Chem. Soc. **128**, 3480–3481 (2006).

[19] M. Brinkmann and P. Rannou. Adv. Funct. Mater. **17**, 101–108 (2007).

[20] J.-M. Verilhac, R. Pokrop, G. LeBlevennec, I. Kulszewicz-Bajer, K. Buga, M. Zagorska, S. Sadki, and A. Pron. J. Phys. Chem. B **110**, 13305–13309 (2006).

[21] M. Brinkmann and P. Rannou. Macromolecules **42**, 1125–1130 (2009).

[22] S. Joshi, P. Pingel, S. Grigorian, T. Panzner, U. Pietsch, D. Neher, M. Forster, and U. Scherf. Macromolecules **42**, 4651–4660 (2009).

[23] S. Joshi, S. Grigorian, U. Pietsch, P. Pingel, A. Zen, D. Neher, and U. Scherf. Macromolecules **41**, 6800–6808 (2008).

[24] R. J. Kline, M. D. McGehee, and M. F. Toney. Nat. Mater. **5**, 222–228 (2006).

[25] J.-F. Chang, J. Clark, N. Zhao, H. Sirringhaus, D. W. Breiby, J. W. Andreasen, M. M. Nielsen, M. Giles, M. Heeney, and I. McCulloch. Phys. Rev. B **74**, 115318 (2006).

[26] M. Halik, H. Klauk, U. Zschieschang, G. Schmid, S. Ponomarenko, S. Kirchmeyer, and W. Weber. Adv. Mater. **15**, 917–922 (2003).

[27] H. E. Katz and Z. Bao. J. Phys. Chem. B **104**, 671–678 (2000).

[28] J. Vrijmoeth, R. W. Stok, R. Veldman, W. A. Schoonveld, and T. M. Klapwijk. J. Appl. Phys. **83**, 3816–3824 (1998).

[29] P. Leclère, M. Surin, P. Viville, R. Lazzaroni, A. F. M. Kilbinger, O. Henze, W. J. Feast, M. Cavallini, F. Biscarini, A. P. H. J. Schenning, and E. W. Meijer. Chem. Mater. **16**, 4452–4466 (2004).

[30] H.-S. Seo, Y. Zhang, Y.-S. Jang, and J.-H. Choi. Appl. Phys. Lett. **92**, 223310 (2008).

[31] C. D. Dimitrakopoulos, B. K. Furman, T. Graham, S. Hegde, and S. Purushothaman. Synth. Met. **92**, 47–52 (1998).

[32] H. E. Katz, J. G. Laquindanum, and A. J. Lovinger. Chem. Mater. **10**, 633–638 (1998).

[33] A. R. Murphy, J. M. J. Fréchet, P. Chang, J. Lee, and V. Subramanian. J. Am. Chem. Soc. **126**, 1596–1597 (2004).

[34] J. H. Kang, D. da Silva, J.-L. Brédas, and X. Y. Zhu. Appl. Phys. Lett. **86**, 152115 (2005).

[35] J. Rivnay, R. Noriega, J. E. Northrup, R. J. Kline, M. F. Toney, and A. Salleo. Phys. Rev. B **83**, 121306 (2011).

[36] E. Lim, B.-J. Jung, M. Chikamatsu, R. Azumi, Y. Yoshida, K. Yase, L.-M. Do, and

H.-K. Shim. J. Mater. Chem. **17**, 1416–1420 (2007).

[37] L. Ma, W. H. Lee, Y. D. Park, J. S. Kim, H. S. Lee, and K. Choa. Appl. Phys. Lett. **92**, 063310 (2008).

[38] J. Sun, B. J. Jung, T. Lee, L. Berger, J. Huang, Y. Liu, D. H. Reich, and H. E. Katz. ACS Appl. Mater. Interfaces **1**, 412–419 (2009).

[39] C. P. Jarrett, R. H. Friend, A. R. Brown, and D. M. de Leeuw. J. Appl. Phys. **77**, 6289–6294 (1995).

[40] J. Blochwitz, M. Pfeiffer, T. Fritz, and K. Leo. Appl. Phys. Lett. **73**, 729–731 (1998).

[41] A. Yamamori, C. Adachi, T. Koyama, and Y. Taniguchi. Appl. Phys. Lett. **72**, 2147–2149 (1998).

[42] E. F. Aziz, A. Vollmer, S. Eisebitt, W. Eberhardt, P. Pingel, D. Neher, and N. Koch. Adv. Mater. **19**, 3257–3260 (2007).

[43] J. Hwang and A. Kahn. J. Appl. Phys. **97**, 103705 (2005).

[44] Y. A. Zhang and P. W. M. Blom. Org. Electron. **11**, 1261–1267 (2010).

[45] Y. Zhang and P. W. M. Blom. Appl. Phys. Lett. **97**, 083303 (2010).

[46] Y. Zhang, B. de Boer, and P. W. M. Blom. Adv. Funct. Mater. **19**, 1901–1905 (2009).

[47] P. Pingel, R. Schwarzl, and D. Neher. Appl. Phys. Lett. **100**, 143303 (2012).

[48] P. Pingel, L. Y. Zhu, K. S. Park, J. O. Vogel, S. Janietz, E. G. Kim, J. P. Rabe, J. L. Brédas, and N. Koch. J. Phys. Chem. Lett. **1**, 2037–2041 (2010).

[49] K. H. Yim, G. L. Whiting, C. E. Murphy, J. J. M. Halls, J. H. Burroughes, R. H. Friend, and J. S. Kim. Adv. Mater. **20**, 3319–3324 (2008).

[50] B. A. Gregg, S. G. Chen, and R. A. Cormier. Chem. Mater. **16**, 4586–4599 (2004).

[51] M. L. Tietze, L. Burtone, M. Riede, B. Luessem, and K. Leo. Phys. Rev. B **86**, 035320 (2012).

[52] J.-H. Lee, H.-M. Kim, K.-B. Kim, R. Kabe, P. Anzenbacher, Jr., and J.-J. Kim. Appl. Phys. Lett. **98**, 173303 (2011).

[53] S. G. Chen, P. Stradins, and B. A. Gregg. J. Phys. Chem. B **109**, 13451–13460 (2005).

[54] K. Walzer, B. Maennig, M. Pfeiffer, and K. Leo. Chem. Rev. **107**, 1233–1271 (2007).

[55] F. C. Spano. J. Chem. Phys. **122**, 234701 (2005).

[56] P. Pingel. *P-halbleitende teilkristalline und amorphe Schichten für organische Feldeffekt-transistoren*. diploma thesis, University of Potsdam (2008).

[57] P. Pingel, A. Zen, D. Neher, I. Lieberwirth, G. Wegner, S. Allard, and U. Scherf. Appl. Phys. A Mater. Sci. Process. **95**, 67–72 (2009).

[58] V. I. Arkhipov, P. Heremans, E. V. Emelianova, G. J. Adriaenssens, and H. Bässler. Appl. Phys. Lett. **82**, 3245–3247 (2003).

[59] V. I. Arkhipov, E. V. Emelianova, P. Heremans, and H. Bässler. Phys. Rev. B **72**, 235202 (2005).

[60] V. I. Arkhipov, P. Heremans, E. V. Emelianova, and H. Bässler. Phys. Rev. B **71**, 045214 (2005).

[61] E. J. W. Crossland, K. Tremel, F. Fischer, K. Rahimi, G. Reiter, U. Steiner, and S. Ludwigs. Adv. Mater. **24**, 839–844 (2012).

[62] E. Mena-Osteritz, A. Meyer, B. Langeveld-Voss, R. Janssen, E. Meijer, and P. Bauerle. Angew. Chem. Int. Ed. **39**, 2680–2684 (2000).

[63] D. T. Grubb. *Materials science and technology*, vol. 12, chap. Elastic Properties of Crystalline Polymers, 301–356. VCH (1993).

[64] M. Mihailov. *New Developments on Polymer Structure and Morphology*, chap. Some properties and structure transformations of crystallizing polymers - polyethylene and polyoxyethylene, 87–108. Hüthig & Wepf (1984).

[65] W. W. Parson. *Modern Optical Spectroscopy*. Springer (2007).

[66] M. Pope and C. E. Swenberg. *Electronic Processes in Organic Crystals and Polymers*. Oxford University Press (1999).

[67] F. C. Spano. Chem. Phys. **325**, 22–35 (2006).

[68] P. J. Brown, D. S. Thomas, A. Köhler, J. S. Wilson, J. S. Kim, C. M. Ramsdale, H. Sirringhaus, and R. H. Friend. Phys. Rev. B **67**, 064203 (2003).

[69] J. Clark, J. F. Chang, F. C. Spano, R. H. Friend, and C. Silva. Appl. Phys. Lett. **94**, 163306 (2009).

[70] P. Pingel, A. Zen, R. D. Abellón, F. C. Grozema, L. D. A. Siebbeles, and D. Neher. Adv. Funct. Mater. **20**, 2286–2295 (2010).

[71] S. T. Turner, P. Pingel, R. Steyrleuthner, E. J. W. Crossland, S. Ludwigs, and D. Neher. Adv. Funct. Mater. **21**, 4640–4652 (2011).

[72] D. Beljonne, J. Cornil, R. Silbey, P. Millié, and J. L. Brédas. J. Chem. Phys. **112**, 4749–4758 (2000).

[73] J. Gierschner, Y. S. Huang, B. Van Averbeke, J. Cornil, R. H. Friend, and D. Beljonne. J. Chem. Phys. **130**, 044105 (2009).

[74] V. Ambegaokar, B. I. Halperin, and J. S. Langer. Phys. Rev. B **4**, 2612–2620 (1971).

[75] A. Miller and E. Abrahams. Phys. Rev. **120**, 745–755 (1960).

[76] R. A. Marcus. J. Chem. Phys. **24**, 966–978 (1956).

[77] H. Bässler. phys. stat. sol. (b) **175**, 15–56 (1993).

[78] M. C. J. M. Vissenberg and M. Matters. Phys. Rev. B **57**, 12964–12967 (1998).

[79] V. I. Arkhipov, P. Heremans, E. V. Emelianova, G. J. Adriaenssens, and H. Bässler. J. Phys. Condens. Matter **14**, 9899–9911 (2002).

[80] R. A. Street, J. E. Northrup, and A. Salleo. Phys. Rev. B **71**, 165202 (2005).

[81] V. I. Arkhipov, E. V. Emelianova, A. Kadashchuk, and H. Bässler. Chem. Phys. **266**, 97–108 (2001).

[82] V. I. Arkhipov, E. V. Emelianova, and G. J. Adriaenssens. Phys. Rev. B **64**, 125125

(2001).

[83] M. Grunewald and P. Thomas. phys. stat. sol. (b) **94**, 125–133 (1979).

[84] A. Dieckmann, H. Bässler, and P. M. Borsenberger. J. Chem. Phys **99**, 8136–8141 (1993).

[85] G. Garcia-Belmonte, E. V. Vakarin, J. Bisquert, and J. P. Badiali. Electrochim. Acta **55**, 6123–6127 (2010).

[86] Y. L. Shen, K. Diest, M. H. Wong, B. R. Hsieh, D. H. Dunlap, and G. G. Malliaras. Phys. Rev. B **68**, 081204 (2003).

[87] O. Tal, Y. Rosenwaks, Y. Preezant, N. Tessler, C. K. Chan, and A. Kahn. Phys. Rev. Lett. **95**, 256405 (2005).

[88] S. D. Baranovskii, O. Rubel, and P. Thomas. J. Optoelectron. Adv. Mater. **7**, 1929–1933 (2005). 2nd International Workshop on Amorphous and Nanostructured Chalcogenides, Sinaia, ROMANIA, JUN 20-24, 2005.

[89] A. Mityashin, Y. Olivier, T. Van Regemorter, C. Rolin, S. Verlaak, N. G. Martinelli, D. Beljonne, J. Cornil, J. Genoe, and P. Heremans. Adv. Mater. **24**, 1535–1539 (2012).

[90] I. Salzmann, G. Heimel, S. Duhm, M. Oehzelt, P. Pingel, B. M. George, A. Schnegg, K. Lips, R.-P. Blum, A. Vollmer, and N. Koch. Phys. Rev. Lett. **108**, 035502 (2012).

[91] C. G. B. Garrett and W. H. Brattain. Phys. Rev. **99**, 376–387 (1955).

[92] S. M. Sze. *Physics of Semiconductor Devices*. Wiley & Sons, 2nd edn. (1982).

[93] J. S. Liu, R. S. Loewe, and R. D. McCullough. Macromolecules **32**, 5777–5785 (1999).

[94] B. C. Thompson and J. M. J. Fréchet. Angew. Chem. Int. Ed. **47**, 58–77 (2008).

[95] T. Agostinelli, S. Lilliu, J. G. Labram, M. Campoy-Quiles, M. Hampton, E. Pires, J. Rawle, O. Bikondoa, D. D. C. Bradley, T. D. Anthopoulos, J. Nelson, and J. E. Macdonald. Adv. Funct. Mater. **21**, 1701–1708 (2011).

[96] Y. Kim, S. Cook, S. M. Tuladhar, S. A. Choulis, J. Nelson, J. R. Durrant, D. D. C. Bradley, M. Giles, I. Mcculloch, C. S. Ha, and M. Ree. Nat. Mater. **5**, 197–203 (2006).

[97] L. H. Nguyen, H. Hoppe, T. Erb, S. Guenes, G. Gobsch, and N. S. Sariciftci. Adv. Funct. Mater. **17**, 1071–1078 (2007).

[98] S. S. van Bavel, E. Sourty, G. de With, and J. Loos. Nano Lett. **9**, 507–513 (2009).

[99] G. Dhanaraj. *Springer Handbook of Crystal Growth*. Springer (2010).

[100] H. Kleemann, B. Lussem, and K. Leo. J. Appl. Phys. **111**, 123722 (2012).

[101] B. Maennig, M. Pfeiffer, A. Nollau, X. Zhou, K. Leo, and P. Simon. Phys. Rev. B **64**, 195208 (2001).

[102] M. Pfeiffer, A. Beyer, T. Fritz, and K. Leo. Appl. Phys. Lett. **73**, 3202–3204 (1998).

[103] W. Y. Gao and A. Kahn. Appl. Phys. Lett. **79**, 4040–4042 (2001).

[104] T. J. Prosa, M. J. Winokur, J. Moulton, P. Smith, and A. J. Heeger. Macromolecules **25**, 4364–4372 (1992).

[105] I. Lange, J. C. Blakesley, J. Frisch, A. Vollmer, N. Koch, and D. Neher. Phys. Rev. Lett. **106**, 216402 (2011).

[106] S. Olthof, S. Mehraeen, S. K. Mohapatra, S. Barlow, V. Coropceanu, J.-L. Brédas, S. R. Marder, and A. Kahn. Phys. Rev. Lett. **109**, 176601 (2012).

[107] X. Jiang, Y. Harima, K. Yamashita, Y. Tada, J. Ohshita, and A. Kunai. Chem. Phys. Lett. **364**, 616–620 (2002).

[108] M. Meneghetti and C. Pecile. J. Chem. Phys. **84**, 4149–4162 (1986).

[109] J. S. Chappell, A. N. Bloch, W. A. Bryden, M. Maxfield, T. O. Poehler, and D. O. Cowan. J. Am. Chem. Soc. **103**, 2442–2443 (1981).

[110] A. Salmerón-Valverde, J. G. Robles-Martínez, J. García-Serrano, R. Gómez, R. M. Ridaura, M. Quintana, and Z. A. Molecular Engineering **8**, 419–426 (1999).

[111] D. Sainova, S. Janietz, U. Asawapirom, L. Romaner, E. Zojer, N. Koch, and A. Vollmer. Chem. Mater. **19**, 1472–1481 (2007).

[112] D. A. Dixon, J. C. Calabrese, and J. S. Miller. J. Phys. Chem. **93**, 2284–2291 (1989).

[113] R. Österbacka, C. P. An, X. M. Jiang, and Z. V. Vardeny. Science **287**, 839–842 (2000).

[114] P. J. Brown, H. Sirringhaus, M. Harrison, M. Shkunov, and R. H. Friend. Phys. Rev. B **63**, 125204 (2001).

[115] J. B. Torrance, J. J. Mayerle, K. Bechgaard, B. D. Silverman, and Y. Tomkiewicz. Phys. Rev. B **22**, 4960–4965 (1980).

[116] A. L. Holt, J. M. Leger, and S. A. Carter. J. Chem. Phys. **123**, 044704 (2005).

Appendix

In the following, the publications which are summarized in this thesis are reprinted with permission of the publishers.

ADVANCED FUNCTIONAL MATERIALS
www.afm-journal.de

Materials Views
www.MaterialsViews.com

FULL PAPER

Temperature-Resolved Local and Macroscopic Charge Carrier Transport in Thin P3HT Layers

By *Patrick Pingel, Achmad Zen, Ruben D. Abellón, Ferdinand C. Grozema, Laurens D.A. Siebbeles,* and *Dieter Neher**

Dedicated to the 70th birthday of Prof. Dr. Gerhard Wegner.

Previous investigations of the field-effect mobility in poly(3-hexylthiophene) (P3HT) layers revealed a strong dependence on molecular weight (MW), which was shown to be closely related to layer morphology. Here, charge carrier mobilities of two P3HT MW fractions (medium-MW: $M_n = 7\,200$ g mol^{-1}; high-MW: $M_n = 27\,000$ g mol^{-1}) are probed as a function of temperature at a local and a macroscopic length scale, using pulse-radiolysis time-resolved microwave conductivity (PR-TRMC) and organic field-effect transistor measurements, respectively. In contrast to the macroscopic transport properties, the local intra-grain mobility depends only weakly on MW (being in the order of 10^{-2} cm^2 V^{-1} s^{-1}) and being thermally activated below the melting temperature for both fractions. The striking differences of charge transport at both length scales are related to the heterogeneity of the layer morphology. The quantitative analysis of temperature-dependent UV/Vis absorption spectra according to a model of F. C. Spano reveals that a substantial amount of disordered material is present in these P3HT layers. Moreover, the analysis predicts that aggregates in medium-MW P3HT undergo a "pre-melting" significantly below the actual melting temperature. The results suggest that macroscopic charge transport in samples of short-chain P3HT is strongly inhibited by the presence of disordered domains, while in high-MW P3HT the low-mobility disordered zones are bridged via inter-crystalline molecular connections.

1. Introduction

Organic electronics are expected to play a major role in the future markets, making research in this field of great interest for science and industry.[1] Solution-processable organic macromolecules, e.g., poly(3-hexylthiophene) (P3HT), are of considerable interest for the realization of low-cost electronic devices.[2–4] For many electronic applications of organic thin films, the charge carrier transport inside the organic layer, i.e., the hopping of charges in an electric field through the arrangement of innumerous molecules, determines the functionality and device performance. It is now well established that the charge carrier mobility in polymer-based devices depends critically on the chemical and electronic structure of the individual molecules as well as on the morphology of the active layer.[5–17]

A strong correlation between the field-effect mobility and the molecular weight (MW) has been observed for P3HT and related polymers. In general, the field-effect mobility was seen to significantly increase by four orders of magnitude, typically from 10^{-6} to 10^{-2} cm^2 V^{-1} s^{-1}, with an increase in the molecular weight from ~3 000 g mol^{-1} to 30 000 g mol^{-1}.[10,11,15,17] This finding stimulated detailed studies related to the morphology of the layers made from different molecular weight P3HT.[5,9–11,15–23] Kline et al. showed in their original work that low molecular weight P3HT layers appear to be more crystalline in atomic force microscopy (AFM) and X-ray investigations than their higher molecular weight counterparts.[10] In particular, the AFM images suggested the formation of rod-like nanocrystallites in low molecular weight samples. The trapping of charges at the grain boundaries between such crystals was proposed to be the cause of the poor field-effect mobility in these samples. In a later study, the same authors pointed out that long polymer chains might bridge the ordered domains in high molecular weight P3HT.[11] In 2006, Kline et al. reported a high mobility in low molecular weight P3HT prepared on a Si/SiO$_2$ substrate that was treated with

[*] Prof. D. Neher, P. Pingel
Institute of Physics and Astronomy
University of Potsdam
Karl-Liebknecht-Straße 24-25
14476 Potsdam (Germany)
E-mail: neher@uni-potsdam.de
Dr. A. Zen
Robert Bosch Pte Ltd
Research and Technology Center Asia Pacific
11 Bishan Street 21
Singapore 537943 (Singapore)
R. D. Abellón, Dr. F. C. Grozema, Prof. L. D. A. Siebbeles
Opto-Electronic Materials Section
Department of Chemical Engineering
Delft University of Technology
Julianalaan 136, 2628 BL Delft (The Netherlands)

DOI: 10.1002/adfm.200902273

octadecyltrichlorosilane (OTS).[21] Based on the results of X-ray rocking-curve measurements, the authors concluded that low molecular weight P3HT on an OTS-treated substrate exhibits highly-oriented crystals at the buried interface to the gate dielectric. High mobilities were attributed to a reduced number of grain boundaries as a consequence of a more uniform crystallite orientation. This interpretation is in good accordance with the outcome of X-ray and mobility experiments undertaken by Karl et al. on layers made from small molecules.[24]

On the contrary, Zen et al. considered that such layers consist of ordered domains with highly-planarized chains and disordered areas with coiled chains. The transport through the disordered areas was proposed to determine the carrier mobility on a macroscopic scale.[15] Zen et al. later showed that the nanorods seen in the AFM images of low molecular weight P3HT are actually embedded in an amorphous phase.[16] Also, a strong dependence of the melting temperature and melting enthalpy on chain length was shown. It was proposed that the amorphous areas consist mainly of very short chains (which are not able to crystallize) and that the macroscopic mobility is largely determined by the degree of crystallinity of the samples and not by the perfection of chain packing within the ordered domains. Further, detailed structural investigations revealed that the perfection of alignment of the crystalline domains in low molecular weight samples improves largely with decreasing layer thickness.[20] However, despite the very uniform orientation of the crystallites in ultra-thin layers, the field effect mobility remained low for all thicknesses. This was attributed to the presence of amorphous regions between highly crystalline domains.

Chang et al. investigated the morphology and transistor properties of P3HT fractions with high molecular weights ($M_w = 15\,000$ to $270\,000$ g mol^{-1}).[22] They found that the morphological nanostructure is largely determined by the speed of film formation, which may be varied by spin coating, drop-casting, or solvent parameters. Variations may give rise to extended nanoribbons, uniformly oriented nanoribbons (upon slow solvent evaporation), or comparatively amorphous structures with a bi-modal orientation of conjugated domains (upon fast solvent evaporation, e.g., by spin-coating from chloroform). For such fast-cast layers, the field-effect mobility was limited to relatively low values, which was explained by the presence of disordered regions.

High-resolution transmission electron microscopy (HR-TEM) on P3HT samples grown by directional epitaxial solidification clearly revealed the presence of disordered regions (denoted as amorphous interlamellar zones) between the rod-like nanocrystals.[5,19] It was shown that these effectively isolate the individual crystalline lamellae in samples of low molecular weight P3HT ($M_w = 7\,300$ g mol^{-1}). Interestingly, these studies revealed the presence of tie-crystallites for a molecular weight higher than 18 000 g mol^{-1}, constituting conjugated bridges between the ordered domains. It is, however, also worth mentioning that the sample preparation by Brinkmann et al. differs significantly from the spin-coating process commonly applied for OFET device preparation and that the conclusions drawn from those studies may not be valid for spin-coated samples.

A common result of the studies described above was that decreasing the molecular weight only has a small effect on the chain packing in the crystalline domains, despite a small decrease of the distance between the main chain (thiophene) layers and a concomitant increase in the π–π stacking distance. All studies agree in the interpretation that the crystallites in low molecular weight samples consist of fully extended chains, meaning that the width of these crystals is determined by the contour length.[16,17,19] It has also been proposed that the chains in high molecular weight samples fold back to form nanoribbons.[16,19,22,25] Besides these differences, the electronic properties of chain segments embedded in the crystalline domains should depend only weakly on molecular weight. In fact, a recent analysis of the optical absorption of P3HT in solution and the solid state revealed that the molecular weight has very little effect on the transition energies.[26,27] The significant increase of the 0–0 band at ~2.05 eV (or 600 nm) in absorption with higher molecular weight could be consistently explained by applying a model developed by Spano.[28,29] Hereby, the conjugated chains are assumed to form H-aggregates. In the limit of weak exciton coupling, the relative intensities of the individual transitions of the vibronic progression are mainly determined by the exciton bandwidth, which itself depends on the length of the correlated conjugated segments in the crystalline domains.[30] It was predicted that this length has rather little effect on the transfer integral, implying the rate of intermolecular hopping of carriers in crystalline domains shall be rather independent of the actual length of planarized chain segments.

In this paper, we present results on the local (nanoscopic) and macroscopic charge transport in layers of P3HT with different molecular weight. The local transport was probed as function of temperature by the measurement of the pulse-radiolysis time-resolved microwave conductivity (PR-TRMC), while the macroscopic transport properties were investigated in the common bottom-gate, top-contact organic field-effect transistor (OFET) geometry. We link these results with information on the length of planarized chain segments as obtained from a detailed analysis of the temperature-dependent UV/Vis absorption spectra. These data provide strong evidence that the mobility in samples from low and medium molecular weight P3HT is controlled by the probability of carriers to cross the disordered regions between nanocrystals.

2. Results and Discussion

The chemical structure of the investigated compound is drawn in Scheme 1. We investigated in detail two molecular weight fractions of regioregular P3HT (denoted by medium-MW and high-MW), the hexyl side chains of which have been deuterated (P3dHT) for potential use in neutron scattering. A former investigation on the molecular weight dependence of field-effect mobility and morphology of P3dHT and P3HT thin films did not reveal any difference in the physical properties of the deuterated fractions as compared to non-deuterated P3HT fractions.[15,16] Additionally, we report OFET and PR-TRMC mobility data of deuterated and

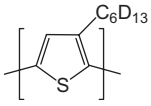

Scheme 1. Chemical structure of P3dHT.

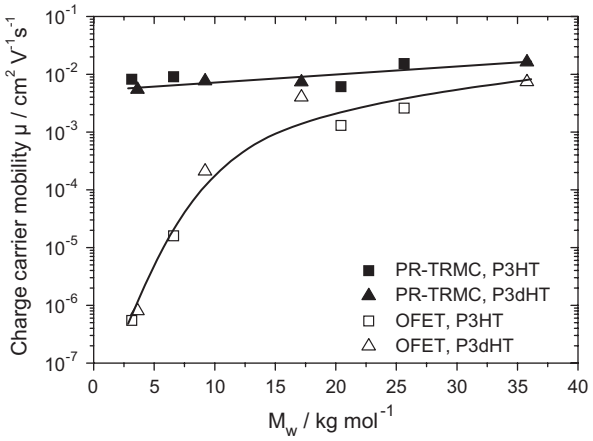

Figure 1. Molecular weight dependence of OFET and PR-TRMC charge carrier mobility of P3dHT and P3HT fractions at room temperature. The lines are guides to the eyes.

non-deuterated P3HT fractions of rather different molecular weight using the same polymer batches as in refs. [15,16].

2.1. Local (Nanoscopic) versus Macroscopic Transport

Figure 1 summarizes the local and macroscopic mobilities measured for deuterated and non-deuterated P3HT for various molecular weights at room temperature. PR-TRMC mobilities have been calculated from the after-pulse microwave conductivities, while the macroscopic OFET mobilities have been taken from the saturation regime of the output characteristics. As published earlier, the OFET mobility exhibits a pronounced increase with molecular weight. Contrary to this, the PR-TRMC values increase only slightly (by a factor of ~2) with chain length. Noticeably, the macroscopic mobility in high molecular weight P3HT differs only slightly from the value measured by PR-TRMC, while there is a huge difference when considering low molecular weights.

In PR-TRMC experiments the charge transport is probed on a local scale and charges moving back and forth inside a single grain of the material contribute mainly to the microwave conductivity signal. Therefore, PR-TRMC mobilities are generally expected to be higher than OFET mobilities, since in the former the mobility is not limited by the charge transport across grain boundaries or by charge carrier trapping on longer time scales. It should be noted that the PR-TRMC mobilities are the minimum values, assuming that all the charge that is initially generated survives until after the pulse. Since charges may decay by recombination and trapping already during the irradiation pulse, the actual microwave mobility is expected to be significantly higher. Due to this complication, it is difficult to compare absolute values for the microwave mobility with data obtained from OFET measurements.

2.1.1. Temperature-Dependent PR-TRMC Studies

In order to identify the processes leading to the difference between local and macroscopic transport in our P3HT samples, the temperature dependence of mobility has been studied in detail for two different molecular weights (Table 1). Also, measurements have been performed on a low-MW P3dHT fraction and the results

Table 1. Molecular parameters of the investigated molecular weight fractions of P3dHT (determined from GPC against polystyrene standards), including weight-average molecular weight (M_w), number-average molecular weight (M_n), and polydispersity index (PDI).

P3dHT fraction	M_w [g mol^{-1}]	M_n [g mol^{-1}]	PDI	Denotation
Hexane fraction	9 200	7 200	1.3	medium-MW fraction
Chloroform fraction	35 800	27 000	1.3	high-MW fraction

are presented in the Supporting Information. We find that low-MW P3dHT essentially behaves like the medium-MW fraction, however, transport and optical properties of the former are more severely affected at lower temperatures due to its lower melting point. During the PR-TRMC experiment the samples were heated step-wise from −75 to 120 °C and the transient microwave conductivity was recorded.

Figure 2a and b show PR-TRMC transients for the medium- and high-MW P3dHT fraction, respectively, at three different temperatures. Since the signal has been normalized to the dose, the absolute height of the signal is a direct measure of the change in conductivity induced per unit charge. For both samples the end-of-pulse conductivity increases with temperature, indicative of temperature-activated transport. Figure 3 summarizes the temperature dependence of the mobility extracted from these data. While these values are slightly lower for the medium-MW fraction, the temperature dependence above room temperature

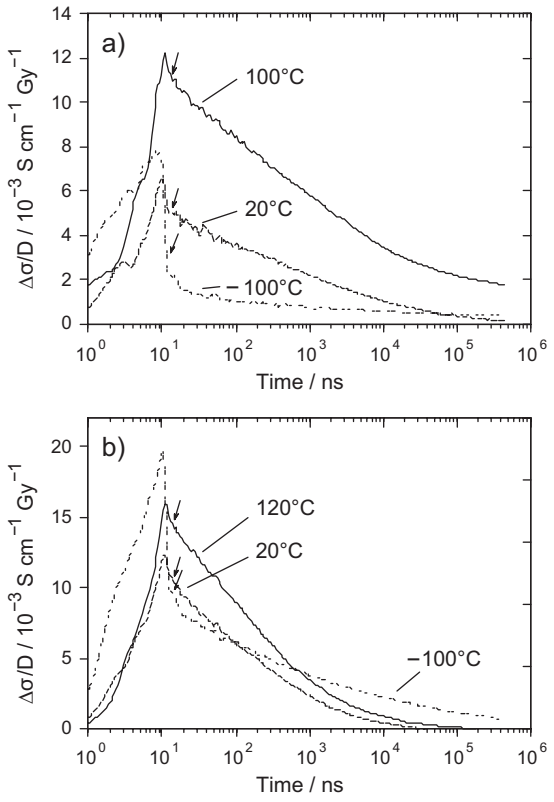

Figure 2. Microwave conductivity transients of the P3dHT medium-MW (a) and high-MW (b) fraction at different temperatures. End-of-pulse conductivities are marked by arrows.

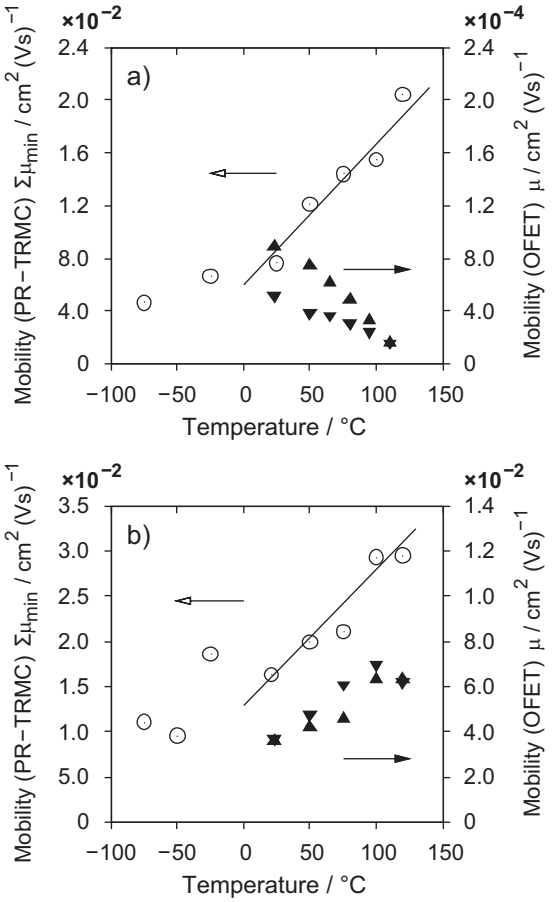

Figure 3. Temperature-dependent charge carrier mobilities of the P3dHT medium-MW (a) and high-MW (b) fraction from PR-TRMC (open symbols, during heating) and OFET experiments (filled symbols, upright and downward triangles during heating and subsequent cooling, respectively). The lines are guides to the eyes.

follows a rather similar trend for both samples. An increase of the microwave mobility with temperature has been often observed for organic conjugated materials and has been attributed to temperature-activated hopping over barriers or detrapping from shallow traps.[31–34] We also observed a rather high microwave mobility in our PR-TRMC studies on a low-MW P3dHT fraction (see Supporting Information). Here, the mobility increases continuously upon heating up to the melting temperature. At even higher temperatures, the mobility drops again, which we assign to the melting of the crystallites.

Regarding the transients shown in Figure 2, the decay characteristics are quite similar for both fractions, discarding the data measured at the lowest temperature of −100 °C. In a detailed study on high molecular weight P3HT samples, this decay has been attributed to carrier trapping rather than recombination with opposite free charges.[31] A good fit to the experimental after-pulse transients was obtained by assuming first-order decay (see Supporting Information), meaning that the number of traps is constant over time and significantly larger than the number of mobile charges generated in the PR-TRMC experiment.

From these fits, the mean decay times have been computed. For both fractions we find the decay times to increase with temperature (see Table S1 of the Supporting Information). This observation is consistent with the assumption drawn from earlier temperature-dependent microwave mobility data that the transport is determined by temperature-activated transport in a density-of-states distribution, where the charges are detrapped from shallow traps at higher temperature that would otherwise remain immobilized at low temperatures.[31,35] On the other hand, the rather rapid initial decay of the microwave conductivity signal at low temperatures (Fig. 2) is assigned to the immobilization of charges by shallow traps, leading to a fast decay of the number of free charges that initially contribute to the microwave conductivity signal.

Interestingly, the decay of the conductivity signal for the medium-MW fraction at room temperature and above is rather slow (slower than for the high-MW fraction, compare Fig. 2a and b), meaning that the carriers created in this sample are less susceptible to immobilization. Taking into account the rather similar intra-grain mobilities of charges in high- and medium-MW P3dHT (and low-MW P3dHT as well; see Supporting Information), this implies that chain ends (the density of which is higher in the short-chain medium-MW fraction) or grain boundaries do not affect the carrier transport on a local scale.

2.1.2. Temperature-Dependent OFET Mobilities

Charge carrier mobilities were extracted from the OFET characteristics at different temperatures in a cycle of heating from 25 to 120 °C (110 °C for the medium-MW fraction) and subsequent cooling back to room temperature and these values are also shown in Figure 3. The temperature dependence is clearly different for both fractions, where a decrease in the mobility of the medium-MW P3dHT sample is opposed to a strong increase in the mobility of the long-chain high-MW fraction. Similar like for the medium-MW fraction, OFETs made from low-MW P3dHT show a decrease of mobility at 50 °C as compared to room temperature (see Supporting Information).

Note that we have recently reported a significant drop of the OFET mobility above ~100 °C for a different P3HT sample with intermediate molecular weight.[23] Extensive X-ray studies on these layers suggested that the impairment of transport properties at higher temperatures cannot be explained by thermally induced morphological changes within the well-ordered crystalline domains, but that this effect must be related to inter-grain transport properties (i.e., the transport through disordered domains). Indeed, the π–π stacking of the aggregated P3HT chains has been shown to stay intact even up to temperatures close to melting (~220 °C). Moreover, we found the in-plane π–π stacking distance to be slightly reduced above 50 °C as compared to room temperature—the expected benefit of this reduction with regard to intra-grain transport was, however, not reflected in the temperature-resolved mobility measurements.

The analysis of the OFET mobility data of the high-MW fraction yields an activation energy of ~60 meV, which is quite comparable to 54 meV as reported by Kline et al. for another high molecular weight P3HT fraction ($M_n = 35\,000$ g mol^{-1}) below room temperature.[11] Interestingly, our experiments yield a rather

similar temperature dependence of the microwave mobility and the OFET mobility for our high-MW P3dHT. Although absolute mobility values are difficult to compare, as pointed out above, similar activation energies for transport on the local and macroscopic scale suggest that charges can move rather freely between crystalline domains, without the need to overcome significant energy barriers.

On the other hand, the data summarized above for medium-MW P3dHT provide convincing proof for the conclusions from structural studies, that the transport of charges over larger distances is actually not determined by the local motion within the individual grains, but by the morphological heterogeneity of the sample, namely the presence of disordered areas in-between crystallites.

2.2. In situ Thermal Dependence of UV/Vis Absorption

A. Zen et al. have shown that the absorption of solid layers of short chain P3HT exhibits a significant blue shift when heating the sample above room temperature.[16] Pronounced spectral changes of absorption as a function of temperature (thermochroism) are generally known for polythiophenes and are explained in terms of a thermally-induced conformational variation of the absorbing molecules.[36–43] It is believed that heating causes the conjugated molecular backbones to deplanarize by enhanced twisting between adjacent thiophene units, resulting in shorter conjugation lengths and wider conjugation length distribution. This very qualitative explanation was further supported by temperature-dependent X-ray investigations, showing that the packing of molecular chains is indeed affected already below melting temperature.[40,44]

Figure 4a shows absorption spectra measured at different temperatures for a layer of medium-MW P3dHT. Upon increasing the temperature, the absorption maximum blue-shifts continuously and looses absorption strength. In particular, the strength of the 2.05 eV (600 nm) transition reduces rapidly with temperature, pointing to significant changes of the nanomorphology. After cooling, the initial absorption is almost recovered, including the reoccurrence of the vibronic structure. The same behavior is found for low-MW P3dHT (see Supporting Information); however, the vibronic structure is far less distinctive than for medium-MW P3dHT due to the lower crystallinity of low-MW P3dHT.[16] Note that all spectra have been recorded at temperatures below the melting transition, which occurs above 150 °C, for medium-MW P3dHT (see the differential scanning calorimetry (DSC) scan inserted in Fig. 4a). For comparison, the absorption of the high-MW P3dHT fraction is shown in Figure 4b, where the thermally induced blue shift is far less pronounced and completely reversible. The DSC scan inset in Figure 4b shows that the melting transition of high-MW P3dHT occurs above 220 °C, which is much higher than the maximum temperature applied in our optical and electrical studies.

J. Clark et al.[45,46] published a sound analysis of the optical absorption data of P3HT layers with respect to the film nanostructure, using a model by Spano.[28,29] In general, the absorption of P3HT in the solid state consists of a low energy vibronic progression attributed to the absorption by planarized chains contained in aggregates, and a broad high-energy part caused by twisted chains in disordered areas. This assignment is

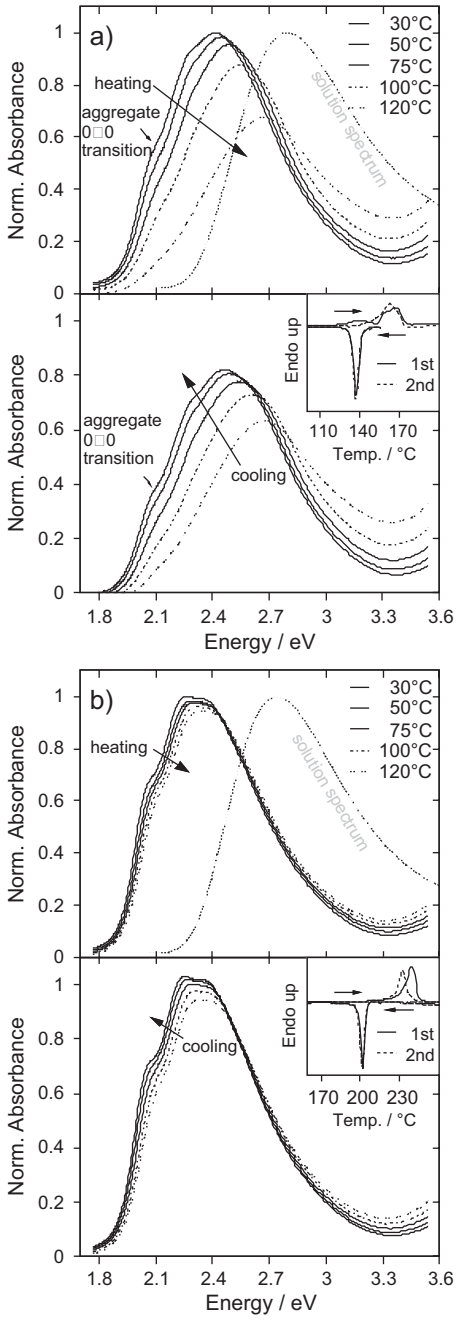

Figure 4. Temperature-dependent UV/Vis absorption of medium-MW (a) and high-MW (b) P3dHT layers during a cycle of heating (upper graphs) and subsequent cooling (lower graphs). The spectra have been normalized to the maximum absorption at 30 °C. Spectra in solution are plotted for comparison. The insets show DSC thermograms of respective solution-crystallized P3dHT samples.

supported by the rather blue-shifted and featureless absorption of P3HT in dilute solution.

As pointed out in the Introduction, Spano modeled the optical properties of P3HT films by assuming the formation of H-aggregates of parallel-aligned cofacially-packed conjugated chains.[28,29] In the case of weak excitonic coupling, the splitting of the electronic levels due to Coulombic interactions is

considerably smaller than the vibrational energy.[28,29,47] As a consequence, interchain coupling leads to a formation of vibronic bands, with their width basically being determined by the exciton bandwidth W. For symmetry reasons, only transitions from the ground state to the highest energy states of these individual bands are optically allowed. In this limit, the aggregate absorption of P3HT can be modeled according to

$$A \propto \sum_{m=0} \left(\frac{S^m}{m!}\right) \cdot \left(1 - \frac{We^{-S}}{2E_p} \sum_{n \neq m} \frac{S^n}{n!(n-m)}\right)^2 \cdot \exp\left(\frac{\left(E - E_0 - mE_p - \frac{1}{2}WS^m e^{-S}\right)^2}{2\sigma^2}\right), \quad (1)$$

where E_0 is the 0–0 transition energy of the aggregated species, E_p is the frequency of the vibronic transition, σ is the width of the line shape that is assumed to be Gaussian, S is the electron–phonon coupling strength (Huang-Rhys factor) and m counts the vibrational excitation. Hereby, the squared pre-factor in brackets is a modification of the Franck–Condon factor including interband mixing. The transition energies are corrected for the blue shift due to the energy splitting, considering only excitations to the top of the exciton bands to be optically allowed. Equation (1) neglects, however, that transitions to lower states within the vibronic bands become weakly allowed if disorder is introduced into the aggregates. It, additionally, assumes that the linewidth σ is the same for all transitions. Evidently, the exciton bandwidth W affects both the position and the relative strength of the individual vibronic transitions. As pointed out in the original paper by Spano,[29] increasing W causes a considerable reduction of the relative 0–0 transition strength. As shown later by Beljonne et al. and Gierschner et al., W is related to the length of the cofacially arranged chain segments L in the crystallites (Fig. 5), which shall be equivalent to the width of the nanoribbons seen in the structural studies described above.[30,48]

We have used Equation (1) to model the aggregate part of our temperature dependent P3dHT spectra. Hereby, we considered all terms up to the 0–6 transition. In the fitting procedure, E_0, σ, W, and a global factor were varied as free parameters, while S and E_p were fixed to 1.0 and 0.179 eV, respectively, as reported in the literature.[22,28,29,45,46,49,50] In P3HT, the main vibrational mode coupled to the UV/Vis electronic transition is known to be the C=C symmetric stretch at 0.179 eV.[49,51] The main difficulty to fit model Equation (1) to the absorption spectra was to identify the contribution stemming from aggregated chains. Experimental and simulated absorption spectra reported by Clark et al. suggested that contributions of non-aggregated molecules should be insignificant at energies below ~2.3 eV.[45] In order to test the consistency of the best-fit parameters, we varied the energy range used to fit the spectra to Equation (1) (see Supporting Information). The values of E_0, σ, and W were found to vary only slightly (max. ±0.5%, ±2%, ±4%, for E_0, σ, W, respectively) within lower and upper bounds of 1.92–2.05 and 2.20–2.35 eV, respectively. Thus, we considered the spectral range from 2.00 to 2.30 eV for the following analysis.

Figure 6 shows exemplary fits of absorption spectra of medium-MW P3dHT recorded at 50 and 120 °C. Further examples for fits to the spectra of the medium- and high-MW fractions are included in the Supporting Information. The black line of the model spectra reproduces very well both 0–0 and 0–1 intermolecular transition features. The difference between the experimental and calculated spectra (lines and filled circles) mostly represents the amorphous phase in the sample, although it is not fully identical to the absorption of P3HT chains in dilute solution. Possibly, the different environment of the chains in the disordered solid state and in solution is mainly responsible for this shift. In addition, the residual is weakly structured, indicating that the fit to Equation (1) does not fully explain the aggregate absorption spectrum over the whole wavelength range. As pointed out above, the applied model does not account for transitions to lower energy states in the vibrational bands, which become weakly allowed due to disorder. Additionally, our choice of a Gaussian line shape might be too simplistic for aggregate absorption.

The best-fit parameters of the aforementioned procedure are summarized in Figure 7. Values for the transition energy E_0 and for the line width σ are relatively similar for both medium- and high-MW samples. Additionally, both samples show the same weak dependence of temperature on E_0. This suggests that the local electronic properties of the chains in the ordered domains are only weakly affected by the molecular weight, in accordance with the results from the PR-TRMC studies described above. Upon heating from 30 to 120 °C, the intermolecular 0–0 transition energy increases by maximal 40 meV, corresponding to a blue shift of only 10 nm for the aggregates of both fractions. We assign this to thermally-induced local torsions of the conjugated backbones within the aggregates. This shift appears to be

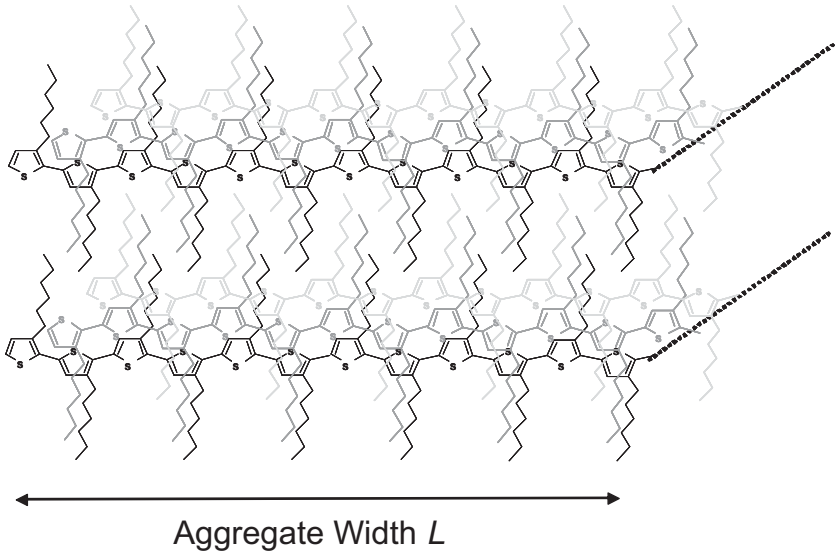

Figure 5. Schematic sketch of the molecular arrangement in a P3HT aggregate (medium-MW fraction, i.e., no chain folding present). The crystallite's long axis is indicated with dotted lines (as virtual third dimension).

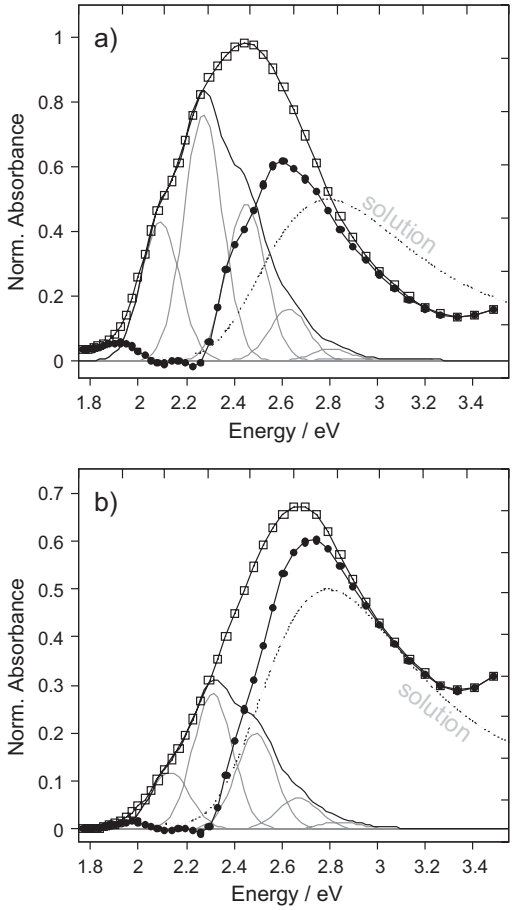

Figure 6. Absorption spectra of medium-MW P3dHT at a) 50 and b) 120 °C (lines and open squares). The spectra have been normalized to the maximum absorption of the 30 °C spectra (Fig. 4). The best-fits according to Equation (1) to the region of aggregate absorption (2.0–2.3 eV) are shown as bold lines, as well as the individual electronic-vibrational transitions (thin grey lines). The differences of the experimental and aggregate model spectra are displayed as lines and filled circles. The spectra of P3dHT in chloroform solution are plotted for comparison (dotted lines, normalized to 0.5).

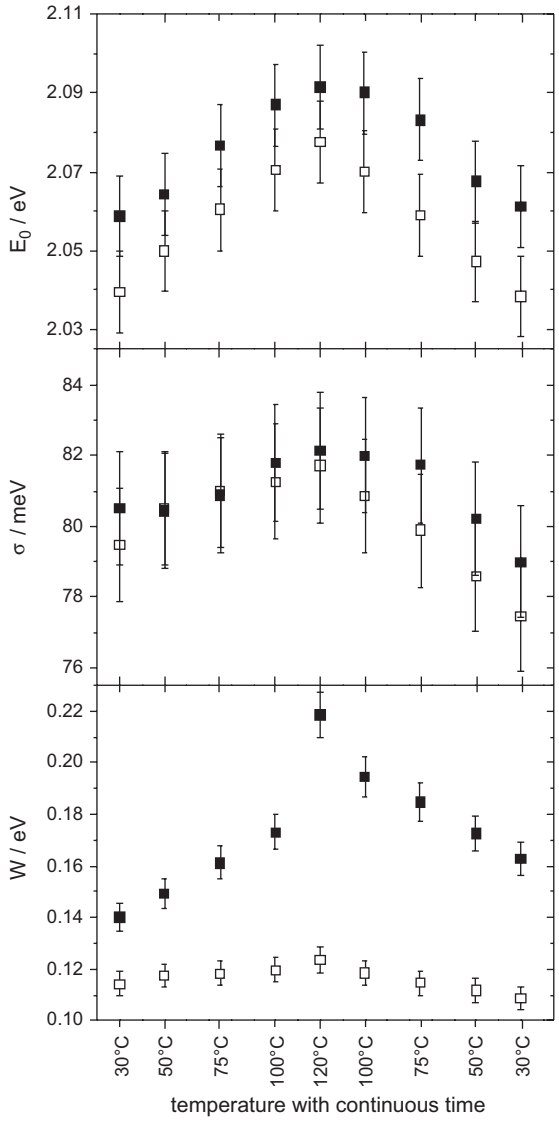

Figure 7. Parameters of the best-fits of Equation (1) to the experimental spectra of medium-MW (solid symbols) and high-MW P3dHT (open symbols) in the region of aggregate absorption (2.0–2.3 eV). E_0, σ and W are the 0–0 intermolecular transition energy, the width of the Gaussian line shape, and the exciton bandwidth, respectively.

insignificant regarding the large spectral changes occurring upon heating for the medium-MW sample in Figure 4a and even when considering the apparent blue shift of the absorption maximum for the high-MW fraction in Figure 4b.

The evaluation of the spectra shows that the thermal dependence of the absorption includes, in addition to the minor blue shift, an overall decrease of the aggregate absorption (Fig. 6 and Supporting Information) and also a significant redistribution of the oscillator strength within the aggregate absorption. The latter can be attributed to a change of the exciton band width in the aggregates of cofacially arranged chains with temperature. In fact, the value of W extracted from the fits is markedly higher for the medium-MW batch and it increases strongly with temperature (while for high-MW P3dHT the free exciton bandwidth remains almost constant over the whole temperature region, Fig. 7). For a large number of chains in an aggregate, the free exciton bandwidth W is twice the exciton coupling strength V_{AB}. Gierschner et al.[30] have performed theoretical calculations on aggregates of thiophene chains with N repeat units (determining the correlation length L) for different values of the intermolecular distance and the number of interacting aggregated chains. According to these calculations, the observed increase in W when heating the medium-MW layer can be caused by *a)* a decrease of the intermolecular π–π stacking distance, *b)* a larger number of molecules constituting the aggregate, and *c)* a smaller correlation length.

In recent X-ray studies we observed a slight decrease of the relevant π–π stacking distance by 3% when the layer was heated from room temperature to its melting regime (starting from ~220 °C).[23] Surprisingly, this decrease occurred abruptly at 50 °C and the intermolecular distance remained constant at higher temperatures. In contrast, the increase of W with temperature

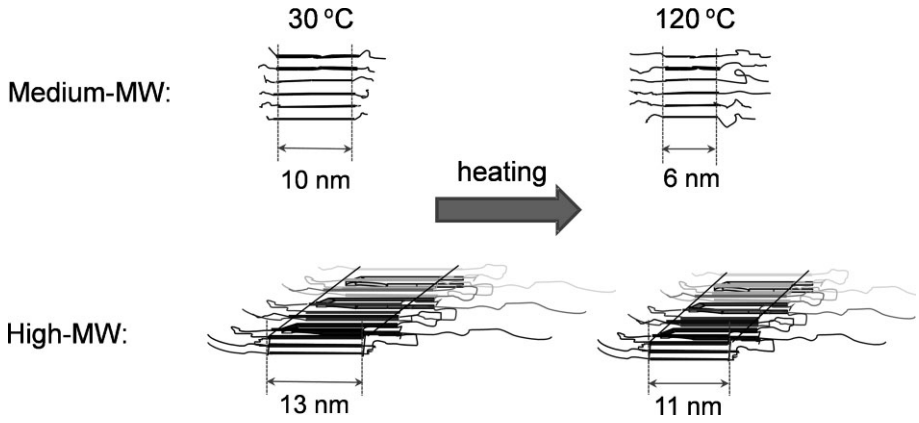

Figure 8. Visualization of the effect of heating of the P3dHT aggregates below the melting temperature.

is continuous, ruling out that the temperature-induced change in stacking distance is the main cause of the continuous and reversible increase of *W*.

An increase of the number of aggregated molecules, i.e., a growth of crystal size with increasing temperature, which is reversible upon cooling, does not seem plausible. Crystal growth during annealing is a known effect and might be the origin of the offset (~20 meV) between the free exciton bandwidths before and after annealing. The shrinkage of the aggregate size upon cooling is, however, highly unlikely.

As a result, we attribute the increase of the free exciton bandwidth in medium-MW P3dHT to the shortening of the interacting conjugated segments upon heating. The process is visualized in Figure 8. Using the simulation data from Gierschner et al. (Fig. 9), an exciton bandwidth of 140 meV, as found for medium-MW P3dHT at room temperature, is equivalent to ~25 interacting repeat units (or an interacting chain length of ~10 nm). This is nearly equivalent to the contour length of the medium-MW chains (27 repeat units on average after molecular weight correction according to Liu et al.[52]), which means that the chains are fully elongated within the aggregates. This result is fully consistent with the findings from structural studies as discussed above. Upon heating to 120 °C, the interacting chain length shortens towards 16 repeat units (equivalent to ~6 nm). This process occurs well below the actual melting temperature of the sample, implying that the medium-MW P3dHT aggregates undergo a "pre-melting," probably starting from its edges.

In high-MW P3dHT the temperature dependence of the exciton bandwidth is much less pronounced: *W* increases nearly reversibly from 114 to 123 meV upon heating from room temperature to 120 °C. This corresponds to a change from 31 to 28 interacting repeat units (or ~12.5 to 11 nm), compared to a contour length of ~26.5 nm). One possible reason for this weak effect of temperature on the interaction length may be the higher melting temperature of the high-MW P3dHT fraction. Alternatively, the number of chains folding back into the same aggregates might become larger with increasing chain length, as suggested by Brinkmann[19] and such backfolds might impede the pre-melting from the edges of the crystallites.

It is worth noting that the thermochroism in our medium-MW sample is characterized by a *continuous* blue shift and that it does not exhibit an isosbestic point. A similar situation was encountered by Holdcroft and co-workers when studying the thermochroism of high-MW regioregular P3HT at higher temperatures.[40] They suggested that this continuous blue shift is caused by the transition between three (rather than two) phases with distinctive absorption properties, namely a crystalline, a quasi-ordered, and a disordered phase. This interpretation was, however, based on the presumption that the absorption of the crystalline phase is independent of temperature. Our analysis of thermochroism in medium-MW P3HT shows conclusive evidence for a significant redistribution of oscillator strength between the individual vibronic transitions upon heating. Thereby, increasing the temperature causes transitions to higher vibronic states to become more intense. As a result, the overall envelope of the crystalline absorption appears to blue-shift with temperature, though the individual transition energies remain almost unaffected.

3. Conclusions

Our investigation of the intragrain charge transport in solid P3HT by pulse-radiolysis microwave conductivity reveals that the local mobility depends only weakly on molecular weight, despite the large effect of chain length on the OFET performance. Local transport is temperature-activated for the low-, medium- and high-MW P3dHT fractions well below the melting temperature,

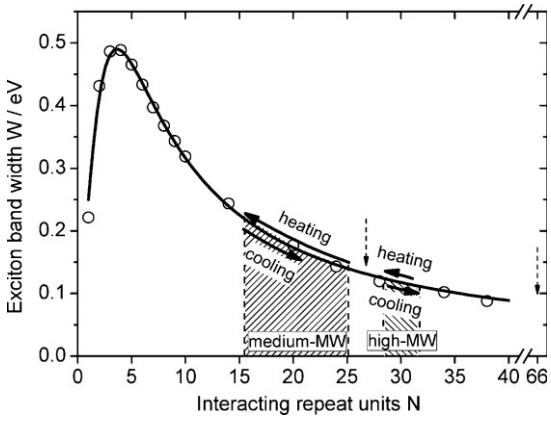

Figure 9. Dependence of the exciton bandwidth on the interacting chain length of aggregated P3HT molecules in terms of planarized thiophene repeat units. Circles show the results of simulations by Gierschner et al. (ref. [30], Fig. 3,) on the exciton coupling energy as function of the number of interacting thiophene rings, taking into account screening effects. The solid curve is a guide to the eye. Bold arrows display the evolution of the interacting chain length upon heating and cooling, as obtained from the analysis of the absorption spectra in Figure 4. Dashed arrows mark the average contour chain length of medium- and high-MW P3dHT as calculated from the number averages in Table 1 and the molecular weight correction according to Liu et al. [52]. Portions adapted with permission from Reference [30]. Copyright 2009, American Institute of Physics.

which can be attributed to hopping in a density-of-states distribution.

In contrast to the local transport properties, we found that the macroscopic mobility of medium-MW P3dHT layers is two orders of magnitude lower than the local mobility and it decreases with increasing temperature. The striking differences of charge transport at both length scales are related to the layer nanomorphology. From the comparison of local and macroscopic mobilities, we conclude that macroscopic transport is not actually determined by the local motion of charges within ordered grains, but by the transport through disordered material surrounding these grains.

The quantitative analysis of temperature-dependent UV/Vis absorption spectra suggests that the aggregates in medium-MW P3dHT undergo a "pre-melting" significantly below the actual melting temperature. As a result, the interacting chain length (i.e., the number of interacting repeat units) of the molecules that constitute an aggregate becomes smaller, i.e., the aggregate width decreases. The concomitant increase in width of the interlamellar zones, as well as the likely increase of disorder in these amorphous regions (as evidenced by the blue-shift of the absorption of the disordered phase) is presumably the main reason for the drop in the macroscopic mobility of short chain P3dHT upon heating. In contrast, long chains may interconnect the crystalline domains in high-MW P3dHT, thus by-passing the disordered interlamellar regions, and rendering the macroscopic charge transport in this material less susceptible to changes of the sample heterogeneity.

4. Experimental

For the investigations, P3dHT was prepared by the Grignard metathesis procedure according to McCullough and co-workers [53]. The deuteration of side chains was chosen in order to perform neutron scattering experiments, which are the subject of further investigations. The raw polymer was fractionated by applying the solvent extraction method [54]. Subsequent extraction steps, with solvents of increasing solubility for P3dHT, yielded polymer fractions with polydispersity indices between 1.3 and 1.4. The average molecular weights were determined by using gel permeation chromatography (GPC) with THF as the solvent (calibration with narrowly distributed polystyrene standards). Powders of the P3dHT fractions were precipitated from solvents into non-solvents, where such powders are often highly crystalline.

Optical absorption spectra were measured in situ with a Perkin-Elmer Lambda 19 UV/Vis spectrometer at various temperatures. Thin polymer films (~50–80 nm in thickness) were spin-coated from chloroform solutions (typically 10 g L^{-1}) on glass substrates that were covered by a transparent indium tin oxide (ITO) electrode on the backside. The sample temperature was controlled by resistive heating of the ITO, where the actual temperature at the polymer surface was measured using a PT100 temperature sensor glued to the front side of the substrate. For technical reasons, the maximum temperature was 120 °C.

PR-TRMC was performed in order to investigate the local charge transport properties. Details about the instrumentation and sample preparation can be found in refs. [31,55,56]. The sample is contained in a microwave cell with rectangular dimensions. Pulsed irradiation with high-energy (3 MeV) electrons leads initially to a low (micro-molar) concentration of positive and negative charge carriers uniformly distributed in the samples. After the incident pulse (1–50 ns duration), the conductivity of the sample is probed as a function of time by monitoring the attenuation of a reflected microwave (frequency range of 28–38 GHz and maximum electric field strength of 10 V m^{-1}). The fractional change in microwave power reflected by the cell is directly proportional to the change in conductivity ($\Delta\sigma$). The concentration of charges that is generated initially can be estimated using dosimetry measurements [57]. Using this estimation the charge carrier mobility can be calculated. Due to trapping or charge carrier recombination during the pulse, PR-TRMC results in a lower limit for the charge carrier mobility (μ_{min}). As both positive and negative charge carriers can contribute to the conductivity signal, μ_{min} represents the sum of hole and electron mobility, the latter is expected to be negligible in P3HT [31]. For a more detailed description of the PR-TRMC technique see refs. [31,56].

For the investigation of charge transport covering macroscopic distances we evaluated the electrical properties of OFETs. In the present OFET geometry, charge carriers—primarily holes in case of P3HT on top of SiO_2—have to move 100 μm from the source to the drain electrode through the polymer layer, parallel and close to the semiconductor-insulator surface. Assuming a domain size of 10 nm [16], holes have to cross 10 000 domains and domain boundaries for crossing the channel. Therefore, the field-effect mobility, as calculated from OFET characteristics, is a macroscopic effective value that results from all local mobilities within the different domains and from potential transport barriers at the domain boundaries.

OFETs were prepared in bottom-gate, top-source/drain geometry. Homogeneous polymer layers with a thickness in the range of 50–80 nm were formed by spin-coating from chloroform solution onto n-doped silicon substrates that are covered with a ~300 nm thick insulating SiO_2 layer. Prior to all processing, the SiO_2 surface was thoroughly cleaned with several common solvents and underwent an oxygen plasma treatment (5 min at a power of 200 W), followed by silanization using hexamethyldisilazane (HMDS) for 26 h at 60 °C. Finally, 100 nm thick evaporated interdigitating gold electrodes served as source and drain contacts. Device characteristics at specific temperatures were recorded using an Agilent 4155C semiconductor parameter analyzer. The temperature was controlled using a Digit Concept DCT 600 thermal controller and heating chuck. Preparation and measurements were performed in an inert nitrogen atmosphere. Charge carrier mobilities were calculated from the saturation region of the output characteristics (drain current, I_{DS} vs. source-drain voltage, V_{DS}) according to

$$I_{DS,sat} = \frac{WC_i}{2L}\mu_{sat}(V_{DS} - V_0)^2, \quad (2)$$

where $W = 14.85$ cm and $L = 100$ μm are the channel width and length, respectively, $C_i = 11.9$ nF cm^{-2} is the capacitance per unit area and V_0 is the onset voltage.

Acknowledgements

We thank Dr. S. Janietz, Fraunhofer Institute for Applied Polymer Research, Potsdam, and Prof. Dr. U. Scherf, University of Wuppertal for providing the molecular weight fractions of P3dHT. We are grateful to Sarah Turner for her valuable help editing the manuscript. This work was financially supported by the Deutsche Forschungsgemeinschaft, Schwerpunktprogramm 1121. Supporting Information is available online from Wiley InterScience or from the author.

Received: December 1, 2009
Revised: March 30, 2010
Published online: June 14, 2010

[1] *Organic Electronics*, (Ed: K. Hecker), VDMA Verlag GmbH, Germany **2007**.
[2] Z. Bao, *Adv. Mater.* **2000**, *12*, 227.
[3] A. Dodabalapur, *Mater. Today* **2006**, *9*, 24.
[4] S. P. Speakman, G. G. Rozenberg, K. J. Clay, W. I. Milne, A. Ille, I. A. Gardner, E. Bresler, J. H. G. Steinke, *Org. Electron.* **2001**, *2*, 65.
[5] M. Brinkmann, P. Rannou, *Adv. Funct. Mater.* **2007**, *17*, 101.
[6] J. F. Chang, B. Q. Sun, D. W. Breiby, M. M. Nielsen, T. I. Solling, M. Giles, I. McCulloch, H. Sirringhaus, *Chem. Mater.* **2004**, *16*, 4772.

[7] D. M. DeLongchamp, B. M. Vogel, Y. Jung, M. C. Gurau, C. A. Richter, O. A. Kirillov, J. Obrzut, D. A. Fischer, S. Sambasivan, L. J. Richter, E. K. Lin, *Chem. Mater.* **2005**, *17*, 5610.
[8] H. Yang, T. J. Shin, L. Yang, K. Cho, C. Y. Ryu, Z. Bao, *Adv. Funct. Mater.* **2005**, *15*, 671.
[9] R. J. Kline, D. M. DeLongchamp, D. A. Fischer, E. K. Lin, L. J. Richter, M. L. Chabinyc, M. F. Toney, M. Heeney, I. McCulloch, *Macromolecules* **2007**, *40*, 7960.
[10] R. J. Kline, M. D. McGehee, E. N. Kadnikova, J. S. Liu, J. M. J. Frechet, *Adv. Mater.* **2003**, *15*, 1519.
[11] R. J. Kline, M. D. McGehee, E. N. Kadnikova, J. S. Liu, J. M. J. Frechet, M. F. Toney, *Macromolecules* **2005**, *38*, 3312.
[12] H. Sirringhaus, *Adv. Mater.* **2005**, *17*, 2411.
[13] H. Sirringhaus, P. J. Brown, R. H. Friend, M. M. Nielsen, K. Bechgaard, B. M. W. Langeveld-Voss, A. J. H. Spiering, R. A. J. Janssen, E. W. Meijer, P. Herwig, D. M. de Leeuw, *Nature* **1999**, *401*, 685.
[14] G. M. Wang, J. Swensen, D. Moses, A. J. Heeger, *J. Appl. Phys.* **2003**, *93*, 6137.
[15] A. Zen, J. Pflaum, S. Hirschmann, W. Zhuang, F. Jaiser, U. Asawapirom, J. P. Rabe, U. Scherf, D. Neher, *Adv. Funct. Mater.* **2004**, *14*, 757.
[16] A. Zen, M. Saphiannikova, D. Neher, J. Grenzer, S. Grigorian, U. Pietsch, U. Asawapirom, S. Janietz, U. Scherf, I. Lieberwirth, G. Wegner, *Macromolecules* **2006**, *39*, 2162.
[17] R. Zhang, B. Li, M. C. Iovu, M. Jeffries-El, G. Sauve, J. Cooper, S. J. Jia, S. Tristram-Nagle, D. M. Smilgies, D. N. Lambeth, R. D. McCullough, T. Kowalewski, *J. Am. Chem. Soc.* **2006**, *128*, 3480.
[18] J. M. Verilhac, R. Pokrop, G. LeBlevennec, I. Kulszewicz-Bajer, K. Buga, M. Zagorska, S. Sadki, A. Pron, *J. Phys. Chem. B* **2006**, *110*, 13305.
[19] M. Brinkmann, P. Rannou, *Macromolecules* **2009**, *42*, 1125.
[20] S. Joshi, S. Grigorian, U. Pietsch, P. Pingel, A. Zen, D. Neher, U. Scherf, *Macromolecules* **2008**, *41*, 6800.
[21] R. J. Kline, M. D. McGehee, M. F. Toney, *Nat. Mater.* **2006**, *5*, 222.
[22] J. F. Chang, J. Clark, N. Zhao, H. Sirringhaus, D. W. Breiby, J. W. Andreasen, M. M. Nielsen, M. Giles, M. Heeney, I. McCulloch, *Phys. Rev. B* **2006**, *74*, 115318.
[23] S. Joshi, P. Pingel, S. Grigorian, T. Panzner, U. Pietsch, D. Neher, M. Forster, U. Scherf, *Macromolecules* **2009**, *42*, 4651.
[24] N. Karl, in: *Organic Electronic Materials*, (Eds: R. Farchioni, G. Grosso), Springer, Berlin **2001**.
[25] S. Malik, A. K. Nandi, *J. Polym. Sci. Part. B: Polym. Phys.* **2002**, *40*, 2073.
[26] R. Kalbitz, diploma thesis, Universität Potsdam **2008**.
[27] R. Kalbitz, F. Jaiser, S. Nahar, M. Forster, S. Allard, U. Scherf, D. Neher, A. Köhler, unpublished.
[28] F. C. Spano, *Chem. Phys.* **2006**, *325*, 22.
[29] F. C. Spano, *J. Chem. Phys.* **2005**, *122*, 234701.
[30] J. Gierschner, Y. S. Huang, B. Van Averbeke, J. Cornil, R. H. Friend, D. Beljonne, *J. Chem. Phys.* **2009**, *130*, 044105.
[31] G. Dicker, M. P. de Haas, J. M. Warman, D. M. de Leeuw, L. D. A. Siebbeles, *J. Phys. Chem. B* **2004**, *108*, 17818.
[32] G. H. Gelinck, J. M. Warman, *J. Phys. Chem.* **1996**, *100*, 20035.
[33] P. Prins, F. C. Grozema, B. S. Nehls, T. Farrell, U. Scherf, L. D. A. Siebbeles, *Phys. Rev. B* **2006**, *74*, 113203.
[34] J. M. Warman, G. H. Gelinck, M. P. de Haas, *J. Phys. Condes. Matter* **2002**, *14*, 9935.
[35] G. Dicker, M. P. de Haas, D. M. de Leeuw, L. D. A. Siebbeles, *Chem. Phys. Lett.* **2005**, *402*, 370.
[36] S. Garreau, M. Leclerc, N. Errien, G. Louarn, *Macromolecules* **2003**, *36*, 692.
[37] O. Inganäs, G. Gustafsson, W. R. Salaneck, J. E. Osterholm, J. Laakso, *Synth. Met.* **1989**, *28*, C377.
[38] O. Inganäs, in: *Handbook of Organic Conductive Molecules and Polymers*, (Ed: H. S. Nalwa), John Wiley & Sons Ltd, New York **1997**, pp. 785–793.
[39] O. Inganäs, W. R. Salaneck, J. E. Osterholm, J. Laakso, *Synth. Met.* **1988**, *22*, 395.
[40] C. Yang, F. P. Orfino, S. Holdcroft, *Macromolecules* **1996**, *29*, 6510.
[41] K. Iwasaki, H. Fujimoto, S. Matsuzaki, *Synth. Met.* **1994**, *63*, 101.
[42] W. R. Salaneck, O. Inganäs, J. O. Nilsson, J. E. Osterholm, B. Themans, J. L. Brédas, *Synth. Met.* **1989**, *28*, C451.
[43] W. R. Salaneck, O. Inganas, B. Themans, J. O. Nilsson, B. Sjogren, J. E. Osterholm, J. L. Brédas, S. Svensson, *J. Chem. Phys.* **1988**, *89*, 4613.
[44] S. Hugger, R. Thomann, T. Heinzel, T. Thurn-Albrecht, *Colloid Polym. Sci.* **2004**, *282*, 932.
[45] J. Clark, C. Silva, R. H. Friend, F. C. Spano, *Phys. Rev. Lett.* **2007**, *98*, 206406.
[46] J. Clark, J. F. Chang, F. C. Spano, R. H. Friend, C. Silva, *Appl. Phys. Lett.* **2009**, *94*, 163306.
[47] *Electronic Processes in Organic Crystals and Polymers*, (Eds: M. Pope, C. E. Swenberg), Oxford University Press, New York **1999**.
[48] D. Beljonne, J. Cornil, R. Silbey, P. Millie, J. L. Brédas, *J. Chem. Phys.* **2000**, *112*, 4749.
[49] P. J. Brown, D. S. Thomas, A. Köhler, J. S. Wilson, J. S. Kim, C. M. Ramsdale, H. Sirringhaus, R. H. Friend, *Phys. Rev. B* **2003**, *67*, 064203.
[50] F. C. Spano, J. Clark, C. Silva, R. H. Friend, *J. Chem. Phys.* **2009**, *130*, 074904.
[51] A. Ruseckas, E. B. Namdas, T. Ganguly, M. Theander, M. Svensson, M. R. Andersson, O. Inganäs, V. Sundstrom, *J. Phys. Chem. B* **2001**, *105*, 7624.
[52] J. S. Liu, R. S. Loewe, R. D. McCullough, *Macromolecules* **1999**, *32*, 5777.
[53] R. S. Loewe, S. M. Khersonsky, R. D. McCullough, *Adv. Mater.* **1999**, *11*, 250.
[54] M. Trznadel, A. Pron, M. Zagorska, *Macromolecules* **1998**, *31*, 5051.
[55] A. Zen, P. Pingel, F. Jaiser, D. Neher, J. Grenzer, W. Zhuang, J. P. Rabe, A. Bilge, F. Galbrecht, B. S. Nehls, T. Farrell, U. Scherf, R. D. Abellón, F. C. Grozema, L. D. A. Siebbeles, *Chem. Mater.* **2007**, *19*, 1267.
[56] J. M. Warman, M. P. De Haas, A. Hummel, *Chem. Phys. Lett.* **1973**, *22*, 480.
[57] J. M. Warman, M. P. de Haas, G. Dicker, F. C. Grozema, J. Piris, M. G. Debije, *Chem. Mater.* **2004**, *16*, 4600.

Submitted to ADVANCED FUNCTIONAL MATERIALS

Supporting Information

for

Temperature-resolved local and macroscopic charge carrier transport in thin P3HT layers

Patrick Pingel[1], *Achmad Zen*[2], *Dieter Neher*[1,*], *Ruben D. Abellón*[3], *Ferdinand C. Grozema*[3], *Laurens D.A. Siebbeles*[3]

[1] Institute of Physics and Astronomy, University of Potsdam, Karl-Liebknecht-Straße 24-25, 14476 Potsdam, Germany

[2] Robert Bosch Pte Ltd, Research and Technology Center Asia Pacific, 50 Nanyang Drive, Singapore 637553

[3] Opto-Electronic Materials Section, Department of Chemical Engineering, Delft University of Technology, The Netherlands

*Corresponding author. E-mail: neher@uni-potsdam.de

Submitted to ADVANCED FUNCTIONAL MATERIALS

Local and macroscopic charge carrier mobilities and optical absorption of a low-MW P3dHT fraction

For comparison to our medium-MW P3dHT fraction, we present here the temperature-dependencies of local and macroscopic charge carrier mobilities and of the optical absorption of a low-MW P3dHT fraction (Mn = 2,600 g mol^{-1}, Mw = 3,600 g mol^{-1}, PDI = 1.4).

Figure S1 shows the dependencies of microwave (PR-TRMC) mobility and field-effect mobility on temperature. We find that the microwave mobility increases with temperature up to the melting region (see DSC thermogram in Figure S2), followed by a rather sharp drop which is most likely related to the melting of the crystallites. On the other hand, macroscopic field-effect mobility is at least three orders of magnitude lower than the local microwave mobility. Upon heating to 50℃, field-effect mobility drop s as compared to room temperature. Unfortunately, we could not observe transistor behaviour at higher temperatures than 50℃ (transistor behaviour did no t recover upon cooling due to dewetting of the polymer layer from the SiO_2 substrate; however, we observed that transistor behaviour recovered upon more subtle sample treatment for another low-MW P3HT fraction[R1]). Essentially, the same temperature dependencies as for medium-MW P3dHT are exhibited, though being shifted to lower temperatures due to the lower melting temperature of low-MW P3dHT.

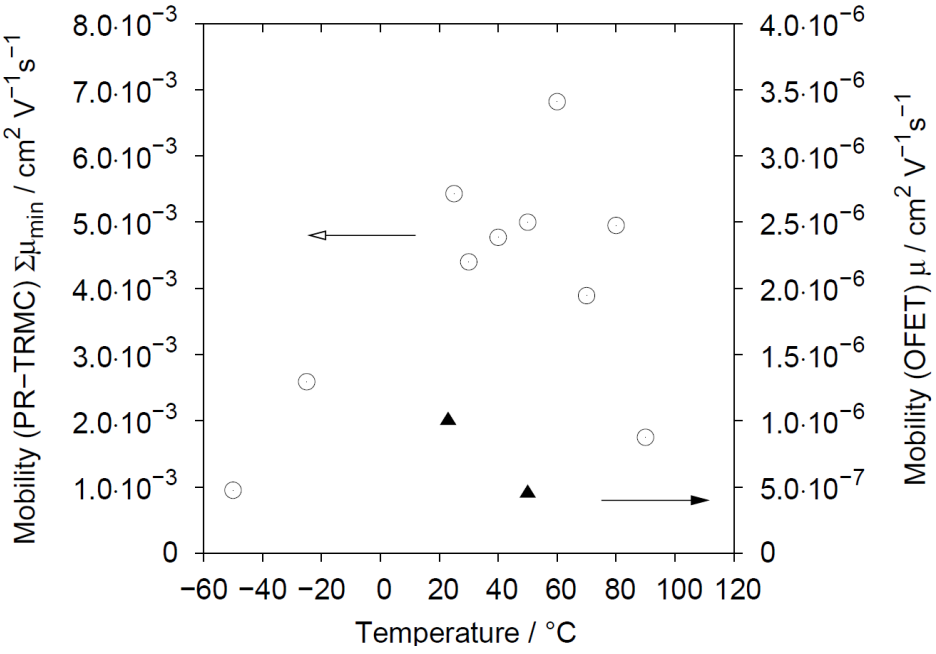

Figure S1. Temperature-dependent charge carrier mobilities of the P3dHT low-MW fraction from PR-TRMC (open symbols, during heating) and OFET experiments (filled symbols, during heating).

Submitted to ADVANCED FUNCTIONAL MATERIALS

Figure S2 shows the temperature-dependence of absorption of a low-MW P3dHT layer. Upon heating, the absorption exhibits a pronounced blue-shift that is associated with *(a)* the melting of the crystallites and *(b)* the shortening of the conjugation lengths due to increased main chain torsion in the whole sample. Note that the intermolecular 0-0 transition at 2.05 eV [600 nm] is barely visible at low temperatures and vanishes upon heating. Therefore, a quantitative analysis according to Spano's model is not possible for that MW-fraction.

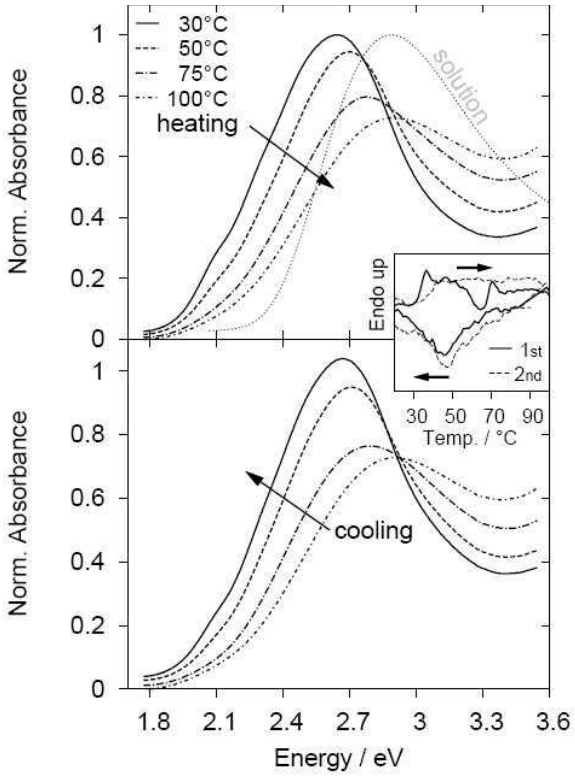

Figure S2. Temperature-dependent UV/Vis absorption of a low-MW P3dHT layer during a cycle of heating (upper graphs) and subsequent cooling (lower graphs). The spectra have been normalized to the maximum absorption at 30℃. The spectrum in sol ution is plotted for comparison. The inset shows the DSC thermogram of a solution-crystallized low-MW P3dHT sample.

Submitted to ADVANCED FUNCTIONAL MATERIALS

Quantitative analysis of the PR-TRMC decay signals

A good fit to the experimental after-pulse transients (Figure S3) was obtained by assuming first-order decay kinetics,

$$\frac{dn_h}{dt} = -k(t)n_h, \qquad \text{(S1)}$$

meaning that the number of traps is constant over time and significantly larger than the number of mobile charges n_h generated in the PR-TRMC experiment. The trapping coefficient $k(t)$ is assumed to be time dependent according to

$$k(t) \propto \kappa t^{\beta-1}, \qquad \text{(S2)}$$

where $\beta \neq 1$ accounts for the dispersive nature of charge transport in our P3dHT samples. Equation (S2) relies on the assumption of a distribution of charge carrier hopping times which emerges from energetical and positional disorder and relaxation in the density-of-states.[R2-R4] The general solution of this differential equation is

$$n(t) = n_0 \exp\left(-\left(\frac{t}{\tau}\right)^{\beta}\right). \qquad \text{(S3)}$$

As shown in **Figures S1a** and **S1b**, this stretched exponential gives rather good fits to the experimental transients (with the fit parameters given in **Table S1**).

It is believed that the non-exponential decay of mobile charge carrier density as expressed by equation (S3) arises from the distribution of the relaxation times, which is connected to the dispersity of charge transport. Therefore, a direct comparison of the characteristic decay times τ' for different samples is problematic, because the distribution function $\rho(\tau')$ is unknown. As a consequence, we used the logarithmic moments of τ, $\langle \ln \tau \rangle$,[R5, R6] which are related to the mean activation energy in case of temperature activated transport (because $\tau = \tau_0 \exp\left(-E(T)/(k_B T)\right)$ is assumed, where $E(T)$ is the activation energy). The first logarithmic moment of a relaxation function $\varphi(t)$ can be computed using

$$\left\langle \ln \tau \right\rangle = \mathrm{Eu} + \left[\ln t\right] \qquad \text{(S4a)}$$

with

$$\left[\ln t\right] = \int_{-\infty}^{\infty} d\ln t \left(-\frac{d\phi}{d\ln t}\right) \ln t, \qquad \text{(S4b)}$$

Submitted to ADVANCED FUNCTIONAL MATERIALS

where Eu ≈ 0.577... (Euler-Gamma constant) and $\phi = n(t)/n_0$ is the normalized after-pulse decay.[R6]

For a Kohlrausch-type decay (equation (S3)) this yields the analytic expression

$$\langle \ln \tau \rangle = \left(1 - \beta^{-1}\right) \mathrm{Eu} + \ln \tau \,. \qquad \text{(S5)}$$

The values of the mean decay times *exp(<ln τ>)* are reported in Table S1. For both fractions, the mean decay times increase with temperature.

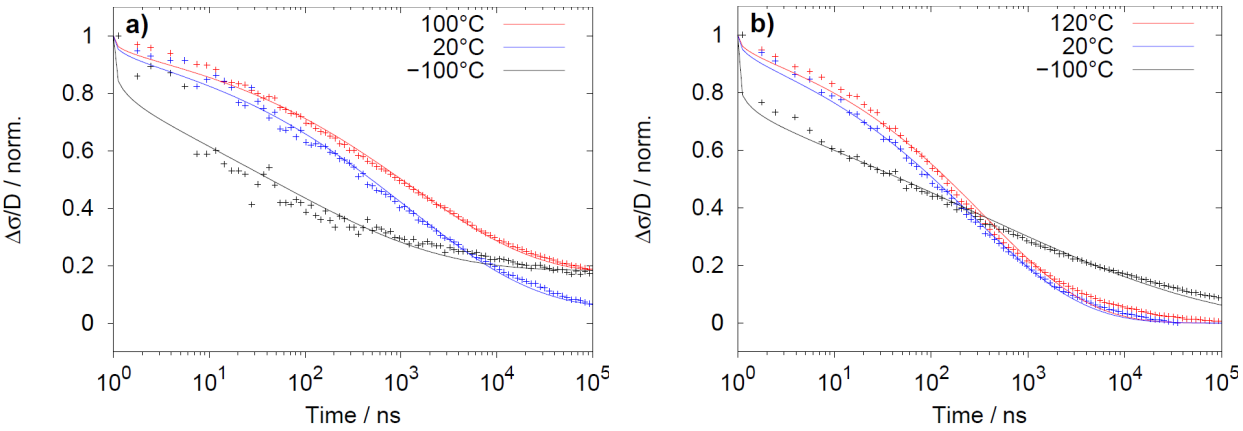

Figure S3. Normalized after-pulse decay of the microwave conductivity of the P3dHT medium-MW (a) and high-MW (b) fraction at different temperatures and respective fits according to equation (S3). Only every second data point is displayed for clarity.

Table S1. Fit of normalized eqn. (S3) to normalized after-pulse decay (standard errors in parentheses). For the medium-MW fraction it was necessary to assume a constant background conductivity n_∞:

medium-MW P3dHT	τ [ns]	*β*	*exp <ln τ>* [ns]
-100℃	52.6 (7.8 %)	0.254 (3.5 %)	10
20℃	1202 (3.3 %)	0.325 (1.1 %)	362
100℃	1280 (2.5 %)	0.333 (0.9 %)	403
high-MW P3dHT			
-100℃	359 (3.1 %)	0.181 (1.2 %)	26
20℃	273 (1.2 %)	0.384 (0.8 %)	108
120℃	363 (1.7 %)	0.402 (1.1 %)	154

Submitted to ADVANCED FUNCTIONAL MATERIALS

Analysis of the temperature dependent UV/Vis absorption spectra for medium- and high MW P3HT

The following figures display the absorption spectra of medium- and high-MW P3dHT layers at specific temperatures (red lines and points). The best-fits according to eqn. (1) (see article) to the region of aggregate absorption (2.0 eV - 2.3 eV) are shown as black lines, as well as the individual electronic-vibrational transitions (grey lines). The differences of the experimental and aggregate model spectra are displayed as blue lines. The figures appear according to the experimental sequence.

Medium-MW P3dHT

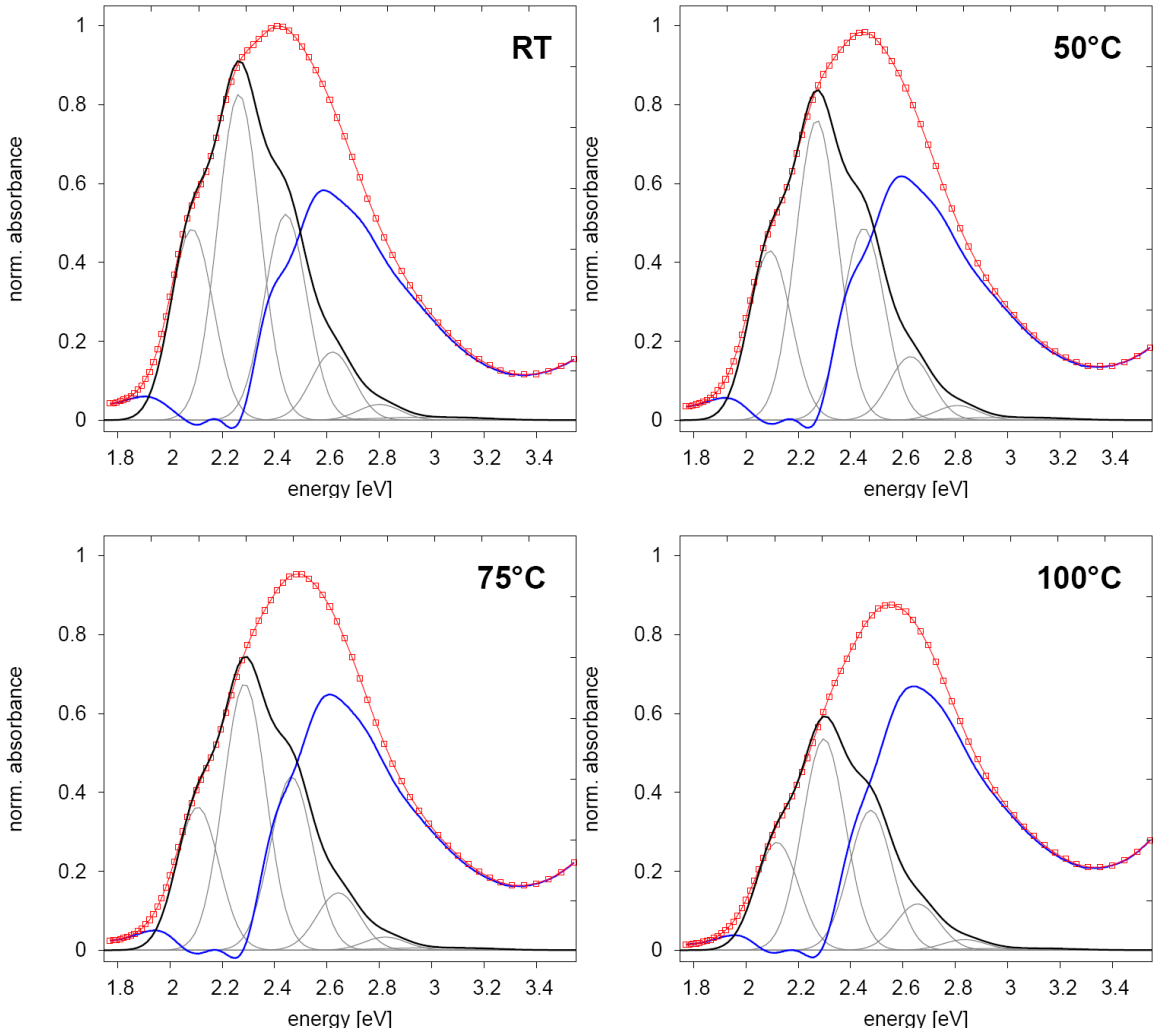

Submitted to ADVANCED FUNCTIONAL MATERIALS

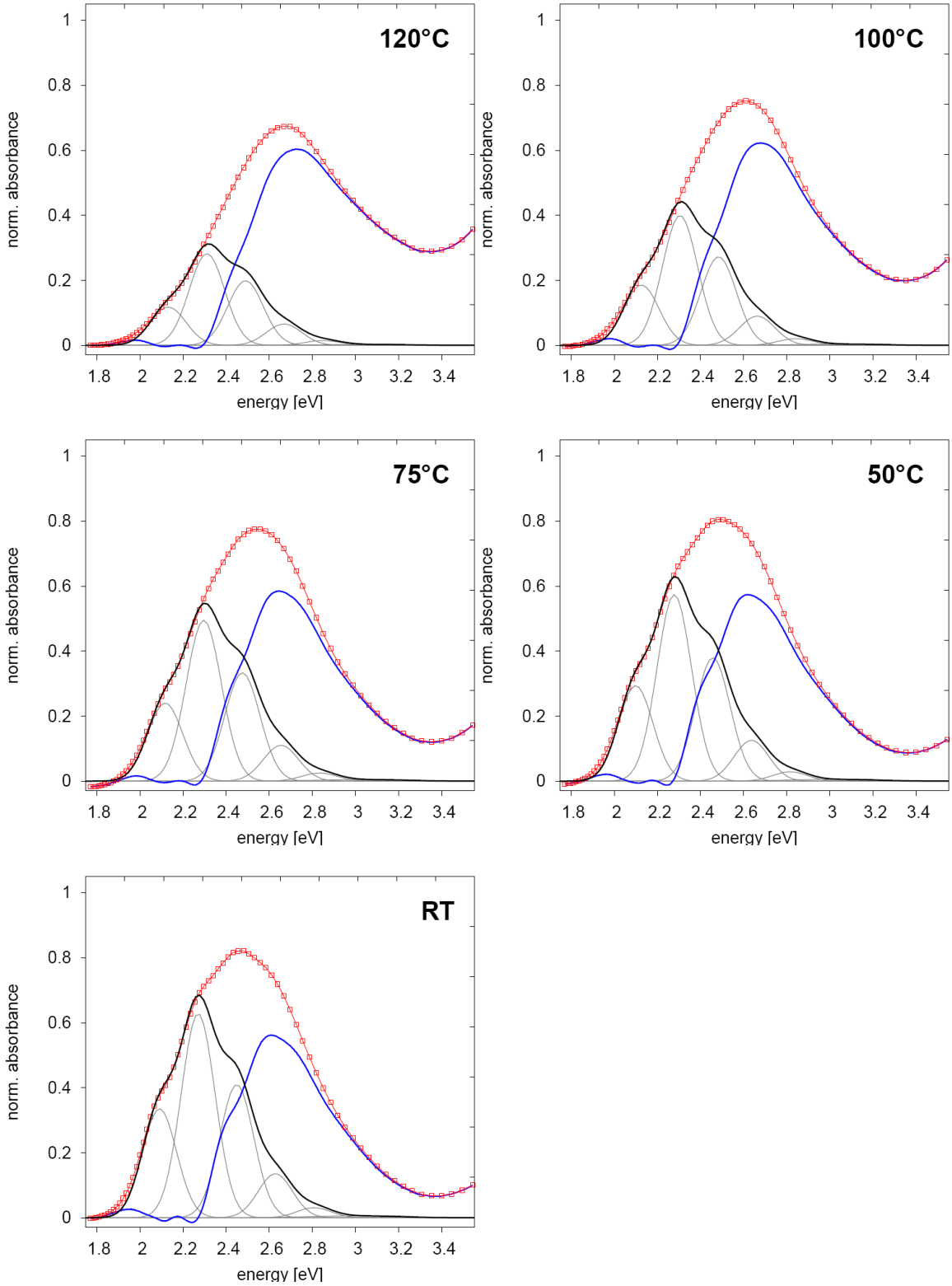

Submitted to ADVANCED FUNCTIONAL MATERIALS

High-MW P3dHT

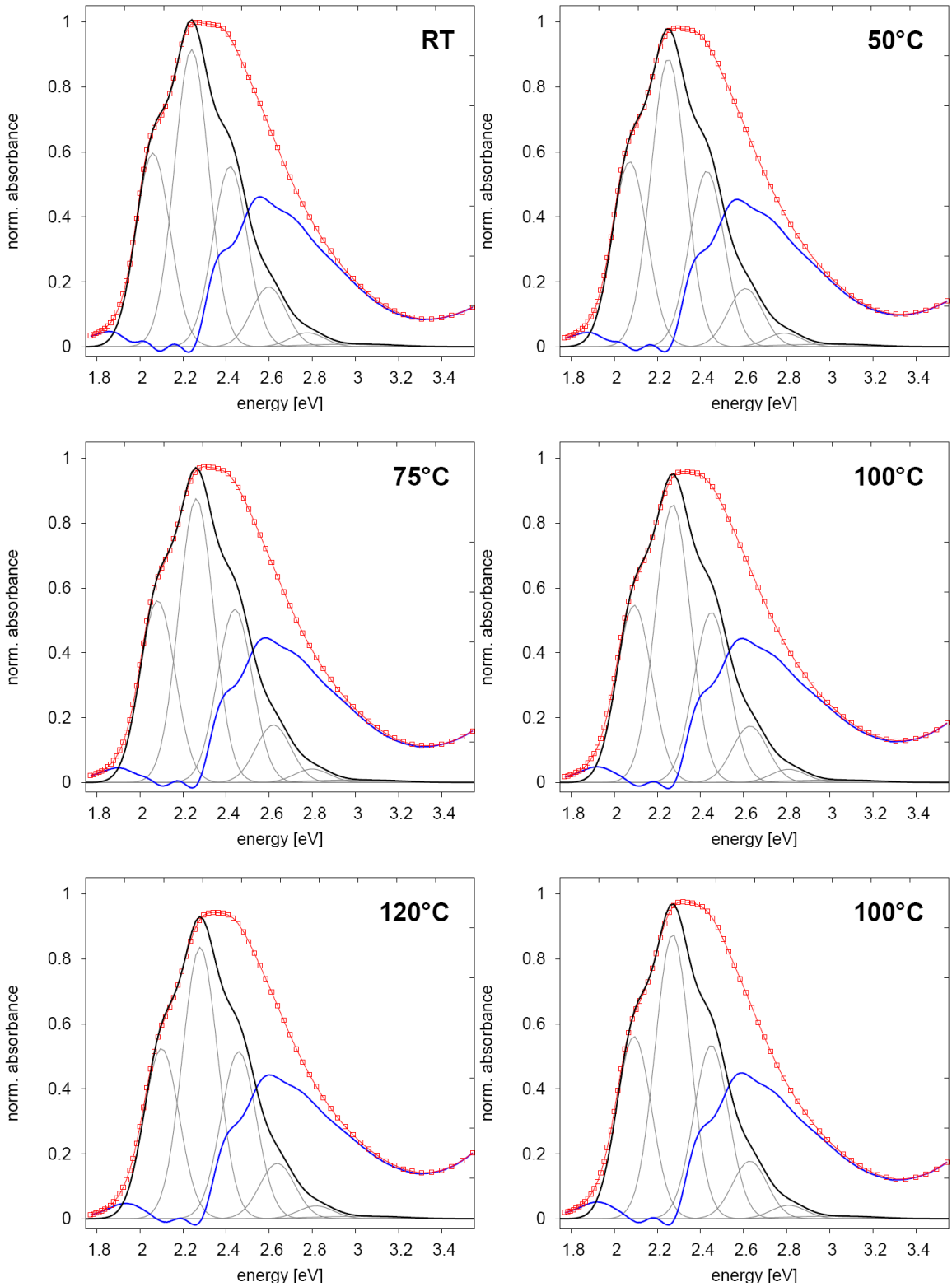

Submitted to ADVANCED FUNCTIONAL MATERIALS

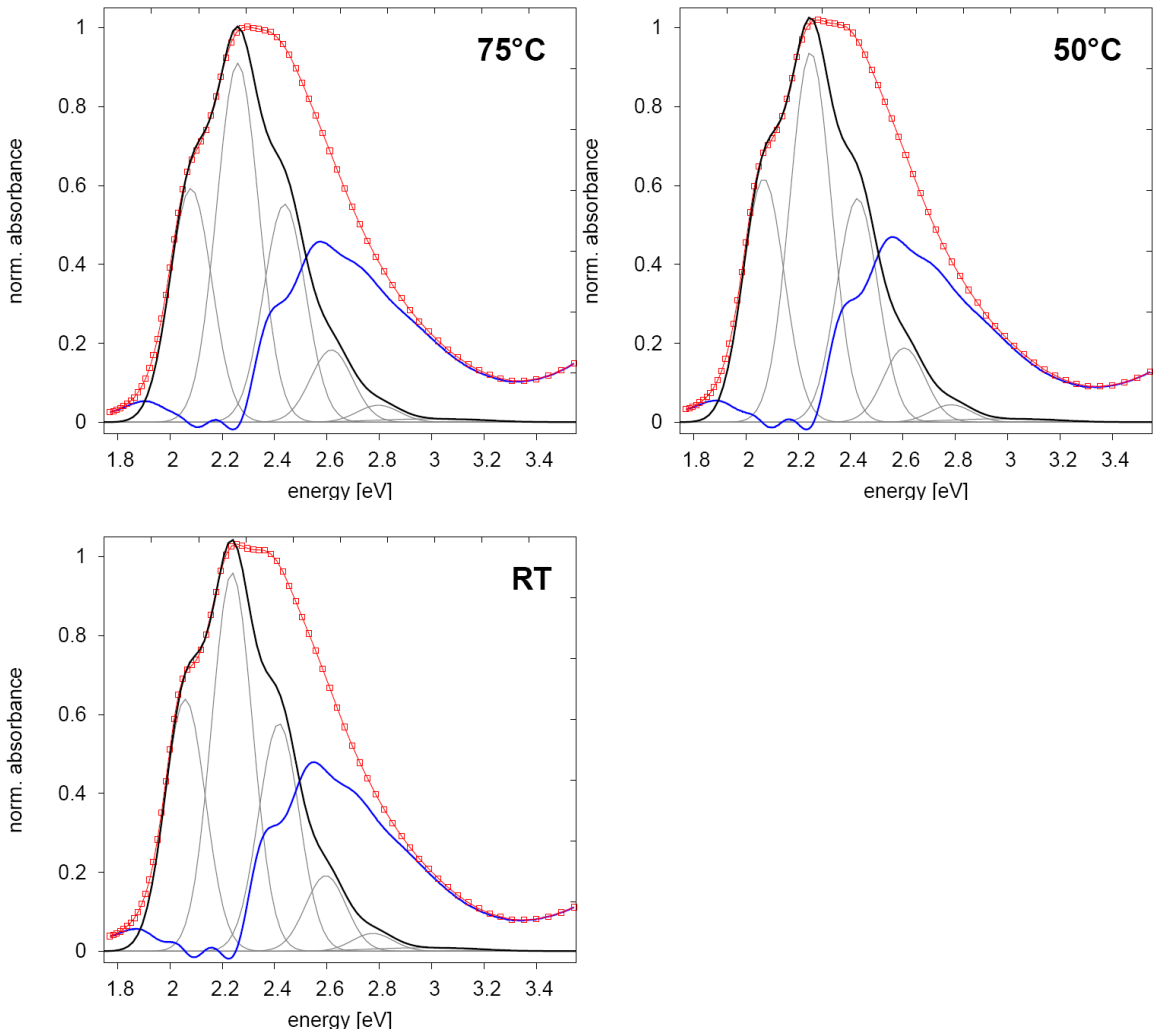

Submitted to ADVANCED FUNCTIONAL MATERIALS

Variation of the lower and upper bounds for fitting Spano's model to the absorption spectra of medium-MW P3dHT at 120℃

Lower and upper bounds have been varied in order to test the consistency of our model fits to the absorption spectra. The parameters *E*, *σ*, and *W* and their standard errors are plotted below. We find that an optimum of the stability of the fit parameters, minimal standard errors, and the inclusion of as much of the experimental data as possible is granted for lower and upper bounds of 2.0 eV and 2.3 eV, respectively. These bounds have been used for all absorption data fits throughout this article.

Variation of the lower bound

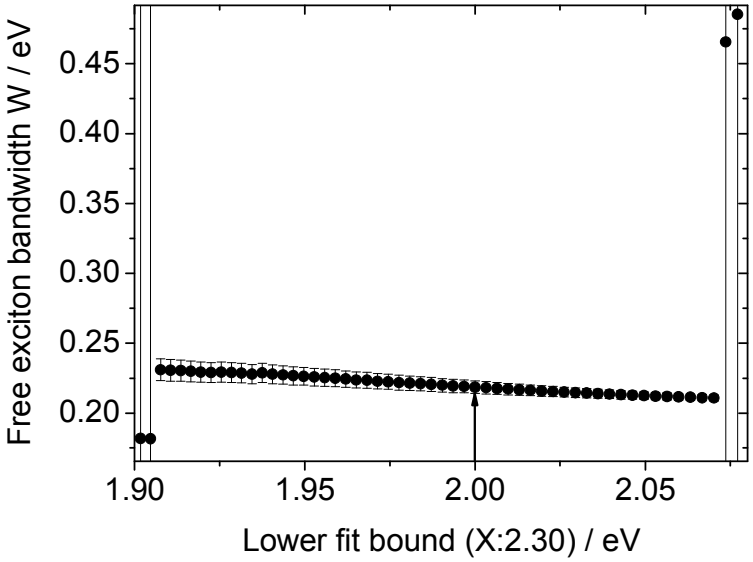

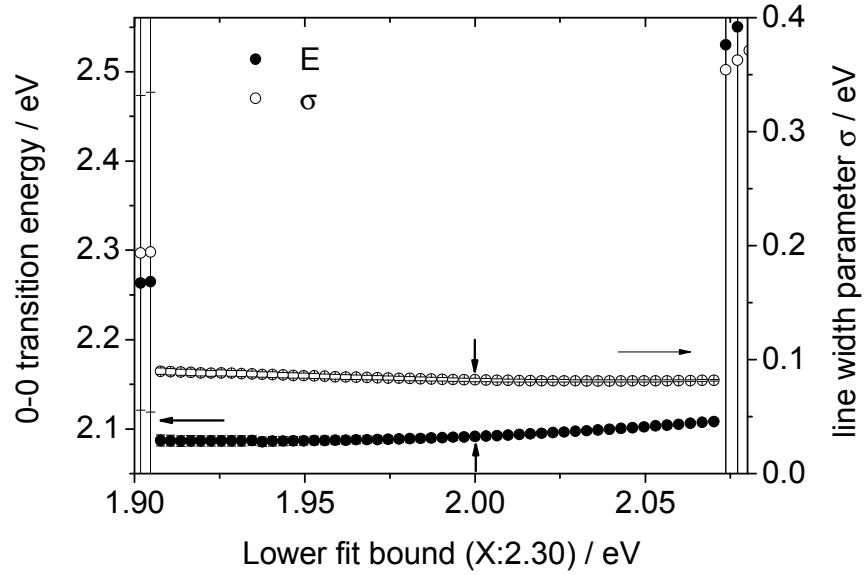

Submitted to ADVANCED FUNCTIONAL MATERIALS

Variation of the upper bound

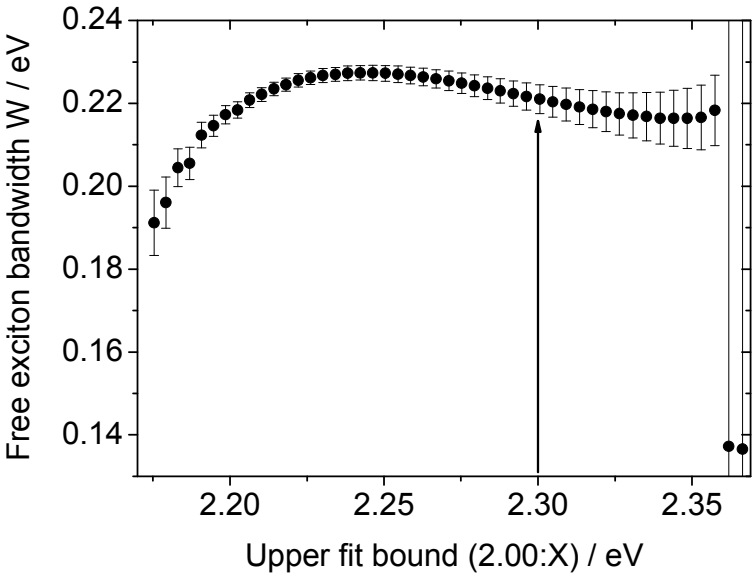

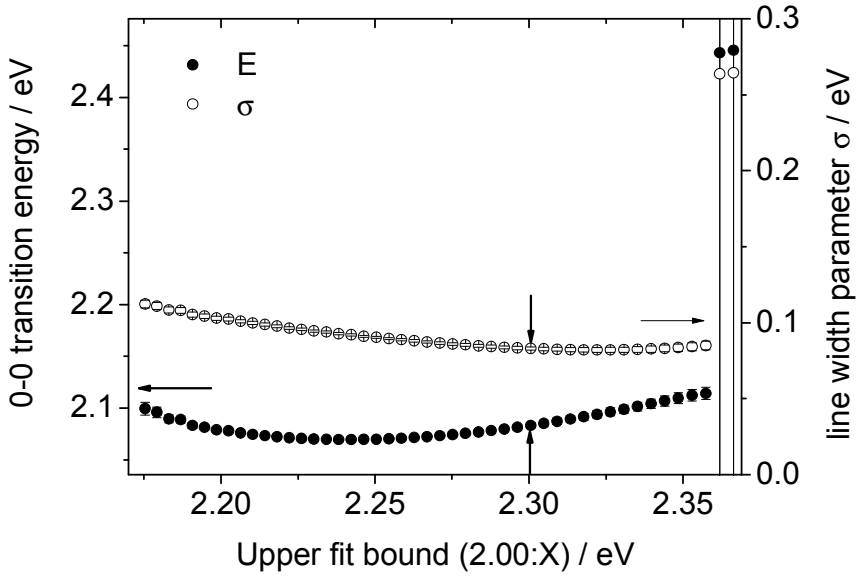

Submitted to ADVANCED FUNCTIONAL MATERIALS

References

[R1] A. Zen, M. Saphiannikova, D. Neher, J. Grenzer, S. Grigorian, U. Pietsch, U. Asawapirom, S. Janietz, U. Scherf, I. Lieberwirth, G. Wegner, *Macromolecules* **2006**, *39*, 2162.

[R2] G. Dicker, M. P. de Haas, D. M. de Leeuw, L. D. A. Siebbeles, *Chem. Phys. Lett.* **2005**, *402*, 370.

[R3] G. Pfister, H. Scher, *Adv. Phys.* **1978**, *27*, 747.

[R4] H. Scher, E. W. Montroll, *Phys. Rev. B* **1975**, *12*, 2455.

[R5] H. J. Winkelhahn, T. K. Servay, D. Neher, *Ber. Bunsen-Ges. Phys. Chem. Chem. Phys.* **1996**, *100*, 123.

[R6] R. Zorn, *J. Chem. Phys.* **2002**, *116*, 3204.

ADVANCED FUNCTIONAL MATERIALS
www.afm-journal.de

Materials Views
www.MaterialsViews.com

FULL PAPER

Quantitative Analysis of Bulk Heterojunction Films Using Linear Absorption Spectroscopy and Solar Cell Performance

*Sarah T. Turner, Patrick Pingel, Robert Steyrleuthner, Edward J. W. Crossland, Sabine Ludwigs, and Dieter Neher**

A fundamental understanding of the relationship between the bulk morphology and device performance is required for the further development of bulk heterojunction organic solar cells. Here, non-optimized (chloroform cast) and nearly optimized (solvent-annealed *o*-dichlorobenzene cast) P3HT:PCBM blend films treated over a range of annealing temperatures are studied via optical and photovoltaic device measurements. Parameters related to the P3HT aggregate morphology in the blend are obtained through a recently established analytical model developed by F. C. Spano for the absorption of weakly interacting H-aggregates. Thermally induced changes are related to the glass transition range of the blend. In the chloroform prepared devices, the improvement in device efficiency upon annealing within the glass transition range can be attributed to the growth of P3HT aggregates, an overall increase in the percentage of chain crystallinity, and a concurrent increase in the hole mobilities. Films treated above the glass transition range show an increase in efficiency and fill factor not only associated with the change in chain crystallinity, but also with a decrease in the energetic disorder. On the other hand, the properties of the P3HT phase in the solvent-annealed *o*-dichlorobenzene cast blends are almost indistinguishable from those of the corresponding pristine P3HT layer and are only weakly affected by thermal annealing. Apparently, slow drying of the blend allows the P3HT chains to crystallize into large domains with low degrees of intra- and interchain disorder. This morphology appears to be most favorable for the efficient generation and extraction of charges.

1. Introduction

Research efforts in the field of organic solar cells continue to expand due to the promise of a more cost efficient energy technology. The bulk heterojunction (BHJ) solar cell system comprising highly regioregular poly(3-hexylthiophene) (P3HT) and [6,6]-phenyl-C_{61}-butyric acid methyl ester (PCBM) is one of the most extensively studied organic-based solar cell systems to date. Nonetheless, knowledge about the evolution of the P3HT:PCBM blend morphology during processing is still rather incomplete. In order to push advances in the field forward, the multifaceted relationship between morphology and device performance requires further exploration.

BHJ solar cell current generation relies on the efficiency of the following steps: photon absorption, exciton diffusion, exciton dissociation at the donor/acceptor interface, generation of free carriers, and collection of these carriers at the electrodes. Effective charge generation and extraction are provided by a balance between the interfacial area and the percolation pathways.[1] Charge recombination detrimental to device efficiency may be reduced by achieving a fast and balanced transport via an increase in the order and crystallinity within the individual phases.[1,2] Thermal annealing of P3HT:PCBM blend films with a non-optimized morphology is known to improve these factors.[3] Upon heating, the crystalline P3HT chains deplanarize and upon cooling replanarize into π-stacked lamellar structures, often with a larger than initial conjugation length.[4] Recent in-situ X-ray diffraction studies have shown that following this initial crystallization of the P3HT phase, a separation between the two components takes place.[5] This promotes the formation of percolation pathways due to the simultaneous aggregation and diffusion of PCBM components out of the amorphous P3HT phases,[6,7] in turn allowing the P3HT chains to form crystallites with high intra- and interchain order.

The relationship between device performance and morphology in BHJ solar cells has been studied in depth over the past decade;[1–36,8] however, these studies typically examine

S. T. Turner, P. Pingel, R. Steyrleuthner, Prof. D. Neher
Institute of Physics and Astronomy
University of Potsdam
Karl-Liebknecht-Straße 24-25, 14476 Potsdam, Germany
E-mail: neher@uni-potsdam.de
Dr. E. J. W. Crossland
Clarendon Laboratory
Parks Road, Oxford, OX1 3PU, UK
Prof. S. Ludwigs
Institute of Polymer Chemistry
University of Stuttgart
Pfaffenwaldring 55, 70569 Stuttgart, Germany
S. T. Turner
Current address: Institute of Chemistry
Stranski Laboratory for Physical and Theoretical Chemistry
Technical University of Berlin
Straße des 17. Juni 124, 10623 Berlin, Germany

DOI: 10.1002/adfm.201101583

one annealing temperature with a variation in the annealing time. For example, Keivanidis et al. found an increase in the charge pair separation upon thermal annealing, which they associate with an increase in the P3HT crystallinity and the domain sizes of both components.[8] Nevertheless, the details of the temperature dependent changes related to the device performance and morphology are missing. Other studies have used a large range of annealing temperatures; however, only focused on the resulting device performance[9,10] or the resulting morphology,[11,12] making a direct comparison between the two difficult. In this study, a quantitative analysis of the evolution of the P3HT morphology in the BHJ film structure as extracted from the optical spectra is related to changes in the solar cell device performance over a range of thermal annealing temperatures.

A recent model by F. C. Spano enables a quantitative analysis of regioregular P3HT absorption spectra in relation to the morphology. This model was developed to describe the absorption of and the emission from H-aggregates comprising parallel-aligned, cofacially packed conjugated chains in the case of weak excitonic coupling.[13,14] In this limit, the splitting of the electronic levels due to Coulombic interactions is considerably smaller than the vibrational energy. As a result, interchain coupling leads to the formation of vibronic bands with their width essentially determined by the exciton bandwidth W. An important prediction of this model is that the relative intensities of the individual transitions of the vibronic progression in the absorption are largely affected by the exciton bandwidth according to:

$$A(E) \propto \sum_{m=0} \left(\frac{S^m}{m!}\right) \times \left(1 - \frac{We^{-S}}{2E_p} \sum_{n \neq m} \frac{S^n}{n!\, n-(m)}\right)^2 \times \exp\left(\frac{\left(E - E_{0-0} - mE_p - \frac{1}{2}WS^m e^{-S}\right)^2}{2\sigma^2}\right), \quad (1)$$

where A is the absorbance as a function of the photon energy (E), S is the Huang-Rhys factor, m and n are differing vibrational levels, $E_{0\text{-}0}$ is the 0-0 transition energy, E_p is the intermolecular vibrational energy, and σ is the Gaussian linewidth. The second bracketed term in Equation 1 is a modification of the Franck-Condon factor to account for the aggregate absorption. The model assumes that only transitions from the ground state to the highest energy state of each vibronic band are optically allowed, as shown in Figure 2 of the original publication by F. C. Spano.[13] This is included as a correction to the transition energy by adding half of the vibronic bandwidth, $\frac{1}{2}WS^m e^{-S}$, to the energy of the isolated single chain. Within the weak excitonic coupling regime this term is likely small compared to the vibronic energy and therefore not considered by Clark et al.[15] Excitations to the lower states of the bands become optically allowed if disorder is present; however, these transitions do not contribute to the absorption in practice due to their weak oscillator strength.[13] The free parameters in the fit of a polythiophene absorption spectrum are: W, $E_{0\text{-}0}$, σ, and a proportionality constant. S is fixed at a value of 1.0, as taken from a Franck-Condon fit of the photoluminescence spectra of a regioregular P3HT film.[16] E_p is taken to be 0.179 eV assuming that the C = C symmetric stretch dominates the electronic transition coupling.[16]

Although the Spano model has been reliably applied to the absorption spectra of pure, thin regioregular P3HT films,[4,13–17] it has not yet been used to analyze the P3HT component of blend spectra. Previous studies applying this model to the absorption spectra of pristine P3HT films have focused on the effect of varying the solvent type[15,16] and the polymer molecular weight[4] on the fit parameters. Clark et al. cast P3HT films from various solvents and found an almost monotonic decrease of the W values with the boiling point of the solvent. Films cast from high boiling point solvents were proposed to contain larger aggregates with high conjugation lengths and interchain order, enabled by the slow drying of the layer. This was verified by atomic force microscopy (AFM) studies of the layer surface. Moreover, layers with lower W values were found to exhibit high mobilities in thin film transistors.[15]

The morphological changes in the polythiophene aggregates caused by variations in the processing conditions are more easily understood by relating W to the length of the planarized interacting chain segments (L) forming these aggregates,[18] as shown in **Figure 1**. Such a relation is available in a model developed by Gierschner et al. that considers non-nearest neighbor interactions in an infinite 1D stack of thiophene oligomers taking dielectric screening effects into account. For sufficiently long oligomers, there is an inverse relationship between W and the number of interacting repeat units N.[15] According to this model, the values of W reported for high molecular weight P3HT thin films by Clark et al. translate into 25 to 30 planarized repeat units (L ca. 10 nm) for layers cast from chloroform and more than 60 repeat units (L exceeding 20 nm) for layers cast from high boiling point solvents.[15] Also, lowering the molecular weight has been shown to increase W,[4] meaning that the length of the planarized thiophene segments in the aggregates is lowered. It is well known that P3HT crystallizes in the form of nanoribbons, whiskers, or nanofibers, with P3HT chains normal to the long axis of the nanocrystallites.[19–21] Interestingly, the range of values reported for the width of these crystalline fibers corresponds rather well to L deduced from the optical analysis of P3HT layers. This means that the application of the Spano-model is suited to extract information related to the morphological aspects of P3HT aggregates. Following these arguments, the observed increase of mobility with decreasing W (increasing L) was attributed to a reduction of the amount of amorphous material separating the individual nanorods.[4]

In this work, a quantitative analysis of thermally induced morphological changes in the P3HT phase of a blend with PCBM is performed by means of linear absorption spectroscopy modeling. Chloroform (CF) and solvent-annealed *o*-dichlorobenzene (DCB) P3HT:PCBM layers were used to determine the effect of thermal annealing on both a non-optimized and a nearly optimized film morphology, respectively. The differences in the preparation methods and the boiling points of the solvents, 61.2 °C for CF and 180.5 °C for DCB, are the cause for the variation in the initial morphology of the films. The results are compared with solar cell device performance, single-carrier device measurements, and AFM image analysis.

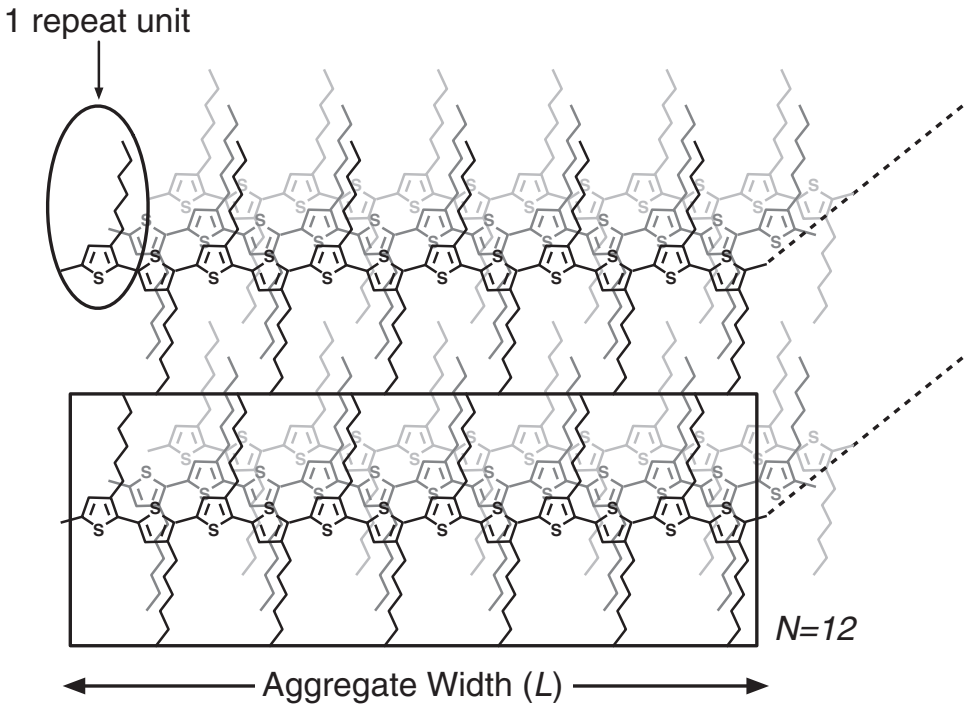

Figure 1. Schematic of the P3HT aggregate adapted from Pingel et al.,[4] where the aggregate width (*L*) is the length of the interacting chain segments comprising a number *N* of interacting thiophene repeat units. The long axis of the aggregate is indicated with dotted lines.

2. Results and Discussion

2.1. Linear absorption spectroscopy modeling of P3HT:PCBM films

The morphological evolution of the P3HT component in a blend with PCBM was studied through modeling of the absorption spectra to obtain fit parameters describing the length of cofacially arranged P3HT chain segments in the polymer aggregates, as well as the degree of crystallinity in the film. Blend P3HT:PCBM film absorption spectra were constructed using transmission and reflection measurements taken on ca. 100 nm thick blend layers with the use of an integrating sphere to obtain spectra free of distortions due to scattering or reflections. As distortions were minimized by using thinner layers prepared from filtered solutions, the performance of the solar cells was poorer compared to devices prepared from 200 nm thick layers cast from unfiltered solutions. Individual films were annealed for 10 min directly from the as-prepared state to the target temperature with values ranging between 30 °C to 180 °C. All films were prepared on a PEDOT:PSS/ITO/glass substrate to obtain a film morphology most comparable to the photoactive layer in solar cells.

In order to properly account for the PCBM contribution to each absorption spectrum, the absorption spectrum of a ca. 100 nm thick as-prepared blend film comprising PCBM and polystyrene (PS) in a 1:1 weight ratio was measured on a PEDOT:PSS/ITO/glass substrate. The PS component was used to mimic the morphology of PCBM in a polymer matrix. A selection of the blend absorption spectra, as well as the PCBM:PS and the pristine P3HT spectra are shown in **Figure 2**a and 2c for films cast from CF and DCB, respectively. All spectra have been corrected for the substrate absorption and they display a similar absorbance at 336 nm, which is the wavelength of the maximum absorption of the PCBM component. Interestingly, the 1:1 PCBM:PS blend with comparable layer thickness exhibits an almost identical absorbance at this wavelength, meaning that the contribution of P3HT to the absorption spectra is small at short wavelengths. For the following analysis, the blend absorption spectra were first normalized to the absorbance at 336 nm. Then, 90% of the normalized PCBM:PS spectrum was subtracted from each blend spectrum to account for the small P3HT absorbance at this wavelength. With this procedure, the spectra of the blends closely resemble the short wavelength absorption of the pristine P3HT layer. The subtracted spectra, as well as the pristine P3HT spectra, of films cast from CF and DCB are shown in Figure 2b and 2d, respectively.

Equation 1, based on weakly interacting H-aggregates in polythiophenes, was used to separate the absorption contributions of aggregated and amorphous P3HT regions and to analyze the former. Exemplary fits are shown in **Figure 3** for the P3HT absorption component of the blend films cast from each solvent and annealed at 180 °C. The fits to all of the measured spectra can be found in the Supporting Information. The spectral range of 641 nm to 550 nm (1.93 eV to 2.25 eV) was used for analysis, as this range was shown to be fully dominated by aggregated chains[4,16] (see Supporting Information for details on the consistency in the resulting fit parameters). The absorbance of the polymer chains in the amorphous phase is determined by subtracting the modeled aggregate absorbance from the total measured absorbance. It is expected that the amorphous absorbance be unstructured (see

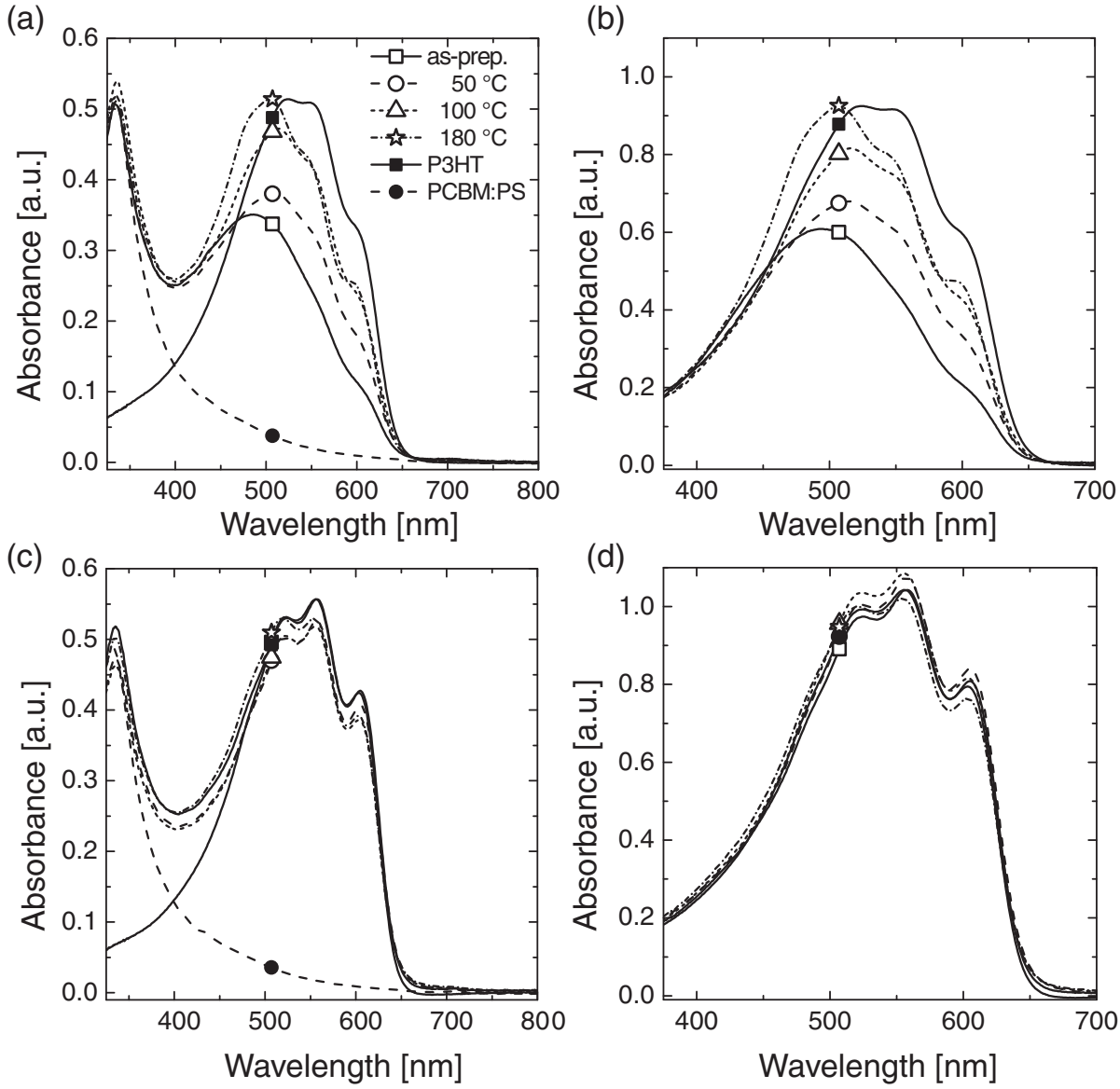

Figure 2. a,c) UV-Vis absorption spectra of ca. 100 nm thick P3HT:PCBM blend films as-prepared and thermally annealed (10 min), and of as-prepared PCBM:PS blend films of similar thickness. Also shown are the absorption spectra of pristine P3HT films (arbitrary units). b,d) Absorption spectra normalized to 336 nm peak after subtraction of 90% of the PCBM:PS blend layer. Films were cast from CF and DCB. Note that both of the PCBM:PS spectra were cast from DCB.

measurements of P3HT in solution);[4,15,16] however, it can be seen that the P3HT amorphous contribution resulting from the analysis of the blend spectra is increasingly more structured with an increase in the aggregate content. This structuring is most likely an artifact proceeding from Equation 1 not fully accounting for the electronic transitions at higher energies, e.g. due to the effects of charge transfer interactions.[4,13] Additionally, small and weakly structured residuals are observed at low energies, suggesting that the Gaussian shaped disorder may be too simple to completely describe the optical properties of a heterogeneous aggregated layer.[4]

The glass transition range of a 1:1 blend of P3HT:PCBM has been observed by differential scanning calorimetry (DSC) to range from ca. 10 °C to 70 °C.[22] Moreover, recent spectroscopic ellipsometry measurements on P3HT:PCBM blend films with a volume ratio of 60:40 have shown a change in the rate of film expansion to occur between 60 °C and 70 °C, likely associated with the glass transition temperature (T_g).[23] In the following figures, the glass transition range is highlighted in light grey and the annealing temperatures beyond this range are highlighted in dark grey.

The best-fit parameters obtained from the analysis of the P3HT components in the absorption spectra of the blend films, as well as from pristine P3HT films, are shown in **Figure 4**. The as-prepared CF cast film has a W value of 197 ± 10 meV. In annealed films the W values are found to be lower than in the as-prepared film, where the most significant changes in W are found to occur within the glass transition range. At higher

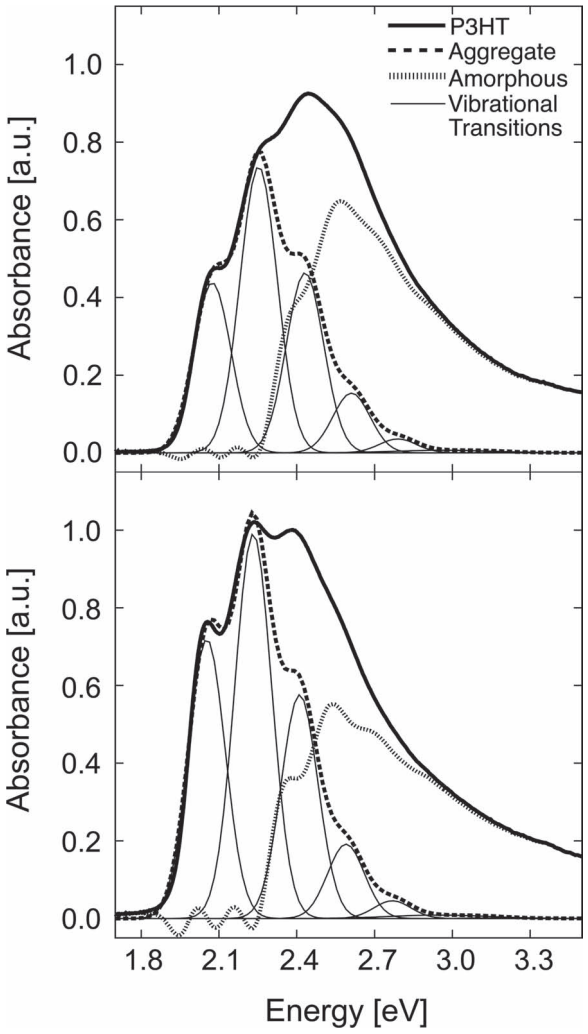

Figure 3. P3HT component of the P3HT:PCBM absorption spectrum for films annealed at 180 °C cast from CF (top) and DCB (bottom). The aggregate P3HT absorbance results from the best fit of the low energy absorbance obtained using Equation 1. The amorphous P3HT absorbance component is the difference between the total measured P3HT absorbance and the fit of the aggregate absorbance. The individual vibrational transitions in the aggregate absorption are also shown.

annealing temperatures the *W* value approaches ca. 140 ± 10 meV. As pointed out above, *W* is inversely related to the width of the cofacially packed chain segments in the P3HT aggregates. The pristine P3HT film cast from CF shows a lower *W* value than achieved in any of the annealed blend films, suggesting that the aggregate widths in the blend never achieve the same *W* value that is reached without PCBM present. The DCB cast solvent-annealed films show only a slight variation in the *W* values over the entire range of thermal treatment with a minimum value of 76 ± 10 meV at 50 °C and a maximum value of 92 ± 10 meV at 160 °C. The *W* value of the pristine P3HT film cast from DCB is within the error limits of all of the blend film *W* values, suggesting that the PCBM component plays little to no role in the formation of the P3HT morphology. Overall, the *W* trends suggest an increase and a slight decrease

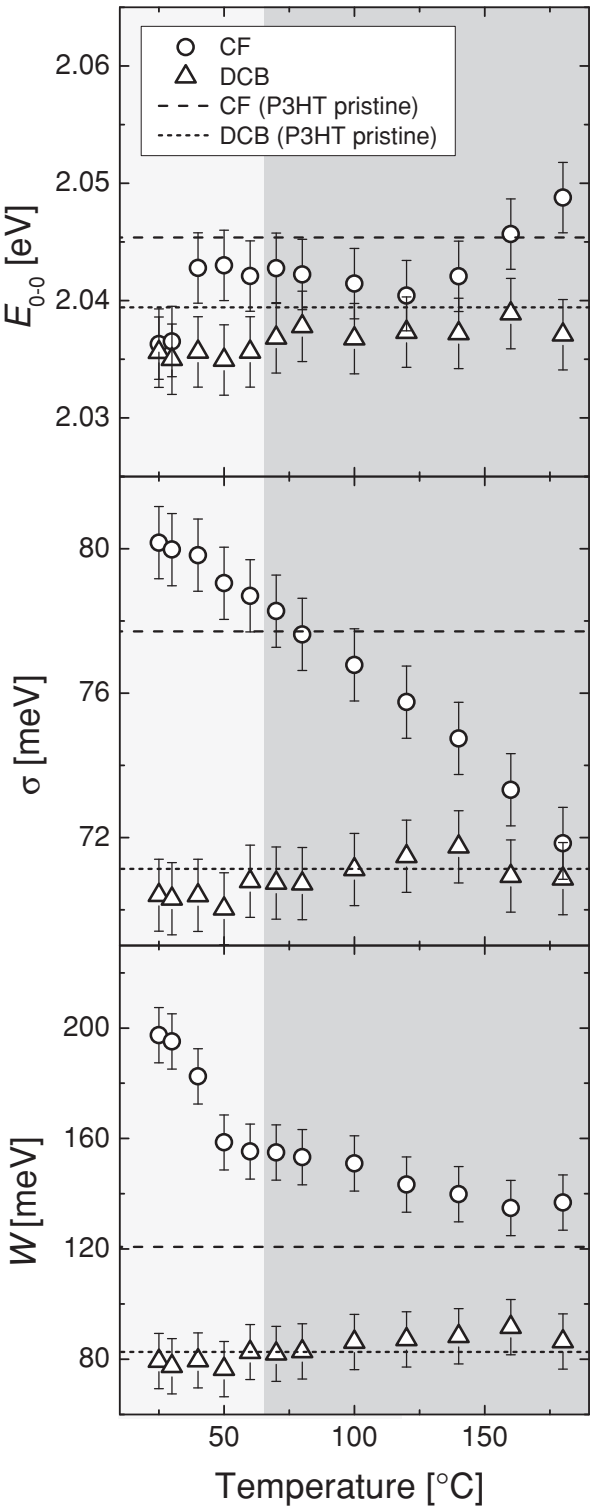

Figure 4. Best-fit parameters of the aggregate P3HT component of the absorption spectra of P3HT:PCBM blend films cast from CF and DCB versus annealing temperature, as well as the pristine P3HT layers cast from each solvent. Thermal annealing was performed on as-prepared films for 10 min at the indicated temperature. The fit parameters were obtained using Equation 1: $E_{0\text{-}0}$ is the 0-0 transition energy, σ is the Gaussian linewidth and measure of energetic disorder, and *W* is the free exciton bandwidth inversely related to the conjugation length.

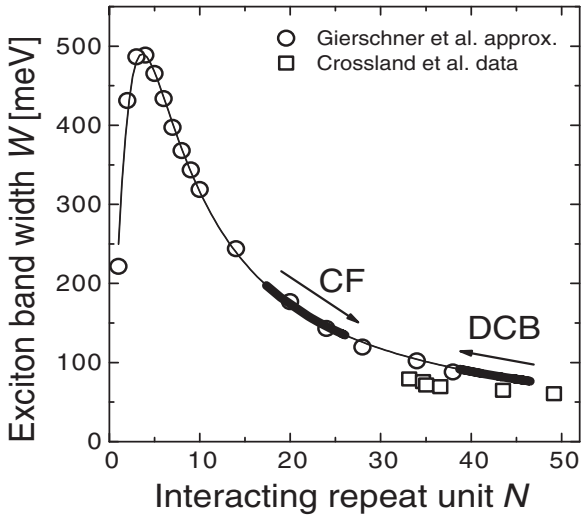

Figure 5. Exciton bandwidth (*W*) dependence on the number of interacting thiophene repeat units (*N*). Open circles by Gierschner et al. are simulations for infinite 1D polythiophene aggregates considering non-nearest neighbor interactions and dielectric screening effects.[4,18] The solid line is a guide to the eye. The *W* fit parameters were obtained using Equation 1 to fit the P3HT component of each P3HT:PCBM blend film absorption spectrum. Arrows show the trend upon an increase in annealing temperature. Note that the as-prepared films were each treated directly at the target annealing temperature and were not heated stepwise. Solid squares show *W* values as a function of *N* from an analysis of the optical spectra and the AFM images by Crossland et al.[17]

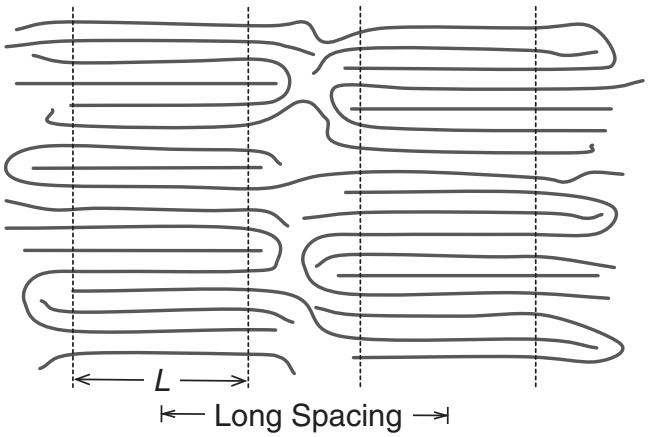

Figure 6. Schematic of the lamellar long spacing in polymer aggregates with an arbitrary chain length distribution. Polymer aggregates with a width of *L* are separated by amorphous regions.

in aggregate width with an increase in annealing temperature for the CF and DCB prepared films, respectively.

Figure 5 shows the predicted relationship between *W* and the number of interacting thiophene repeat units (*N*) by Gierschner et al.[18] Additionally, experimental data by Crossland et al.[17] was used to estimate the relationship between *W* and *N* for large *N* values. In this previous study, the solvent vapor pressure was varied to prepare pure P3HT films with different degrees of crystallinity. These films were crystallized for 2000 s at a solvent vapor pressure of 91% and drying proceeded by decreasing the solvent vapor pressure by 2% per minute. AFM measurements on these layers exhibited extended lamellae of crystallized polymer chains separated by amorphous areas. The absorption spectra of the films were used to calculate *W* according to Equation 1 and the percentages of film aggregation were determined using the method by Clark et al.[15] The length of the lamellar long spacing as a function of P_{cryst}, as shown in Figure 5 of Crossland et al.,[17] was obtained using fast Fourier transform (FFT) of the tapping mode AFM images.[17] The lamellar long spacing is shown schematically in **Figure 6**. By assuming that the fraction of the surface area occupied by crystallized chains is equal to the degree of crystallinity obtained from the optical analysis, the number of interacting repeat units may be estimated according to:

$$N = \frac{\text{Long spacing [nm]} \times \%\,\text{Aggregate}}{0.385\ [\text{nm r.u.}^{-1}]}, \quad (2)$$

where 0.385 nm r.u.$^{-1}$ is the length of a P3HT repeat unit (r.u.) estimated by X-ray diffraction.[24] See the Supporting Information for the absorption spectra, long spacing,% Aggregate, and *W* versus solvent vapor pressure plots. The similarity between the Gierschner et al. theoretical calculations of *W* versus *N* and the approximations based upon the experimental data by Crossland et al. show that these estimations are reasonable.

Upon thermal annealing as-prepared films, the lengths of the interacting P3HT chain units increase in size in the CF cast films and decrease in size in the DCB cast films. For CF cast films annealed at 180 °C, *N* is ca. 25 r.u., corresponding to a planarized chain of ca. 10 nm. Note that *N* in annealed CF cast blends does not reach the same value as the films cast from DCB, despite the fact that the same level of energetic disorder is achieved. Van Bavel et al. deduced the P3HT aggregate width in P3HT:PCBM blend films cast from DCB and annealed for 20 min at 130 °C from electron tomography (ET) measurements, revealing P3HT nanorods with a width of ca. 15 nm.[25] This corresponds to ca. 39 repeat units and is within the range of widths determined by our optical analysis of the DCB prepared films.

The energetic disorder (σ) comprises contributions from both the interchain packing and the intrachain conformation, relating it directly to the charge and energy transfer behavior in BHJ organic solar cells.[26] The CF cast films show a near steady decrease in σ with an increase in the annealing temperature, from an initial value of 80 ± 1 meV down to 72 ± 1 meV at the highest annealing temperature, where σ continues to dramatically change beyond the glass transition range, in contrast to *W*. On the other hand, the σ values of the DCB cast films show a variation of only 70 ± 1 meV to 72 ± 1 meV. The striking approach of σ values in the films cast from both solvents at high annealing temperatures, despite marked differences in the values of percent crystallinity (**Figure 7**) and *W*, suggests that the maximum order available in the system is not directly correlated to the degree of crystallinity and the length of the correlated chain segments. The σ value of the largely disordered as-prepared sample from CF agrees well with the σ value of 82 ± 1.5 meV obtained by Pingel et al. for a high molecular weight P3HT sample at an in situ temperature of 130 °C.[4]

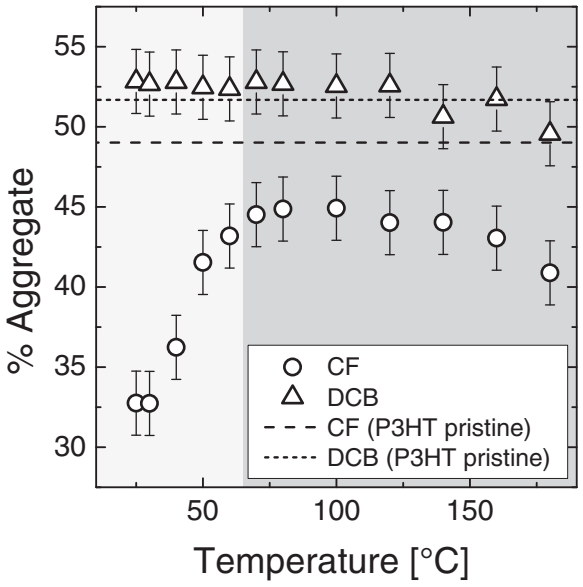

Figure 7. Percentage of aggregates within the P3HT phase of the P3HT:PCBM films annealed at varying temperatures and cast from CF and DCB.

Significantly higher values of σ were reported by Clark et al. for pure P3HT layers cast from CF (113 ± 1 meV) and isodurene (97 ± 1 meV).[15–16] These differences may be caused by variations in the degree of regioregularity, molecular weight distribution or preparation conditions. The σ values from the pristine P3HT films cast from DCB are within the error limits of the blend σ values. On the contrary, the σ value from the pristine P3HT film cast from CF is at the same value achieved in the blend film annealed at the end of the glass transition range. This shows that beyond the glass transition range annealing facilitates the achievement of higher molecular ordering beyond that possible in the as-prepared pristine state.

Finally, we find the 0-0 transition energy ($E_{0\text{-}0}$) to vary little over the range of thermal treatment for both of the film types. This indicates relatively constant local electronic properties of the individual polymer chains. As pointed out above, only the transition from the ground state to the highest energy state of each vibronic band is optically allowed in the absence of disorder. The slight increase in the $E_{0\text{-}0}$ values in the CF cast films treated at higher annealing temperatures may therefore partially be caused by an increase in order, as suggested by the decrease in the linewidth.

The percentages of P3HT chains contained in aggregates were deduced from the absorption spectra using the approach published by Clark et al. in 2009[15] and are shown in Figure 7. The pristine P3HT film cast from CF was found to have ca. 49% of aggregation. The P3HT component in the as-prepared blend film was determined to have ca. 33% of aggregation, less than two-thirds the value of the pristine film. Upon thermal annealing the degree of aggregation approaches that of the pristine film, but does not reach the same level. For DCB cast solvent-annealed layers, we find a crystallinity of ca. 53% for the as-prepared film, which drops gradually to 50% with increasing annealing temperature. Within the error limits, the crystallinity values of the as-prepared and thermally treated solvent-annealed DCB cast blends are the same as that of the crystallinity value in the pristine P3HT film. Recent ET measurements on thermally treated 100 nm thick 1:1 P3HT:PCBM films cast from DCB showed an overall crystallinity of 55%.[27] The good correspondence between our values deduced from analysis of the optical spectra and the P3HT crystallinity deduced from ET data is rather striking.

Based upon this work, we conclude that P3HT chains cast from CF do not have enough time during solution casting to form large aggregates, where the high solvent boiling point of DCB and the subsequent solvent annealing applied to the films allows for the formation of large P3HT aggregates. Interestingly, the major increase in P3HT crystallinity in the CF cast blend upon annealing is accompanied by a significant decrease in W and these changes are most pronounced for an annealing temperature of up to 70 °C. Apparently, the onset of segmental chain motion within the glass transition range is sufficient to allow for the rearrangement of the P3HT chains required for the observed growth of the number and length of P3HT segments contained in the aggregates. Further annealing above the glass transition range causes additional changes in the local interchain order, as expressed by the decrease in σ, but no added improvements in the overall aggregation beyond that which occurred within the glass transition range.

The low values of W and σ observed for the P3HT aggregates in the DCB cast blend films suggest that casting from the high boiling point solvent and subsequent solvent annealing leads to large and well-ordered aggregates. Noticeably, the crystallinity and the length of the aggregated chains are lower in the CF cast films even after annealing at the highest temperature. This means that the thermal energy supplied during annealing on the tested time-scale was not sufficient to induce a complete transition from the non-equilibrium disordered morphology of the as-prepared CF cast layers to the highly ordered structure seen in the solvent-annealed DCB cast films. On the other hand, the observed increase in W in the DCB cast films at higher temperatures also suggests that the cooling rate is too fast to recover the same size aggregates obtained by solvent annealing and/or that the aggregation of PCBM upon annealing blocks the recrystallization of the polymer chains.

2.2. Surface Morphology

AFM analysis was completed to determine the root mean square (RMS) roughness of the CF and DCB prepared films. Although this method is only sensitive to the surface-near morphology and maps features from both the P3HT and PCBM components, an increase in the RMS roughness may be associated with an improvement in the self-organization of the blend.[28] As PCBM aggregation is known to occur upon annealing of the P3HT:PCBM blend,[6,7] this may also contribute to the changes in the RMS roughness. As a result, large PCBM peaks in the AFM images were not taken into account in the RMS roughness determination. **Figure 8** shows the RMS roughness values plotted versus annealing temperature, where an increase is seen in the CF cast films and a decrease is observed in the DCB cast films. This suggests that the P3HT aggregate sizes increase upon annealing in the CF prepared films and decrease upon annealing

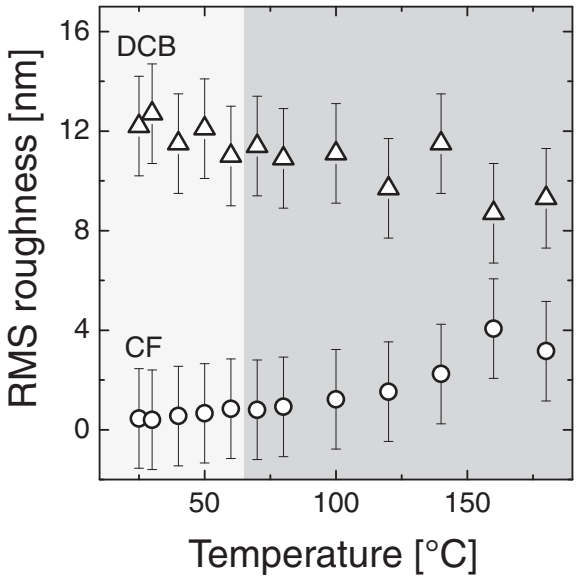

Figure 8. Root mean square roughness versus annealing temperature from AFM images of P3HT:PCBM blend films cast from CF and DCB. Note that the as-prepared films were each treated directly at the target annealing temperature.

in the DCB prepared films, which corresponds well with the trends we obtained from analysis of the absorption spectra of the films shown in Figure 5. AFM images used for RMS roughness analysis are shown in the Supporting Information.

2.3. Solar cells

The photoactive layer in each BHJ P3HT:PCBM solar cell was prepared in the same manner as the films used in the absorption spectroscopy investigations. **Figure 9** shows exemplary current density-voltage (*J–V*) characteristics of solar cell devices and **Figure 10** shows the full range of device properties versus annealing temperature. Both device types are seen to improve over the entire range of thermal treatment, where the improvement is most significant within the glass transition range for the CF cast devices. The overall improvement in CF prepared device performance is mainly caused by two processes: a pronounced increase in the short circuit current (J_{SC}) for annealing within the glass transition range and a continuous increase of the fill factor (FF) for annealing at or above 50 °C. Agostinelli et al. recently observed that improvements in the structural order and in the photovoltaic performance upon annealing at a fixed temperature of 140 °C proceeds in two time windows.[5] While a large increase in the J_{SC} was seen in the first window (the first 5 min), prolonged annealing for up to 30 min led to an increase of mainly the FF. This is quite comparable to the two-step process seen here. The dependence of the open circuit voltage (V_{OC}) on annealing temperature is rather complex; however, we note a weak anti-correlation between the trends of V_{OC} and of the percentage of aggregates shown in Figure 5. It is plausible to assume that the aggregation of polymer chains causes the highest occupied

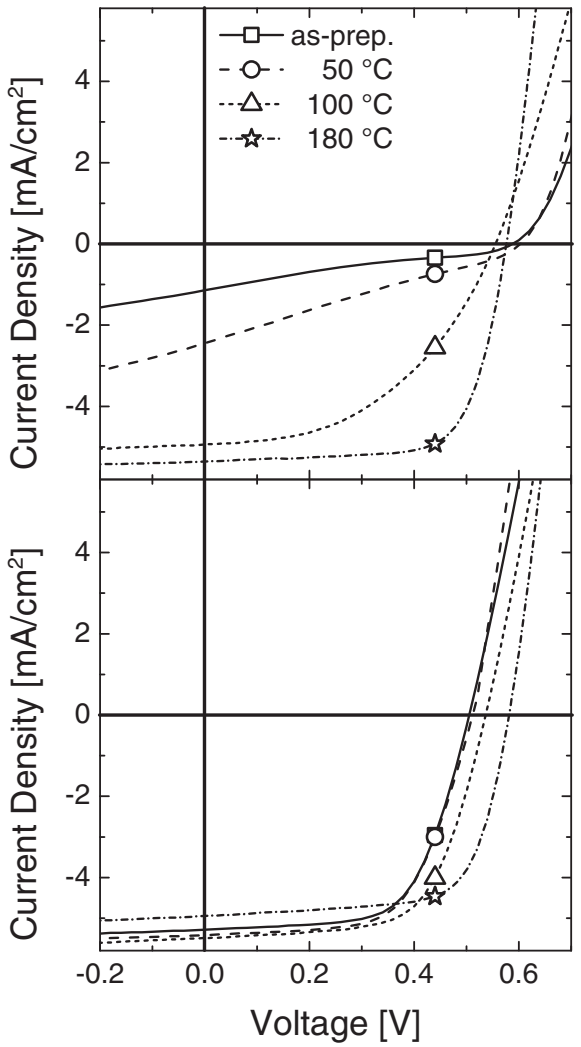

Figure 9. Select *J–V* curves of solar cell devices with ca. 100 nm photoactive layers cast from CF (top) and DCB (bottom), as-prepared and with a range of annealing temperatures. Devices were tested under AM1.5 illumination conditions in an inert atmosphere.

molecular orbital (HOMO) of P3HT to move to higher energies, thus decreasing the V_{OC}.

Interestingly, the efficiency of both solar cell types reaches the same value (ca. 2.5%) within the standard error at an annealing temperature of 180 °C. It was shown via the absorption spectroscopy modeling that the width of the P3HT conjugated segments in the films cast from CF are smaller than in the films cast from DCB throughout the entire range of thermal treatment. Furthermore, the power conversion efficiency (PCE) of the DCB cast layers increases with annealing temperature while the aggregate widths were seen to decrease upon thermal annealing. This suggests that as long as the P3HT aggregate widths are within a certain range, the precise size does not control the device performance. On the other hand, the disorder was found to be the same for the devices prepared from both CF and DCB at an annealing temperature of 180 °C. As pointed out above, the coating conditions for our blend layers have been optimized for the optical analysis rather than for high

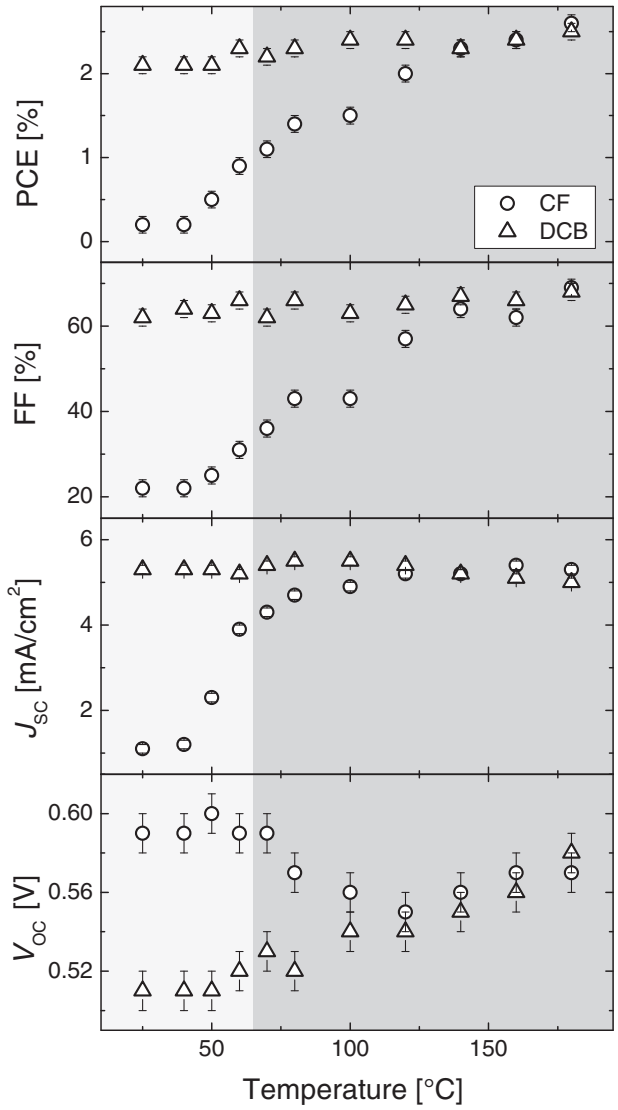

Figure 10. BHJ P3HT:PCBM solar cell device characteristics, power conversion efficiency (PCE), fill factor (FF), short circuit current (J_{SC}), and open-circuit voltage (V_{OC}) versus annealing temperature. Photoactive layers cast from CF and DCB.

efficiencies. A PCE of typically 3.5% is achieved when coating thicker blend layers from unfiltered solutions.

The low FF values of the CF prepared devices treated within the glass transition range may be attributed to field dependent free charge carrier generation, bimolecular recombination, or space charge effects.[29] In order to clarify the origin of these low FF values, the solar cells were tested over a range of light intensities, where a linear dependence on the photocurrent versus light intensity is expected if space charge buildup is not present.[30] The resulting photocurrent in the working range of 0.4 V was plotted versus the light intensity on a log-log scale, as shown for select devices cast from CF and DCB in **Figure 11**a and 11b, respectively. The resulting slopes are plotted versus the annealing temperature in Figure 11c. With a slope of ca. 3/4, the photogenerated current is space charge limited and bimolecular recombination occurs.[30] It can be seen that space charge effects are likely present in the

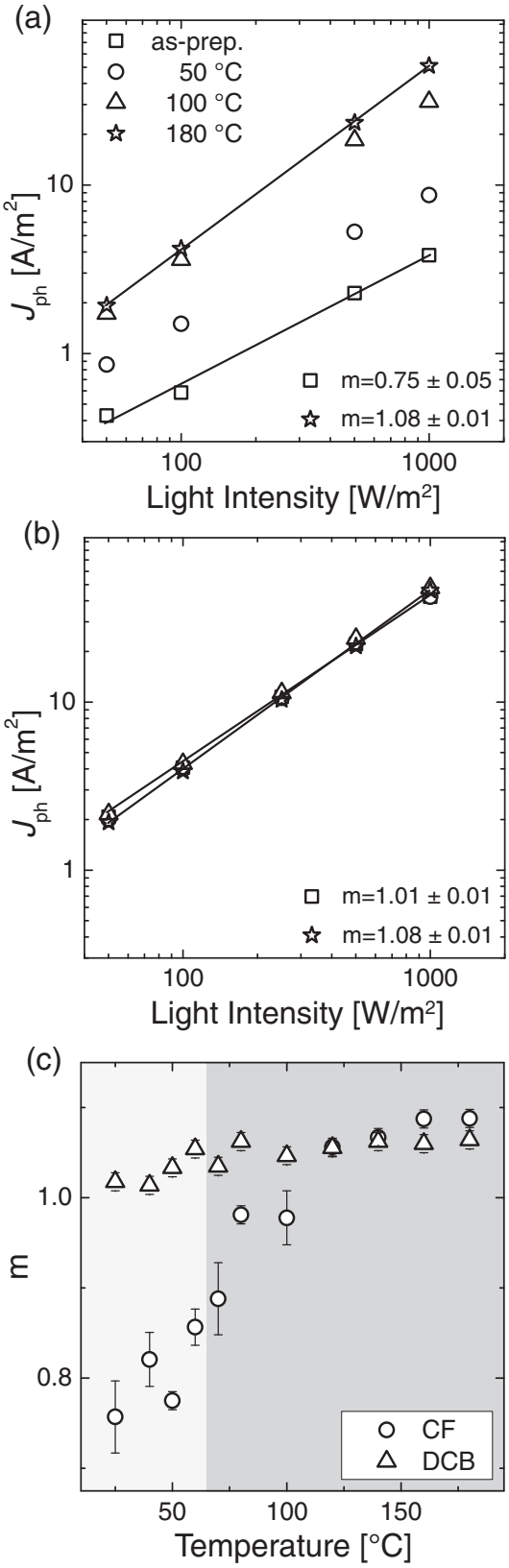

Figure 11. Photocurrent at 0.4 V versus light intensity of P3HT:PCBM BHJ solar cells cast from a) CF and b) DCB. The slopes of these plots on a log-log scale versus the annealing temperature are shown in (c).

CF prepared devices annealed at temperatures within the glass transition range. This may be due to the small width and/or connectivity of the P3HT aggregates, which reduces the percolation pathway in the BHJ system.

2.4. Mobility trends

Single carrier device measurements were completed to determine the trend of the electron and hole mobilities as a function of annealing temperature in the CF prepared devices. MoO_3 served as the hole-injecting contact in hole-only devices while Sm/Al was used as the injecting top contact in the electron-only devices. Under these conditions, the current should be determined by the bulk transport rather than by the efficiency for carrier injection. Unambiguous proof of space charge limited transport would require measurements on a series of devices with different layer thickness,[31,32] given as: $J(E) \propto d^{-1}$. On the other hand, work by Mihailetchi et al. proposed that currents through P3HT:PCBM photoactive layers are transport-limited even when using PEDOT:PSS and LiF/Al as injecting contacts in hole- and electron-only devices, respectively.[10]

The resulting current density versus voltage curves of the single carrier devices are shown in **Figure 12**. The electron-only devices exhibit a quadratic dependence of the current on the bias, as is predicted for trap-free space charge limited transport. The hole-only as-prepared device exhibits a slope of ca. 5, where a slope larger than two in most hole-only devices indicates that traps affect the transport through the sample.[29,33,34] The slope decreases monotonically with increasing annealing temperature, consistent with a reduction of the electronic disorder found in the optical spectra. Note that the slope is 1.35 in the device annealed at 140 °C, which implies that the transition from the ohmic to the space charge limited range has not yet been reached. For a slope unequal to two, the free carrier mobility cannot be determined directly from the J–V curves. We, therefore, plotted the current density at 2 V versus annealing temperature for a qualitative comparison of the carrier mobility in the electron- and hole-only devices. The electron current at this bias increases by almost an order of magnitude up to the end of the glass transition range, while it decreases slightly above this range. This decrease might be caused by the growth of large isolated PCBM clusters. The hole-only currents show a steep rise up to the end of the glass transition range and a less steep rise at higher annealing temperatures.

The trends obtained in this work compare very well to the results shown in Mihailetchi et al.[10] The hole mobility trend versus annealing temperature suggests that the sublinear decrease of the photocurrent with intensity at low annealing temperatures results from the low hole mobility as already proposed by Mihailetchi et al.[10] Furthermore, it is proposed that the low hole mobilities are a result of small P3HT aggregates and low overall crystallinity, as indicated by the Spano fits shown in Figure 4. On the other hand, the structural changes caused by annealing at temperatures beyond the glass transition region lead to sufficiently high mobilities for electrons and holes to suppress any of the build-up of space charge at AM1.5 illumination conditions.

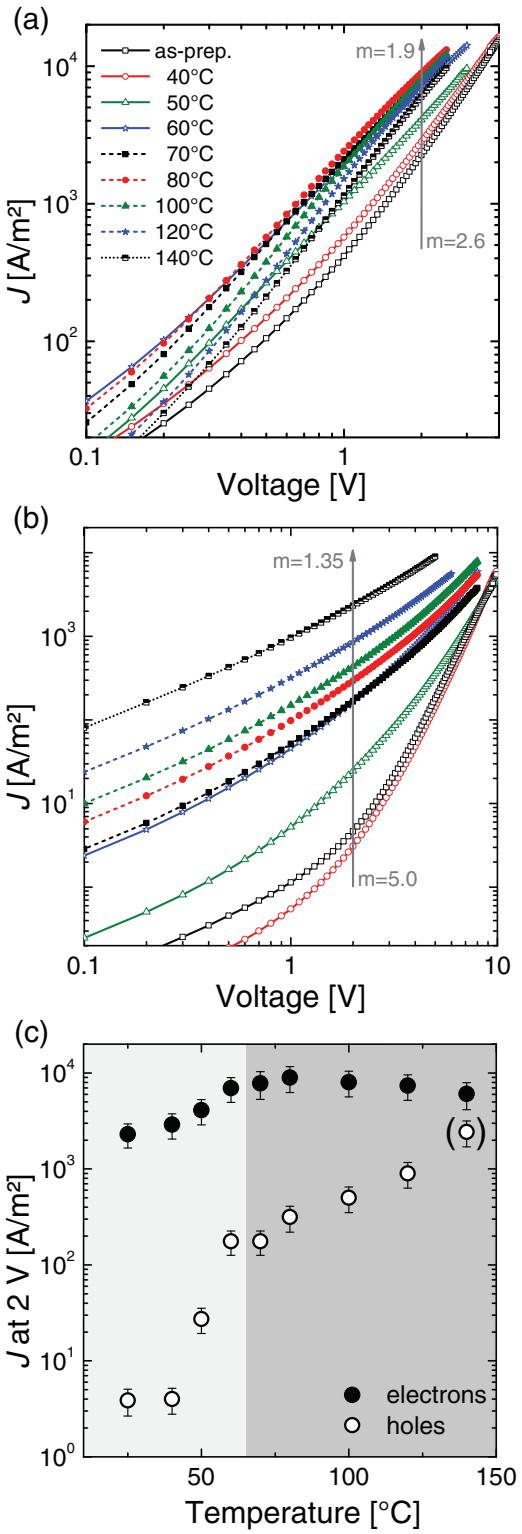

Figure 12. Current density versus voltage characteristics for single carrier devices of P3HT:PCBM blend films cast from CF: a) electron-only, b) hole-only, and c) current density at 2 V versus annealing temperature, representing the mobility trends. The current density of the hole-only device annealed at 140 °C is in parenthesis as the transition from the ohmic to the space charge limited range may not have been achieved for this device.

ADVANCED FUNCTIONAL MATERIALS
www.afm-journal.de

www.MaterialsViews.com

3. Discussion and Conclusions

A quantitative determination of morphological properties in P3HT:PCBM BHJ systems was achieved through absorption spectra analysis. The Spano-model, based upon weakly interacting H-aggregates, was successfully applied to analyze the P3HT component of the blend P3HT:PCBM absorption spectra. The results were compared with solar cell device characteristics, mobility, and AFM results. A low- and a high boiling point solvent were used to prepare films for analysis under a range of thermal treatment, where the former produced a non-optimized initial film morphology and the latter used in conjunction with solvent annealing produced a near optimized initial film morphology. As-prepared films of each type were thermally treated directly at the target temperature and not through a stepwise increase, providing a better determination of the effects of individual annealing temperatures.

The non-optimized initial morphology in the as-prepared CF cast layer comprised small P3HT aggregate widths and low total film crystallinity: only 33% of the P3HT chains are contained in aggregates, the length of the interacting chains (corresponding to the width of the aggregate along the chain direction) is rather small and the Gaussian linewidth is large. In particular, the degree of aggregation and the aggregate width are substantially smaller than in the pristine P3HT layers cast from CF. It has been pointed out that the presence of PCBM substantially disrupts the crystallization of P3HT.[12] Recent studies of as-prepared P3HT:PCBM blends cast from chlorobenzene (CB) displayed 10 nm PCBM rich domains randomly distributed in a P3HT phase comprising both amorphous and aggregated chains.[35] Also, recent studies with grazing incidence X-ray diffraction (GIXD) showed that the polymer crystallites in the as-prepared blends are rather imperfect and possess a significant degree of paracrystalline disorder in the alkyl stacking direction.[36,37] J. Loos and coworkers pointed out that P3HT crystals in solution cast P3HT:PCBM blends are rather imperfect and full of stacking defects.[25]

Upon thermal annealing the non-optimized films, two discrete temperature regimes were found describing changes in the film morphology: the first comprising the glass transition range up to ca. 70 °C and the second comprising temperatures beyond the glass transition range. Within the glass transition range, the fraction of chains contained in P3HT aggregates increases substantially from ca. 33% to almost 50%, accompanied by an increase of the aggregate width from ca. 7 nm to 10 nm. Beyond the glass transition range, annealing has a surprisingly weak effect on the further changes to the degree of crystallinity. Neither the percentage of aggregated P3HT chains nor the aggregate width of annealed CF cast layers reaches the same level as found in the pristine P3HT layer cast from CF or as found in any of the DCB cast blends. It is plausible to assume that a further growth of P3HT crystallites in the CF cast layers upon annealing at higher temperatures is prevented by the network of PCBM crystallites that has already formed by the agglomeration of PCBM-rich domains.[35] The melting temperature of the crystalline phase of PCBM in a 1:1 P3HT:PCBM blend was shown to be ca. 250 °C,[22] which is well beyond the temperature range considered here.

On the other hand, the Gaussian linewidth of the CF cast films decreases continuously with the annealing temperature throughout the entire temperature range studied here with the largest change above the glass transition range. The absorption linewidth in H-aggregates is determined by the statistical variation of the transition frequencies of the individual chain segments forming the stack (diagonal disorder) or by changes of the electronic coupling between neighboring segments (off-diagonal disorder).[13] Recently, paracrystalline disorder along the π–π stacking direction was predicted to cause significant broadening of the density of state distribution in H-aggregates of a semicrystalline semiconducting polymer.[38] Though we do not know the exact physical process determining the absorption linewidth in our samples, its continuous decrease with annealing temperature in our CF cast samples points to a steady improvement of intra- and/or interchain order, e.g. by the reduction of the number of stacking faults in the P3HT aggregates.[39] It has been pointed out that annealing CB cast 1:1 P3HT:PCBM blends at 140 °C substantially reduces the paracrystalline disorder along the alkyl stacking direction.[36] Unfortunately, comprehensive information on the degree of structural order along the π–π stacking direction is currently missing, though this direction is most relevant for the transport of excitons and charges.

In contrast to the CF cast blends discussed above, the properties of the P3HT phase in the solvent-annealed DCB cast blends (as deduced from the optical analysis) are almost indistinguishable from those of the corresponding pristine P3HT layer and are only weakly affected by thermal annealing. Apparently, slow drying of the blend allows the P3HT chains to form large aggregates with a low degree of intra- and interchain disorder. This morphology appears to be most favorable for the efficient generation and extraction of charges.

We now turn to the relation between structural and (opto-) electronic properties. There is a firm belief that the current-voltage characteristics of 1:1 blends of highly regioregular P3HT with PCBM is determined by the competition between the field-induced extraction and the bimolecular recombination of photoinduced free carriers.[40–42] Also, recent studies showed consistently that the efficiency for free carrier formation in as-prepared and annealed P3HT:PCBM blends is not dependent upon the electric field.[40,43–45] In other words, the number of free carriers formed upon photoexcitation in these blends is not limited by geminate recombination in competition with field-driven exciton dissociation. For our CF cast as-prepared device, the solar cell performance is deteriorated by space charge effects in combination with bimolecular recombination. This is clearly seen by the sublinear increase in photocurrent with intensity. Most likely, these effects are caused by poor hole transport in the highly disordered P3HT phase, which is additionally disrupted by small PCBM-rich domains. The structural changes induced by annealing of the blend in the glass transition range cause the hole mobility to rise significantly and space charge effects become essentially irrelevant in samples annealed at 80 °C or above. At the same time the short circuit current approaches values comparable to those measured on high temperature annealed CF cast blends or on DCB cast layers. Accordingly, the improvement of the device performance upon annealing beyond the glass transition range is primarily caused

by the continuous increase of the FF. As space charge effects are absent in these devices and the efficiency of carrier generation is independent of bias, the main reason for the increase of the FF must lie in the reduction of the bimolecular recombination rate. Several groups reported that the bimolecular recombination coefficient in annealed P3HT:PCBM blends is largely inhibited when compared to the value predicted for the recombination of point charges in a homogeneous medium.[43,46,47] This reduction has been attributed to the phase separated layer morphology. Interestingly, we find an apparent anticorrelation between the energetic disorder in the P3HT crystallites (as expressed by the Gaussian linewidth) and the FF. In fact, CF and DCB cast blends exhibit almost identical values of the FF and the linewidth after annealing at high temperatures, though they differ significantly in the degree of aggregation and in the aggregate width. Increasing the diagonal and off-diagonal order will decrease the probability that holes become localized on specific chain segments, which in turn might render them less vulnerable for bimolecular recombination.

We, finally, would like to point out that according to our analysis the as-prepared CF cast layer already contains a significant number of aggregated chains. It has been postulated that free carrier generation in P3HT-based solar cells is assisted by the delocalization of holes along fully conjugated chain segments.[48] Such chain segments are mainly located within H-aggregates, as chains within the amorphous regions exhibit significant twisting and bending. Howard et al. reported that 68% of the charge transfer excitons formed at the P3HT:PCBM heterojunction in the as-prepared blends cast from either CB or CF dissociate into free carriers.[44] Annealing at 120 °C increased this fraction only slightly to about 85%. We, therefore, conclude that the number of aggregated P3HT chains in as-prepared CF cast samples is sufficiently high for the efficient photogeneration of free carriers, while the poor structural order in these layers prevents the efficient extraction of free carriers to the external circuit.

4. Experimental Section

Materials: Regioregular P3HT Sepiolid P200 was purchased from BASF. PC[61]BM was purchased from Solenne. Poly(3,4-ethylenedioxythiophene):Poly(styrenesulfonate) (PEDOT:PSS) (Baytron P VP AI 4083) was purchased from H.C. Starck. Polystyrene (PS) 81410 (M_w = 94,900 g mol^{-1} and M_n = 89,300 g mol^{-1}) was purchased from Fluka AG. All materials were used as received.

Solutions: Blend P3HT:PCBM and PCBM:PS solutions were prepared in 50:50-wt%. The CF solutions were prepared at a concentration of 14.5 mg mL^{-1} and the DCB solutions were prepared at a concentration of 21.0 mg mL^{-1}. The solutions were filtered at room temperature with a 0.45 µm PTFE filter and mixed to the desired concentration.

Device Preparation: Fully coated indium tin oxide (ITO) glass substrates (Präzisions Glas & Optik GmbH) were used for absorption spectroscopy sample preparation. The substrates were cleaned by ultrasonic treatment implementing a range of solvent and rinsing steps. The cleaned substrates were subjected to an oxygen plasma surface treatment for 2 min at 200 W. PEDOT:PSS was filtered through a 0.2 µm nylon filter and solution cast onto the clean and cooled substrate under ambient conditions. The substrates were then dried at 180 °C for 10 min under inert atmosphere. The prepared 50:50-wt% solutions were cast onto the dried PEDOT:PSS layer to produce an active layer thickness of 100 ± 5 nm. The samples cast from DCB were further subjected to solvent annealing directly after solution casting for 30 min in a closed Petri dish. Thermal annealing was applied to the as-prepared films at various temperatures between 30 °C and 180 °C for 10 min each. Structured U-shaped ITO coated glass substrates were used for solar cell device preparation. The fabrication followed as outlined above with the additional step of top electrode vacuum deposition comprising a 20 nm samarium layer topped with a 100 nm aluminum layer. The hole-only devices were prepared on an ITO pattern prepared via wet etching of the fully coated ITO glass substrates. The preparation followed as for the solar cell devices with the top electrode comprising a 20 nm molybdenum trioxide layer topped with a 100 nm aluminum layer. Electron-only devices were prepared on PEDOT:PSS covered glass substrates[34]. After PEDOT:PSS drying, a 50 nm layer of aluminum was applied via vacuum deposition. The active layer and top electrode deposition proceeded as outlined above for the solar cell devices.

Measurements: UV-Vis absorption spectra were recorded with a Varian Cary 5000 spectrophotometer in combination with a DRA 2500 integrating sphere accessory. The current-voltage characteristics of the solar cell devices were measured using AM1.5 solar simulation (K.H. Steuernagel Lichttechnik GmbH) with a Keithley 2400 Sourcemeter under inert atmosphere. The single-carrier devices were measured with a Keithley 2400 Sourcemeter under inert atmosphere. Layer thicknesses were determined with a Dektak 3ST (Veeco) profilometer.

Supporting Information

Supporting Information is available from the Wiley Online Library or from the author.

Acknowledgements

We thank Prof. Joachim Loos (University of Glasgow) for fruitful discussions and Burkhard Stiller (University of Potsdam) for AFM measurements. Financial support from the German Federal Ministry of Science and Education (BMBF) within SOHyb (FKZ 03X3525D) and Ausbau PVComB (FKZ 03IS2151D) is gratefully acknowledged. Supporting Information is available from the Wiley Online Library or from the author.

Received: July 12, 2011
Published online: October 19, 2011

[1] L. H. Nguyen, H. Hoppe, T. Erb, S. Günes, G. Gobsch, N. S. Sariciftci, *Adv. Funct. Mater.* **2007**, *17*, 1071.
[2] Y. Kim, S. Cook, S. M. Tuladhar, S. A. Choulis, J. Nelson, J. R. Durrant, D. D. C. Bradley, M. Giles, I. McCulloch, C.-S. Ha, M. Ree, *Nature Materials* **2006**, *5*, 197.
[3] J. Jo, S.-S. Kim, S.-I. Na, B.-K. Yu, D.-Y. Kim, *Adv. Funct. Mater.* **2009**, *19*, 866.
[4] P. Pingel, A. Zen, R. D. Abellón, F. C. Grozema, L. D. A. Siebbeles, D. Neher, *Adv. Funct. Mater.* **2010**, *20*, 2286.
[5] T. Agostinelli, S. Lilliu, J. G. Labram, M. Campoy-Quiles, M. Hampton, E. Pires, J. Rawle, O. Bikondoa, D. D. C. Bradley, T. D. Anthopoulos, J. Nelson, J. E. Macdonald, *Adv. Funct. Mater.* **2011**, *21*, 1701.
[6] D. Chirvase, J. Parisi, J. C. Hummelen, V. Dyakonov, *Nanotechnology* **2004**, *15*, 1317.
[7] M. Campoy-Quiles, T. Ferenczi, T. Agostinelli, P. G. Etchegoin, Y. Kim, T. D. Anthopoulos, P. N. Stavrinou, D. D. C. Bradley, J. Nelson, *Nature Materials* **2008**, *7*, 158.

[8] P. E. Keivanidis, T. M. Clarke, S. Lilliu, T. Agostinelli, J. E. Macdonald, J. R. Durrant, D. D. C. Bradley, J. Nelson, *J. Phys. Chem. Lett.* **2010**, *1*, 734.
[9] R. Mauer, M. Kastler, F. Laquai, *Adv. Funct. Mater.* **2010**, *20*, 2085.
[10] V. D. Mihailetchi, H. Xie, B. de Boer, L. J. A. Koster, P. W. M. Blom, *Adv. Funct. Mater.* **2006**, *16*, 699.
[11] A. Swinnen, I. Haeldermans, M. vande Ven, J. D'Haen, G. Vanhoyland, S. Aresu, M. D'Olieslaeger, J. Manca, *Adv. Funct. Mater.* **2006**, *16*, 760.
[12] E. Verploegen, R. Mondal, C. J. Bettinger, S. Sok, M. F. Toney, Z. Bao, *Adv. Funct. Mater.* **2010**, *20*, 3519.
[13] F. C. Spano, *J. Chem. Phys.* **2005**, *122*, 234701.
[14] F. C. Spano, *Chem. Phys.* **2006**, *325*, 22.
[15] J. Clark, J.-F. Chang, F. C. Spano, R. H. Friend, C. Silva, *Appl. Phys. Lett.* **2009**, *94*, 163306.
[16] J. Clark, C. Silva, R. H. Friend, F. C. Spano, *Phys. Rev. Lett.* **2007**, *98*, 206406.
[17] E. J. W. Crossland, K. Rahimi, G. Reiter, U. Steiner, S. Ludwigs, *Adv. Funct. Mater.* **2011**, *21*, 518.
[18] J. Gierschner, Y.-S. Huang, B. Van Averbeke, J. Cornil, R. H. Friend, D. Beljonne, *J. Chem. Phys.* **2009**, *130*, 044105.
[19] S. Malik, A. K. Nandi, *J. Polym. Sci. B* **2002**, *40*, 2073.
[20] A. Zen, M. Saphiannikova, D. Neher, J. Grenzer, S. Grigorian, U. Pietsch, U. Asawapirom, S. Janietz, U. Scherf, I. Lieberwirth, G. Wegner, *Macromolecules* **2006**, *39*, 2162.
[21] R. Zhang, B. Li, M. C. Iovu, M. Jeffries-EL, G. Sauvé, J. Cooper, S. Jia, S. Tristram-Nagle, D. M. Smilgies, D. N. Lambeth, R. D. McCullough, T. Kowalewski, *JACS* **2006**, *128*, 3480.
[22] J. Zhao, A. Swinnen, G. Van Assche, J. Manca, D. Vanderzande, B. Van Mele, *J. Phys. Chem. B* **2009**, *113*, 1587.
[23] T. Wang, A. J. Pearson, D. G. Lidzey, R. A. L. Jones, *Adv. Funct. Mater.* **2011**, *21*, 1383.
[24] T. J. Prosa, M. J. Winokur, J. Moulton, P. Smith, A. J. Heeger, *Macromolecules* **1992**, *25*, 4364.
[25] S. S. van Bavel, E. Sourty, G. de With, J. Loos, *Nano Lett.* **2009**, *9*, 507.
[26] S. T. Hoffmann, H. Bässler, A. Köhler, *J. Phys. Chem. B* **2010**, *114*, 17037.
[27] S. van Bavel, E. Sourty, G. de With, K. Frolic, J. Loos, *Macromolecules* **2009**, *42*, 7396.
[28] G. Li, V. Shrotriya, J. Huang, Y. Yao, T. Moriarty, K. Emery, Y. Yang, *Nature Materials* **2005**, *4*, 864.
[29] M. M. Mandoc, W. Veurman, L. J. A. Koster, B. de Boer, P. W. M. Blom, *Adv. Funct. Mater.* **2007**, *17*, 2167.
[30] V. D. Mihailetchi, J. Wildeman, P. W. M. Blom, *Phys. Rev. Lett.* **2005**, *94*, 126602.
[31] W. Brütting, S. Berleb, A. G. Mückl, *Synth. Met.* **2001**, *122*, 99.
[32] R. Steyrleuthner, M. Schubert, F. Jaiser, J. C. Blakesley, Z. Chen, A. Facchetti, D. Neher, *Adv. Mater.* **2010**, *22*, 2799.
[33] P. Mark, W. Helfrich, *J. Appl. Phys.* **1962**, *33*, 205.
[34] R. Steyrleuthner, S. Bange, D. Neher, *J. Appl. Phys.* **2009**, *105*, 064509.
[35] R. M. Beal, A. Stavrinadis, J. H. Warner, J. M. Smith, H. E. Assender, A. A. R. Watt, *Macromolecules* **2010**, *43*, 2343.
[36] S. Lilliu, T. Agostinelli, E. Pires, M. Hampton, J. Nelson, J. E. Macdonald, *Macromolecules* **2011**, *44*, 2725.
[37] M. Shin, H. Kim, J. Park, S. Nam, K. Heo, M. Ree, C.-S. Ha, Y. Kim, *Adv. Funct. Mater.* **2010**, *20*, 748.
[38] J. Rivnay, R. Noriega, J. E. Northrup, R. J. Kline, M. F. Toney, A. Salleo, *Phys. Rev. B* **2011**, *83*, 121306.
[39] S. S. van Bavel, J. Loos, *Adv. Funct. Mater.* **2010**, *20*, 3217.
[40] J. Kniepert, M. Schubert, J. C. Blakesley, D. Neher, *J. Phys. Chem. Lett.* **2011**, *2*, 700.
[41] R. Mauer, I. A. Howard, F. Laquai, *J. Phys. Chem. Lett.* **2010**, *1*, 3500.
[42] C. G. Shuttle, R. Hamilton, B. C. O'Regan, J. Nelson, J. R. Durrant, *PNAS* **2010**, *107*, 16448.
[43] J. Guo, H. Ohkita, H. Benten, S. Ito, *JACS* **2010**, *132*, 6154.
[44] I. A. Howard, R. Mauer, M. Meister, F. Laquai, *JACS* **2010**, *132*, 14866.
[45] R. A. Street, S. Cowan, A. J. Heeger, *Phys. Rev. B* **2010**, *82*, 121301.
[46] C. Deibel, A. Baumann, V. Dyakonov, *Appl. Phys. Lett.* **2008**, *93*, 163303.
[47] A. Pivrikas, G. Juška, A. J. Mozer, M. Scharber, K. Arlauskas, N. S. Sariciftci, H. Stubb, R. Österbacka, *Phys. Rev. Lett.* **2005**, *94*, 176806.
[48] C. Deibel, T. Strobel, V. Dyakonov, *Phys. Rev. Lett.* **2009**, *103*, 036402.

Supporting Information

Quantitative analysis of BHJ films using linear absorption spectroscopy and solar cell performance

Sarah T. Turner[1,4], *Patrick Pingel*[1], *Robert Steyrleuthner*[1], *Edward J. W. Crossland*[2], *Sabine Ludwigs*[3], *and Dieter Neher*[1],*

[1] Institute of Physics and Astronomy
University of Potsdam
Karl-Liebknecht-Straße 24-25
14476 Potsdam, Germany
E-mail: neher@uni-potsdam.de

[2] Clarendon Laboratory
Parks Road, Oxford
OX1 3PU, UK

[3] Institute of Polymer Chemistry
University of Stuttgart
Pfaffenwaldring 55
70569 Stuttgart, Germany

[4] Current address: Institute of Chemistry
Stranski Laboratory for Physical and Theoretical Chemistry
Technical University of Berlin
Straße des 17. Juni 124
10623 Berlin, Germany

1 Spano Fits

Figures S1 and S2 show the individual absorption spectra of the P3HT component in a BHJ P3HT:PCBM blend for films cast from CF and DCB, respectively. The spectrum of a 100 nm thick 1:1 PCBM:PS film cast from DCB was chosen to subtract the PCBM contribution from all spectra (even for the CF cast blend films) as the subtraction of this background led to more reasonable final spectra for analysis with the Spano-model, matching the trend of the pristine P3HT film. This is likely a result of the slower drying time provided by the DCB solvent, which better mimics the PCBM aggregation upon annealing even in the CF blend films. Equation 1 (see article), developed by F.C. Spano based upon weakly interacting H-aggregates [F. C. Spano, *J. Chem. Phys.* **2005**, *122*, 234701], was used to fit these spectra in the energy regions of 1.93 eV to 2.25 eV.

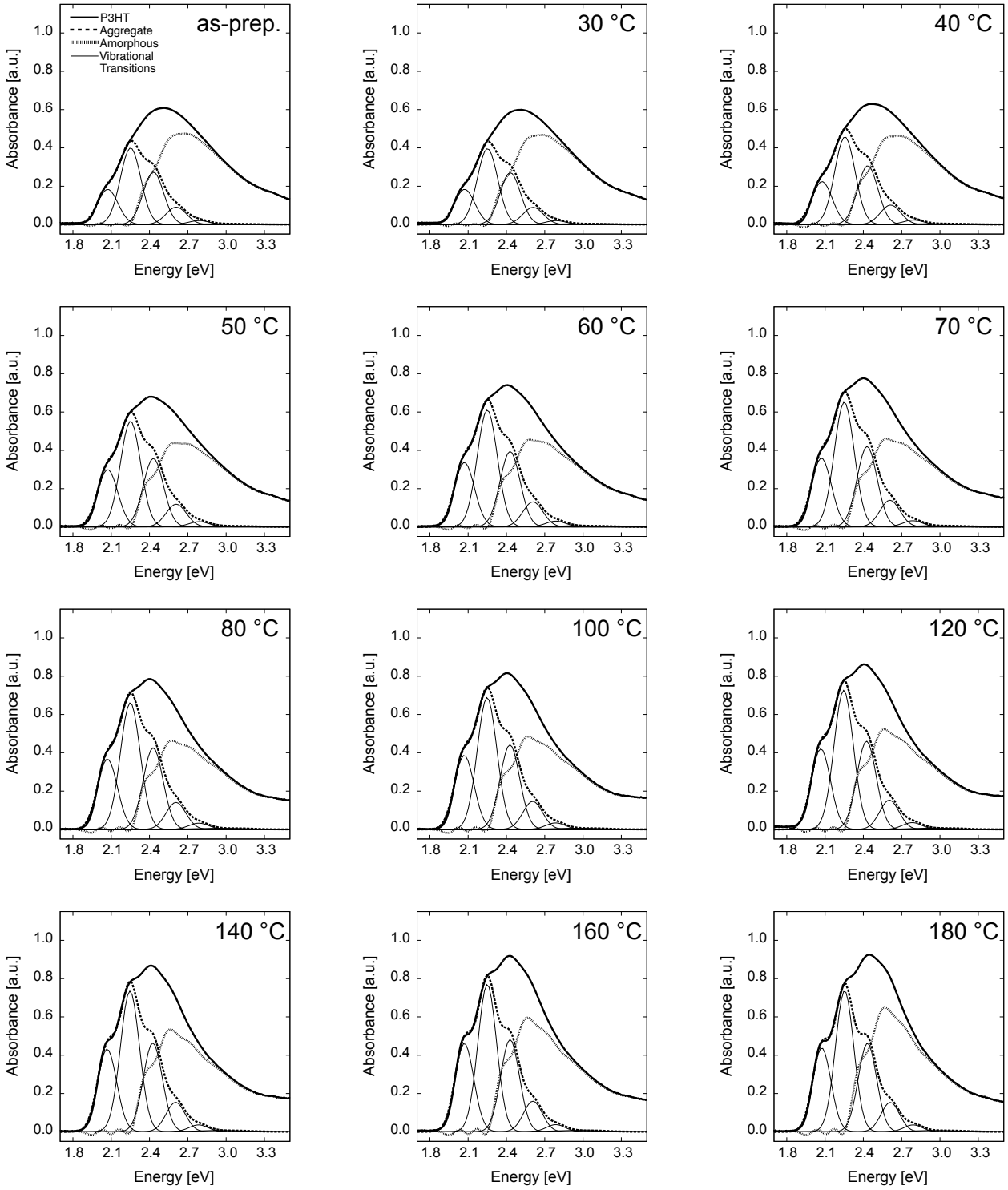

Figure S1: P3HT component of the P3HT:PCBM absorption spectrum for films annealed at the given temperature, cast from CF. The aggregate P3HT absorbance results from the best fit of the low energy absorbance obtained using Equation 1 (see article). The amorphous P3HT absorbance component is the difference between the total measured P3HT absorbance and the fit of the aggregate absorbance. The individual electronic vibrational transitions are also shown.

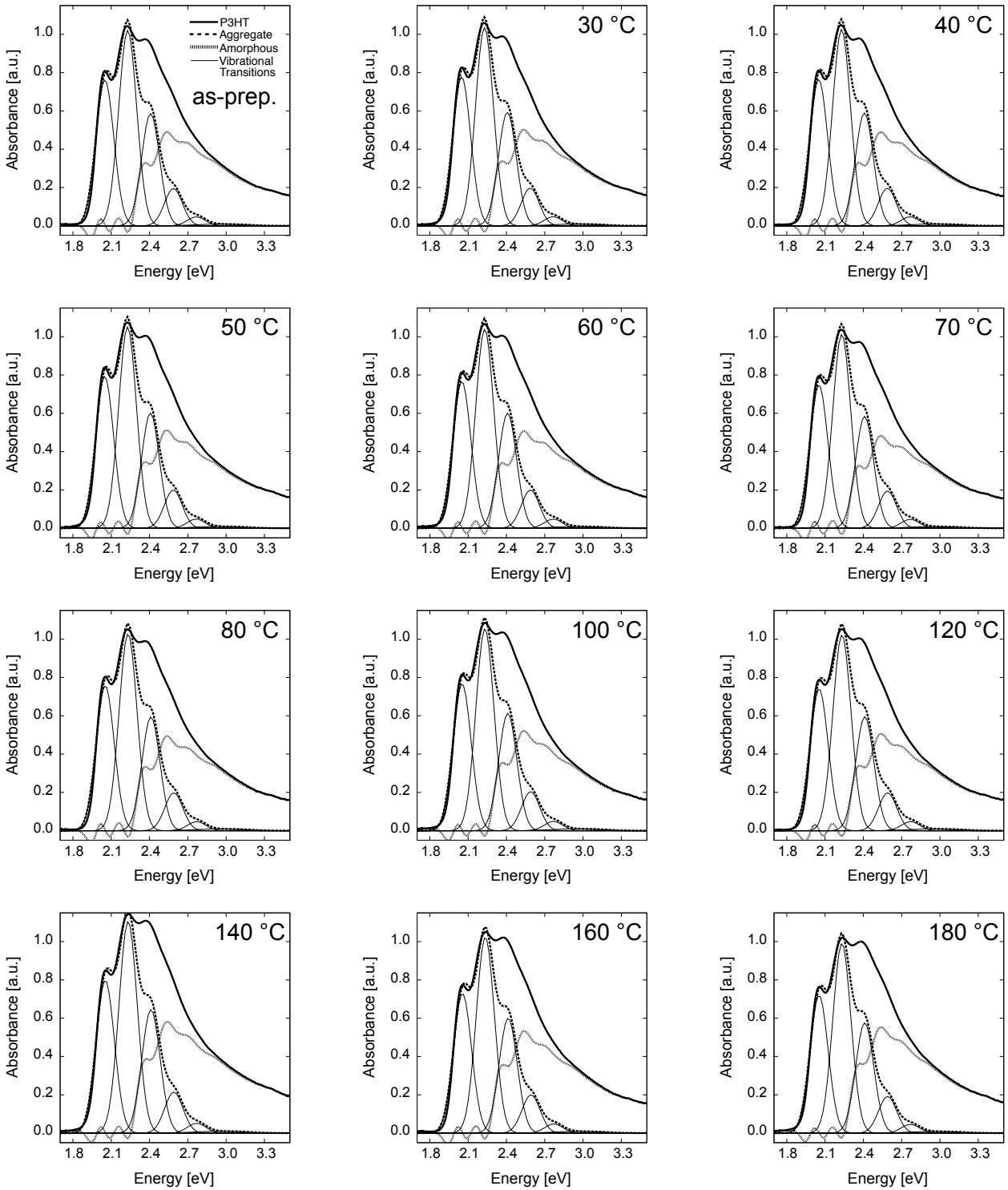

Figure S2: P3HT component of the P3HT:PCBM absorption spectrum for films annealed at the given temperature, cast from DCB. The aggregate P3HT absorbance results from the best fit of the low energy absorbance obtained using Equation 1 (see article). The amorphous P3HT absorbance component is the difference between the total measured P3HT absorbance and the fit of the aggregate absorbance. The individual electronic vibrational transitions are also shown.

2 Variation of upper and lower bounds

The lower and upper bounds used to fit the P3HT component of the blend P3HT:PCBM absorption spectra were analyzed for consistency. Absorption spectra from the following films were used for analysis: the as-prepared film cast from CF and the films annealed at 180 °C cast from CF and DCB. The best fitting upper boundary was chosen by holding the lower boundary constant at 1.93 eV. The fit parameters obtained from Equation 1 (see article) are plotted versus the upper boundary value in Figure S3. With the upper boundary set below 2.20 eV the 0-1 absorbance peak is not properly accounted for and deviations are seen in the fit parameters. With the upper boundary set above 2.25 eV the σ and E_{0-0} values show deviations. As a result, the best fitting upper boundary was chosen to be 2.25 eV to allow for the largest fit region possible while remaining in the plateau regions of all of the fit parameters for all of the samples. The lower boundary was then varied while holding the upper boundary constant at 2.25 eV. The fit parameters versus lower boundary value are shown in Figure S4. At energies below 1.93 eV no deviations were found in any of the fit parameters and the absorption at lower energies than this is negligible. As a result, 1.93 eV was chosen to be the lower boundary. The absorption spectra between 2.25 eV and 1.93 eV were further analyzed using the model by F.C. Spano (see Equation 1 in main article [F. C. Spano, *J. Chem. Phys.* **2005**, *122*, 234701]).

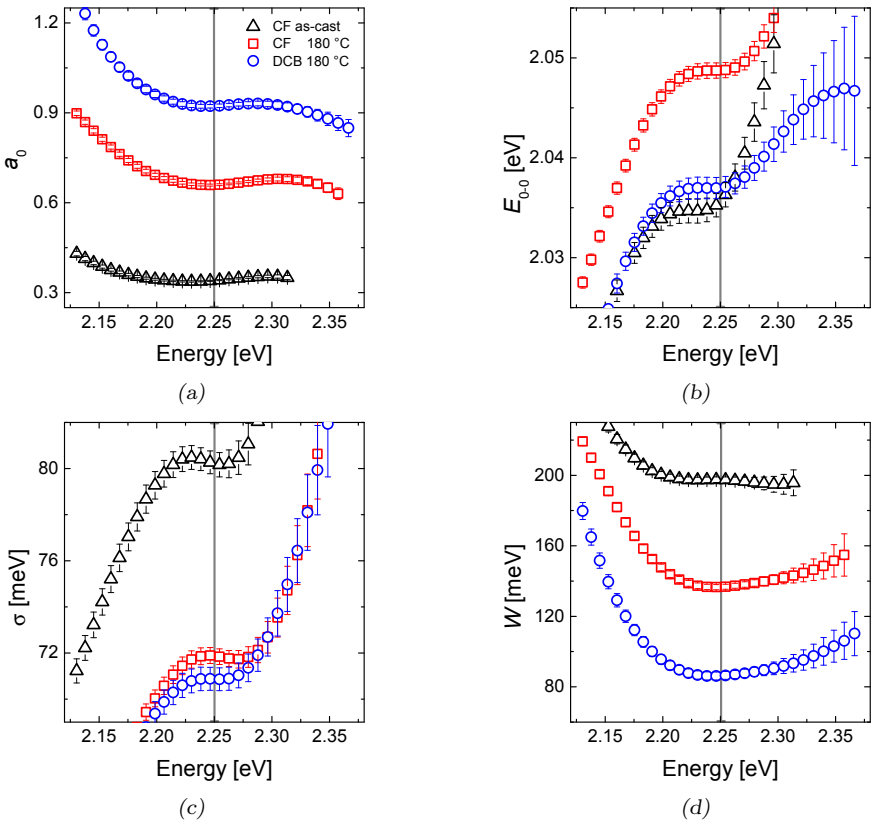

Figure S3: Fit parameters obtained from Equation 1 (see article) by holding the lower boundary constant at 1.93 eV and varying the upper boundary. The best-fit upper boundary is highlighted with a grey line at a value of 2.25 eV. a_0 is the proportionality constant, E_{0-0} is the 0-0 transition energy, σ is the Gaussian linewidth, and W is the free exciton bandwidth.

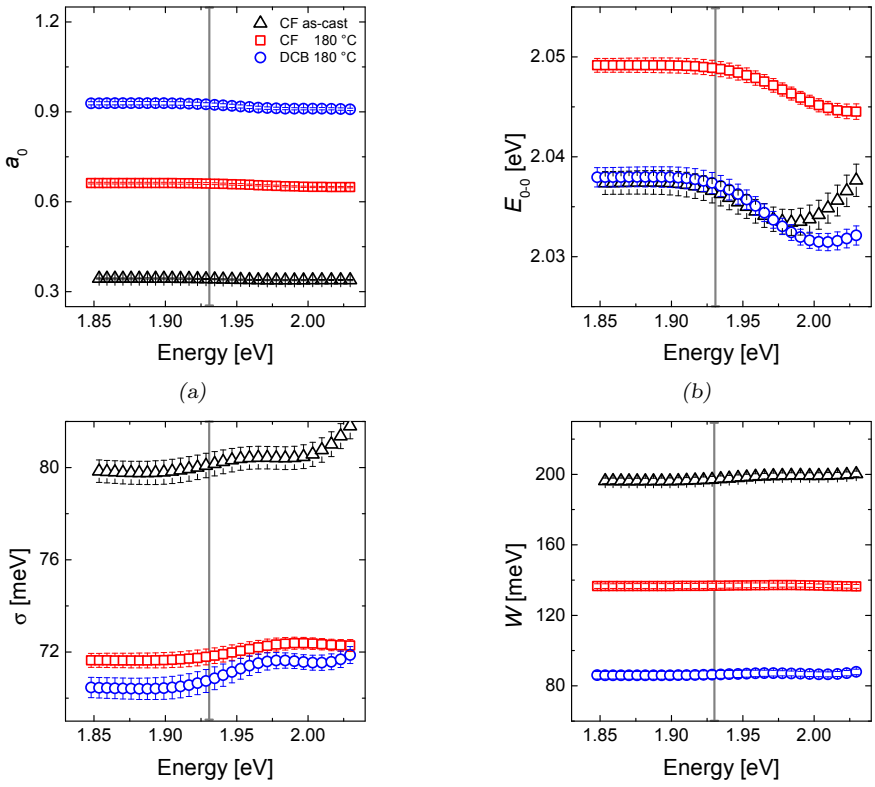

Figure S4: Fit parameters obtained from Equation 1 (see article) by holding the upper boundary constant at 2.25 eV and varying the lower boundary. The best-fit lower boundary is highlighted with a grey line at a value of 1.93 eV. a_0 is the proportionality constant, E_{0-0} is the 0-0 transition energy, σ is the Gaussian linewidth, and W is the free exciton bandwidth.

3 W versus N approximations from Crossland et al. data

Absorption spectra and AFM images from Crossland et al. [E. J. W. Crossland et al., *Adv. Funct. Mater.* **2011**, *21*, 518.] were used to estimate the relationship between W and N for comparison to the theoretical calculations by Gierschner et al. [J. Gierschner et al., *J. Chem. Phys.* **2009**, *130*, 044105.] Figure S5 shows the absorption spectra of pristine P3HT films prepared by crystallization for 2000 s at varying solvent vapor pressures and dried by decreasing the pressure by 2 % per minute. These absorption spectra correspond to the lamellar long spacing measurements shown in Crossland et al. [E. J. W. Crossland et al., *Adv. Funct. Mater.* **2011**, *21*, 518.] W values were determined using Equation 1 (see article). The long spacing and % Aggregate, shown in Figure S7, were used to approximate the number of repeat units and are correlated to the value of W, as shown in the main section of the paper.

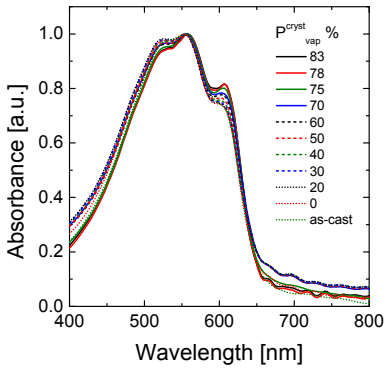

Figure S5: Normalized absorption spectra of pristine P3HT films dried under varying concentrations of a CS_2 solvent vapor pressure. Films were dried by decreasing the pressure by 2 % per minute.

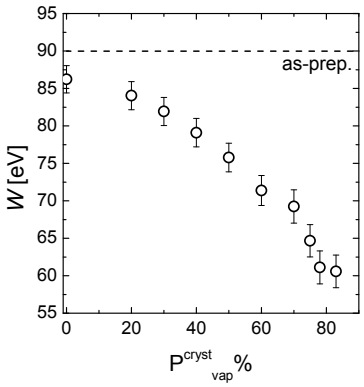

Figure S6: W value of the corresponding absorption spectra determined using the Spano method (see Introduction) versus the solvent vapor concentration used to prepare the pristine P3HT films.

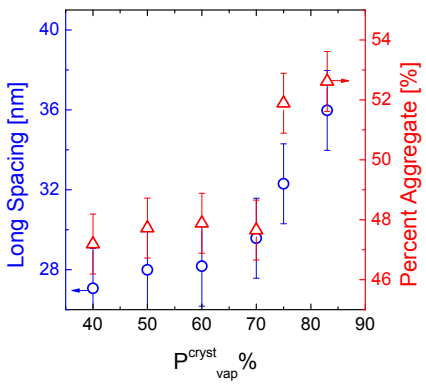

*Figure S7: The long spacing and % Aggregate, calculated by the Clark et al. [J. Clark et al., Appl. Phys. Lett. **2009**, 94, 163306.] method, versus the solvent vapor concentration used to prepare the pristine films.*

4 AFM

AFM images of the P3HT:PCBM films cast from CF and DCB on a PEDOT:PSS/ITO/glass substrates are shown in Figures S8 and S9, respectively. The RMS roughness values are shown in Figure 8 in the main article.

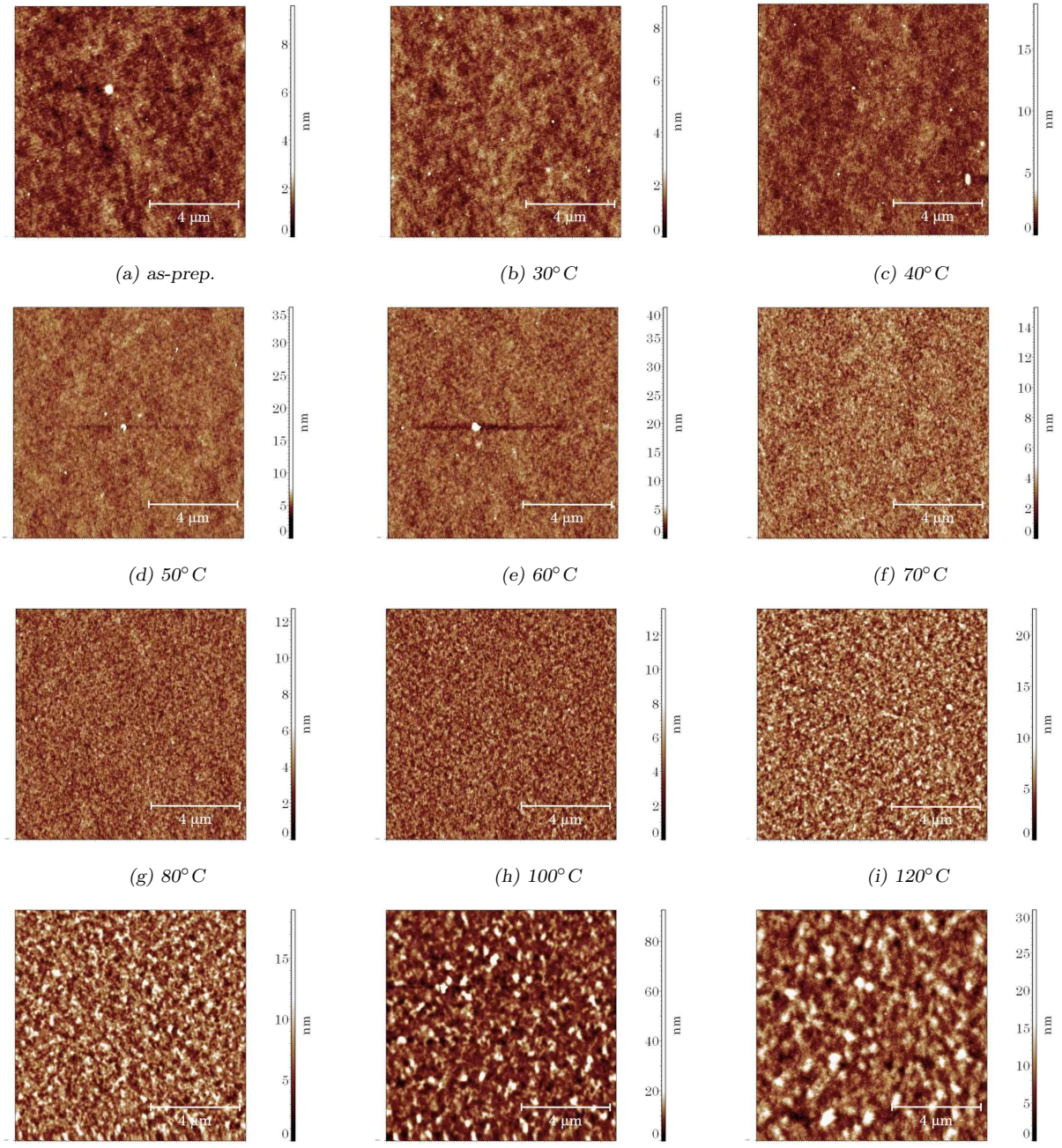

(a) as-prep. (b) 30° C (c) 40° C

(d) 50° C (e) 60° C (f) 70° C

(g) 80° C (h) 100° C (i) 120° C

(j) 140° C (k) 160° C (l) 180° C

Figure S8: AFM images of P3HT:PCBM films cast from CF on PEDOT:PSS/ITO/glass substrates. Films were thermally annealed at the given temperature for 10 min.

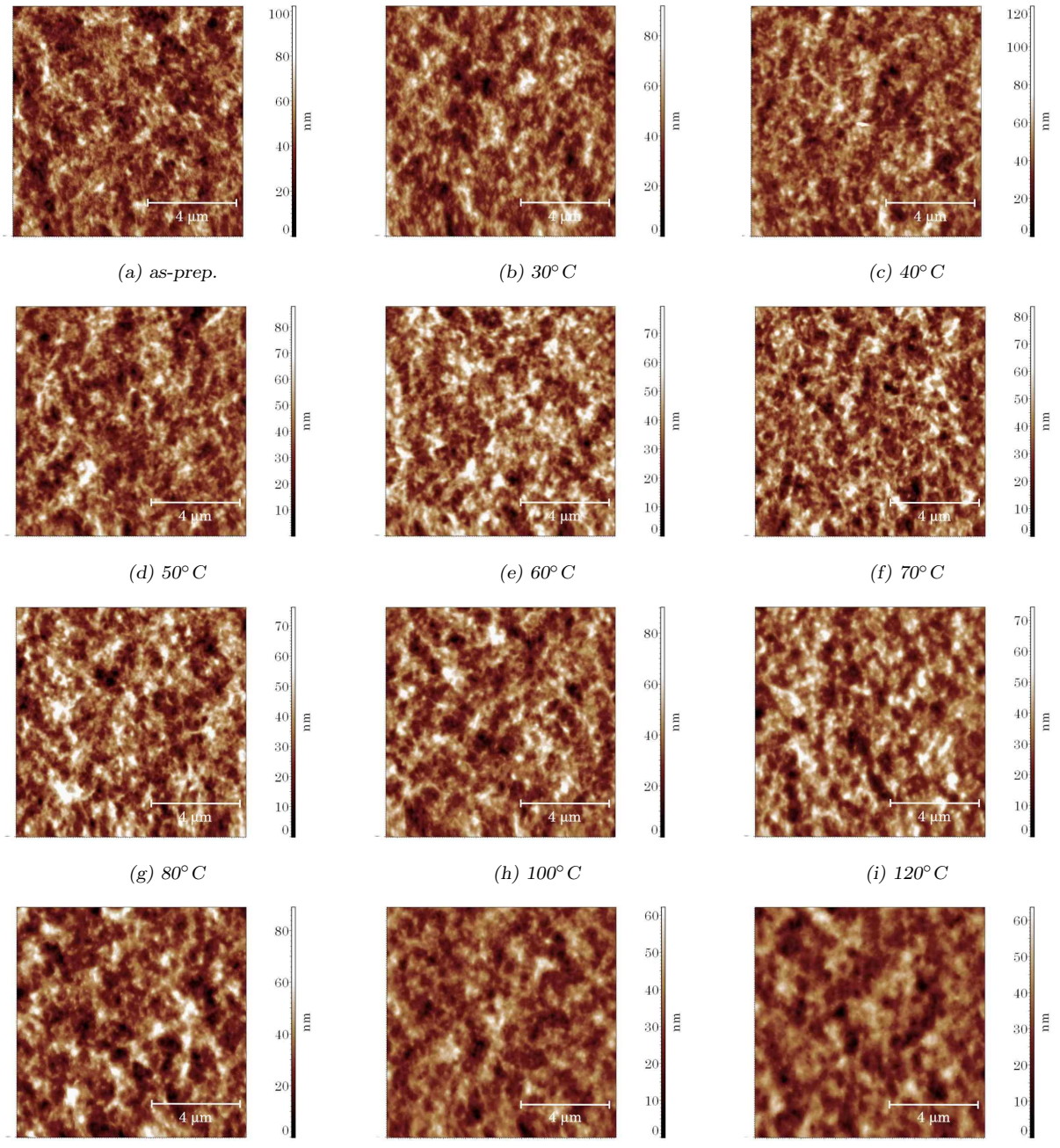

(a) as-prep. (b) 30° C (c) 40° C

(d) 50° C (e) 60° C (f) 70° C

(g) 80° C (h) 100° C (i) 120° C

(j) 140° C (k) 160° C (l) 180° C

Figure S9: AFM images of P3HT:PCBM films cast from DCB on PEDOT:PSS/ITO/glass substrates. Films were thermally annealed at the given temperature for 10 min.

ADVANCED FUNCTIONAL MATERIALS
www.afm-journal.de

Materials Views
www.MaterialsViews.com

FULL PAPER

High-Resolution Near-Field Optical Investigation of Crystalline Domains in Oligomeric PQT-12 Thin Films

Sergei Kuehn, Patrick Pingel, Markus Breusing, Thomas Fischer, Joachim Stumpe, Dieter Neher, and Thomas Elsaesser*

The structure and morphology on different length scales dictate both the electrical and optical properties of organic semiconductor thin films. Using a combination of spectroscopic methods, including scanning near-field optical microscopy, we study the domain structure and packing quality of highly crystalline thin films of oligomeric PQT-12 with 100 nanometer spatial resolution. The pronounced optical anisotropy of these layers measured by polarized light microscopy facilitates the identification of regions with uniform molecular orientation. We find that a hierarchical order on three different length scales exists in these layers, made up of distinct well-ordered dichroic areas at the ten-micrometer-scale, which are sub-divided into domains with different molecular in-plane orientation. These serve as a template for the formation of smaller needle-like crystallites at the layer surface. A high degree of crystalline order is believed to be the cause of the rather high field-effect mobility of these layers of 10^{-3} cm^2 V^{-1} s^{-1}, whereas it is limited by the presence of domain boundaries at macroscopic distances.

1. Introduction

The enormous potential of organic semiconductor materials for the technologically undemanding and low-cost realization of electronic devices has generated a broad interest in the detailed understanding of their physical working principles. Thiophene-containing conjugated molecules have attracted attention because of their relatively high charge-carrier mobility, which is essential, for instance, in organic field-effect transistors (OFETs).[1–5] This class of materials can be generally divided into small, oligomeric molecules (oligothiophenes) and polymers (polythiophenes). Mobilities of 10^{-1} to 1 cm^2 V^{-1} s^{-1} have been reported for evaporated multicrystalline layers of linear α-oligothiophenes.[6–9] Structural studies on these high-mobility samples revealed that the molecules are almost planar (with a very small torsion angle between the thiophene rings) and that the conjugated molecules are oriented perpendicular on the substrate.[7,10–12] This provides pathways for the fast motion of charge carriers in a typical transistor geometry. However, macroscopic charge-carrier transport across the channel of an OFET might ultimately be determined by the presence of grain boundaries. Layers of soluble oligothiophenes, for instance, α-ω-dihexylsexithiophene, processed from solution exhibit lower mobilities of typically around 10^{-2} cm^2 V^{-1} s^{-1}.[13,14] Again, molecules were shown to stand upright on the substrate.[1,12,14,15] The overall poorer performance compared to the evaporated layers has been attributed to imperfections in the chain packing quality, in other words, the formation of less-ordered domains, which arise from the rapid solidification of the dissolved molecules during, for instance, spin coating or doctor blading.

For polythiophenes, high mobilities were reported if the solubilizing chains were attached at the 3-position of the thiophene heterocycles, such as in poly(3-hexylthiophene) (P3HT).[16–30] Naturally, the morphology of polymer layers at the mesoscopic scale is highly complex because of the long contour length (often several tens of nanometers) and the chemical inhomogeneity (polydispersity). In particular, solution-processed layers of P3HT were shown to exhibit domains of planar and fully crystallized chain segments, separated by disordered regions containing mainly chain backfolds and chain ends. It was further proposed that long chains interconnect these crystallites, allowing charges to rapidly bypass disordered regions.[17,20–23,25–31] This model explains the dramatic increase in OFET mobility, from typically 10^{-6} cm^2 V^{-1} s^{-1} to 10^{-2} cm^2 V^{-1} s^{-1} upon a 10-fold increase of molecular weight (from ca. 3 kg mol^{-1} to 30 kg mol^{-1}).[17,19,21,25,30] Within the crystallites, sheets of co-facially stacked conjugated backbones are separated by isolating sheets of alkyl chains. These sheets lie flat on the substrate, with upright-standing side chains and the conjugated chains are oriented parallel to the substrate plane.[17,18,20–23,27–30] This particular arrangement guarantees efficient in-plane transport of charges along and between the conjugated chains within individual crystallites.[18]

Dr. S. Kuehn, M. Breusing, Prof. T. Elsaesser
Max-Born-Institute for Nonlinear Optics
and Short Pulse Spectroscopy
Max-Born-Straße 2A, D-12489 Berlin, Germany
E-mail: skuehn@mbi-berlin.de
P. Pingel, Prof. D. Neher
Institute of Physics and Astronomy
University of Potsdam
Karl-Liebknecht-Straße 24—25, D-14476 Potsdam, Germany
Dr. T. Fischer, PD Dr. J. Stumpe
Fraunhofer Institute for Applied Polymer Research
Geiselbergstraße 69, D-14476 Potsdam, Germany

DOI: 10.1002/adfm.201001978

In general, the morphology of layers processed from solution is highly hierarchical and different processes and interactions determine the order at the nanoscopic or mesoscopic scale. These structural inhomogeneities are seen as a major cause for current performance limitations. On the molecular scale, the conformation of the conjugated segments, the crystal structure and the perfection of molecular packing within the individual crystallites determine the electrical and optical properties, such as optical absorption and luminescence, as well as charge carrier motion, charge separation and recombination, which are fundamental to device operation. On the mesoscopic scale, two major morphological defects have been identified to be detrimental for charge carrier transport: these are grain boundaries between crystalline domains and the presence of extended disordered zones within the pathway of charge flow. Though different in nature, both kinds of morphological defects affect the transport of charges over larger distances in a similar way. The occurrence of these features is highly dependent on the layer preparation conditions and the molecules' chemical structure.[1–3,16,18,19,24,32–34]

Up to now, incomplete knowledge of the heterogeneous morphologies of solution-processed layers render reasoning of structure-mobility relationships extremely difficult. X-ray diffraction has intensively been applied to reveal detailed information about the local packing and molecular orientation of the charge transporting units within the crystalline regions, but this method typically lacks the spatial resolution to investigate the chain packing and orientation at the micro- to nanoscopic scale. Current technological advances, however, promise to fill this deficiency though under highly restrictive experimental conditions.[35,36] Transmission electron microscopy (TEM), on the other hand, is highly suited to image the layer morphology with ultra-high resolution, but this method requires potentially perturbing preparation techniques.[37] In particular, TEM investigations of organic layers on insulating substrates (e.g., the gate insulator) have thus far been impossible to carry out. Atomic force microscopy (AFM) [38] or scanning tunneling microscopy (STM) are restricted to the surface regions of the layer and the information gained from these methods cannot account for the bulk morphology, though these methods are particularly useful for studying phenomena in field-effect devices having a top-gate geometry. In contrast, laterally resolved optical spectroscopy and polarimetry are powerful tools to study the actual film characteristics.

Here, we show the results of a detailed investigation of the morphology of oligo-PQT-12, a short-chain fraction of poly(3,3‴-didodecyl-[2,2′:5′,2″:5″,2‴]-quaterthiophene), PQT-12,[39–45] using spectrally resolved and polarized optical microscopy. By combining conventional, confocal, and scanning probe near-field optical microscopy (SNOM), we obtain detailed information about the chain orientation and the quality of chain packing from the micrometer-scale down to the level of individual crystallites. In particular, the high spatial resolution of SNOM of the order of 100 nm provides new and highly specific insight into the morphology and allows a clear separation of different domains from a structural point of view. Moreover, laterally resolved optical absorption spectroscopy allows us to link information on the quality of crystalline packing and the molecular order with information on topography, domain size, and orientation. We reveal a hierarchy of three different length scales in oligo-PQT-12 films, which is made up of areas at the ten-micrometer scale that are delimited by clear domain boundaries and subdivided into domains with different uniform molecular in-plane orientation with less abrupt transition regions, the counterparts of which can be found in TEM and AFM images. These domains finally host extensions in the form of oriented needle-like crystallites at the layer surface.

2. Results and Discussion

2.1. Chemical Structure and Common Layer Morphology

The chemical structure of oligo-PQT-12 is shown in **Scheme 1**. Details on the synthesis can be found in the literature.[45] In short, our oligo-PQT-12 is a solvent-extracted molecular weight fraction (M_n = 1.65 kg mol^{-1}, M_w = 1.7 kg mol^{-1}, polydispersity index: 1.1) of a polydisperse PQT-12 polymer sample. The use of a quaterthiophene building block as a monomer and the choice of a suitable extraction solvent lead oligo-PQT-12 to consist of mainly quaterthiophene dimers (ca. 85 mol%) and only small traces of the corresponding trimer and tetramer. In contrast to small molecular weight fractions of other polythiophenes, oligo-PQT-12 exhibits a relatively high field-effect mobility of about 10^{-3} cm^2 V^{-1}s^{-1}. AFM and TEM revealed a highly crystalline layer morphology with micrometer-sized, plate-like crystals.[45] The high-quality and anisotropic orientation of these crystals in the layer is documented by the results of X-ray diffraction studies (see Supporting Information, Figure S1).

Figure 1 displays information on the layer morphology of oligo-PQT-12 films obtained with different methods and at different length scales. Topographical AFM images (Figure 1a and b) show tabular sheets decorated with elongated crystalline needles. Interestingly, these needles form distinct regions that have a common, correlated orientation of their long axes. In contrast, TEM bright- and dark-field images (Figure 1c and d) of the same layers mostly display the underlying plate-like crystalline texture with domains on the micrometer scale. Selected-area electron diffraction revealed that these crystals are well ordered.[45] Distinct morphological features can also be observed in conventional optical polarization microscopy (Figure 1e and f). Here, orientation-correlated anisotropy is present on the ten-micrometer scale.

2.2. Far-field Optical Microscopy

Figure 2 shows the results of optical investigation by means of a microscope spectrometer under polarized light. In polythiophenes, the absorption and emission dipoles are essentially

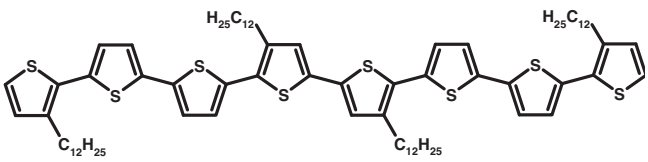

Scheme 1. Chemical structure of oligo-PQT-12.

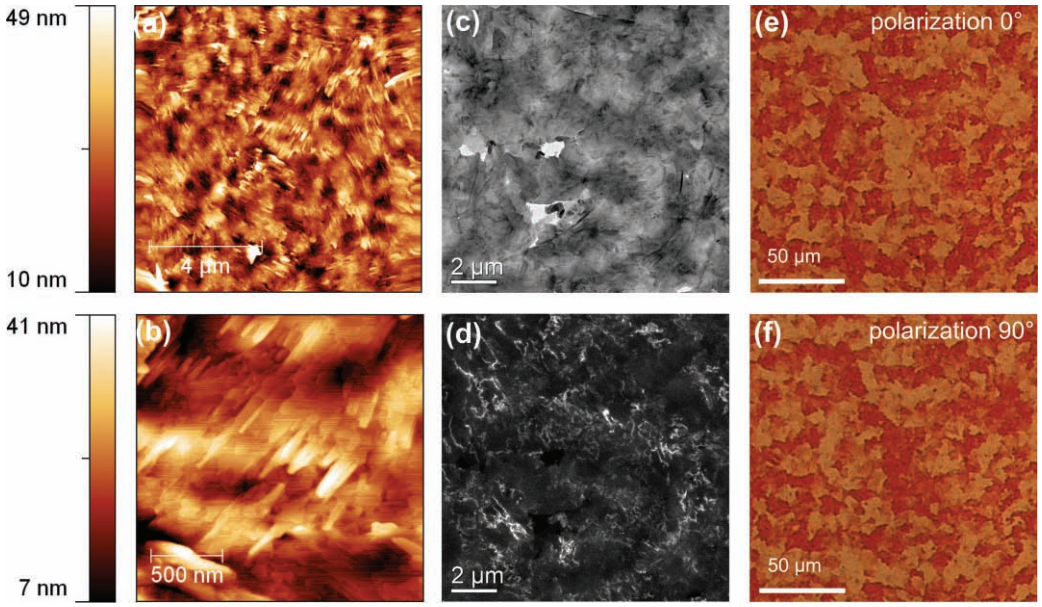

Figure 1. Images of oligo-PQT-12 film: a,b) AFM topography, c) TEM bright-field, d) TEM dark field, e,f) optical polarization microscopy.

oriented along the molecular backbone, with a small perpendicular component that is experimentally insignificant for octathiophene oligomers.[46–48] When illuminated with unpolarized light, the predominant orientation of the molecular axis with respect to the crystal axes causes a relative macroscopic dichroism defined according to:

$$\rho = (I_{max} - I_{min})/(I_{max} + I_{min}) \quad (1)$$

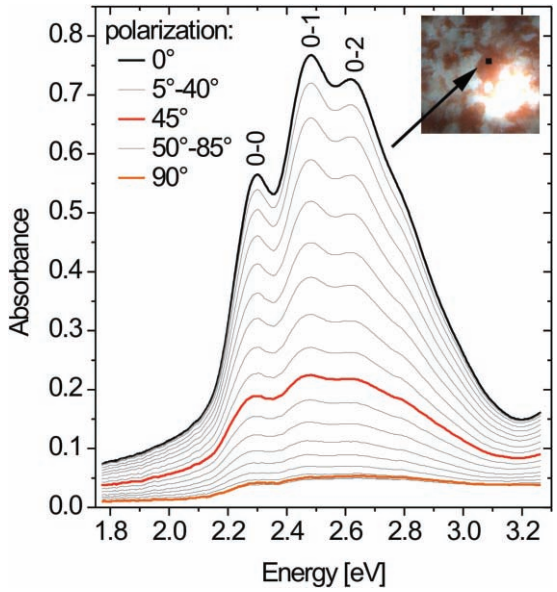

Figure 2. Optical absorption of linearly polarized light of a selected 6 µm × 6 µm oligo-PQT-12 domain (black square in the inset figure) using polarization angles in steps of 5°.

Here, I_{min} and I_{max} denote the extreme values of transmitted intensity when passed through a linear polarizer in front of the detector. For the data displayed in Figure 2 the degree of dichroism amounts to $\rho = 69\%$.

The very high optical anisotropy on the micrometer scale confirms an almost perfect orientation of the oligo-PQT-12 molecules parallel to the substrate. As pointed out above, parallel chain alignment is commonly observed for alkyl-substituted polythiophenes on a passivated surface,[17,18,20–23,27–30] whereas soluble oligothiophenes (with alkyl substituents at the terminal positions) tend to stand upright on the substrate surface.[1,12] Therefore, our oligo-PQT-12 fraction displays the properties of a low-MW polymer but with the field-effect performance and large-area crystallization of a typical oligothiophene.

Interestingly, spectra measured at different positions within an area of 5 µm × 5 µm using a confocal scanning microscope were noticeably different. Comparison with the spatially averaged spectrum shows deviations in the spectral power distribution among the vibronic progression at the high and low energy tails of the spectral envelope. When normalized at ν_{0-1} = 2.5 eV, these deviations can be accounted for by comparing the spectral power in the low-energy (2.18–2.34 eV, LE) and in the high-energy (2.64–2.88 eV, HE) part of the spectra. Increased absorption at lower energies is attributed to planar molecules with higher effective conjugation and therefore to highly ordered areas. Vice versa, an increase in spectral power in the high-energy part is assigned to the presence of chains with large inter-ring torsion, implying less-ordered regions that are rich in packing defects. An absorbance difference map (**Figure 3**a) can be constructed by calculating the difference

$$\Delta\alpha = \langle\alpha\rangle_{HE} - \langle\alpha\rangle_{LE} \quad (2a)$$

of the spectrally averaged absorbances:

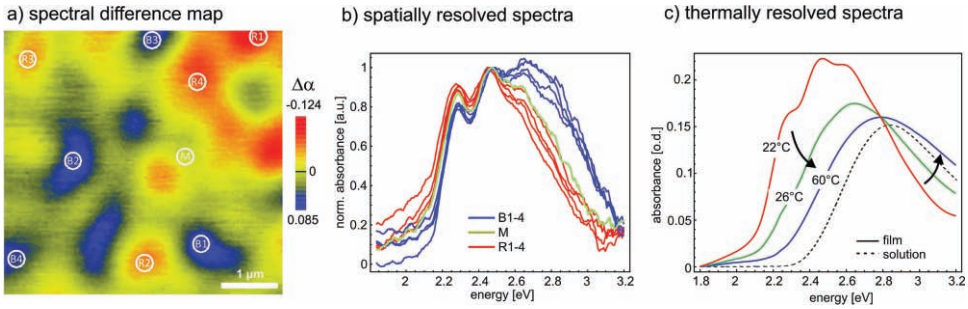

Figure 3. a) Absorption difference map, displaying less-conjugated regions in blue and more-ordered areas in red color. b) Optical absorption spectra at representative positions as marked in (a). c) Absorbance spectra of solid (red), heated (green), and melted (blue) oligo-PQT-12 films (solid lines). The solution spectrum is shown for comparison (dashed line).

$$\langle \alpha \rangle_{\mathrm{LE,HE}} = \frac{1}{\Delta \nu_{\mathrm{LE,HE}}} \int_{\mathrm{LE,HE}} \alpha(\nu) \mathrm{d}\nu \tag{2b}$$

Here, less-ordered and more-ordered regions appear in blue and red color, respectively. Figure 3b shows exemplary spectra at different red (R), yellow (M), and blue (B) positions that are marked in the map. It becomes evident that the molecular order of the film varies on the micrometer scale and that there are regions with different crystalline perfection. The limited spatial resolution, on the order of 500 nm for the confocal images, appears to be insufficient to resolve the true size of order-related domains and at the same time underestimates the true magnitude of the spectral deviations, that is, the degree of molecular order. The two length scales in question – the size of plates and the size of needles – can be accessed using optical near-field scanning probe microscopy.

To obtain quantitative information on the degree of molecular order from the optical absorption spectra we recall that disorder can also be purposefully induced by heating of the film. Eventually, the melted film represents the most disordered, isotropic state in the molecular arrangement. The corresponding optical absorption spectrum is shown in Figure 3c (blue curve, at 60 °C). It is important to note the existence of an isosbestic point, IBP, in the evolution of the temperature-dependent film spectrum from the original film (red curve, at 20 °C). It arises due to the fact that the molar extinction coefficient for all states of the film has the same value at one particular energy ν_{IBP} = 2.77 eV (see Figure 3c and Figure S4 in the Supporting Information). Once an arbitrary spectrum is decomposed into its constituent neat component spectra $\alpha_{\mathrm{c,a}}(\nu)$ (c: crystalline, a: amorphous), the relative amount of each phase can directly be read from the absorbance values $\alpha_{\mathrm{c,a}}(\nu_{\mathrm{IBP}})$ at the IBP. The amount of ordered molecules relative to the total amount of molecules is thus expressed as:

$$\xi = \frac{\alpha_{\mathrm{c}}(\nu_{\mathrm{IBP}})}{\alpha_{\mathrm{c}}(\nu_{\mathrm{IBP}}) + \alpha_{\mathrm{a}}(\nu_{\mathrm{IBP}})} \tag{3}$$

and has the meaning of an *optical order parameter*. Although this relation is typical for two-phase transitions commonly encountered in polymers, the model also applies to the situation where disorder is due to distributed order-related defects within the crystal lattice, which is shown to apply to oligo-PQT-12 films.

2.3. Microcrystal Structure and Morphology

The spectrum of the pristine crystalline phase could not be obtained by conventional methods as to our knowledge bulk single crystals have not been grown for oligo-PQT-12. In order to study the optical properties of the purely crystalline phase we produced a sample that consisted of isolated microcrystals being distinctly distributed across the substrate surface. These samples were prepared by spin-coating from a dilute solution (2 mg mL^{-1}), resulting in relatively large elongated crystallites of several micrometers in length that were several hundred nanometers wide and up to 100 nm high. Details of the oligo-PQT-12 crystallite morphology are shown in the AFM image (**Figure 4**a). The general morphology is polycrystalline with co-aligned daughter crystals frequently originating from a germinating point around the center of the structure (see Figure S3 in the Supporting Information). In some cases crystallites of different orientation grow on top of each other as reflected by a non-uniform topographical height over such structures (e.g., in the top-left region of Figure 4a). The existence of *single* crystals cannot be proven with our current experimental methods. Crystal facets are clearly distinguished, yet there is significant irregularity, particularly at the ends of the crystals where dendritic extensions protrude. Away from the germinating points, unhindered volume reconstruction at room temperature presumably leads to the formation of a well-ordered molecular structure that can be regarded as prototypically crystalline. Spectra recorded at such locations therefore serve as a reference for the crystalline phase in the investigation of continuous oligo-PQT-12 layers.

Local absorption spectra of oligo-PQT-12 microcrystals measured by SNOM are shown in Figure 4b (curve A). Similar to the far-field spectra of the more-ordered regions of oligo-PQT-12 films, they display a vibronic progression with its origin at 2.3 eV. The zero-phonon peak is further suppressed, which might indicate stronger intermolecular interactions within aggregates of improved crystallinity at these spatially selected locations, although this conclusion is controversial (see the report of Spano et al.[49] vs. that of Kim et al.[50]). Absorption spectra measured at different crystals and sites all lay within the gray shaded area in Figure 4b. The data points of a typical spectrum (black dots) are shown along with the average spectrum (black line), which serves as the reference for a structurally well-ordered, crystalline phase. The spectrum of the

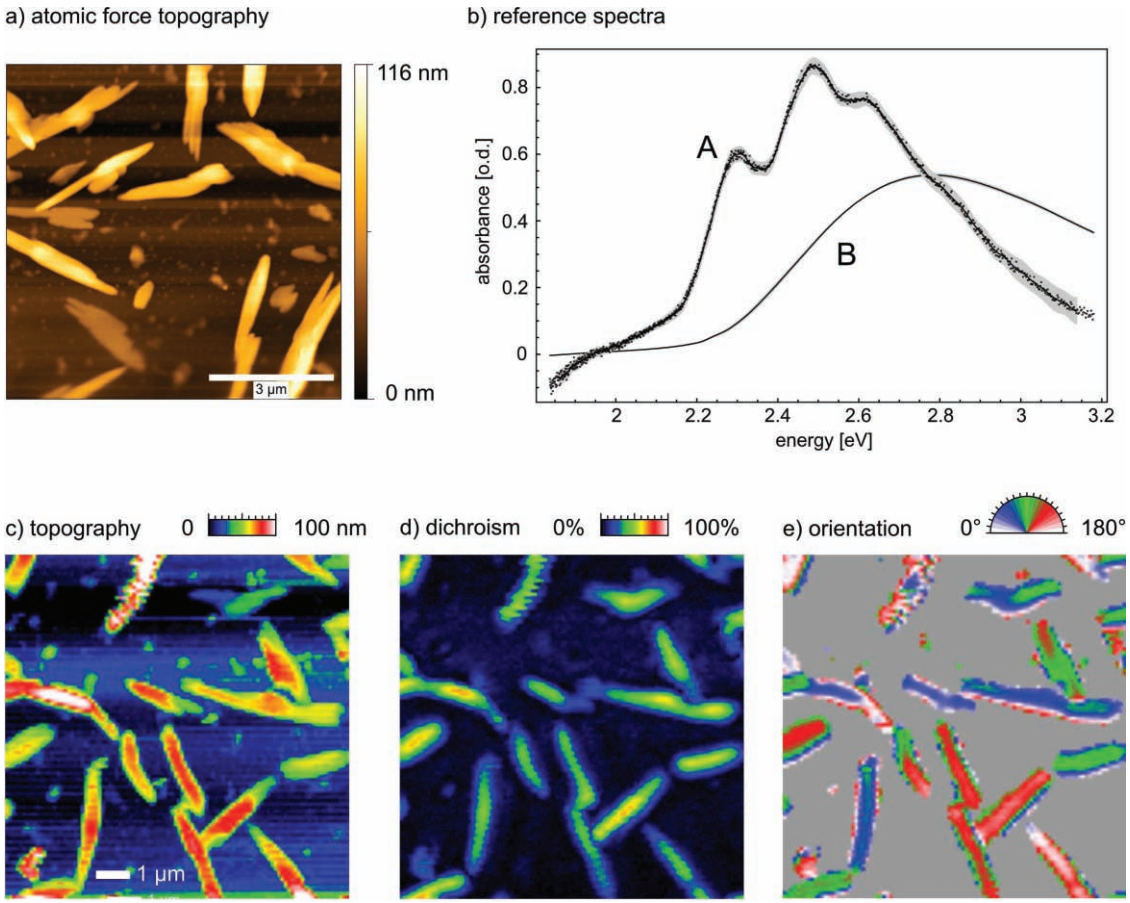

Figure 4. a) AFM topography of microcrystals. b) Reference spectra for the two constituent phases: A) Spectrum of microcrystallites recorded by SNOM, B) spectrum of melted oligo-PQT-12 at 70 °C recorded on a UV–vis spectrometer. c–e) SNOM images of optical properties and topography of oligo-PQT-12 crystallites. c) Topography. d) Degree of linear dichroism ρ at 2.29 eV. e) Molecular orientation from (d).

disordered phase (curve B in Figure 4b) was recorded in the far field on an encapsulated film several hundreds of nanometers thick and heated above 70 °C, well beyond the melting point of oligo-PQT-12, which is around 35 °C (see Figure S4). A lower boundary for the accuracy in the determination of the order parameter is estimated from the variation in the shape of the crystal spectra. The deviations from the mean crystalline spectrum allow for the addition/subtraction of about ± 5% of the spectrum B (normalized at ν_{IBP}).

Figure 4c, d, and e show the topography, the spatially resolved magnitude of the dichroism ρ, and the orientation ϕ, corresponding to the polarization angle under which I_{min} is observed, measured at a photon energy of 2.79 eV using SNOM. The magnitude of the dichroism ranges between 60–90% depending on the crystal height. At the edges of the crystals light scattering leads to depolarization and ρ is poorly defined until it eventually vanishes in the space in-between on the bare substrate. The orientation ϕ remains uniform across each crystal structure which evidences the well-directed alignment of the molecules. (For clarity, ϕ has been made gray in regions of vanishing dichroism.) This strongly suggests a single-type, uniform crystalline order within one microcrystallite and confirms the assignment of the spectrum to a highly crystalline phase of oligo-PQT-12.

The shape of the crystals and the molecular orientation are obviously not linked. Different molecular orientations exist relative to the elongated direction of the microcrystals, without, however, affecting the magnitude of the dichroism. In all cases, the molecular backbone thus retains its in-plane alignment relative to the substrate.

2.4. Thin-Film Structure and Morphology

Having characterized the optical signature of isolated ordered and disordered oligo-PQT-12 phases, we now present our evaluation of the laterally resolved optical spectra on continuous oligo-PQT-12 films. Absorbance spectra measured with SNOM were decomposed into the spectra of the crystalline and disordered phases and the local optical order parameter ξ was determined as described in the preceding section. **Figure 5**a maps the order parameter in a region of 10 µm × 10 µm and Figure 5b gives three representative examples of the fitted spectra at different positions with different compositions. The procedure involved an unbiased least-squares fit of the reference curves with only the two respective weights as free parameters. The confidence interval for the spectral weight estimated from the fit is in the

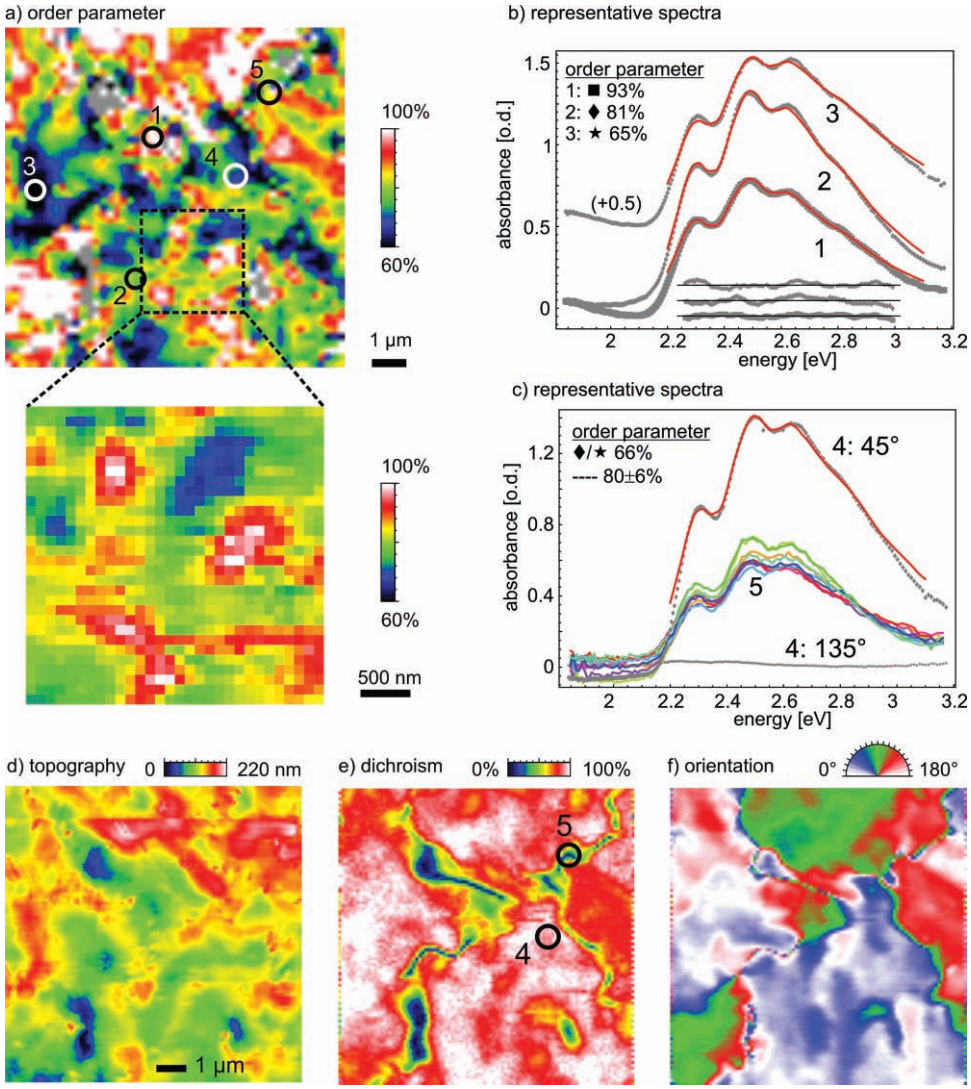

Figure 5. Optical and topographical data of the oligo-PQT-12 film: a) Order parameter ξ determined from the optical spectra: *gray* regions: at film defects (holes are shown in black to blue color in (d)) the absorbance vanishes and spectral fitting fails. Below: Zoom-in with reduced pixel size and extended integration time. b) Example spectra and fits for three locations in (a), including residuals over the fitting range. c) Absorption spectra at two locations in (a/e) and at different polarizations: 4: crystalline region (polarizations with highest, 45°, and lowest, 135°, absorbance), 5: domain boundary (series of spectra for different polarizations in steps of 22.5°). d) Topography. e) Linear dichroism at 2.7 eV. f) Dichroic orientation at the same location as in (a). Cross-sections are shown in the Supporting information (Figure S7).

percent range (<3%, see Figure S5) and the deviation of the fitted curve from the data (residuals) rarely exceeds 5% (see residuals in Figure 5b), meaning that there are no systematic deviations between the model and experimental spectra.

Large variations of ξ from 100% down to 60% on the submicrometer scale are clearly resolved in Figure 5a. The finite lower limit implies that a well-ordered, crystalline material is distributed throughout the entire scan area. This is supported by the well-pronounced vibronic peak structure in each of the sample spectra in Figure 5b regardless of the magnitude of ξ. A portion of the scan (inset in Figure 5a) was repeated with higher resolution (smaller pixel size) and extended integration time to obtain a more detailed picture of the structural morphology of the film. Both the magnitude and spatial distribution of ξ are well reproduced validating the original image. The smallest feature size remains in the range of 300 nm despite the higher resolution of the image. It is conceivable that the actual resolution is set by the thickness of the film rather than by the size of the probe aperture. According to Leviatan the resolution of an aperture-type SNOM starts to deteriorate rapidly at probe-sample separations exceeding the aperture diameter, which in our case is around 100 nm.[51] Although the nominal thickness of the film is around 100 nm partial dewetting and reconstruction may give rise to topographical features up to 200 nm in height and holes down to the substrate.

A critical question in this context is the issue of topographical artifacts which may give rise to an optical signature that is caused by the vertical movement of the tip rather than by the actual

composition of the film material. Our experimental results, however, show that these effects are negligible in our measurements: first, the near-field data are in excellent agreement with the far-field spectra; second, we see virtually no optical signal when the polarization of the analyzer is turned perpendicular to the molecular orientation. As a typical example the spectrum shown in Figure 5c (4) was recorded at polarizations of maximal (4: 45°) and minimal (4: 135°) optical density at location (4) in Figure 5a. It evidences the pronounced dichroism present throughout the entire film except at physical defects and domain boundaries. The vanishing absorbance at one particular polarization means that the experiment truly measures the absorption of the film and parasitic scattering is insignificant in the absorption range.

Location (5) turned out to be of special interest. Here, spectra were recorded for different analyzer settings in steps of 22.5°. The absorbance and the spectral shape remain nearly unaffected (Figure 5c). To obtain a clearer picture, the dichroism and the dichroic orientation were recorded from the same area on the sample at 2.79 eV (IBP). From Figure 5e and f it becomes evident that point (4) is located within a crystal domain whereas point (5) lies on a domain boundary. The sudden change in the polarization direction is accompanied by a line of vanishing dichroism and – depending on the width of the transition region – by a reduction in the structural order. The transition at (5) has a width below 200 nm and is possibly beyond the optical resolution limit of SNOM. The optical order parameter ξ remains at a high level of 80 ± 6%, which is evident for a rather narrow transition region between highly crystalline domains. Bearing in mind the spatial resolution, we conclude that the crystalline domains are close to each other, separated only by a very narrow transition region of disordered material. Also note that the domain boundary (5) does not appear in the topographical image and is only revealed by optical methods.

Throughout large areas of the film, the dichroism remains high varying only between 80–100% depending on the film thickness. Exceptions are only found at physical defects of the film and at grain boundaries, which is in agreement with the changing molecular orientation of Figure 5f. Moreover, the orientation is not strictly constant over an entire domain, but shows continuous variations on the order of tens of degrees on the micrometer length scale (see Figure S6). Such an orientational variety has also been observed in TEM diffraction studies of oligo-PQT-12 films where the diffraction spots are smeared out over small circular segments.[45] The cause for the finite orientational correlation length may – just as the spectral variations – be sought in the structural imperfections of the molecular crystal order affording some flexibility to the in-plane lattice spacing and allowing the crystal axis to bend gently.

To our very surprise, a local correlation between order and dichroism is not very evident (**Figure 6**a). Moreover, we do not observe optical signals that originate from the isotropically oriented material throughout the domains. The molecular orientation is preserved throughout the depth of the film, which rules out the existence of a multilayered film with differently oriented crystalline sheets as a cause for the slow variations in the dichroic orientation. It remains open whether the film consists of contiguous domains at the nanoscale or of an ensemble of closely packed elongated nanocrystallites that are oriented in the same direction. However, the absence of a correlation between the geometry and molecular orientation that we observed in the isolated oligo-PQT-12 crystallites does not support in-depth dichroism. We therefore adopt the hypothesis, that there are different degrees of crystalline order, that is, order-related defect concentrations, in the film rather than a binary mixture of distinct phases co-existing side-by-side.[50]

When the optical order parameter is locally compared to the film thickness, a weak negative correlation of –0.31 (Pearson coefficient, see Figure 6b) can be noted, meaning that thicker film regions appear to be less ordered than thinner ones. Judging by the AFM topography this may indicate that the top portion of the film is less ordered whereas the crystalline material resides at the bottom. This would have implications for the design of OFET devices where it is desirable to obtain the best film quality within the conductive channel close to the gate electrode.

2.5. Thin-Film Global Morphology

We now turn to the third length scale in the morphological hierarchy, the size of the crystalline domains. As the acquisition of absorption spectra with high spatial resolution is rather time-consuming, we restricted the optical analysis to the dichroism at a single photon energy of 2.29 eV. As stated above, the linear dichroism allows the visualization of film defects, domain boundaries, and the molecular orientation. Domain boundaries are regarded as a main impediment to carrier mobility in organic semiconductor films.[52] Their identification is therefore important in order to assess the relationship between the morphology and the device performance. The dichroic orientation is helpful to visualize the crystalline domains and to identify grain boundaries that are often concealed in topography and dichroism maps because of limited resolution and contrast.

The experimental results for a sample area of 30 µm × 30 µm are presented in **Figure 7**. The major part of the sample exhibits a high dichroism of 80–100% (Figure 5a). The domain size ranges from 5 to 20 µm. Although a preferred orientation exists within a domain, there is considerable variation in

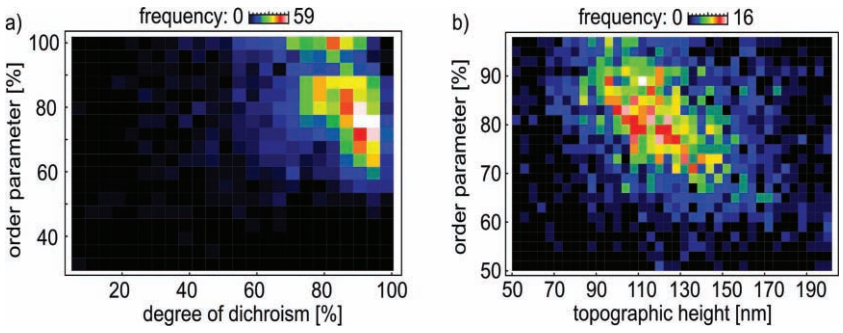

Figure 6. a) Scatter plot of crystalline order ξ against the degree of dichroism (obtained from Figure 5). b) Scatter plot of crystalline order against topographic height. A Pearson correlation coefficient of –0.31 is found.

orientation on the micrometer length scale (see Figure S6). Adjacent domains can have a different or the same dichroic orientation. No globally preferred orientation is evident. Defects and grain boundaries make up roughly 5% of the area of the film. Defects usually are on the sub- to one micrometer length scale and are accompanied by high orientational disorder. The width of grain boundaries is on the order of 100 nm or less.

To date, the conditions that cause the formation of specific film discontinuities have not been investigated. They may be related to the growth mode of the film from several independent seeding sites on the surface, an initial domain structure of the underlying monolayer of silanization molecules, and the hydrodynamics and the dynamics of solvent evaporation during the spin-coating process. Inspection of the dichroic orientation map in Figure 7b and particularly the star-shaped defects shows a striking similarity to liquid crystals although our preliminary experiments showed no evidence that such a phase exists for oligo-PQT-12 films.

3. Conclusions

We have found that spin-coated oligo-PQT-12 films consist of three-dimensional interconnected domains of crystalline material that are several tens of micrometers in size. The crystallinity of the film was estimated by local absorption spectroscopy to be 60–100% within these domains. A pronounced linear dichroism indicates a distinctive molecular orientation that is uncorrelated with the crystallinity. The reduced crystallinity is thus proposed to be caused by disorder on the molecular scale rather than by the co-existence of different phases. On the micrometer scale, this high orientational order is maintained, in particular throughout the depth of the film. Beyond several micrometers, however, the orientational correlation is lost, even when no domain boundaries are crossed. The slight imperfections of the crystal structure afford a liquid-like flexibility in the film morphology whereby hard grain boundaries seem to be avoided. Finally, the increasing crystallinity with decreasing film thickness indicates that close to the supporting substrate the film is more ordered. These two facts may be the cause for the good charge-transport properties observed in OFET devices based on this material.

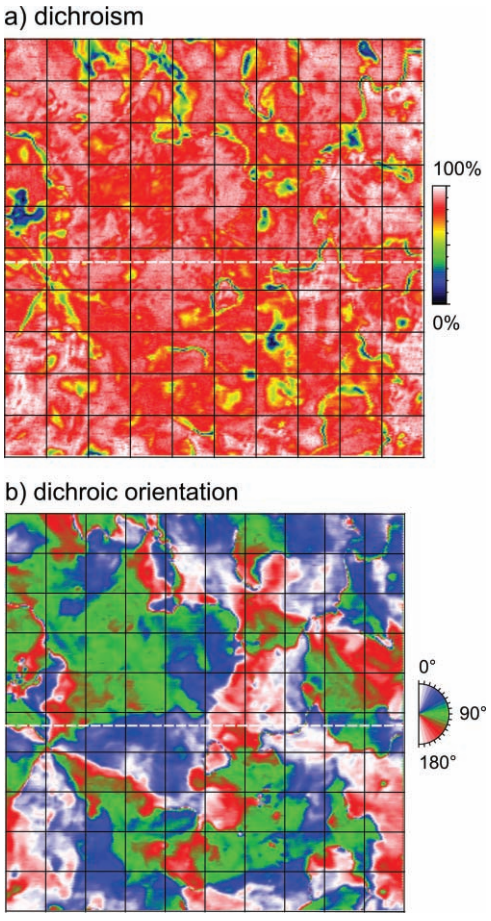

Figure 7. Extended area (30 µm × 30 µm) SNOM images of oligo-PQT-12 at 2.29 eV. a) Degree of polarization for the transmitted light. b) Orientation of the transmitted polarization. For easier navigation grid lines are drawn with a spacing of 3 µm. Cross-sections are shown in Figure S6 of the Supporting Information.

4. Experimental Section

Details on the synthesis, preparation, and characterization of oligo-PQT-12 can be found in the literature.[45] Briefly, PQT-12 films were spin-coated onto hexamethyldisilazane (HMDS)-modified microscope glass slides at 1500 rpm from chloroform solutions at two different concentrations: i) 2 mg mL^{-1}, yielding a film of isolated microcrystals, and ii) 10 mg mL^{-1}, yielding a continuous film of 100 nm mean thickness. The material was processed under a nitrogen atmosphere in a glove box. Although PQT-12 is stable in air,[40] optical measurements were carried out under an oxygen-depleted (<1%) nitrogen purge.

The dichroism within a domain was measured using a microspectrometer (Resultec Inc.) based on an Olympus BX 51 microscope, equipped with a motorized rotating polarization prism placed next to the 75 W Xe arc lamp. The intensity of the transmitted light passing a mirror with a pin hole was measured by an attached diode array spectrometer. The linearly polarized absorbance was calculated from an object scan and a reference scan at a PQT-free place of the sample substrate at every 5° up to 175°. Spatially resolved studies of optical absorption and dichroism were performed with a modified confocal microscope (Olympus, IX 71, 50x, 0.85 NA objective) and a home-built scanning near-field optical microscope (SNOM). The pronounced dichroism of ordered molecular layers requires the control of the polarization state of the light used for the absorption measurement. Although the birefringence of a fiber-based aperture tip can be easily compensated at a *single* wavelength it is illusive to obtain polarization control over a broad spectral range. This applies particularly to supercontinuum light sources.[53] Instead, a Xe arc lamp (75 W, LOT-Oriel) was found to provide sufficiently unpolarized light at the fiber aperture output and at reasonable power levels in the energy range of interest (2.2 to 2.9 eV) (see Figure S2). Variations of the illumination spectrum with polarization are also caused by asymmetries in the tip shape, causing distortions in the absorption spectrum of samples with strong in-plane dichroism.[54] Therefore a polarization analyzer was used to select one specific linear polarization for the absorption measurement. The absorbance at each polarization was calculated using reference spectra recorded at the same polarization in a substrate region free of PQT. The absorption spectra were then decomposed into experimentally determined constituent components in order to obtain the degree of molecular order at each measurement point. The domain structure of the film was revealed by the measurement of the linear dichroism using SNOM with shear-force proximity control. Thus the film structure and morphology were characterized on length scales reaching from one hundred nanometers to tens of micrometers.

Aluminum-coated fiber tips with a nominal aperture diameter of 50–80 nm (VEECO, NSOM 1730–00) were used as received. A HeNe laser of 2.3 eV served as the light source for the measurement of the

dichroic properties of the film. Other individual wavelengths were selected from a photonic-crystal fiber white-light source (NKT Photonics, FemtoWhite-800) pumped by a Ti:sapphire laser (Spectra Physics, Tsunami) using filters, or produced by frequency doubling using a beta-BaB_2O_4 (BBO) crystal (typically 2.79 eV). The birefringence of the fiber at a given wavelength needs to be pre-compensated to obtain a well-defined polarization state at the output of the SNOM probe. Using quarter- and half-wave plates, the input polarization of the fiber was adjusted so that the probe output polarization became circular when observed in a film-free region of the substrate. This adjustment was carried out before and checked after each measurement. As a fast polarization detection scheme we applied a revolving polarizer (analyzer) in the detection path and a phase-sensitive detector locked in the same position as the angle of the polarizer. The transmitted light was detected with an avalanche photodetector (EG&G, SPCM-200 CD 2027). Spectra where recorded on a grating spectrometer (Acton Research, SpectaPro 2500i) equipped with a liquid nitrogen-cooled CCD camera (Roper Scientific, Spec-10 100B/LN).

Supporting Information

Supporting Information is available from the Wiley Online Library or from the author.

Acknowledgements

We are grateful to Dr. Sybille Allard and Prof. Ullrich Scherf, University of Wuppertal, for providing oligo-PQT-12, to Dr. Joerg Grenzer from the Research Center Dresden-Rossendorf for the X-ray investigations, and to Dr. Ingo Lieberwirth from the Max-Planck-Institute for Polymer Research, Mainz, for the electron microscopy measurements.

Received: September 20, 2010
Published online: February 2, 2011

[1] C. Reese, Z. Bao, *Mater. Today* **2007**, *10*, 20.
[2] A. Salleo, *Mater. Today* **2007**, *10*, 38.
[3] H. Sirringhaus, *Adv. Mater.* **2005**, *17*, 2411.
[4] S. Allard, M. Forster, B. Souharce, H. Thiem, U. Scherf, *Angew. Chem. Int. Ed.* **2008**, *47*, 4070.
[5] A. Facchetti, *Mater. Today* **2007**, *10*, 28.
[6] F. Garnier, *Chem. Phys.* **1998**, *227*, 253.
[7] M. Halik, H. Klauk, U. Zschieschang, G. Schmid, S. Ponomarenko, S. Kirchmeyer, W. Weber, *Adv. Mater.* **2003**, *15*, 917.
[8] H. S. Seo, Y. Zhang, Y. S. Jang, J. H. Choi, *Appl. Phys. Lett.* **2008**, *92*, 3.
[9] C. D. Dimitrakopoulos, B. K. Furman, T. Graham, S. Hegde, S. Purushothaman, *Synth. Met.* **1998**, *92*, 47.
[10] F. Garnier, A. Yassar, R. Hajlaoui, G. Horowitz, F. Deloffre, B. Servet, S. Ries, P. Alnot, *J. Am. Chem. Soc.* **1993**, *115*, 8716.
[11] H. E. Katz, Z. Bao, *J. Phys. Chem. B* **2000**, *104*, 671.
[12] P. Leclere, M. Surin, P. Viville, R. Lazzaroni, A. F. M. Kilbinger, O. Henze, W. J. Feast, M. Cavallini, F. Biscarini, A. Schenning, E. W. Meijer, *Chem. Mater.* **2004**, *16*, 4452.
[13] H. E. Katz, J. G. Laquindanum, A. J. Lovinger, *Chem. Mater.* **1998**, *10*, 633.
[14] A. R. Murphy, J. M. J. Frechet, P. Chang, J. Lee, V. Subramanian, *J. Am. Chem. Soc.* **2004**, *126*, 1596.
[15] H. E. Katz, W. Li, A. J. Lovinger, J. Laquindanum, *Synth. Met.* **1999**, *102*, 897.
[16] J. F. Chang, B. Q. Sun, D. W. Breiby, M. M. Nielsen, T. I. Solling, M. Giles, I. McCulloch, H. Sirringhaus, *Chem. Mater.* **2004**, *16*, 4772.
[17] R. J. Kline, M. D. McGehee, E. N. Kadnikova, J. Liu, J. M. J. Frechet, M. F. Toney, *Macromolecules* **2005**, *38*, 3312.
[18] H. Sirringhaus, P. J. Brown, R. H. Friend, M. M. Nielsen, K. Bechgaard, B. M. W. Langeveld-Voss, A. J. H. Spiering, R. A. J. Janssen, E. W. Meijer, P. Herwig, D. M. de Leeuw, *Nature* **1999**, *401*, 685.
[19] A. Zen, D. Neher, K. Silmy, A. Hollander, U. Asawapirom, U. Scherf, *Jpn. J. Appl. Phys. Part 1* **2005**, *44*, 3721.
[20] A. Zen, M. Saphiannikova, D. Neher, J. Grenzer, S. Grigorian, U. Pietsch, U. Asawapirom, S. Janietz, U. Scherf, I. Lieberwirth, G. Wegner, *Macromolecules* **2006**, *39*, 2162.
[21] R. Zhang, B. Li, M. C. Iovu, M. Jeffries-El, G. Sauve, J. Cooper, S. J. Jia, S. Tristram-Nagle, D. M. Smilgies, D. N. Lambeth, R. D. McCullough, T. Kowalewski, *J. Am. Chem. Soc.* **2006**, *128*, 3480.
[22] M. Brinkmann, P. Rannou, *Adv. Funct. Mater.* **2007**, *17*, 101.
[23] M. Brinkmann, P. Rannou, *Macromolecules* **2009**, *42*, 1125.
[24] Z. Bao, A. Dodabalapur, A. J. Lovinger, *Appl. Phys. Lett.* **1996**, *69*, 4108.
[25] R. J. Kline, M. D. McGehee, E. N. Kadnikova, J. S. Liu, J. M. J. Frechet, *Adv. Mater.* **2003**, *15*, 1519.
[26] P. Pingel, A. Zen, R. D. Abellon, F. C. Grozema, L. D. A. Siebbeles, D. Neher, *Adv. Funct. Mater.* **2010**, *20*, 2286.
[27] S. Joshi, S. Grigorian, U. Pietsch, P. Pingel, A. Zen, D. Neher, U. Scherf, *Macromolecules* **2008**, *41*, 6800.
[28] S. Joshi, P. Pingel, S. Grigorian, T. Panzner, U. Pietsch, D. Neher, M. Forster, U. Scherf, *Macromolecules* **2009**, *42*, 4651.
[29] R. J. Kline, M. D. McGehee, M. F. Toney, *Nat. Mater.* **2006**, *5*, 222.
[30] A. Zen, J. Pflaum, S. Hirschmann, W. Zhuang, F. Jaiser, U. Asawapirom, J. P. Rabe, U. Scherf, D. Neher, *Adv. Funct. Mater.* **2004**, *14*, 757.
[31] C. Yang, F. P. Orfino, S. Holdcroft, *Macromolecules* **1996**, *29*, 6510.
[32] D. M. DeLongchamp, B. M. Vogel, Y. Jung, M. C. Gurau, C. A. Richter, O. A. Kirillov, J. Obrzut, D. A. Fischer, S. Sambasivan, L. J. Richter, E. K. Lin, *Chem. Mater.* **2005**, *17*, 5610.
[33] J. A. Merlo, C. D. Frisbie, *J. Polym. Sci. Part B-Polym. Phys.* **2003**, *41*, 2674.
[34] L. A. Majewski, J. W. Kingsley, C. Balocco, A. M. Song, *Appl. Phys. Lett.* **2006**, *88*, 3.
[35] C. Hub, M. Burkhardt, M. Halik, G. Tzvetkov, R. Fink, *J. Mater. Chem.* **2010**, *20*, 4884.
[36] B. Braeuer, A. Virkar, S. C. B. Mannsfeld, D. P. Bernstein, R. Kukreja, K. W. Chou, T. Tyliszczak, Z. Bao, Y. Acremann, *Chem. Mater.* **2010**, *22*, 3693.
[37] X. Zhang, S. D. Hudson, D. M. DeLongchamp, D. J. Gundlach, M. Heeney, I. McCulloch, *Adv. Funct. Mater.* **2010**, *20*, 4098.
[38] V. Kalihari, E. B. Tadmor, G. Haugstad, C. D. Frisbie, *Adv. Mater.* **2008**, *20*, 4033.
[39] M. L. Chabinyc, F. Endicott, B. D. Vogt, D. M. DeLongchamp, E. K. Lin, Y. L. Wu, P. Liu, B. S. Ong, *Appl. Phys. Lett.* **2006**, *88*, 3.
[40] B. S. Ong, Y. Wu, P. Liu, S. Gardner, *J. Am. Chem. Soc.* **2004**, *126*, 3378.
[41] B. Ong, Y. Wu, P. Liu, S. Gardner, *Adv. Mater.* **2005**, *17*, 1141.
[42] A. Salleo, T. W. Chen, A. R. Volkel, Y. Wu, P. Liu, B. S. Ong, R. A. Street, *Phys. Rev. B* **2004**, *70*, 10.
[43] Y. O. Wu, P. Liu, B. S. Ong, T. Srikumar, N. Zhao, G. Botton, S. P. Zhu, *Appl. Phys. Lett.* **2005**, *86*, 3.
[44] N. Zhao, G. A. Botton, S. P. Zhu, A. Duft, B. S. Ong, Y. L. Wu, P. Liu, *Macromolecules* **2004**, *37*, 8307.
[45] P. Pingel, A. Zen, D. Neher, I. Lieberwirth, G. Wegner, S. Allard, U. Scherf, *Appl. Phys. A: Mater. Sci. Processing* **2009**, *95*, 67.
[46] F. C. Spano, *J. Chem. Phys.* **2005**, *122*, 4701.
[47] F. Meinardi, M. Cerminara, A. Sassella, A. Borghesi, P. Spearman, G. Bongiovanni, A. Mura, R. Tubino, *Phys. Rev. Lett.* **2002**, *89*, 7403.
[48] F. Kouki, P. Spearman, P. Valat, G. Horowitz, F. Garnier, *J. Chem. Phys.* **2000**, *113*, 385.
[49] F. C. Spano, *Acc. Chem. Res.* **2010**, *43*, 429.
[50] D. H. Kim, B.-L. Lee, H. Moon, H. M. Kang, E. J. Jeong, J.-I. Park, K.-M. Han, S. Lee, B. W. Yoo, B. W. Koo, J. Y. Kim, W. H. Lee, K. Cho, H. A. Becerril, Z. Bao, *J. Am. Chem. Soc.* **2009**, *131*, 6124.
[51] Y. Leviatan, *J. Appl. Phys.* **1986**, *60*, 1577.
[52] G. Horowitz, M. E. Hajlaoui, *Synth. Met.* **2001**, *122*, 185.
[53] R. Pomraenke, C. Ropers, J. Renard, C. Lienau, I. Lüer, D. Polli, G. Cerullo, *J. Microscopy* **2008**, *229*, 197.
[54] M. Savoini, P. Biagioni, G. Lakhwani, S. C. J. Meskers, L. Duò, M. Finazzi, *Opt. Lett.* **2009**, *34*, 3571.

Submitted to ADVANCED FUNCTIONAL MATERIALS

Supporting Information

for

High-resolution near-field optical investigation of crystalline domains in oligomeric PQT-12 thin films

Sergei Kuehn[1*], Patrick Pingel[2], Markus Breusing[1], Thomas Fischer[3], Joachim Stumpe[3], Dieter Neher[2] Thomas Elsaesser[1]

[1] Max-Born-Institute for Nonlinear Optics and Short Pulse Spectroscopy, Max-Born-Strasse 2A, D-12489 Berlin (Germany)

[2] Institute of Physics and Astronomy, University of Potsdam, Karl-Liebknecht-Straße 24-25, 14476 Potsdam (Germany)

[3] Fraunhofer Institute for Applied Polymer Research, Geiselbergstraße 69, D-14476 Potsdam (Germany)

[*]Corresponding author. E-mail: skuehn@mbi-berlin.de

Submitted to ADVANCED FUNCTIONAL MATERIALS

1. X-ray diffraction measurements of oligo-PQT-12 powder and thin films

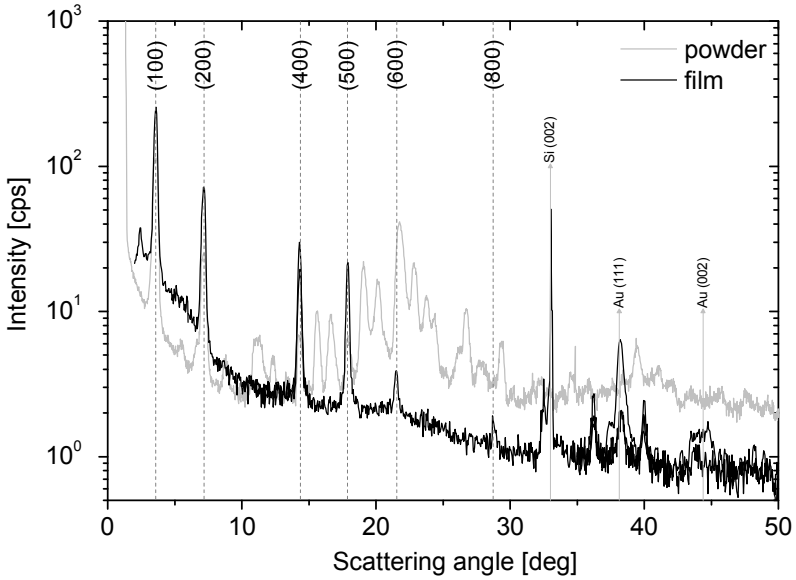

Figure S1. X-ray diffraction measurement of oligo-PQT-12 powder and thin film.

The high crystallinity of oligo-PQT-12 is confirmed by X-ray diffraction measurements of powder and thin film (Figure S1). A number of distinct peaks are present for the oligo-PQT-12 powder which are, however, still insufficient to confidently deduce the crystal structure. Most importantly, in the thin film only one peak family is exhibited in X-ray reflection, meaning that the oligo-PQT-12 film is preferentially oriented. The associated lattice constant is ca. 2.5 nm, which can be related to the intermolecular stacking distance. Note that for the high-molecular weight PQT-12 polymer slightly smaller interchain distances have been reported (B.S. Ong et al., *J. Am. Chem. Soc.* **2004**, 126, 3378; B.S Ong et al., *Adv. Mater.* **2005**, 17, 1141), which indicates distinct differences in the molecular packing of oligomeric and macromolecular PQT-12, similar to what has been shown for poly(3-alkylthiophene)s.

Submitted to ADVANCED FUNCTIONAL MATERIALS

2. Excitation spectrum at the fiber tip

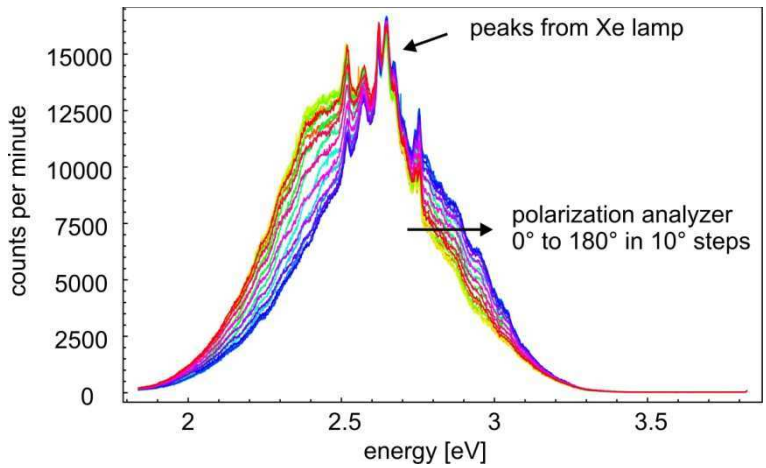

Figure S2: Spectrum transmitted through the SNOM tip recorded with a linear polarization filter in the detection path for different angular settings.

The spectrum of a high pressure Xe arc lamp is rather flat in the near IR to the UV (1.4 ~ 4.1 eV) region. However, the limited transmission of the single-mode fiber and the characteristics of the aperture strongly limit the usable region due to cutoff, high-loss and absorption effects. Moreover, the precise shape of the fiber taper and the aperture introduce an axial isotropy to the transmitted spectrum. The magnitude of the variation is shown in Figure S2 for different polarization angles which have been selected using an analyzer-filter just after the objective lens of the microscope. It is clearly seen, that the weight of the spectrum wanders between 2.5 and 2.7 eV for angles 0-90°. Now, let us assume that a molecule has an absorption spectrum that is flat over the entire spectral range. If the molecule is aligned at 0° it will predominantly be excited by the red portion of the spectrum while the blue component, which is orthogonal to the molecular dipole axis, will pass unattenuted. The absorption spectrum, if measured unpolarized, will thus have an excessive red weight. Such a distortion is avoided by the selection of a single specific polarization for the absorption measurement in witch case the projection of the excitation spectrum onto the molecular orientation is equal for all selected wavelengths.

Submitted to ADVANCED FUNCTIONAL MATERIALS

When experimenting with coherent light from a photonic crystal white-light source, the full rotation of the polarization occurred on the scale of 11 nm in the spectrum of the fiber output (depending on the stress-induced birefringence of the SNOM fiber). This makes such light sources unusable for absorption measurement of highly anisotropic material.

3. Formation and reconstruction of oligo-PQT-12 microcrystals

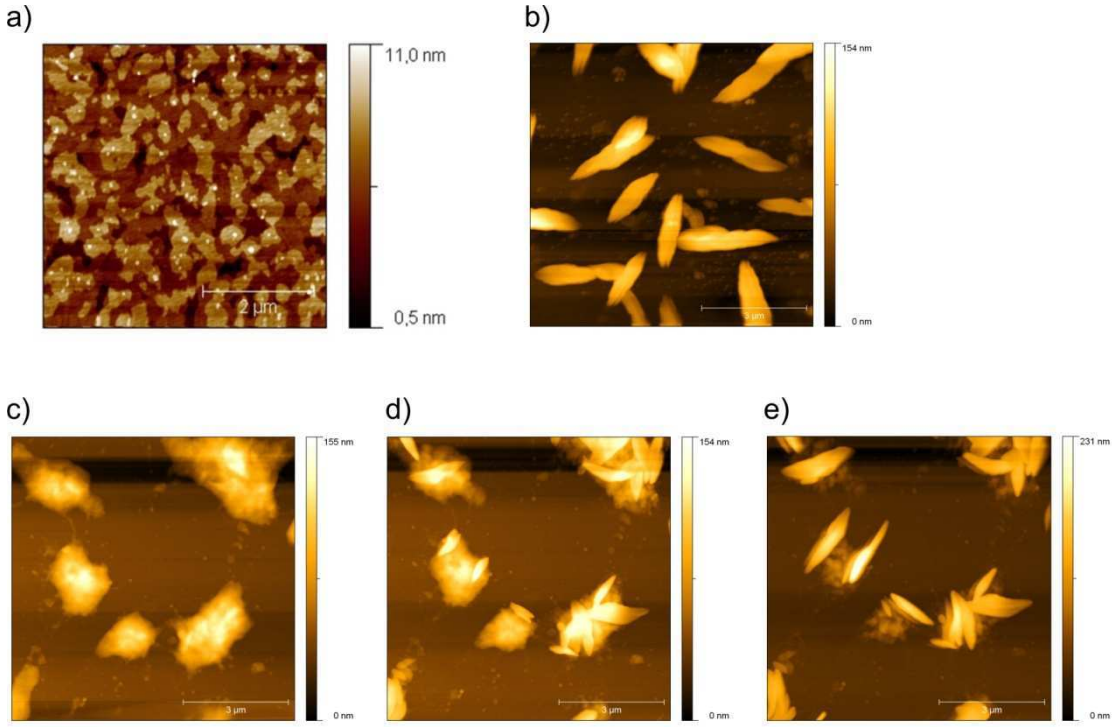

Figure S3: AFM topography of spin-coated c-PQT-12 films. a) as cast, b) after storage under nitrogen for several weeks, c) sample (b) after 1 hour annealing at 110 °C under ambient atmosphere and subsequent shock-freezing in liquid nitrogen, d) crystal formation after 17 hours under nitrogen atmosphere at room temperature, e) same after 36 hours.

Thin films of PQT-12 do not appear to be physically stable below a certain thickness threshold under ambient conditions. A semi-continuous film with an average height below 10 nm as shown in Figure S3a will reorganize into a system of microcrystallites in a period of days to weeks. The result of the ripening process is shown in Figure S3b. By heat treatment (here: for 1 hour at 110°C under ambient conditions), the facetted crystals can be partly melted into rather shapeless droplets (Figure S3c). These will act as germinating sites for the growth of new microcrystallites. For the same site, we followed the formation of such crystals

Submitted to ADVANCED FUNCTIONAL MATERIALS

by AFM over the course of two days. Figure S3d and e show the development of new crystallites after 17 and 36 hours in a dry, nitrogen-rich atmosphere (less than 0.1% oxygen) at room temperature. Due to the high mobility of oligo-PQT-12 molecules on the substrate it is expected that the newly formed crystallites are highly ordered. At the original locations of the amorphous droplets, i.e. the germination points, a portion of the material will remain in a disordered state. Thus, spectra of the crystalline phase were preferably recorded close to the extremities of the crystallites.

4. Thermal cycling of oligo-PQT-12 thick film

To obtain the spectral signature of the amorphous phase measurements were carried out on heated oligo-PQT-12 films. Annealing cycles on exposed films can lead to complete, irreversible dewetting of the substrate at temperatures above 60 °C. To prevent such irreversible modifications of the samples, the films were encapsulated between two glasses slides and sealed from the sides with epoxy glue. The samples were subsequently heated by electrical resistors and the temperature was recorded at each spectrometer exposure using a calibrated platinum resistor glued to the sample. Visible in Figure S4 is a sensitive spectral reaction even at slightly elevated temperatures. Diminishing absorption at the red edge of the spectrum is concomitant with a rise in the blue region around 3 eV. The well resolved vibronic features also gradually smoothen out and are no longer recognized in the heated state due to increasing heterogeneity in the molecular conformation. The asymptotic spectrum is assumed above and below 40°C and 30°C during melting and solidification, respectively, considerably lower than the 120-140°C have been reported for the octa- to decamer of PQT-12. We explain the lowered melting temperature by the lowered enthalpy of fusion for the dimer, where the number of π-π interacting thiophen rings per molecule is four to five times lower. The shape of the melted phase spectrum is similar to the solution spectrum.

Considering the observations on oligo-PQT-12 microcrystals it is likely that reconstruction proceeds even after cool-down. In this respect it may be inaccurate to associate a specific state of the film with the instantaneous substrate temperature on the time-scale of minutes.

Annealing cycles did not improve the field-effect mobility of oligo-PQT-12 OFET devices as has been reported for the longer oligomers. This supports the high crystalline quality of our as-spun films.

Submitted to ADVANCED FUNCTIONAL MATERIALS

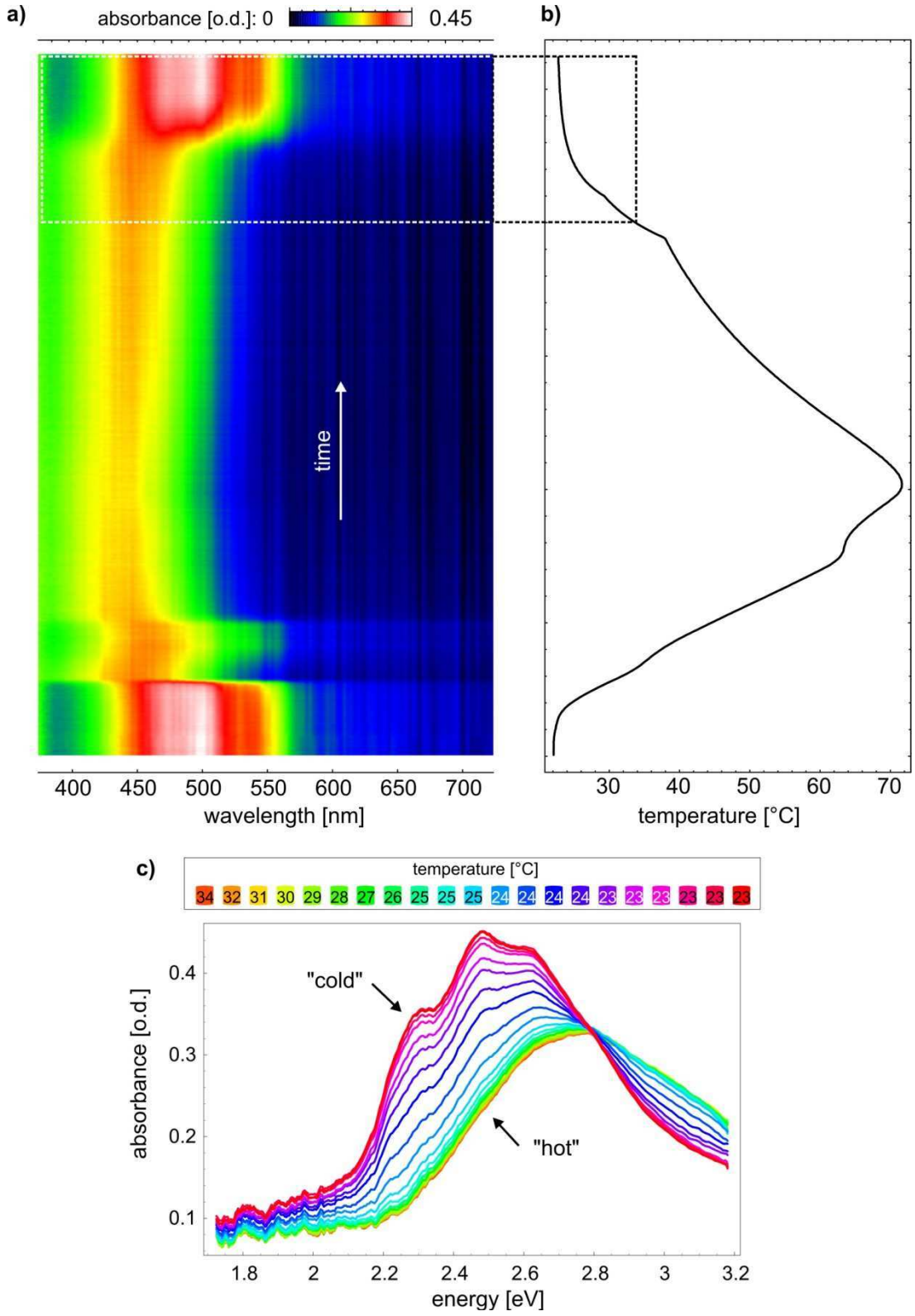

Figure S4: Temperature dependent absorption spectrum of f-PQT-12. a) Absorption spectra (in nm), b) Corresponding film temperature, c) Spectral evolution during cooling from the melted to solid state (as indicated by the broken line rectangle in a-b).

Submitted to ADVANCED FUNCTIONAL MATERIALS

5. Accuracy in the determination of the crystallinity

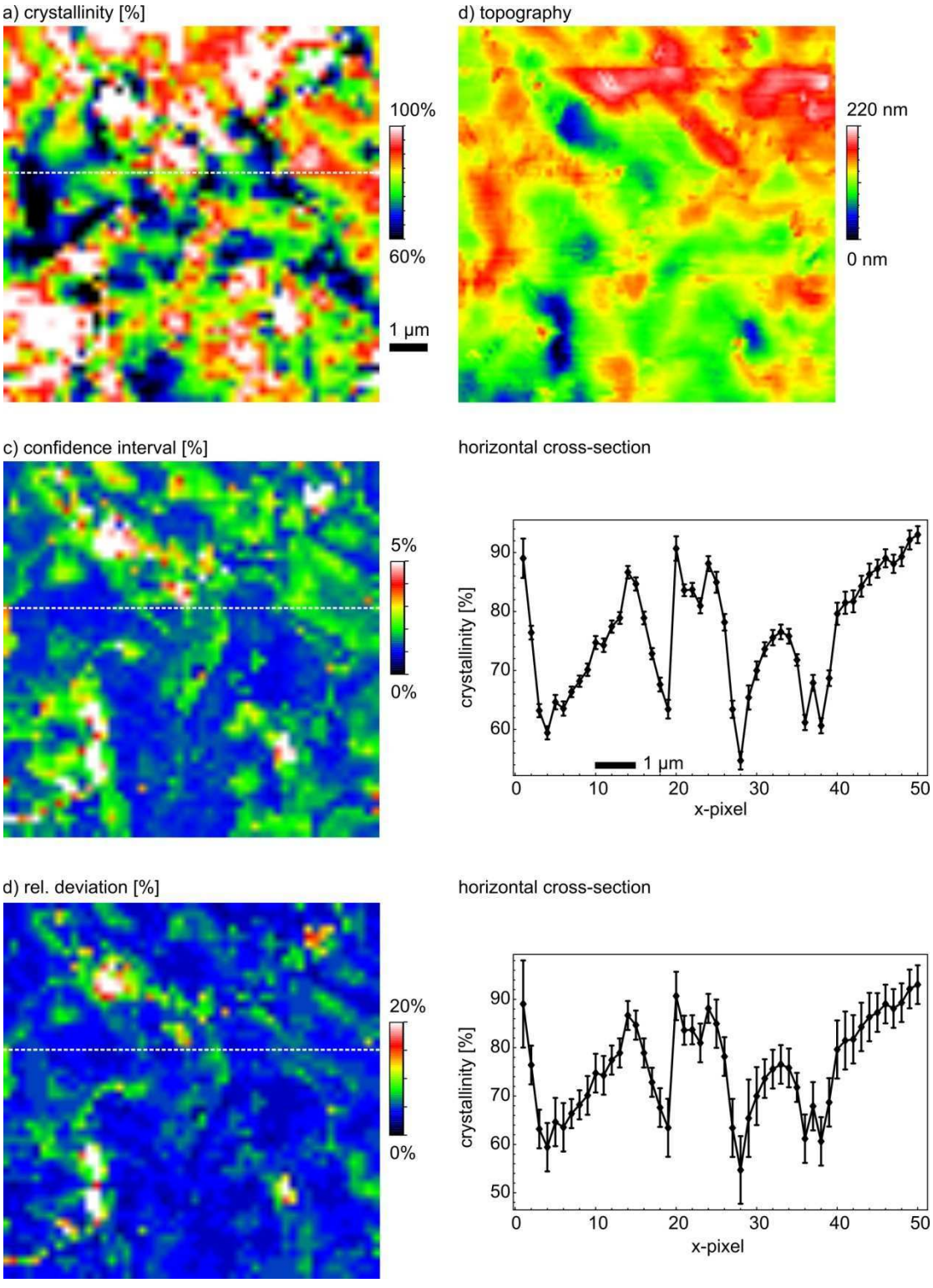

Figure S5: a) Map of the crystallinity and b) topography (as in main text). c) Estimated confidence interval of the two-component fit. d) Mean relative deviation (fit residual) in the fitting energy range.

Submitted to ADVANCED FUNCTIONAL MATERIALS

The accuracy to which ξ can be determined is limited by the spectral overlap, the confidence in the absorption measurement itself, and in the reference spectra (M. Otto, W. Wegscheider. *Analytical Chemistry* **1985**, *57*, 1 63). For an energy interval for analysis between 2.2 and 3 eV, a condition number of 4.2 is determined. This means that - as an upper boundary - the relative uncertainty in the absorbance will translate into a 4.2-fold relative uncertainty in the predicted concentrations. A compromise between integration time, resolution and acquisition time limits the accuracy of the component assignment to approximately 15% as estimated from the noise of the absorbance measurement and the condition number. Since the concentrations here are determined by numerically fitting the reference curves A and B (as opposed to independent measurements at all individual wavelengths of the spectrum), we expect a somewhat better performance due to noise cancellation (L. Antonov, D. Nedeltcheva. *Chemical Society Reviews* **2000**, *29*, 3 217).

The success of the spectral decomposition is decided from two factors: the quality of the fit and the deviations from the model. The former depends on the inter-dependence of the fitted parameters, the second on distortions and artifacts in the absorption measurement and the presence of impurites, i.e. PQT-12 oligomers of different length or other molecules. Both are, of course sensitive to measurement noise. Figure S5c shows the map of the confidence interval for the crystallinity fit associated with the crystallinity map in (S5a). Over most of the area the value is found within the range of 1-3%. Larger deviations (see topography S5b) only occur around film defects due to the vanishing absorption signal. The same holds for the relative deviations from the two-component model. Here, in Figure S5d the ratio of mean absorbance residuals to the absolute mean absorbance due to measurement noise is mostly found to lie below 5 %, except for film defects. From the maps and cross-sections it is evident that the accuracy is well adequate to reproduce the variations of the crystallinity in the film.

Submitted to ADVANCED FUNCTIONAL MATERIALS

6. Cross-sectional cuts of optical and topographical images of oligo-PQT-12 thin film

For clarity, Figure S6 shows cross-sectional cuts for the maps of the dichroism and the dichroic orientation of Figure 6 in the main text. Grain boundaries are clearly resolved by drops in the dichroism and jumps in the orientation, at x-positions about 3, 22 and 24 µm. The gradual change of the molecular orientation in the region 7-18 µm is significant and amounts to 90°. It therefore appears that the notion of clearly defined grains does not strictly apply. The morphology is rather floating, yet clear breaks do also exist.

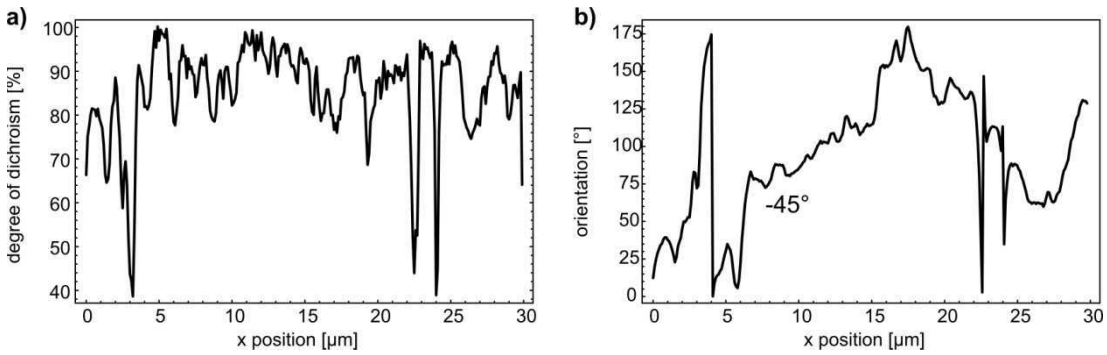

Figure S6: Cross-sectional horizontal cuts from along a line 1 µm below the center of the scans in Figure 7 of the main text. a) Dichroism, b) Orientation. (The orientation has been offset by -45° to avoid breaks due to angular ambiguity at 180°.)

At this point it should be noted that the relative dichrosim, in general, cannot indicate the presence of an isotropically oriented absorbing phase since it only depends on the thickness of the anisotropic, uniaxial phase (see eqn. 2 in the main text). However, because the absorbance vanishes at a particular polarization at all locations with high dichroism regardless of crystallinity the conclusions still hold. It is possible to obtain ξ from the data of $I_{min/max/mean}$ under the condition that the disorderd phase is isotropic. But this is not fulfilled in the present case. In short, we do not observe an optical signal that originates from isotropically oriented material throughout domains. It can also be concluded, that the molecular orientation is preserved throughout the *depth* of the film which rules out the existence of a multilayerd film with differently oriented crystalline sheets as a cause for the variable dichroic orientation.

Submitted to ADVANCED FUNCTIONAL MATERIALS

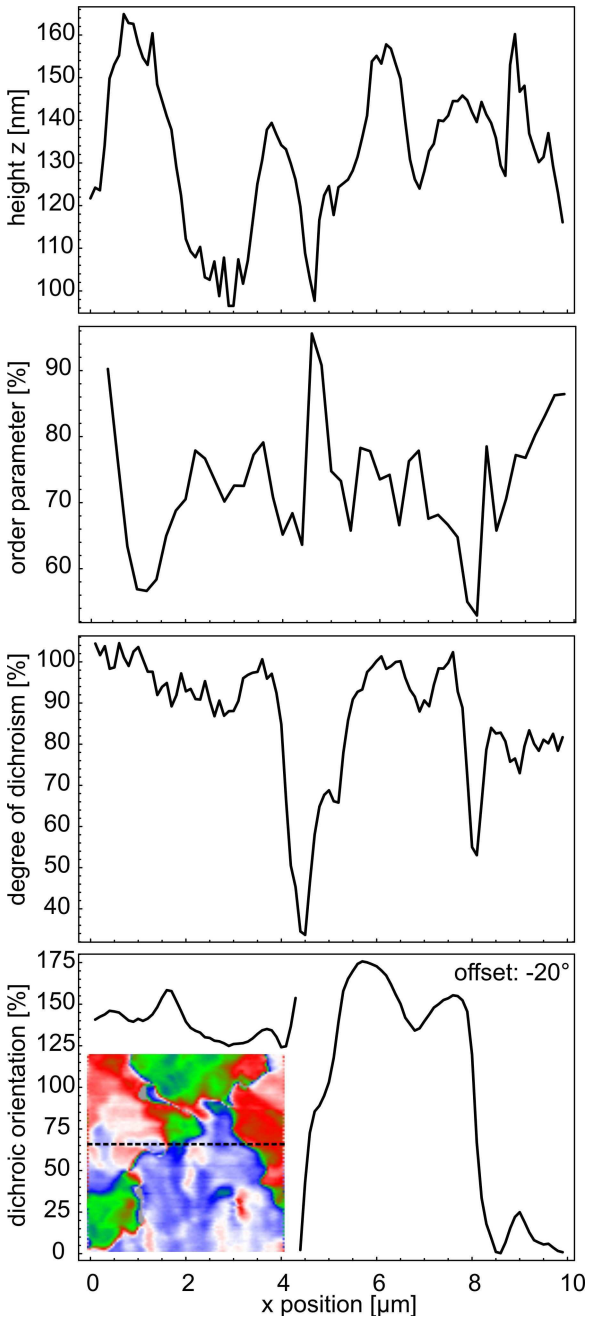

Figure S7: Cross-sectional horizontal cuts through images of Figure 5 in the main text along a line as indicated in the inset.

APPLIED PHYSICS LETTERS **100**, 143303 (2012)

Effect of molecular p-doping on hole density and mobility in poly(3-hexylthiophene)

P. Pingel, R. Schwarzl, and D. Neher[a)]
Soft Matter Physics, Institute of Physics and Astronomy, University of Potsdam, Karl-Liebknecht-Str. 24-25, D–14476 Potsdam, Germany

(Received 10 February 2012; accepted 16 March 2012; published online 6 April 2012)

Employing impedance spectroscopy, we have studied the hole density, conductivity, and mobility of poly(3-hexylthiophene), P3HT, doped with the strong molecular acceptor tetrafluorotetracyanoquinodimethane, F_4TCNQ. We find that the hole density increases linearly with the F_4TCNQ concentration. Furthermore, the hole mobility is decreased upon doping at low-to-medium doping level, which is rationalized by an analytic model of carrier mobility in doped organic semiconductors [V. I. Arkhipov, E. V. Emelianova, P. Heremans, and H. Bässler, Phys. Rev. B **72**, 235202 (2005)]. We infer that the presence of ionized F_4TCNQ molecules in the P3HT layer increases energetic disorder, which diminishes the carrier mobility. © *2012 American Institute of Physics*. [http://dx.doi.org/10.1063/1.3701729]

Molecular doping, in particular p-doping with the strong acceptor tetrafluorotetracyanoquinodimethane, F_4TCNQ, has been widely applied to soluble and insoluble organic semiconductors in attempting to advance organic electronic devices. For instance, an improvement of the efficiency of small-molecule organic light emitting diodes has been achieved by incorporating doped layers in proximity to the electrical contacts.[1,2] Molecular doping has also been employed on polymer field-effect transistors, where an improvement of the charge carrier mobility was attributed to the filling of deep traps in the channel region by doping-induced charge carriers.[3–6]

F_4TCNQ-doping has been shown to be applicable to a variety of hole-transporting polymers.[7] Apart from the generally observed increase of conductivity, systematic studies of the doping mechanism and how it affects charge carrier density and transport in the bulk of doped polymer layers are, however, rare. The electrical properties of F_4TCNQ-doped poly(2-methoxy-5-(2′-ethylhexyloxy)-p-phenylene vinylene), MEH-PPV, layers have been studied by Zhang *et al.* Based on the modelling of unipolar *I-V* characteristics, they found that only a small fraction of the applied F_4TCNQ dopants is active in creating free holes in the polymer layer.[8] Moreover, the ionization of the F_4TCNQ dopants was reported to depend on the electric field and temperature.[9] These findings are in accordance with reports on the nature of the charge transfer in F_4TCNQ-doped polythiophenes and small hole-transporting molecules:[10–13] It has been suggested that the donor-acceptor interaction leads to a bound charge transfer (CT) state between F_4TCNQ and the donor site. In these complexes, supramolecular orbitals are formed as a result of hybridization of the acceptor's lowest unoccupied molecular orbital (LUMO) and the donor's highest occupied molecular orbital (HOMO). The band gap of the CT complex is significantly reduced when compared to those of the isolated donor and acceptor components, and the generation of free charges probably involves excitation into the energetically deep-lying LUMO of the complexes.

As a point of criticism, the aforementioned electrical studies neglect the effect that ionized dopant molecules supposedly have on the charge transport in doped polymer layers. Arkhipov *et al.* modeled the motion of free charge carriers within doped disordered media.[14,15] They have pointed out that the ionized dopants act as long-range trapping centers owing to the Coulomb attraction of mobile charge carriers. Effectively, this leads to a broadening of the density-of-states (DOS) distribution, which might cause a reduction of mobility at low-to-moderate doping concentrations. This prediction is in contrast to the usual presumption that the mobility is increased upon doping due to the filling of traps by doping-induced charge carriers. Interestingly, a decrease of mobility upon molecular doping has never been experimentally observed.

In the present Letter, we independently determine the hole density and low-field bulk conductivity of F_4TCNQ-p-doped P3HT layers at low to moderate doping concentration. For that, we employ admittance spectroscopy to a metal–insulator–semiconductor (MIS) structure as depicted in the inset of Fig. 1(b). The samples were prepared on glass substrates with a patterned indium-tin-oxide (ITO) electrode. On top of that, we spin-cast a methyl-/phenyl-substituted polysilsesquioxane (PSQ) solution that was rendered insoluble after heat treatment. Continuing in N_2 atmosphere, the F_4TCNQ-doped or undoped P3HT was spin-cast from chloroform solution, yielding a layer thickness in the range of 0.35 to 1.2 μm. The devices were completed by evaporation of 5 nm MoO_3 and 100 nm Al, followed by encapsulation using a glass sheet and an epoxy resin. Device stability without noticeable change in the measurement results has been maintained for at least one week. Details of the sample preparation and experimental setup can be found in the supplementary information.[16]

From the complex admittance, $Y = G_p + i\omega C_p$, we extract the parallel capacitance C_p and the loss G_p/ω. Fig. 1 shows exemplary C_p–DC bias curves and the loss spectra of

[a)]Electronic mail: neher@uni-potsdam.de.

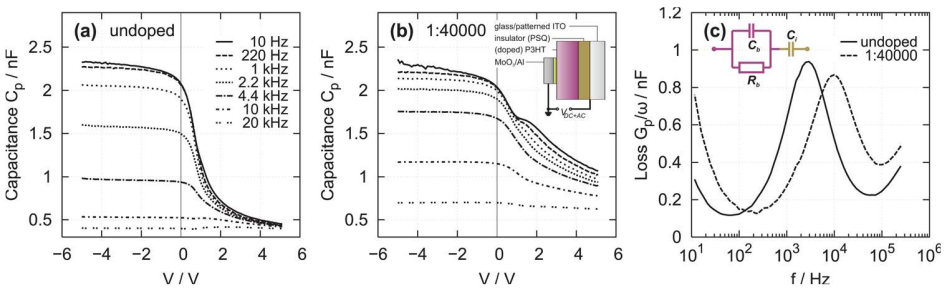

FIG. 1. Capacitance vs. DC bias of (a) undoped and (b) 1:40 000-doped MEH-PPV MIS samples. The inset depicts the MIS sample structure. (c) shows the corresponding loss spectra and the equivalent circuit in accumulation (at −5 V DC bias).

undoped and 1:40 000 F_4TCNQ-doped P3HT MIS samples. Note that a doping ratio χ of 1:40 000, or equivalently 2.5×10^{-5}, refers to the addition of 1 F_4TCNQ molecule per 40 000 thiophene repeat units of P3HT. At low frequency and negative bias, the devices exhibit the capacitance of the insulator layer C_i due to the accumulation of holes. Sweeping to positive bias, C_p drops as the semiconductor is depleted. From that region, we determine the hole density p following standard MIS theory.[17] Hence,

$$p = \frac{2}{e\varepsilon_0\varepsilon_r A^2 \frac{\partial C_p^{-2}}{\partial V}}, \tag{1}$$

where A is the active area of the device and $\varepsilon_r = 3.5$ is the dielectric constant of P3HT. The capacitance drop of the 1:40 000-doped sample shows a shoulder at low frequencies ($f = 10$ Hz). This is typical of an inversion layer at the insulator interface, whose charging/decharging dynamics are slower than the cycles of the applied AC voltage, and whose capacitance contribution is therefore less than C_i.[17] The coincidence of depletion and inversion features renders the evaluation of the hole density difficult. In order to determine p most reliably in these layers, we evaluate the C_p–V curve at a frequency at which the inversion feature is minimized and C_i is still retained at accumulation bias. This was possible up to dopant concentrations of 10^{-4}.

At higher frequencies, C_p is reduced towards the geometrical capacitance even at negative DC bias, because charging and discharging inside the device cannot keep track with the applied AC voltage. Concomitantly, this leads to a peak in the loss spectrum, which is related to the conductivity of the bulk semiconductor layer. Applying the equivalent circuit shown in Fig. 1(c), the characteristic frequency is given by $f_p = [2\pi R_b(C_i + C_b)]^{-1}$ in accumulation, i.e., at highly negative bias, with C_b being the bulk layer capacitance. Knowing the geometric dimensions of the semiconductor layer, the bulk conductivity can be calculated according to

$$\sigma = 2\pi f_p (C_i + C_b)\frac{d}{A}, \tag{2}$$

where d is the semiconductor layer thickness. Note that σ is the conductivity at very low field where bulk transport is governed by intrinsic charges. Applying an AC signal of $V_{rms} = 20$ mV, the rms electric field in the bulk layer typically amounts to $F \sim 2 \times 10^4$ V/m.

The hole density and bulk conductivity determined in this manner are shown in Fig. 2. A significant increase of the hole density is seen at doping ratios χ exceeding 10^{-6}. The data can be well described by a linear function of the form $p = D\chi + p_0$, considering a background density of $p_0 = 1.2 \times 10^{21}$ m^{-3} and a slope parameter of $D = 2.0 \times 10^{26}$ m^{-3}.

From that we conclude first that the amount of doping-induced holes is increasing linearly with the concentration of dopants. This is in accordance with our previous finding that CT complexes between F_4TCNQ and P3HT are highly localized and, thus, do not interact even if they are located on the same P3HT chain at very high doping densities.[10] Note that linear dependencies between hole density and doping ratio have been reported in F_4TCNQ-doped MEH-PPV (Ref. 8) and P3HT (Ref. 18) at higher doping concentrations than we used here.

Second, the slope of the linear increase allows an estimate of the doping efficiency. Taken a mass density of P3HT (Ref. 19) of 1.1 g/cm^3 and a molecular mass of one thiophene unit of 166.28 g/mol, the number density of thiophene units per volume is 4.0×10^{27} m^{-3}. In considering our previous findings that, at our low doping ratios, almost every F_4TCNQ acceptor forms a CT complex with P3HT,[10] the doping efficiency amounts to ca. 5%.

The trend of the conductivity vs. doping ratio resembles that of the hole density, i.e., a strong increase is seen at doping ratios higher than 10^{-6} (Fig. 2(b)). However, the log-log representation suggests a weaker, sublinear dependency according to a power law $\sigma \propto \chi^{\gamma}$ with $\gamma \sim 0.63$, indicating that the hole mobility is not constant upon doping. The hole mobility, calculated according to $\mu = \sigma/(pe)$, is depicted in

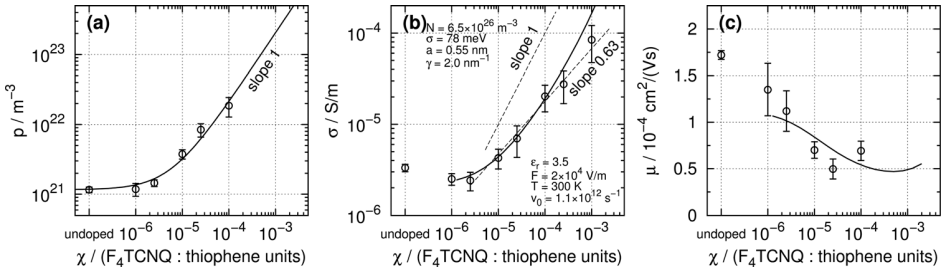

FIG. 2. (a) Hole density of undoped and doped P3HT layers. The line models a linear increase of hole density, starting from a background of 1.2×10^{21} m^{-3}. (b) Low-field bulk conductivity and (c) hole mobility. The solid lines are calculated according to the model of Arkhipov *et al.*[15] using the parameters given in the inset. Physical symbols are the same as in Ref. 15.

Fig. 2(c). Compared to the undoped sample, the mobility is steadily reduced up to doping ratios approaching 3×10^{-5}. Due to the increasing uncertainty in determining p, it was not possible to clarify if the mobility settles or eventually increases at higher doping ratios.

Most importantly, the trends of bulk conductivity and mobility from low to moderate dopant concentrations are in line with the above mentioned model by Arkhipov *et al.*[14,15] Simulated conductivity and mobility curves that reproduce our experimental data are shown in Figs. 2(b) and 2(c) (solid lines). We used a parameter set which contains the total site density $N = 6.5 \times 10^{26}$ m^{-3}, the Gaussian disorder parameter $\sigma = 78$ meV, the bound pair distance $a = 0.55$ nm, the inverse carrier localization length $\gamma = 2.0$ nm^{-1}, and the attempt-to-hop frequency $\nu_0 = 1.1 \times 10^{12}$ s^{-1}. These values compare well to those used by Arkhipov *et al.*[15] for electrochemically doped P3HT.

Following Arkhipov *et al.*, we infer that the reduction of hole mobility and, hence, the sublinear increase of conductivity with increasing doping ratio is most likely caused by a doping-induced broadening of the DOS distribution. The actual dependence of the mobility on the dopant density is governed by the counteracting occurrence of doping-induced tail broadening and the filling of the DOS distribution by doping-induced charges. Especially at low electric fields and low intrinsic electronic disorder, the combination of these effects can result in a reduced charge carrier mobility at low-to-moderate doping as seen in this work.

At higher dopant concentrations, it is expected that the individual Coulomb potentials of the countercharges overlap, such that the trap depth is essentially reduced.[15] Hence, the drop of the mobility should be reversed at sufficiently high doping levels. Indeed, the mobility of electrochemically or chemically doped P3HT was shown to increase for doping levels in the percent regime.[20] This may be as well the case for our F_4TCNQ-doped P3HT system, as indicated by our simulation. In the strong-doping regime, the mobility enhancement is due to the filling of the DOS distribution by doping-induced charges.

In summary, we have measured the hole density, bulk conductivity, and bulk mobility in F_4TCNQ-doped P3HT layers within a broad range of doping ratios, particularly including very low dopant concentrations. The free hole density increases linearly with doping ratio, suggesting that the charge transfer between F_4TCNQ and P3HT is electronically localized. We point out that the mobility is decreasing from low to moderate doping levels, which can be rationalized by the broadening of the DOS distribution owing to the Coulomb potential of the ionized acceptor molecules.

We gratefully acknowledge Professor Scherf, University of Wuppertal, for providing the P3HT sample and financial support from the Bundesministerium für Bildung und Forschung (BMBF project "NEMO," FKZ 13N10622).

[1]A. Yamamori, C. Adachi, T. Koyama, and Y. Taniguchi, Appl. Phys. Lett. **72**, 2147 (1998).
[2]J. Blochwitz, M. Pfeiffer, T. Fritz, and K. Leo, Appl. Phys. Lett. **73**, 729 (1998).
[3]E. Lim, B. J. Jung, M. Chikamatsu, R. Azumi, Y. Yoshida, K. Yase, L. M. Do, and H. K. Shim, J. Mater. Chem. **17**, 1416 (2007).
[4]L. Ma, W. H. Lee, Y. D. Park, J. S. Kim, H. S. Lee, and K. Choa, Appl. Phys. Lett. **92**, 063310 (2008).
[5]J. Sun, B. J. Jung, T. Lee, L. Berger, J. Huang, Y. Liu, D. H. Reich, and H. E. Katz, ACS Appl. Mater. Interfaces **1**, 412 (2009).
[6]C. P. Jarrett, R. H. Friend, A. R. Brown, and D. M. de Leeuw, J. Appl. Phys. **77**, 6289 (1995).
[7]K. H. Yim, G. L. Whiting, C. E. Murphy, J. J. M. Halls, J. H. Burroughes, R. H. Friend, and J. S. Kim, Adv. Mater. **20**, 3319 (2008).
[8]Y. Zhang, B. de Boer, and P. W. M. Blom, Adv. Funct. Mater. **19**, 1901 (2009).
[9]Y. A. Zhang and P. W. M. Blom, Org. Electron. **11**, 1261 (2010).
[10]P. Pingel, L. Y. Zhu, K. S. Park, J. O. Vogel, S. Janietz, E. G. Kim, J. P. Rabe, J. L. Brédas, and N. Koch, J. Phys. Chem. Lett. **1**, 2037 (2010).
[11]E. F. Aziz, A. Vollmer, S. Eisebitt, W. Eberhardt, P. Pingel, D. Neher, and N. Koch, Adv. Mater. **19**, 3257 (2007).
[12]I. Salzmann, G. Heimel, S. Duhm, M. Oehzelt, P. Pingel, B. M. George, A. Schnegg, K. Lips, R.-P. Blum, A. Vollmer, and N. Koch, Phys. Rev. Lett. **108**, 035502 (2012).
[13]L. Zhu, E.-G. Kim, Y. P. Yi, and J. L. Brédas, Chem. Mater. **23**, 5149 (2011).
[14]V. I. Arkhipov, P. Heremans, E. V. Emelianova, and H. Bässler, Phys. Rev. B **71**, 045214 (2005).
[15]V. I. Arkhipov, E. V. Emelianova, P. Heremans, and H. Bässler, Phys. Rev. B **72**, 235202 (2005).
[16]See supplementary material at http://dx.doi.org/10.1063/1.3701729 for details on the experimental procedures and admittance data.
[17]S. M. Sze, *Physics of Semiconductor Devices*, 2nd ed. (Wiley, New York, 1982).
[18]Y. Zhang and P. W. M. Blom, Appl. Phys. Lett. **97**, 083303 (2010).
[19]T. J. Prosa, M. J. Winokur, J. Moulton, P. Smith, and A. J. Heeger, Macromolecules **25**, 4364 (1992).
[20]X. Jiang, Y. Harima, K. Yamashita, Y. Tada, J. Ohshita, and A. Kunai, Chem. Phys. Lett. **364**, 616 (2002).

Supplementary Material to

Effect of molecular p-doping on hole density and mobility in P3HT

P. Pingel,[1] R. Schwarzl,[1] and D. Neher[1, a)]

Soft Matter Physics, Institute of Physics and Astronomy, University of Potsdam, Karl-Liebknecht-Str. 24-25, D–14476 Potsdam, Germany

[a)]Electronic mail: neher@uni-potsdam.de

Samples for admittance spectroscopy have been prepared in a metal-insulator-semiconductor (MIS) geometry on glass substrates with patterned indium-tin-oxide (ITO). After thorough cleaning of the substrates by ultrasonication in common organic solvents, an electrically insulating layer of methyl-/phenyl-substituted polysilsesquioxane (PSQ, purchased from Gelest Inc.) was spin-cast at 1500 rpm for 30 s from a filtered 40 mg/ml solution in butanone. This layer was rendered insoluble by annealing at 350°C for 1 h. The following steps were continued in an N_2 glovebox under inert conditions.

Poly(3-hexylthiophene), P3HT, and tetrafluorotetracyanoquinodimethane, F_4TCNQ, were dissolved at 60 mg/ml and 0.5 mg/ml in chloroform, respectively, applying 50°C and stirring. The P3HT sample is a deuterated high-molecular weight fraction. Deuteration has been done for potential neutron scattering experiments. From our extensive previous investigations it is known that the physical properties are not altered by the deuteration and that the performance of this P3HT fraction is outstanding in field-effect devices.[1–3] F_4TCNQ was purchased from Sigma-Aldrich. The chloroform solutions of P3HT and F_4TCNQ were blended at the desired dopant concentration and processed immediately to prevent aggregation. Upon blending, the color of the solution turned immediately dark, indicative of the formation of charge transfer complexes. The semiconductor layer was then spin-cast at 1000 rpm for 30 s, yielding a visually homogeneous film. Next, electrical hole-injecting contacts were formed by evaporation of 5 nm MoO_3 at 2 Å/s and 100 nm Al at 3-7 Å/s. Devices were completed by encapsulation with a glass sheet and Araldite 2011 epoxy resin.

In order to determine the thicknesses of the insulator and semiconductor layers, these films were prepared on cleaned glass substrates and investigated with a DEKTAK 3 surface profilometer. Typically, the thickness of the PSQ insulator amounts to 155 nm and the thicknesses of the various doped polymer layers ranges from 350 nm to 1200 nm.

Admittance spectroscopy on MIS devices was performed using our home-built setup including an EG & G DSP 7260 lock-in amplifier and a Stanford Research SR570 low noise current amplifier. Typically, we applied an AC voltage of 20 mV to the samples.

In the following, exemplary capacitance-voltage curves and loss spectra for each of the investigated dopant concentrations are presented.

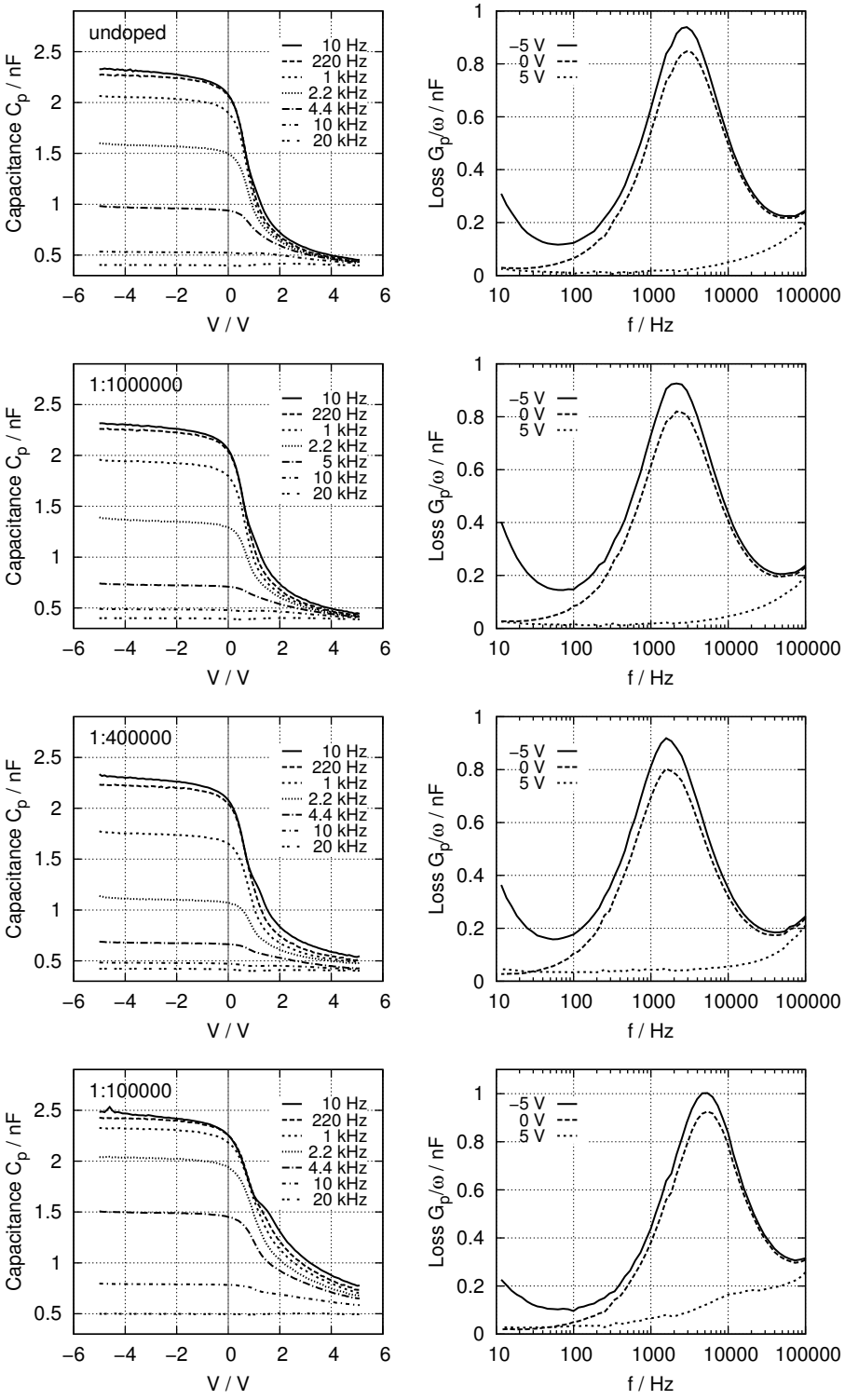
undoped
1:1000000
1:400000
1:100000
Capacitance C_p / nF
Loss G_p/ω / nF
V / V
f / Hz
10 Hz
220 Hz
1 kHz
2.2 kHz
4.4 kHz
5 kHz
10 kHz
20 kHz
−5 V
0 V
5 V

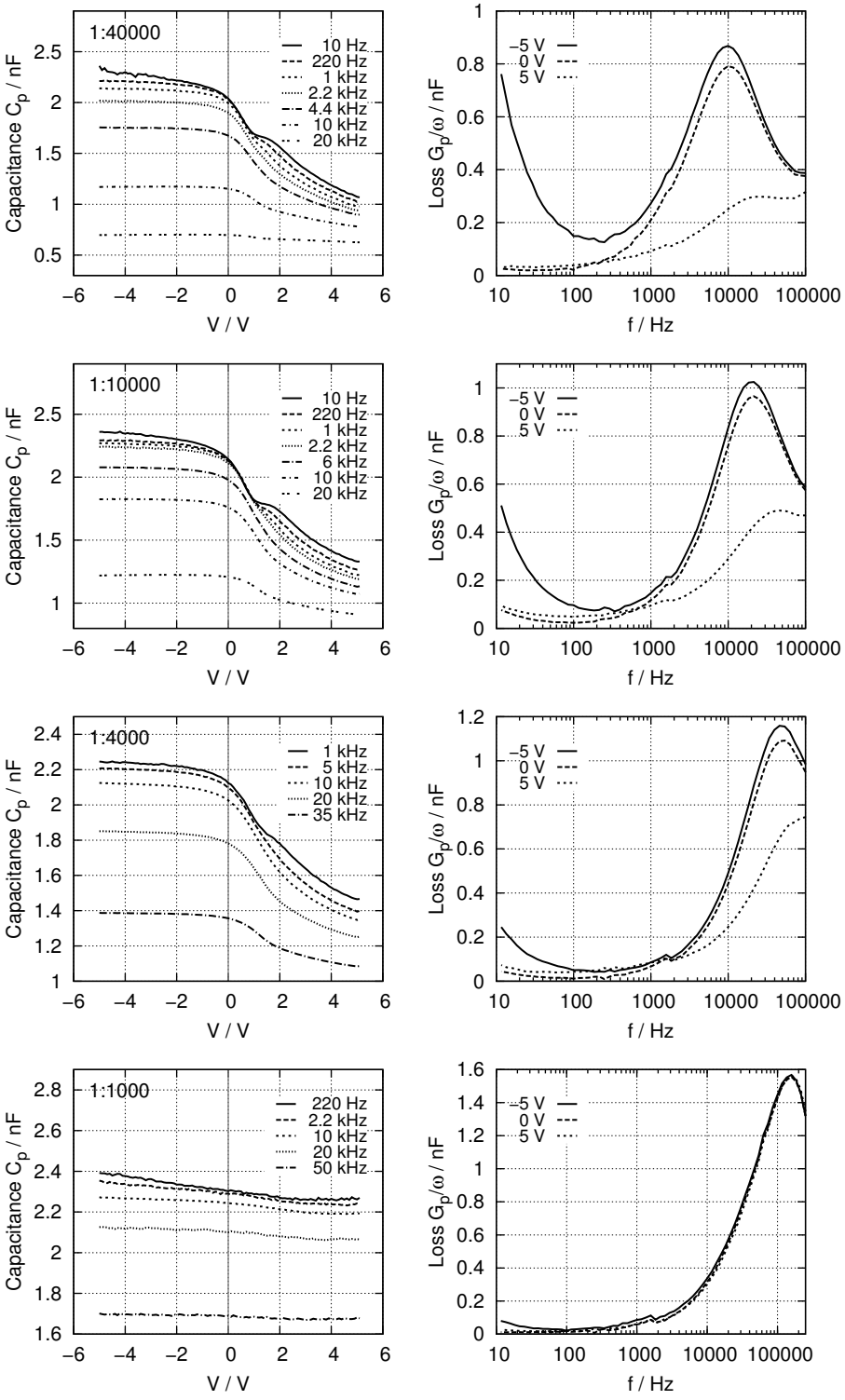
1:40000
10 Hz
220 Hz
1 kHz
2.2 kHz
4.4 kHz
10 kHz
20 kHz
Capacitance C_p / nF
V / V
−5 V
0 V
5 V
Loss G_p/ω / nF
f / Hz
1:10000
10 Hz
220 Hz
1 kHz
2.2 kHz
6 kHz
10 kHz
20 kHz
Capacitance C_p / nF
V / V
−5 V
0 V
5 V
Loss G_p/ω / nF
f / Hz
1:4000
1 kHz
5 kHz
10 kHz
20 kHz
35 kHz
Capacitance C_p / nF
V / V
−5 V
0 V
5 V
Loss G_p/ω / nF
f / Hz
1:1000
220 Hz
2.2 kHz
10 kHz
20 kHz
50 kHz
Capacitance C_p / nF
V / V
−5 V
0 V
5 V
Loss G_p/ω / nF
f / Hz

[1]A. Zen, J. Pflaum, S. Hirschmann, W. Zhuang, F. Jaiser, U. Asawapirom, J. P. Rabe, U. Scherf, and D. Neher, Adv. Funct. Mater. **14**, 757 (2004).

[2]A. Zen, M. Saphiannikova, D. Neher, J. Grenzer, S. Grigorian, U. Pietsch, U. Asawapirom, S. Janietz, U. Scherf, I. Lieberwirth, and G. Wegner, Macromolecules **39**, 2162 (2006).

[3]P. Pingel, A. Zen, R. D. Abellon, F. C. Grozema, L. D. A. Siebbeles, and D. Neher, Adv. Funct. Mater. **20**, 2286 (2010).

THE JOURNAL OF PHYSICAL CHEMISTRY Letters

pubs.acs.org/JPCL

Charge-Transfer Localization in Molecularly Doped Thiophene-Based Donor Polymers

Patrick Pingel,[†,‡] Lingyun Zhu,[§] Kue Surk Park,[†] Jörn-Oliver Vogel,[†] Silvia Janietz,[¶] Eung-Gun Kim,[§] Jürgen P. Rabe,[†] Jean-Luc Brédas,[§] and Norbert Koch*[,†]

[†]Institut für Physik, Humboldt University Berlin, Newtonstrasse 15, 12489 Berlin, Germany, [‡]Institute of Physics and Astronomy, University of Potsdam, Karl-Liebknecht-Strasse 24-25, 14476 Potsdam, Germany, [§]School of Chemistry and Biochemistry and Center for Organic Photonics and Electronics, Georgia Institute of Technology, Atlanta, Georgia 30332-0400, and [¶]Fraunhofer Institute for Applied Polymer Research, Geiselbergstrasse 69, 14476 Potsdam, Germany

ABSTRACT We provide evidence for highly localized charge-transfer complex formation between a series of thiophenetetrafluorobenzene donor copolymers and the molecular acceptor tetrafluorotetracyanoquinodimethane (F_4TCNQ). Infrared absorption spectra of diagnostic vibrational bands in conjunction with theoretical modeling show that one acceptor molecule undergoes charge transfer with a quaterthiophene segment of the polymers, irrespective of the macroscopic polymer ionization energy and acceptor concentration in thin films. The interaction is thus determined by the "local ionization potential" of quaterthiophene. Consequently, using materials parameters determined on a macroscopic length scale as a guideline for making new charge-transfer complex materials for high electrical conductivity turns out to be oversimplified, and a reliable material design must take into account property variations on the nm scale as well.

SECTION Macromolecules, Soft Matter

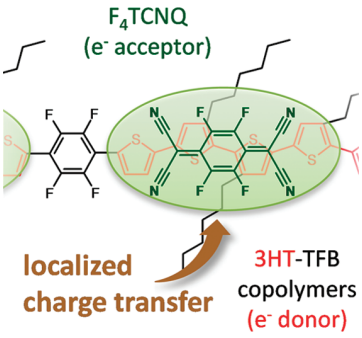

The field of organic electronics has made tremendous progress within the last two decades, which has led to electroluminescent, photovoltaic, and transistor devices in the stage of (or close to) commercialization.[1] However, there is still a lack of comprehensive understanding of some fundamental processes in conjugated organic materials, such as the nature of charge transfer and electrical conductivity associated with oxidation and reduction (doping) of organic molecular compounds. From an application standpoint, the realization of printed all-organic circuits requires highly conductive organic layers that can be processed from solution, potentially even to serve as conductive wires.[2,3] The materials presently available for that purpose almost exclusively comprise aqueous dispersions of poly(3,4-ethylenedioxythiophene)/poly(styrene sulfonate) (PEDOT/PSS); however, controlling thin-film properties is challenging because of the presence of residual water.[4] Replacing PEDOT/PSS in devices is moreover desirable to avoid luminescence quenching and possible acidic etching of indium tin oxide due to excess PSS.[5]

A promising approach to achieving highly conductive polymer films free from water is the intentional molecular doping of conjugated polymers with organic compounds. An appropriate combination of soluble acceptor and donor systems can lead to ground-state charge transfer and a considerable increase in electrical conductivity with respect to the pure materials.[6−8] Recently, we reported that a high conductivity of 1 S/cm can be reached in thin films when oxidizing (p-type doping) poly(3-hexylthiophene) (P3HT) in solution with the strong acceptor tetrafluorotetracyanoquinodimethane (F_4TCNQ; see Scheme 1).[9] F_4TCNQ doping was also applied to other conjugated polymers; however, to date, the combination of F_4TCNQ with P3HT has resulted in the highest conductivities.[5,10−13] In order to achieve further improvements of highly conductive organic materials, it is important to understand the fundamental mechanisms of charge transfer and its relationship to individual material properties.

In ref 9, we pointed out that the formation of charge-transfer complexes between F_4TCNQ and P3HT involves hybridization of donor and acceptor molecular orbitals. Moreover, we found that only one specific charge-transfer species is predominant in these samples, despite the potentially large number of different local conformations that could be expected due to the flexibility of the polymer chains and the manifold of possible interchain interactions. Hence, it appears that charge transfer is spatially restricted such that F_4TCNQ interacts with only a few connected thiophene repeat units.

In order to test the hypothesis of localization, we report here on F_4TCNQ-doped layers of a series of soluble thiophene-based donor copolymers (3HT−TFB; see Scheme 1), which comprise various amounts of tetrafluorobenzene (TFB) units. TFB units are introduced into the main chain in order to interrupt the thiophene sequence and to provide a variation in effective conjugation length of the thiophene blocks, which

Received Date: April 16, 2010
Accepted Date: June 9, 2010
Published on Web Date: June 16, 2010

DOI: 10.1021/jz100492c | *J. Phys. Chem. Lett.* **2010**, *1*, 2037–2041

THE JOURNAL OF PHYSICAL CHEMISTRY Letters

pubs.acs.org/JPCL

Scheme 1. Chemical Structures of F_4TCNQ (**1**) and 3HT-TFB (**2a**−**c**)

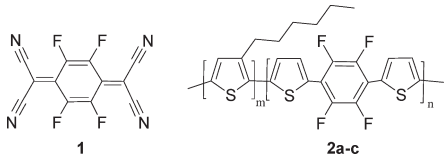

Table 1. Properties of the P3HT and 3HT−TFB (**2a**−**c**) Copolymers

compound	M_n[a] [g/mol]	$A_{TFB/Th}$[b] [mol %]	IP[c] [eV]
P3HT	19 200	0	4.80 ± 0.05
2a	19 800	3.0	5.00 ± 0.05
2b	14 800	5.1	5.05 ± 0.05
2c	14 500	9.5	5.10 ± 0.05

[a] Number-average molecular weight. [b] Relative amount of TFB and thiophene units in the main chain. [c] Ionization potential from photoemission measurements.[14]

are intended to interact with F_4TCNQ. We find that despite this variation and the presence of TFB, only a single charge-transfer species is formed, that is, a highly localized complex between F_4TCNQ and a thiophene segment of the main chain.

The synthesis of the donor copolymers followed the McCullough−Grignard metathesis method and is described in detail in ref 14. 1,4-Dithienyl-2,3,5,6-tetrafluorobenzene (TFB) units were introduced along the 3-hexylthiophene main chain, resulting in regioregularly linked random 3HT−TFB copolymers (**2a**−**c**) with similar molecular weights and a moderate polydispersity index of 1.5. The relevant materials parameters of 3HT−TFB are summarized in Table 1. Notably, the variation of the TFB amount along the main chain leads to a systematic change of the polymer ionization potential (IP) due to the electron-accepting character of TFB, that is, the IP varies from 4.8 to 5.1 eV in going from P3HT to compound **2c**, as determined by ultraviolet photoelectron spectroscopy (see Supporting Information). We recall that the electron affinity (EA) of F_4TCNQ is 5.24 eV.[15] Thus, the acceptor EA is larger than the donor polymer IP in all cases. Nonetheless, differences in the amount of charge transfer could be expected as the charge redistribution along the polymer chain should be impacted by the various amounts of TFB units.

Blend films of F_4TCNQ and the various 3HT−TFB copolymers were prepared by drop-casting from chloroform solution [F_4TCNQ/(thiophene monomer) ratios of 1:10 and 1:3 were used, typically 1 mg/mL] onto Si wafers with native oxide surfaces. We used infrared (IR) spectroscopy as a direct diagnostic tool to investigate the degree of charge transfer. Upon (partial) ionization, for example, following charge transfer, F_4TCNQ changes its geometry from a quinoidal to a more aromatic structure.[16,17] This is accompanied by a red shift of specific vibrational modes that serve as an indicator of charge transfer, in particular, the IR bands that are assigned to asymmetric C═C stretching (at 1547 and 1598 cm^{-1}) and asymmetric C≡N stretching (at 2214 and 2227 cm^{-1} for neutral F_4TCNQ). The red shift of these IR bands was found to increase linearly with increasing degree of charge transfer.[18−21]

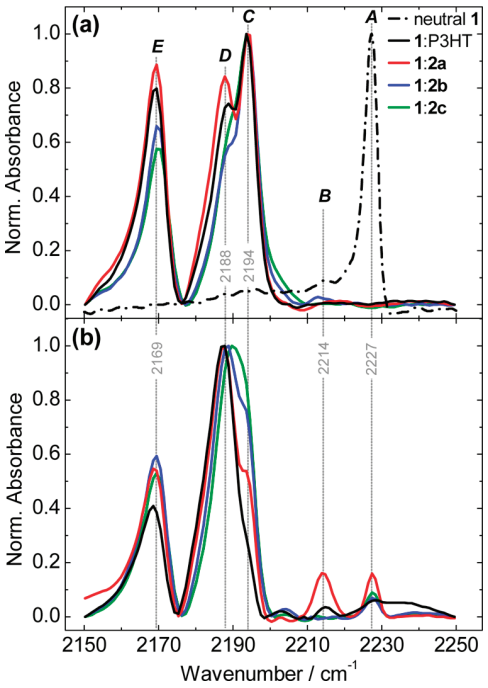

Figure 1. IR spectra of neutral F4TCNQ (**1**) and the F4TCNQ/(co)polymer blends [F4TCNQ/(thiophene monomer) ratios of 1:10 (a) and 1:3 (b)] in the C≡N stretching region, indicative of the degree of charge transfer.

Full-range IR spectra of the pure and blended compounds [1:10 ratio of F_4TCNQ/(thiophene monomer)] are provided in the Supporting Information, including the vibrational bands of the thiophene-based polymers in the C═C stretching region. In the following, we focus on the variations of the C≡N stretching modes of the F_4TCNQ cyano groups. Figure 1 shows the corresponding region of the IR spectra of neutral F_4TCNQ thin films and of F_4TCNQ/polymer blends. In neutral F_4TCNQ films, a strong band is centered at 2227 cm^{-1} (labeled A), and a weak band appears at 2214 cm^{-1} (labeled B). It is known that F_4TCNQ crystallizes in an orthorhombic structure when deposited from solution;[22] following the assignment of Meneghetti et al.,[17] these bands can be assigned to vibrational modes derived from molecular modes with symmetry labels b_{1u} and b_{2u}, respectively. Our density functional theory (DFT) calculations of the vibrational frequencies (at the B3LYP/6-31G(d) level) show that the b_{1u}- and b_{2u}-derived modes (the only ones with significant IR intensity in this energy region) are separated by ∼18 cm^{-1} in the F_4TCNQ crystal (calculated at 2252−2255 and 2235 cm^{-1}; see Supporting Information). We note that an isolated F_4TCNQ molecule in the gas phase has b_{1u} and b_{2u} transitions with reversed intensities (the calculated intensity of A for isolated F_4TCNQ is ∼10 times lower than that of B). The asymmetry in the shapes of the A and B bands with respect to their centers suggests a superposition of features due to crystallized and nonaggregated molecular species.

In the blend layers, the bands are considerably red-shifted, indicative of strong charge transfer. According to our model calculations on F_4TCNQ/quaterthiophene (4T) complexes (at the B3LYP-D/6-31+G(d) level, which includes dispersion

DOI: 10.1021/jz100492c | J. Phys. Chem. Lett. 2010, 1, 2037–2041

THE JOURNAL OF PHYSICAL CHEMISTRY Letters

pubs.acs.org/JPCL

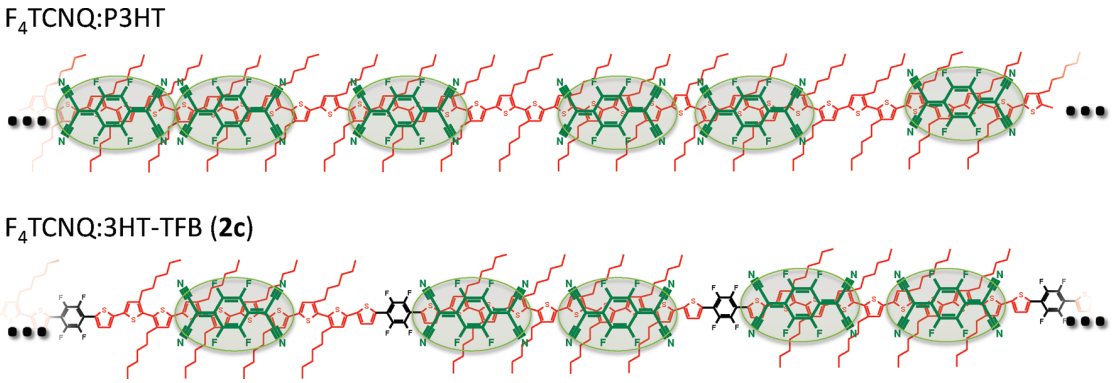

Figure 2. Sketch of charge-transfer complex formation of F_4TCNQ (green) with the oligothiophene building blocks (red) of P3HT and 3HT−TFB. In the latter, the thiophene segments are interrupted by TFB units (black).

corrections), features C and E can be assigned to the b_{1u} and b_{2u} modes, respectively (red-shifted features with respect to A and B of neutral F_4TCNQ). In addition, feature E contains a contribution from a formerly IR-forbidden mode with symmetry b_{3g}. The new intense feature D is related to the in-plane a_g mode of symmetric C≡N stretching, which is also IR-inactive in neutral F_4TCNQ. The appearance of the formerly IR-inactive modes in the charge-transfer complexes points toward a change of the F_4TCNQ geometry to a nonplanar conformation, as suggested previously[9] (see also Supporting Information, Figure S3). Note that all charge-transfer complexes, including doped P3HTand 3HT−TFB, exhibit IR bands at exactly the same positions. (The slight shift (< 1 cm^{-1}) in the peak maxima of C, D, and E is not significant as it is due to the different amplitudes of superimposed neighboring features). This means that despite the potentially large number of different possible conformations, only one specific charge-transfer species with a defined degree of charge transfer is actually formed between F_4TCNQ and an oligothiophene segment of the various donor polymers.

B3LYP-D/6-31+G(d) calculations on F_4TCNQ/4T and F_4TCNQ/(dithiophene-TFB-thiophene) model complexes where the spatial positions of F_4TCNQ are varied along the donor support this conclusion (see Supporting Information, Figures S4 and S5). The amount of charge transfer obtained from these calculations varies between 0.33 (F_4TCNQ located above the TFB unit) and 0.51 electron (F_4TCNQ centered above 4T). In fact, following the usual linear relationship between IR frequency and degree of charge transfer, this variation in charge-transfer strength should have led to noticeably different red shifts of the IR bands between $\Delta\nu = 10$ and 17 cm^{-1} (using $\Delta\nu = Z\nu_0[1 - \nu_1^2/\nu_0^2]/2$, with $\nu_0 = 2227$ cm^{-1} and $\nu_1 = 2194$ cm^{-1} as the positions of the b_{1u} bands of neutral F_4TCNQ and its anion, respectively; Z is the degree of charge transfer).[19,23] However, such a wide range of shifts or a comparable line width broadening is not evident in the experimental spectra (Figure 1). This is the consistent with the conclusion that a single charge-transfer species is predominantly formed.

Importantly, the peak positions at 1:10 (Figure 1a) and 1:3 (Figure 1b) F_4TCNQ/(thiophene monomer) doping ratios are identical (i.e., the degree of charge transfer is maintained), even though in the latter, one could expect that the close proximity of charge-transfer complexes along a polymer chain would lead to intercomplex interactions, potentially reducing the amount of charge transfer per complex. At the high 1:3 doping concentration, however, the number of charge-transfer complexes formed is already saturated, as can be deduced from the occurrence of IR signatures of neutral F_4TCNQ molecules (peaks A and B in Figure 1b). Hence, F_4TCNQ appears to interact with a polymer segment of approximately four connected thiophene units, as can be inferred from the molar ratio of F_4TCNQ and polythiophene monomer units when saturation of complex formation occurs. The interaction between F_4TCNQ and the donor polymers is bimodal; acceptor molecules that could not be accommodated to react with suitably conjugated polymer segments remained neutral.

This behavior is particularly remarkable for the copolymers that incorporate TFB units. Upon increasing the TFB content, the average length of uninterrupted thiophene blocks decreases. For instance, in the case of compound **2c**, which incorporates 9.5 mol % of the TFB building block, the average length of uninterrupted thiophene segments is approximately 10 connected thiophene units (including the unsubstituted thiophene units of the TFB monomer; see Scheme 1). Thus, in blend layers of F_4TCNQ and 3HT−TFB, adjacent complexes frequently form along the same uninterrupted thiophene segment (see Figure 2); otherwise, a higher concentration of unreacted neutral F_4TCNQ would be present in these layers, leading to stronger A and B features in Figure 1b. The fact that these neighboring complexes do not result in a shift or broadening of the IR bands indicates that the charge-transfer interaction is actually a highly localized phenomenon, approximately limited to the spatial extent of F_4TCNQ (or, equivalently, a quaterthiophene unit). If neighboring charge-transfer complexes were to interact, a decrease in the amount of charge transfer would have been expected since a single thiophene donor segment would have had to donate charge to multiple acceptors.

The absence of peaks A and B of neutral F_4TCNQ for layers at 1:10 doping concentration (see Figure 1a) evidence that phase separation into the pristine compounds does not occur, which is also not expected since charge-transfer complex

DOI: 10.1021/jz100492c | J. Phys. Chem. Lett. 2010, 1, 2037–2041

THE JOURNAL OF PHYSICAL CHEMISTRY Letters

pubs.acs.org/JPCL

formation already occurred in solution prior to film formation. Phase separation and formation of F_4TCNQ aggregates, however, may indeed occur at the relatively high doping concentration of 1:3 as clear IR signatures of neutral bulk F_4TCNQ are observed. In this context, we note that the intensity of peaks A and B for mixed films with **2a** at a doping concentration of 1:3 is higher than that for the other polymers (Figure 1b). We speculate that this is most likely due to a particular preferred orientation of F_4TCNQ aggregates in films with this polymer (i.e., phase separation of unreacted F_4TCNQ), which leads to a higher cross section for IR absorption in our experimental geometry.

To gain further insight into this phenomenon, we also performed model calculations on F_4TCNQ/5T complexes (at the same B3LYP-D/6-31+G(d) level; see Supporting Information, Figures S6 and S7). Inspection of bond lengths in 5T upon complex formation indicates that geometric changes essentially remain localized over four thiophene units (the bond length changes less than 0.004 Å in the fifth thiophene ring).

In conclusion, we have documented that for P3HT and a series of 3HT−TFB copolymers, doping with the strong molecular acceptor F_4TCNQ leads to highly localized charge transfer, presumably involving four connected thiophene segments as donor site. This implies that the interaction is determined by the "local IP" of quaterthiophene (i.e., a parameter on the nm length scale) rather than depending on macroscopic material parameters, such as IP and EA from (direct and inverse) photoemission methods (determined on the mm length scale). In fact, the macroscopic IPs of the donor polymers differ by as much as 0.3 eV. Moreover, neighboring charge-transfer complexes of F_4TCNQ on a polythiophene chain do not influence each other notably, and F_4TCNQ molecules that cannot be accommodated on accessible 4T segments do not undergo a weaker charge transfer but remain neutral instead. Thus, using materials parameters determined on a macroscopic length scale as guidelines for making new composite materials, for example, charge-transfer complexes, is oversimplified. A reliable material design must take into account property variations on the nm scale as well. Moreover, the self-localization of charges owing to the highly localized character of charge transfer possibly may reduce the charge carrier mobility and conductivity in these systems.

SUPPORTING INFORMATION AVAILABLE Experimental and preparation details, full-range IR spectra, theoretically modeled charge-transfer complexes, and vibrational frequencies/intensities. This material is available free of charge via the Internet at http://pubs.acs.org.

AUTHOR INFORMATION

Corresponding Author:

*To whom correspondence should be addressed. E-mail: norbert.koch@physik.hu-berlin.de.

ACKNOWLEDGMENT The authors are grateful to Georg Heimel and Narges Ghani for valuable discussions. This work was supported by the DFG (Sfb448 and SPP1355), Solvay, and the U.S. Department of Energy (DE-FG02-04ER46165). N.K. acknowledges financial support by the Emmy Noether Program (DFG).

REFERENCES

(1) Katz, H. E.; Huang, J. Thin-Film Organic Electronic Devices. *Annu. Rev. Mater. Res.* **2009,** *39*, 71–92.

(2) Forrest, S. R. The Path to Ubiquitous and Low-Cost Organic Electronic Appliances on Plastic. *Nature* **2004,** *428*, 911–918.

(3) Sirringhaus, H.; Kawase, T.; Friend, R. H.; Shimoda, T.; Inbasekaran, M.; Wu, W.; Woo, E. P. High-Resolution Inkjet Printing of All-Polymer Transistor Circuits. *Science* **2000,** *290*, 2123–2126.

(4) Koch, N.; Vollmer, A.; Elschner, A. Influence of Water on the Work Function of Conducting Poly(3,4-ethylenedioxythiophene)/Poly(styrenesulfonate). *Appl. Phys. Lett.* **2007,** *90*, 3.

(5) Yim, K. H.; Whiting, G. L.; Murphy, C. E.; Halls, J. J. M.; Burroughes, J. H.; Friend, R. H.; Kim, J. S. Controlling Electrical Properties of Conjugated Polymers Via a Solution-Based P-Type Doping. *Adv. Mater.* **2008,** *20*, 3319–3324.

(6) Basescu, N.; Liu, Z. X.; Moses, D.; Heeger, A. J.; Naarmann, H.; Theophilou, N. High Electrical-Conductivity in Doped Polyacetylene. *Nature* **1987,** *327*, 403–405.

(7) Chiang, C. K.; Fincher, C. R.; Park, Y. W.; Heeger, A. J.; Shirakawa, H.; Louis, E. J.; Gau, S. C.; Macdiarmid, A. G. Electrical-Conductivity in Doped Polyacetylene. *Phys. Rev. Lett.* **1977,** *39*, 1098–1101.

(8) Kumai, R.; Okimoto, Y.; Tokura, Y. Current-Induced Insulator−Metal Transition and Pattern Formation in an Organic Charge-Transfer Complex. *Science* **1999,** *284*, 1645–1647.

(9) Aziz, E. E.; Vollmer, A.; Eisebitt, S.; Eberhardt, W.; Pingel, P.; Neher, D.; Koch, N. Localized Charge Transfer in a Molecularly Doped Conducting Polymer. *Adv. Mater.* **2007,** *19*, 3257–3260.

(10) Hwang, J.; Kahn, A. Electrical Doping of Poly(9,9-dioctylfluorenyl-2,7-diyl) with Tetrafluorotetracyanoquinodimethane by Solution Method. *J. Appl. Phys.* **2005,** *97*, 103705.

(11) Lim, E.; Jung, B. J.; Chikamatsu, M.; Azumi, R.; Yoshida, Y.; Yase, K.; Do, L. M.; Shim, H. K. Doping Effect of Solution-Processed Thin-Film Transistors Based on Polyfluorene. *J. Mater. Chem.* **2007,** *17*, 1416–1420.

(12) Ma, L.; Lee, W. H.; Park, Y. D.; Kim, J. S.; Lee, H. S.; Choa, K. High Performance Polythiophene Thin-Film Transistors Doped with Very Small Amounts of an Electron Acceptor. *Appl. Phys. Lett.* **2008,** *92*, 063310.

(13) Zhang, Y.; de Boer, B.; Blom, P. W. M. Controllable Molecular Doping and Charge Transport in Solution-Processed Polymer Semiconducting Layers. *Adv. Funct. Mater.* **2009,** *19*, 1901–1905.

(14) Sainova, D.; Janietz, S.; Asawapirom, U.; Romaner, L.; Zojer, E.; Koch, N.; Vollmer, A. Improving the Stability of Polymer Fets by Introducing Fixed Acceptor Units into the Main Chain: Application to Poly(alkylthiophenes). *Chem. Mater.* **2007,** *19*, 1472–1481.

(15) Gao, W. Y.; Kahn, A. Controlled P-Doping of Zinc Phthalocyanine by Coevaporation with Tetrafluorotetracyanoquinodimethane: A Direct and Inverse Photoemission Study. *Appl. Phys. Lett.* **2001,** *79*, 4040–4042.

(16) Emge, T. J.; Bryden, W. A.; Wiygul, F. M.; Cowan, D. O.; Kistenmacher, T. J.; Bloch, A. N. Structure of an Organic Charge-Transfer Salt Derived from Dibenzotetrathiafulvalene and "Tetrafluorotetracyanoquinodimethane (DBTTF-TCNQF4) — Observation of a High-Temperature Phase-Transition. *J. Chem. Phys.* **1982,** *77*, 3188–3197.

DOI: 10.1021/jz100492c | *J. Phys. Chem. Lett.* **2010,** *1*, 2037–2041

THE JOURNAL OF PHYSICAL CHEMISTRY Letters

pubs.acs.org/JPCL

(17) Meneghetti, M.; Pecile, C. Charge-Transfer Organic-Crystals — Molecular Vibrations and Spectroscopic Effects of Electron—Molecular Vibration Coupling of the Strong Electron-Acceptor TCNQF4. *J. Chem. Phys.* **1986,** *84*, 4149–4162.

(18) Chappell, J. S.; Bloch, A. N.; Bryden, W. A.; Maxfield, M.; Poehler, T. O.; Cowan, D. O. Degree of Charge-Transfer in Organic Conductors by Infrared Absorption Spectroscopy. *J. Am. Chem. Soc.* **1981,** *103*, 2442–2443.

(19) Salmerón-Valverde, A.; Robles-Martínez, J. G.; García-Serrano, J.; Gómez, R.; Ridaura, R. M.; Quintana, M.; Zehe, A. A Study of the Degree of Charge Transfer in Ttf Molecular Complexes with Nitro-Carboxylated Fluorene Derivatives. *Mol. Eng.* **1999,** *8*, 419–426.

(20) Stires, J. C.; McLaurin, E. J.; Kubiak, C. P. Infrared Spectroscopic Determination of the Degree of Charge Transfer in Complexes of TCNE with Methyl-Substituted Benzenes. *Chem. Commun.* **2005,** 3532–3534.

(21) Mulliken, R. S.; Person, W. B. Donor-Acceptor Complexes. *Annu. Rev. Phys. Chem.* **1962,** *13*, 107–126.

(22) Emge, T. J.; Maxfield, M.; Cowan, D. O.; Kistenmacher, T. J. Solution and Solid-State Studies of Tetrafluoro-7,7,8,8-Tetracyano-P-Quinodimethane, TCNQF4 — Evidence for Long-Range Amphoteric Intermolecular Interactions and Low-Dimensionality in the Solid-State Structure. *Mol. Cryst. Liq. Cryst.* **1981,** *65*, 161–178.

(23) Robles-Martínez, J. G.; Salmerón-Valverde, A.; Argüelles-Ramírez, J.; Zehe, A. Variation of Charge Transfer in Zn-Naphtholimines with TCNQ. *Mol. Eng.* **1999,** *8*, 411–417.

DOI: 10.1021/jz100492c | *J. Phys. Chem. Lett.* **2010,** *1*, 2037–2041

Supporting Information

for

Charge Transfer Localization in Molecularly Doped Thiophene-Based Donor Polymers

Patrick Pingel,[†,‡] Lingyun Zhu,[§] Kue Surk Park,[†] Jörn-Oliver Vogel,[†] Silvia Janietz,[¶] Eung-Gun Kim,[§] Jürgen P. Rabe,[†] Jean-Luc Brédas,[§] and Norbert Koch[†]*

[†] Institut für Physik, Humboldt University Berlin, Newtonstr. 15, 12489 Berlin, Germany

[‡] Institute of Physics and Astronomy, University of Potsdam, Karl-Liebknecht-Str. 24-25, 14476 Potsdam, Germany

[§] School of Chemistry and Biochemistry and Center for Organic Photonics and Electronics, Georgia Institute of Technology, Atlanta, Georgia 30332-0400, USA

[¶] Fraunhofer Institute for Applied Polymer Research, Geiselbergstr. 69, 14476 Potsdam, Germany

*Corresponding author. E-mail: norbert.koch@physik.hu-berlin.de

Preparation of F_4TCNQ and F_4TCNQ:polymer layers

2,3,5,6-tetrafluoro-7,7,8,8-tetracyanoquinodimethane (F_4TCNQ) was purchased from Fluka and was used as received. Pure and blend layers of F_4TCNQ and the thiophene-based polymers were prepared by drop-casting from chloroform solution (typically 1 mg/ml) on Si wafers with native oxide. For the blend layers mixing ratios of 1:10 and 1:3 F_4TCNQ:(thiophene monomers) were used. Preparation was performed in inert argon atmosphere.

Ultraviolet Photoelectron Spectroscopy (UPS)

Ultraviolet photoelectron spectroscopy (UPS) spectra for P3HT and the various 3HT-TFB copolymer (structures **2a-c**) thin films (ca. 10 nm) on poly(3,4-ethylenedioxythiophene)/ poly(styrenesulfonate) (PEDT:PSS) substrates were measured, see Fig. S1. The spectra show that the width of the delocalized π-band is independent of the TFB content.

Infra-red (IR) spectroscopy

IR spectra were taken immediately after preparation with a BRUKER IFS 66v/S FT-IR spectrometer using a liquid-nitrogen-cooled mercury-cadmium-telluride detector and a mid-IR light source. Full-range IR spectra of pure and doped layers [1:10 F_4TCNQ:(thiophene monomer) concentration] are shown in Fig. S2. The pure donor polymers have no IR bands in the C≡N asymmetric stretching region of F_4TCNQ.

Theoretical studies of F_4TCNQ, F4TCNQ:(dithiophene-TFB-thiophene) complexes, and F_4TCNQ:*n*T complexes

Methodology

We employed B3LYP functional including dispersion corrections and 6-31+G(d) basis set (B3LYP-D/6-31+G(d)) to optimize the geometries of charge-transfer complexes. The geometries of the isolated neutral and anionic F_4TCNQ molecules were also optimized at the same level of theory (B3LYP/6-31+G(d). Based on the optimized structures, harmonic vibrational frequencies were calculated by means of a numerical Hessian at the same level. All the calculations were performed with the performed with the TURBOMOLE6.0 package.[1]

A fragmental orbital approach,[2] in combination with a basis set orthogonalization procedure,[3] was used to evaluate the effective transfer integral (*t*) between the donor and the acceptor in the complex. These calculations were performed at the B3LYP/6-31+G (d) level by using the Gaussian 03 package.[4]

The geometry optimization of the F_4TCNQ crystal structure[5] was performed using the B3LYP functional with the 6-31G(d) basis set as implemented in the CRYSTAL06 package.[6] During the optimization, the unit cell parameters were fixed at the experimental values and the structural relaxations were limited to the positional parameters of the atoms. A uniform 4×6×6 Monkhorst-Pack *k*-point mesh was employed. Based on the optimized crystal structure, harmonic vibrational frequencies and intensities at the Γ-point were calculated. B3LYP/6-31G(d)-calculated frequencies were scaled down by a factor of 0.9614, which has been shown to reproduce the experimental frequencies very well.[7]

Optimized structures

The calculated normal modes of the isolated F_4TCNQ molecule are given in Fig. S3.

Fig. S4-S6 shows three B3LYP-D/6-31+G(d)-optimized complex structures of F_4TCNQ:4T, F_4TCNQ:(dithiophene-TFB-thiophene) and F_4TCNQ:5T. In the case of F4TCNQ:4T complexes, F_4TCNQ was moved along the long molecular axis of 4T in the cofacial structure; the F_4TCNQ center can be located: above the bond connecting two inner thiophene rings (F_4TCNQ:4T(1)); above one inner thiophene ring (F_4TCNQ:4T(2)); or above the bond connecting outer and inner thiophene rings (F_4TCNQ:4T(3)). It is found that the F_4TCNQ moiety is not fully planar, which relaxes the symmetry constraints. In the case of F_4TCNQ:(dithiophene-TFB-thiophene) complexes, the F_4TCNQ center locate above the TFB ring (F_4TCNQ:(dithiophene-TFB-thiophene)(1)) or above the bond connecting one inner thiophene ring and TFB ring (F_4TCNQ:(dithiophene-TFB-thiophene)(2)) or above the bond connecting dithiophene rings (F_4TCNQ:(dithiophene-TFB-thiophene)(3)). In the case of F4TCNQ:5T complexes, the F_4TCNQ center located above above one inner thiophene ring (F_4TCNQ:5T (1)) or the bond connecting two inner thiophene rings (F_4TCNQ:5T (2)).

Fig. S7 shows bond length changes in 5T between the isolated 5T molecule and the F4TCNQ/5T complex.

The F_4TCNQ crystal belongs to the orthorhombic *Pbca* space group (group number 61) with the unit cell parameters a = 14.678 Å, b = 9.337 Å, c = 8.174 Å, and contains four molecules per unit cell located at inversion centers.[6] The differences in bond lengths between the optimized structure and the experimental structure are lower than 0.05 Å.

A comparison of the calculated and observed frequencies for F_4TCNQ and its complexes is given in Table S1.

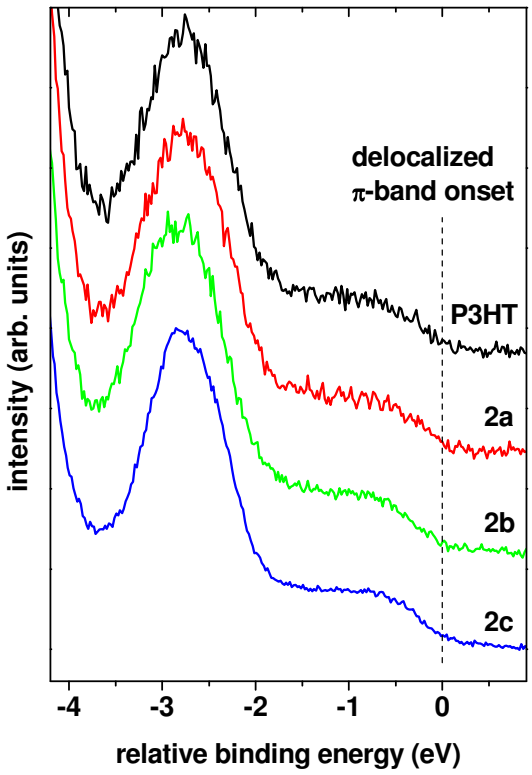

Fig. S1. UPS spectra of P3HT and 3HT-TFB copolymers **2a-c**. All spectra are shifted to align the maximum of the localized π-bands (at ca. -2.7 eV relative binding energy). The low binding energy onset (valence p-band edge) is indicated by the dashed line.

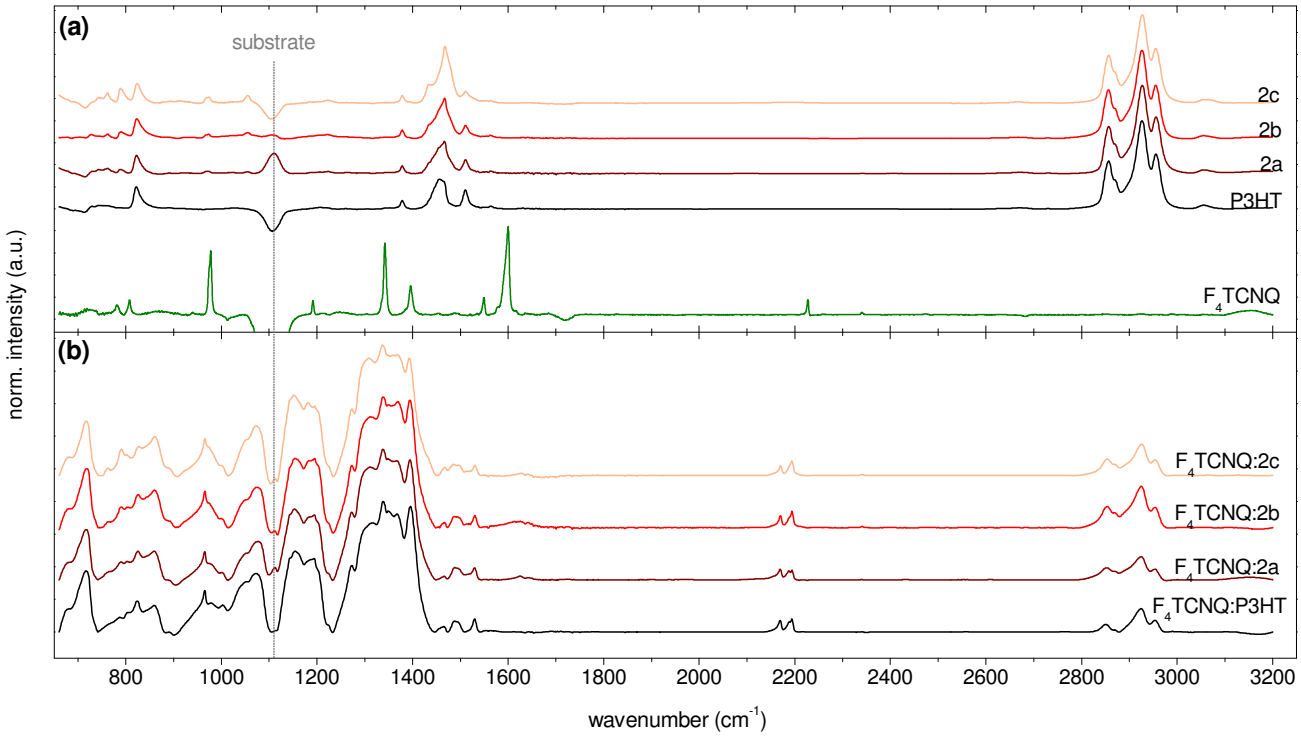

Fig. S2. Full-range IR spectra of (a) pure layers and (b) blend layers at 1:10 [F_4TCNQ:(thiophene monomer)] concentration.

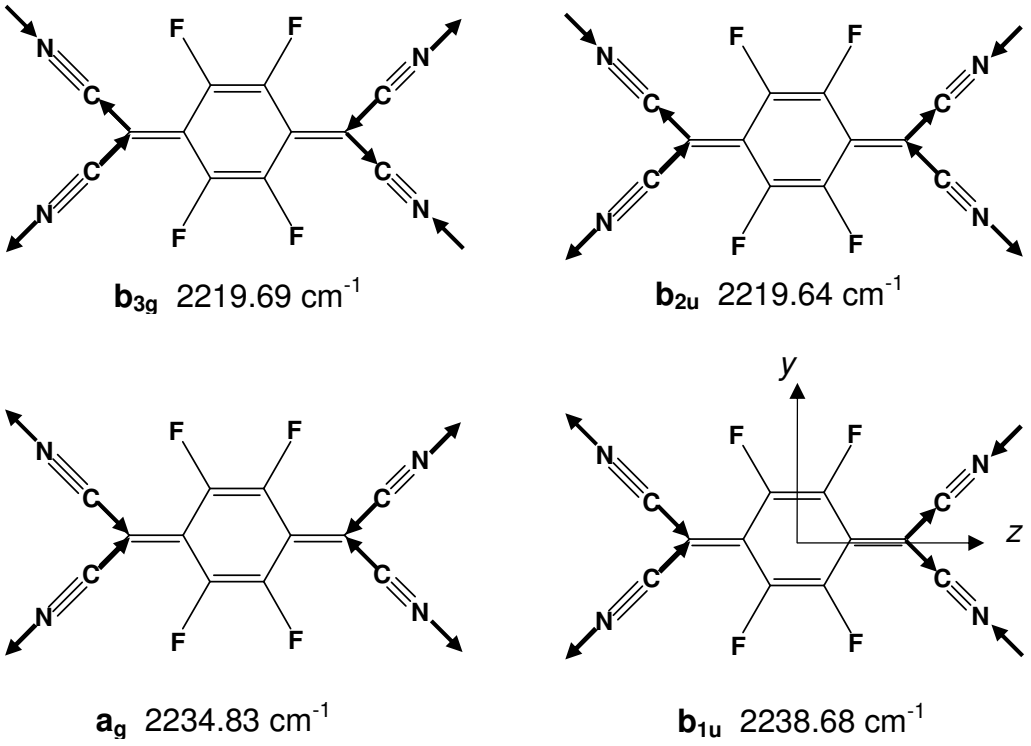

Fig. S3. B3LYP/6-31+G(d)-calculated normal modes and symmetry labels for isolated F_4TCNQ. The b_{3g} and a_g modes are IR-inactive while b_{2u} and b_{1u} are IR-active. F_4TCNQ is in the *yz*-plane.

F_4TCNQ:4T (1)

CT: 0.51e; $t_{eff\ H(D)-L(A)}$ = 692.92 meV; $\Delta E_{H(D)-L(A)}$ = 0.35 eV

F_4TCNQ:4T (2)

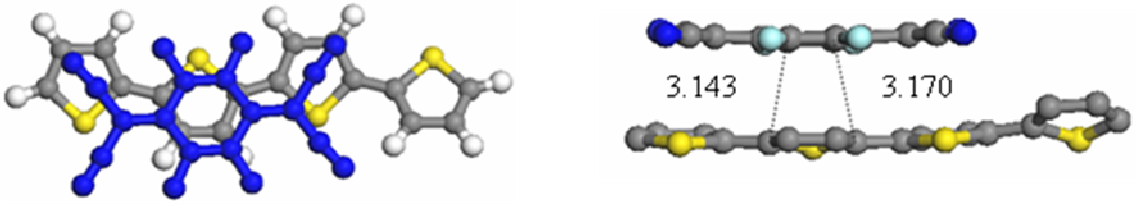

CT: 0.43e; $t_{eff\ H(D)-L(A)}$ = 532.55 meV; $\Delta E_{H(D)-L(A)}$ = 0.35 eV

F_4TCNQ:4T (3)

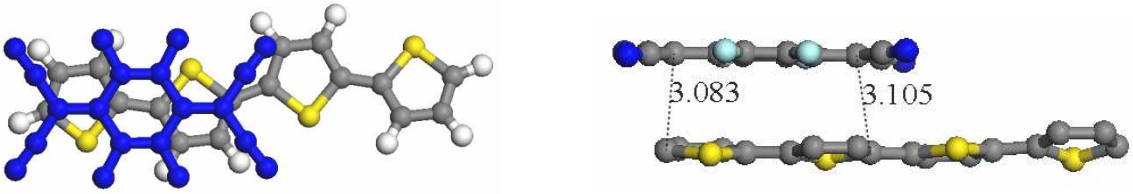

CT: 0.46e; $t_{eff\ H(D)-L(A)}$ = 598.31 meV; $\Delta E_{H(D)-L(A)}$ = 0.35 eV

Fig. S4. B3LYP-D/6-31+G(d)-optimized structures of three variants of the F_4TCNQ:4T charge-transfer complexes: (left) top view and (right) side view (for the sake of clarity, the hydrogen atoms are not shown). CT denotes the degree of charge transfer (in terms of partial electron charges from the donor to the acceptor); $t_{eff\ H(D)-L(A)}$ denotes the B3LYP/6-31+G(d)-calculated effective transfer integrals between HOMO of donor and LUMO of F_4TCNQ; $\Delta E_{H(D)-L(A)}$ is B3LYP/6-31+G(d)-calculated energy difference between HOMO of donor and LUMO of F4TCNQ.

F_4TCNQ:(dithiophene-TFB-thiophene) (1)

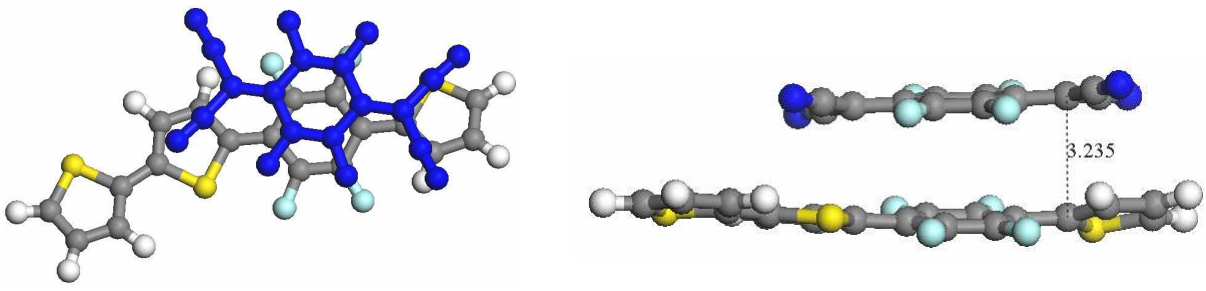

CT: 0.33e; $t_{eff\ H(D)-L(A)}$ = 506.45 meV; $\Delta E_{H(D)-L(A)}$ = − 0.09 eV

F_4TCNQ:(dithiophene-TFB-thiophene) (2)

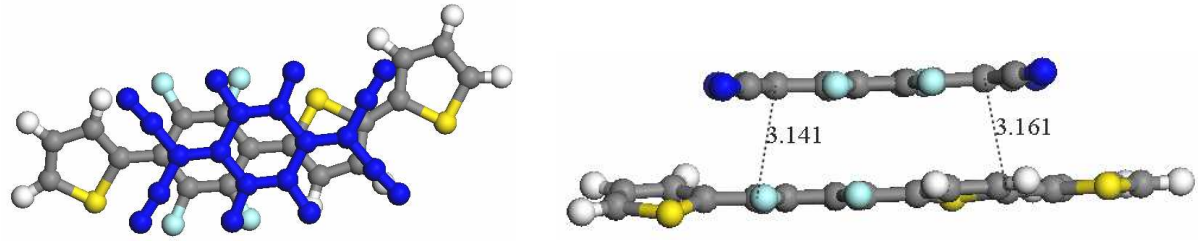

CT: 0.37e; $t_{eff\ H(D)-L(A)}$ = 618.21 meV; $\Delta E_{H(D)-L(A)}$ = −0.09 eV

F_4TCNQ:(dithiophene-TFB-thiophene) (3)

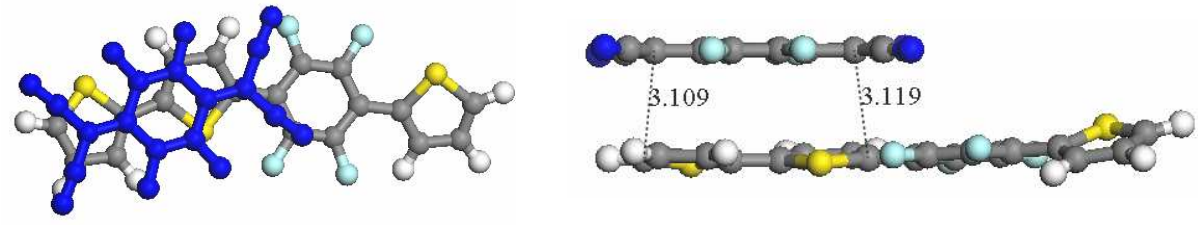

CT: 0.34e ; $t_{eff\ H(D)-L(A)}$ = 622.96 meV; $\Delta E_{H(D)-L(A)}$ = −0.09 eV

Fig. S5. B3LYP-D/6-31+G (d)-optimized structures of three variants of the F_4TCNQ:(dithiophene-TFB-thiophene) charge-transfer complexes: (left) top view and (right) side view. CT denotes the degree of charge transfer (in terms of partial electron charges from the donor to the acceptor); $t_{eff\ H(D)-L(A)}$ denotes the B3LYP/6-31+G(d)-calculated effective transfer integrals between HOMO of donor and LUMO of F_4TCNQ; $\Delta E_{H(D)-L(A)}$ is B3LYP/6-31+G(d)-calculated energy difference between HOMO of donor and LUMO of F4TCNQ.

F_4TCNQ:5T (1)

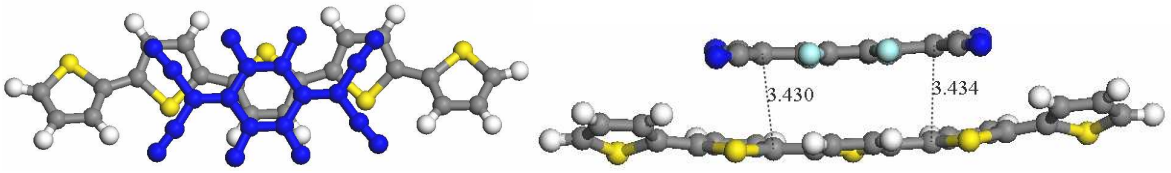

CT: 0.50e; $t_{eff\ H(D)-L(A)}$ = 527.76 meV; $\Delta E_{H(D)-L(A)}$ = 0.53 eV

F_4TCNQ:5T (2)

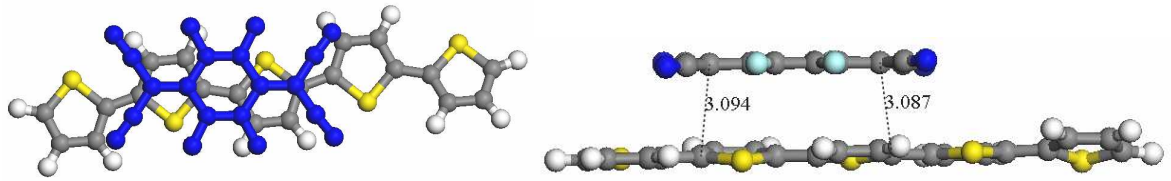

CT: 0.55e; $t_{eff\ H(D)-L(A)}$ = 647.22 meV; $\Delta E_{H(D)-L(A)}$ = 0.53 eV

Fig. S6. B3LYP-D/6-31+G (d)-optimized structures of three variants of the F_4TCNQ:5T charge-transfer complexes: (left) top view and (right) side view. CT denotes the degree of charge transfer (in terms of partial electron charges from the donor to the acceptor); $t_{eff\ H(D)-L(A)}$ denotes the B3LYP/6-31+G(d)-calculated effective transfer integrals between HOMO of donor and LUMO of F_4TCNQ; $\Delta E_{H(D)-L(A)}$ is B3LYP/6-31+G(d)-calculated energy difference between HOMO of donor and LUMO of F4TCNQ.

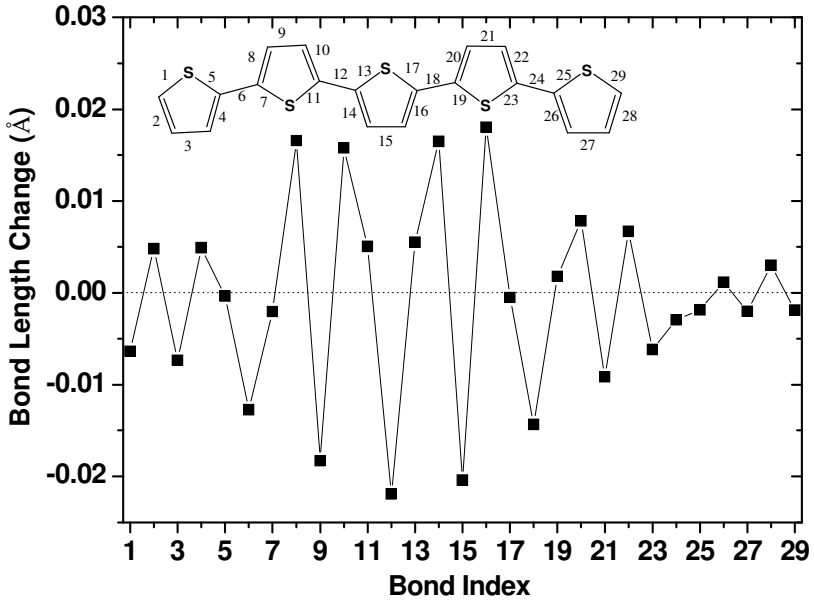

Fig. S7. Bond length changes in 5T between the isolated 5T molecule and the F4TCNQ/5T(2) complex.

Table S1. Theoretical and experimental vibrational frequencies of F_4TCNQ and the F_4TCNQ:oligothiophene/polymer complexes.[a]

F_4TCNQ							
Sym.[c]	*crystal*			Sym.	*isolated*		
	B3LYP/6-31G*[b]				B3LYP/6-31G*[b]		B3LYP/6-31+G*[b]	
A_u	2235.03	(0)		**b_{2u}**	**2227.22**	**(6.03)**	**2219.64**	**(6.23)**
B_{2u}	2235.07	(0)						
B_{1u}	2235.56	(45.27)						
B_{3u}	2235.43	(16.25)						
B_{3g}	2235.49	(0)		b_{3g}	2227.28	(0)	2219.69	(0)
B_{1g}	2235.36	(0)						
B_{2g}	2235.83	(0)						
A_g	2235.84	(0)						
B_{3g}	2250.74	(0)		a_g	2242.65	(0)	2234.83	(0)
B_{2g}	2250.82	(0)						
A_g	2250.98	(0)						
B_{1g}	2251.26	(0)						
B_{2u}	**2252.49**	**(532.61)**		b_{1u}	2246.40	(0.36)	2238.68	(1.31)
B_{3u}	2252.52	(10.76)						
A_u	2253.21	(0)						
B_{1u}	**2254.87**	**(669.61)**						
Experimental observation (F_4TCNQ solid film):								
	2214	**(weak)**	b_{2u}					
	2227	**(strong)**	b_{1u}					

F_4TCNQ:4T complexes						
	F_4TCNQ:4T (1)		*F_4TCNQ/4T (2)*		*F_4TCNQ/4T(3)*	
Sym.	B3LYP-D/6-31+G*					
b_{3g}	2205.30	(11.29)	2207.06	(20.91)	2207.64	(18.02)
b_{2u}	2206.84	(12.09)	2210.95	(8.95)	2211.19	(9.52)
a_g	**2224.87**	**(85.54)**	**2226.53**	**(80.62)**	**2226.84**	**(96.51)**
b_{1u}	**2228.02**	**(119.89**	**2232.40**	**(96.65)**	**2230.39**	**(182.41)**
Exp. observation (F_4TCNQ:P3HT/3HT-TFB):						
2169	**(strong)**	b_{3g}, b_{2u}				
2188	**(strong)**	a_g				
2194	**(strong)**	b_{1u}				

[a] All frequencies are related to C≡N stretching modes and given in cm^{-1}; intensities (km/mol) are given in brackets and can be compared within the same column; **large**, medium, and small (or IR-inactive) intensities are marked in **bold**, narrow, and grey, respectively.

[b] Scaled frequencies (x 0.9614).

[c] Regarding the symmetry of normal modes: capital letters are used for the crystal in order to distinguish with the isolated molecules and complexes.

References

(1) TURBOMOLE 6.0, a development of University of Karlsruhe and Forschungszentrum Karlsruhe GmbH, 1989-2007, TURBOMOLE GmbH, since 2007; available from http://www.turbomole.com.

(2) Senthilkumar, K.; Grozema, F. C.; Bichelhaupt, F. M.; Siebbeles, L. D. A. *J. Chem. Phys.* **2003**, *119*, 9809.

(3) Valeev, E. F.; Coropceanu, V.; da Silva Filho, D. A.; Salman, S.; Brédas, J.-L. *J. Am. Chem. Soc.* **2006**, *128*, 9882.

(4) Gaussian 03 E. 01, F., M. J.; Trucks, G. W.; Schlegel, H. B.; Scuseria, G. E.; Robb, M. A.; Cheeseman, J. R.; Montgomery, Jr., J. A.; Vreven, T.; Kudin, K. N.; Burant, J. C.; Millam, J. M.; Iyengar, S. S.; Tomasi, J.; Barone, V.; Mennucci, B.; Cossi, M.; Scalmani, G.; Rega, N.; Petersson, G. A.; Nakatsuji, H.; Hada, M.; Ehara, M.; Toyota, K.; Fukuda, R.; Hasegawa, J.; Ishida, M.; Nakajima, T.; Honda, Y.; Kitao, O.; Nakai, H.; Klene, M.; Li, X.; Knox, J. E.; Hratchian, H. P.; Cross, J. B.; Bakken, V.; Adamo, C.; Jaramillo, J.; Gomperts, R.; Stratmann, R. E.; Yazyev, O.; Austin, A. J.; Cammi, R.; Pomelli, C.; Ochterski, J. W.; Ayala, P. Y.; Morokuma, K.; Voth, G. A.; Salvador, P.; Dannenberg, J. J.; Zakrzewski, V. G.; Dapprich, S.; Daniels, A. D.; Strain, M. C.; Farkas, O.; Malick, D. K.; Rabuck, A. D.; Raghavachari, K.; Foresman, J. B.; Ortiz, J. V.; Cui, Q.; Baboul, A. G.; Clifford, S.; Cioslowski, J.; Stefanov, B. B.; Liu, G.; Liashenko, A.; Piskorz, P.; Komaromi, I.; Martin, R. L.; Fox, D. J.; Keith, T.; Al-Laham, M. A.; Peng, C. Y.; Nanayakkara, A.; Challacombe, M.; Gill, P. M. W.; Johnson, B.; Chen, W.; Wong, M. W.; Gonzalez, C.; and Pople, J. A.; ; E. 01 ed.; Gaussian, Inc., Wallingford CT, 2004.

(5) T. J. Emge; M. Maxfield; D. O. Cowan; Kistenmacher, T. J. *Mol. Cryst. Liq. Cryst.* **1981**, *65*, 161.

(6) Saunders, V. R.; Dovesi, R.; Roetti, C.; Orlando, R.; Zicovich-Wilson, C. M.; Harrison, N. M.; Doll, K.; Civalleri, B.; Bush, I. J.; D'Arco, P.; Llunell, M. *CRYSTAL06 User's Manual* **2006**.

(7) Scott, A. P.; Radom, L. *J. Phys. Chem.* **1996**, *100*, 16502.

PHYSICAL REVIEW B **87**, 115209 (2013)

Comprehensive picture of *p*-type doping of P3HT with the molecular acceptor F_4TCNQ

P. Pingel and D. Neher*

Soft Matter Physics, Institute of Physics and Astronomy, University of Potsdam, Karl-Liebknecht-Str. 24-25, D-14476 Potsdam, Germany

(Received 1 February 2013; published 28 March 2013)

By means of optical spectroscopy, Kelvin probe, and conductivity measurements, we study the *p*-type doping of the donor polymer poly(3-hexylthiophene), P3HT, with the molecular acceptor tetrafluorotetracyanoquinodimethane, F_4TCNQ, covering a broad range of molar doping ratios from the ppm to the percent regime. Thorough quantitative analysis of the specific near-infrared absorption bands of ionized F_4TCNQ reveals that almost every F_4TCNQ dopant undergoes integer charge transfer with a P3HT site. However, only about 5% of these charge carrier pairs are found to dissociate and contribute a free hole for electrical conduction. The nonlinear behavior of the conductivity on doping ratio is rationalized by a numerical mobility model that accounts for the broadening of the energetic distribution of transport sites by the Coulomb potentials of ionized F_4TCNQ dopants.

DOI: 10.1103/PhysRevB.87.115209 PACS number(s): 81.05.Fb, 68.55.Ln, 72.80.Le, 73.61.Ph

I. INTRODUCTION

Intentionally doped organic semiconductors are nowadays commonly used as transport and injection layers in state-of-the-art organic electronic devices.[1] Being the key concept for the versatility of inorganic semiconductors, controlled doping suggests tremendous benefit by enabling the tuning of the organic semiconductor's electrical, optical, and morphological properties.

Stable doping of organic semiconductors has been realized by adding strong molecular donors or acceptors to conjugated small molecules or polymers. In particular, 2,3,5,6-tetrafluoro-7,7,8,8-tetracyanoquinodimethane (F_4TCNQ) has been used as electron acceptor to *p* dope evaporated[2–6] and solution-processed[7–16] organic semiconductors due to its high electron affinity of 5.24 eV.[2] Upon doping the prototypical polymeric semiconductor poly(3-hexylthiophene) (P3HT) with F_4TCNQ, electrical conductivities up to 100 S/m have been reported.[7]

It is well established that the doping effect, i.e., the increase of the majority charge carrier density, is based on a charge transfer reaction involving an appropriate donor and acceptor. Two contradictory models that are commonly used to explain the donor-acceptor ground-state interaction are sketched in Fig. 1 using the example of P3HT being doped with F_4TCNQ. In the integer charge transfer model [see Fig. 1(a)], an electron is completely transferred from P3HT to the F_4TCNQ acceptor. Since the concentration of F_4TCNQ in the P3HT matrix is typically low (usually a few mol % or below), it is expected that the transferred electron remains fixed at the F_4TCNQ molecule. The associated hole on P3HT can be either Coulombically bound by the F_4TCNQ anion or may move freely within the matrix of P3HT. The notion of a strong Coulomb binding is in line with the peculiar observation that the free-charge carrier density is often far lower than the dopant concentration.[13,17–20] The strong Coulomb binding is mediated by the low permittivity in organic semiconductor solids. In contrast, it has been reported that the free-charge carrier density does not depend on temperature in some F_4TCNQ-doped small-molecule organic semiconductors.[3,5,6] This has been explained in terms of the entire ionization of all applied acceptors and, if at all, the only shallow trapping of the doping-induced majority charge carriers.

Figure 1(b) illustrates an alternative model of molecular doping that relies on the formation of hybrid charge transfer complexes upon the interaction of the donor and acceptor. Based on density functional theory, studies using a quaterthiophene model for P3HT and F_4TCNQ as dopant, Aziz *et al.*[7] suggested partial charge transfer between these donor and acceptor species and that a supramolecular charge transfer complex (CTC) is formed whose highest occupied and lowest unoccupied molecular orbitals, HOMO and LUMO, respectively, are derived from both the neutral P3HT HOMO and F_4TCNQ LUMO. Similar results have been obtained for a number of F_4TCNQ-*p*-doped oligothiophenes and pentacene and for naphthalene-tetracaboxylic-dianhydride (NTCDA) *n*-doped with a tetrathiafulvalene (TTF) derivative.[21,22] In this model, holes are created due to the electron deoccupation of P3HT HOMOs (and electron occupation of CTC LUMOs) as a consequence of Fermi-Dirac statistics. Whether these holes are free or Coulombically bound to charged CTCs is open to question.

In a previous report, we characterized the free-hole density and conductivity of P3HT layers that have been doped by F_4TCNQ at low to moderate dopant concentrations, i.e., in the ppm to per mill regime. We found that only 5% of the F_4TCNQ dopants took effect in creating free holes that contribute to electrical conduction. Moreover, we found that the conductivity increases sublinearly (with an exponent of approximately 0.6) with doping ratio. The latter is in conflict with the frequent observation of a superlinear increase of the conductivity, which has been related to trap filling by the doping-induced charge carriers[1] or an increase of permittivity in highly doped layers.[20]

Here, we aim at understanding the process of doping P3HT with F_4TCNQ and the electrical characteristics of such doped layers by means of optical absorption spectroscopy, surface potential measurements, and conductivity measurements of hole-only devices. We can now confirm that the concentration of ionized F_4TCNQ molecules is (within an error of 50%) given by the molecular ratio of the donor and acceptor in solution, meaning that most acceptor molecules are incorporated into the layer and that almost every F_4TCNQ dopant undergoes integer charge transfer with a P3HT donor site. Therefore the low concentration of mobile holes implies that

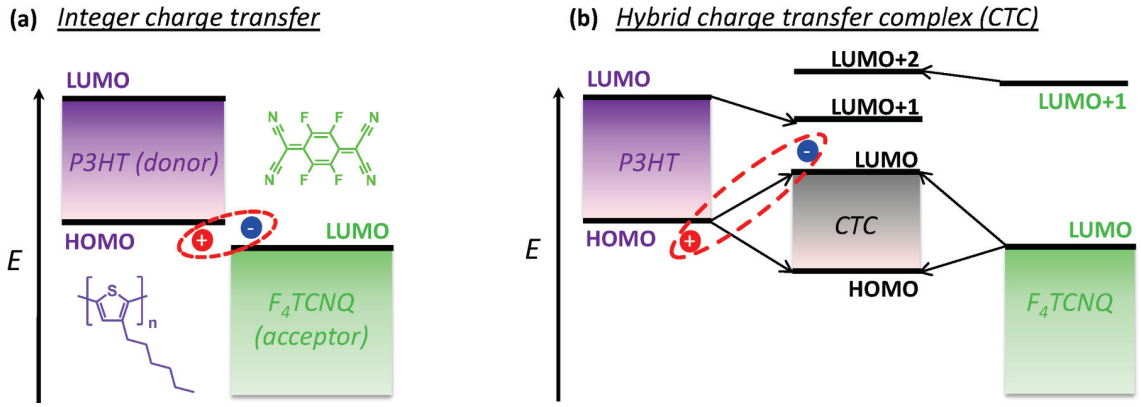

FIG. 1. (Color online) Contradictory models of the charge transfer between P3HT and F_4TCNQ. (a) Integer charge transfer model that presumes full ionization of donor and acceptor, resulting in a hole-F_4TCNQ anion pair that is bound or can split up. (b) Hybrid charge transfer model according to Ref. 7, which presumes the formation of hybrid supramolecular orbitals upon electronic interaction of P3HT and F_4TCNQ. Free-charge generation might occur by intermolecular excitation involving the HOMO of unreacted P3HT and the LUMO of a nearby CTC.

most of the created P3HT polarons remain strongly bound to a F_4TCNQ anion. The electrical conductivity turns from a sublinear increase at low to moderate doping ratios towards a superlinear increase at high doping ratios in the mol% regime. This dependency is quantitatively reproduced by a numerical mobility model of Arkhipov *et al.*,[23,24] which considers the broadening of the energetic landscape for charge transport upon doping by the Coulomb potential of the left-behind F_4TCNQ anions.

II. EXPERIMENT

F_4TCNQ has been obtained and used as received from Sigma-Aldrich. Our P3HT sample is a molecular weight fraction ($M_w = 35.8$ kg/mol, $M_n = 27.0$ kg/mol) with deuterated hexyl side chains for prospective neutron scattering experiments. Our extensive previous investigations show that the structural and electronic properties are not altered by the deuteration and that the performance of this P3HT fraction is outstanding in field-effect devices.[25–27] Doped samples have been prepared by mixing separate chloroform solutions of P3HT and F_4TCNQ according to the desired doping ratio χ. A doping ratio of, for instance, 1:1000 means that one F_4TCNQ molecule is added per 1000 thiophene repeat units of P3HT and is equivalent to $\chi = 10^{-3}$.

UV-Vis-NIR absorption spectra have been recorded with a Cary 5000 photospectrometer. Solution samples were prepared from 2 and 0.5 g/l solutions of P3HT and F_4TCNQ, respectively. The optical path length of the quartz cuvette was 1 mm and 10 mm, respectively. The presented solution spectra are the averages of five consecutive scans in order to reduce the noise in the NIR. Solid samples have been prepared on glass substrates after cleaning with common organic solvents in an ultrasonic bath. Sample solutions, based on 10-g/l P3HT and 0.5-g/l F_4TCNQ in chloroform, were spin coated on the glass substrates at 1000 rpm for 30 sec in inert N_2 atmosphere, yielding layers with a thickness of typically ~100 nm. Film spectra have been recorded using an integrating sphere in order to account for light scattering and reflection. The presented spectra are based on the averages of ten consecutive transmission/reflection scans.

Surface (Kelvin) potential measurements of undoped and doped layers on metal substrates have been repeatedly performed in the dark using a SKM KP 4.5 (KP Technology Ltd.) with 2-mm probe diameter in a N_2-filled glovebox with <1 ppm O_2 and H_2O contamination. Typically, fresh samples were stored in the glovebox for 30 min prior to the measurement in order to allow for degassing of residual solvent traces. Calibration of the tip work function was done against highly ordered pyrolytic graphite (HOPG), for which we assumed a work function of 4.6 eV.[28] Metal electrodes have been prepared on cleaned glass substrates. The glass surface was precovered with a smoothing layer of the PEDOT:PSS formulation Clevios™ P VP AI 4083 by spin-coating at 5000 rpm for 30 sec and subsequent annealing at 180 °C for 10 min. Then, 50 nm of aluminum or copper was evaporated under high-vacuum conditions. Sample preparation and handling continued in N_2 atmosphere. Undoped and doped P3HT layers were deposited by spin-coating at 1500 rpm for 30 sec. Solutions were based on 0.5–25-g/l P3HT and 0.02–0.5-g/l F_4TCNQ in chloroform, depending on the desired layer thickness. Note that the present preparation conditions typically result in layer structures with a considerable amount of disordered material and, therefore, random molecular orientations.[16,25,27] Due to the large probe diameter, the surface potential data represent macrocopic means across these portions of the layer surfaces.

Current-voltage characteristics have been recorded with a Keithley 2400 source-measure unit. Hole-only devices were prepared on glass substrates with patterned indium-tin-oxide electrodes. After oxygen plasma treatment at 200 W for 3 min, Clevios™ P VP AI 4083 PEDOT:PSS has been spin-coated at 1500 rpm for 30 sec, followed by annealing at 180 °C for 10 min. Sample preparation continued under inert conditions. Undoped and doped P3HT layers were spin-coated at 500 rpm for 30 sec from solutions based on 30-g/l P3HT and 0.5-g/l F_4TCNQ, yielding thick layers in the range of 250–900 nm similar to our previous metal-insulator-semiconductor devices.[15] The samples were completed by evaporation of 5-nm MoO_3 and 100-nm Al as top electrodes. The devices have been encapsulated using Araldite 2011 two-component epoxy resin and measured outside the glovebox.

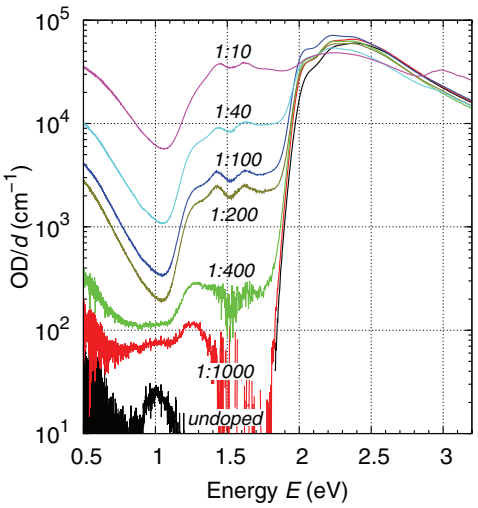

FIG. 2. (Color online) Thickness-normalized absorbance of undoped and F_4TCNQ-doped P3HT layers.

III. RESULTS & DISCUSSION

A. Optical spectroscopy

In order to gather information on the nature of the F_4TCNQ-P3HT charge transfer, we performed UV-Vis-NIR absorption spectroscopy on thin films and in solution. Figure 2 shows the optical absorbance normalized by layer thickness of undoped and F_4TCNQ-doped P3HT layers. The thickness of these layers was typically around 100 nm. Upon doping, a pronounced subband gap absorption occurs in addition to the absorption of undoped P3HT. A qualitative comparison of the NIR region to published spectra of P3HT polarons[29,30] and fully ionized F_4TCNQ anions[31,32] allows a clear assignment of the prominent 1.43 and 1.62 eV peaks to the absorption of singly negatively charged F_4TCNQ. The rectangular-shaped broad band between 1.2 and 1.8 eV and the increasing absorption below 1 eV are typical features of polarons in P3HT. Note that if the F_4TCNQ-P3HT charge transfer resulted in hybrid supramolecular species with partial electron transfer, their spectra should be severely different from the observed case. In particular, these species would introduce new absorption transitions between their hybrid supramolecular orbitals.

In order to quantify the absolute concentration of ionized acceptors formed in blends of F_4TCNQ and P3HT, we decompose the NIR absorption into the P3HT polaron and F_4TCNQ anion parts. For this analysis, suitable reference spectra of the charged compounds are essentially needed. Unfortunately, spectra and absolute values of the extinction coefficients (or absorption cross-sections) of P3HT[29,30,33–36] and F_4TCNQ polarons in solid thin films are not consistent or not available. Moreover, the P3HT polaron absorption is very sensitive to the layer's preparation conditions and the properties of the specific P3HT sample, rendering a meaningful algebraic decomposition difficult. We, therefore, start by analyzing the absorption spectra of F_4TCNQ-P3HT blends in chloroform solution.

The spectra of F_4TCNQ-P3HT chloroform solutions with varied doping ratios are displayed in Fig. 3(a). Qualitatively, the solution spectra coincide with the spectra of the doped layers, meaning that charge transfer takes place already in solution upon the admixture of F_4TCNQ and P3HT. In more detail, the solution spectra reveal a further distinct absorption feature at 2.0 eV which is only present if F_4TCNQ was added. This transition is hidden in the thin-film spectra by the strongly red-shifted absorption of neutral planarized P3HT.

Next, we reconstruct the NIR absorption of the doped solution spectra by weighted sums of a F_4TCNQ anion and a P3HT polaron reference spectrum. An example of the reconstruction of the 1:100-doped sample is plotted in Fig. 3(b). As a reference for the extinction of F_4TCNQ anions we use the molar extinction coefficient spectrum published in Ref. 32. There, the extinction coefficients of neutral, singly, and doubly ionized F_4TCNQ bound in charge-transfer salt crystals are reported. The advantage of using these spectra is that the amount of ionized F_4TCNQ is exactly known from

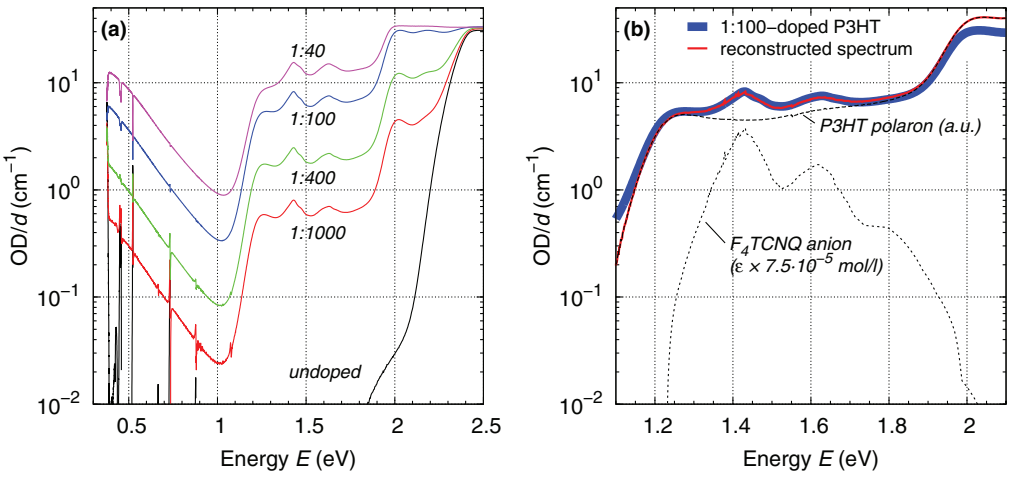

FIG. 3. (Color online) (a) Absorbance per length of pure (undoped) P3HT and mixtures with F_4TCNQ (molar mixing ratios given in the figure) in chloroform solution. The undoped sample had a concentration of 2-g/l P3HT in chloroform. Absorbance is cut off beyond 2 eV for the 1:40-doped sample due to instrumental limitations. (b) Reconstruction of the P3HT polaron/F_4TCNQ anion absorption of the 1:100-doped P3HT sample from reference spectra. The F_4TCNQ anion spectrum is reprinted with permission from Ref. 32. Copyright 1989 American Chemical Society.

TABLE I. Concentrations of ionized F_4TCNQ found in a mixture of F_4TCNQ and P3HT in chloroform at various doping ratios.

Doping ratio	P3HT[a] repeat units (10^{-2} mol/l)	F_4TCNQ[a] (10^{-5} mol/l)	F_4TCNQ^-[b] (10^{-5} mol/l)	Ionized fraction
1:1000	1.19	1.19	0.6	0.50
1:400	1.18	2.96	2.0	0.68
1:100	1.13	11.3	7.5	0.66
1:40	1.03	25.8	18	0.70

[a]Intentionally applied amount in solution.
[b]Measured by decomposition of the optical spectra.

stoichiometry. A comparison between the reported spectra and our own absorption measurements of neutral F_4TCNQ in chloroform solution gives a close absolute agreement of the spectral shape and extinction coefficients. Another solution sample with a high but unknown amount of ionized F_4TCNQ matches the spectral shape of the crystal reference spectrum with respect to the anion absorption bands in the NIR (see Supplemental Material[37] and Ref. 32 therein). A P3HT polaron reference spectrum was realized by doping the neutral P3HT powder in saturated iodine vapor. The exposed powder was then dissolved into chloroform at a concentration of 0.025 g/l (higher concentrations were not possible due to the limited solubility of the doped compound).

The algebraic reconstruction of the F_4TCNQ-P3HT blend spectra in solution allows for an estimate of the F_4TCNQ anion concentration. Table I compares these values with the concentrations of actually applied F_4TCNQ upon blending with P3HT. Approximately 50–70% of the initial quantity of F_4TCNQ is retrieved as anions. As expected, this ionization efficiency is lower in very dilute solutions (see Supplemental Material[37] and Ref. 38 therein). Assuming that the F_4TCNQ anion and donor-acceptor charge transfer pair concentrations are equal, we can now calculate the molar extinction coefficient of the charge transfer pairs. At 1.52 eV, the notable minimum in between the two major F_4TCNQ anion peaks, the molar extinction coefficient amounts to $(8.3 \pm 1.8) \times 10^4$ l/mol/cm. We use this value for a rough estimate of the concentration of donor-acceptor pairs that have undergone charge transfer in the F_4TCNQ-doped P3HT layers, the results of which are summarized in Table II.

It turns out that the concentration of ionized F_4TCNQ is only little lower than the molecular concentration calculated from the molar mixing ratio in solution (assuming a mass density of 1.1 g/cm^3 of the solid film[39]). This means that the majority of the applied F_4TCNQ acceptor molecules undergoes integer charge transfer with P3HT. This is a vitally important finding, because it is usually found from electrical and electrostatic measurements that the density of doping-induced free holes is drastically lower than the dopant density,[13,17–20] as we will also show in the following. By the same token, the significant formation of isolated clusters of F_4TCNQ, which has been suggested to explain the reduced free-charge carrier density by some authors[14,40] and has been excluded by others,[1,8,16] can be ruled out here as well.

TABLE II. Concentrations of ionized F_4TCNQ found in F_4TCNQ-doped P3HT layers at various doping ratios.

Doping ratio	F_4TCNQ^-[a] (m^{-3})	F_4TCNQ[b] (m^{-3})	Ionized fraction
1:200	$(1.5 \pm 0.3) \times 10^{25}$	2×10^{25}	0.77 ± 0.17
1:100	$(2.0 \pm 0.5) \times 10^{25}$	4×10^{25}	0.51 ± 0.11
1:40	$(6.3 \pm 1.3) \times 10^{25}$	1×10^{26}	0.64 ± 0.14
1:10	$(2.7 \pm 0.6) \times 10^{26}$	4×10^{26}	0.67 ± 0.15

[a]Measured by analysis of the optical spectra in Fig. 2.
[b]Intentional amount according to the doping ratio, assuming a mass density of P3HT[39] of $\rho = 1.1$ g/cm^3.

B. Surface (Kelvin) potential measurements

Generally, a comparison of the surface potentials of an uncovered conductive substrate and the same substrate coated with a polymer yields combined information on the interface energetics and on the electronic structure of the polymer bulk.[41,42] As we have shown recently, deposition of an undoped conjugated polymer on an electrode with sufficiently small work function leads to electron transfer from the electrode into tail states of the polymer's lowest unoccupied molecular orbital (LUMO) manifold (see Fig. 4, left panels). This process is accompanied by a continuous increase of the work function of the sample (band bending) with increasing polymer layer thickness.[43] From a numerical analysis of the band bending, quantitative information on the density of tail states (DOTS) can be obtained. Similar to this, deposition of the same polymer on an electrode with sufficiently high work function induces holes into the polymer and allows for measuring the DOTS derived from the HOMO manifold.

Experimental work functions at the surface of undoped P3HT layers with varied thicknesses are plotted as solid black symbols in Fig. 5(a). These measurements have been performed with layers on aluminum ($\Phi_{Sub} \approx 3.15$–3.3 eV, upper circles) and on copper ($\Phi_{Sub} \approx 4.5$–4.6 eV, lower triangles). Note that the work functions of the covered metal electrodes can be offset from that of the bare metals due to the formation of interface dipoles.[44] As for other conjugated polymers, we find that the sample work function increases with P3HT thickness on aluminum, while it decreases on copper. The observation that both work function curves tend to saturate at well-separated values is consistent with the injection of electrons into LUMO-derived states on aluminum and the injection of holes into HOMO-derived states on copper, as explained above.

As seen in Fig. 5(a), the course of the work function of F_4TCNQ-doped P3HT on aluminum as a function of film thickness is qualitatively different from the undoped samples. When a *p*-doped layer is deposited onto a low work function metal such as aluminum, a classical Schottky contact is formed. Thereby, mobile doping-induced holes in the HOMO distribution of P3HT drift towards the aluminum contact and get neutralized at the metal interface. The immobile F_4TCNQ anions are left behind and form a negatively charged depletion zone (see Fig. 4, right panels). If all holes created by doping were extracted, the charge density in the depletion zone would be determined by the total density of ionized F_4TCNQ. We will show later that this is not the case in F_4TCNQ-doped P3HT

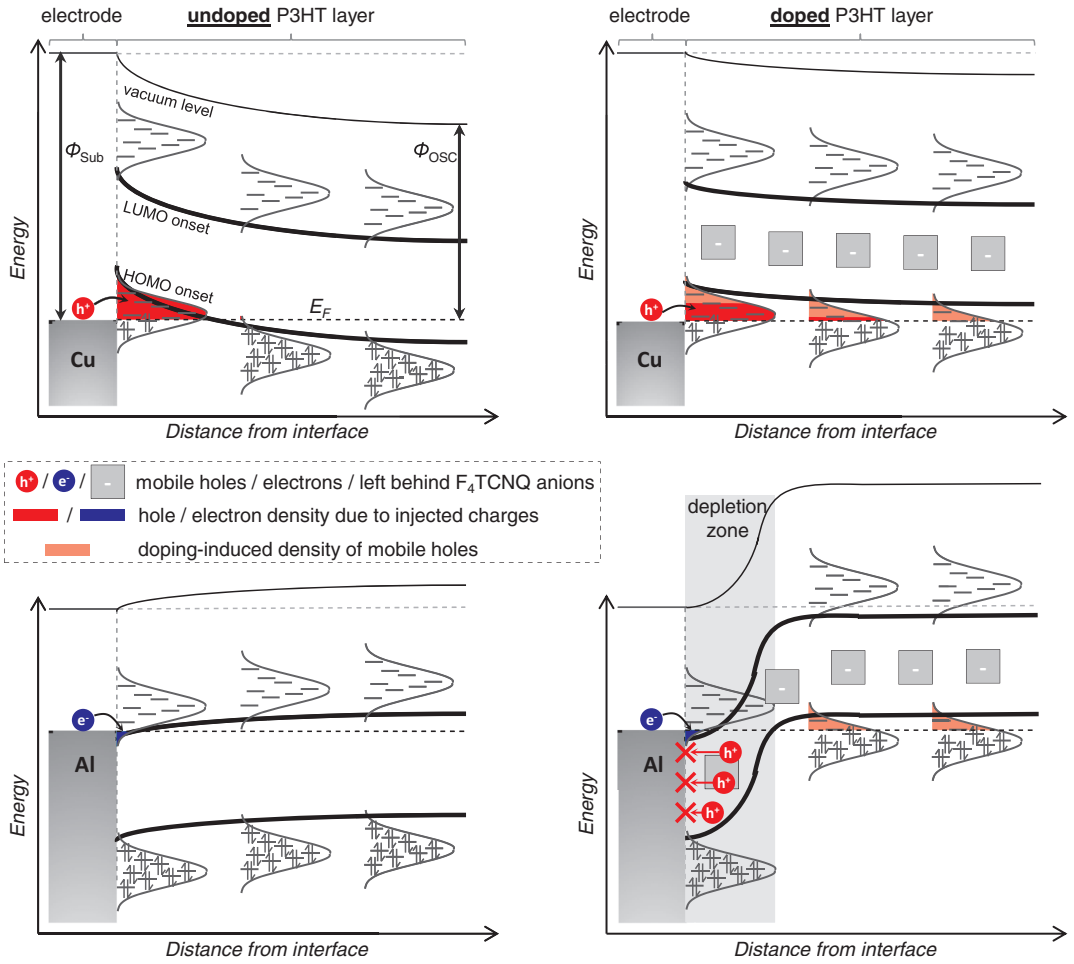

FIG. 4. (Color online) Scheme of the electron and hole transfer of undoped (left) and doped (right) P3HT layers on high (Cu, top) and low work function (Al, bottom) metal substrates.

layers. For layer thicknesses that are thinner than the depletion zone width, the work function curve has a parabolic shape [see Fig. 5(a)], which implies a homogeneous distribution of F_4TCNQ in the sample. From the width of the depletion layer, the anion density—and, therefore, the mobile-hole density—can be calculated. For larger layer thicknesses, the work function of doped P3HT layers on both aluminum and copper will merge to a common value, which is the bulk Fermi level of the doped semiconductor. Note that this value is about 4.45 eV, which is well within the tail of the typical distribution of HOMO levels in P3HT. However, the change of the surface potential of P3HT on aluminum is rather gradual. In order to gather information on the density-of-states (DOS) distributions and the hole densities in the polymer layers, we have numerically analyzed the work function versus layer thickness curves following the general procedures by Lange *et al.*,[43] but now including doping.

The surface potential is measured using the capacitor-like configuration of a Kelvin probe setup. The potential difference between the sample and a reference tip is adjusted such that the gap in between those is field free. The electrical potential $\phi(x)$ in the polymer layer hence follows the Poisson equation

$$\frac{d^2\phi}{dx^2} = \frac{e}{\epsilon_r \epsilon_0}[n(x) - p(x) + N_a] \tag{1}$$

with the boundary condition $\frac{d\phi}{dx}(L) = 0$, where $n(x)$ and $p(x)$ are the electron and hole densities in the LUMO and HOMO, respectively, N_a is the density of ionized F_4TCNQ acceptor molecules, x is the distance from the electrode, L is the total layer thickness, and $\epsilon_r = 3.5$ is the relative permittivity. The equilibrium local charge densities are related to the HOMO- and LUMO-derived density-of-states (DOS) distributions g_{HOMO} and g_{LUMO}, the Fermi level E_F, and the local potential according to

$$n(x) = \int_{-\infty}^{\infty} \frac{g_{\mathrm{LUMO}}[E + e\phi(x)]}{1 + \exp\left(\frac{E - E_F}{k_B T}\right)} dE \quad \text{and} \tag{2}$$

$$p(x) = \int_{-\infty}^{\infty} \frac{g_{\mathrm{HOMO}}[E + e\phi(x)]}{1 + \exp\left(\frac{E_F - E}{k_B T}\right)} dE. \tag{3}$$

Due to the large reservoir of electrons, the common Fermi level is assumed to be equal to the work function of the (metal)

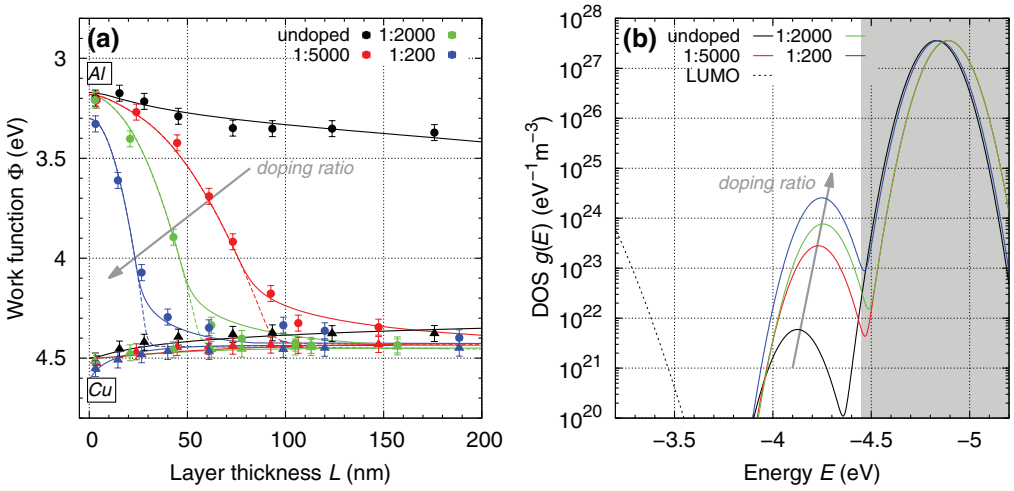

FIG. 5. (Color online) (a) Experimental data (symbols) and numerical calculated work functions (lines) of undoped and F_4TCNQ-doped P3HT layers on aluminum and copper. Numerical calculations assume Arkhipov's DOS distribution including doping-induced tail states (solid lines) or a single-Gaussian DOS shape (dashed lines). (b) Corresponding HOMO DOS distributions based on Arkhipov's model. The unshaded energy range is probed in the Kelvin probe experiment. A minor contribution of LUMO levels (dotted line) is inferred from the work-function curve of undoped P3HT on aluminum.

substrate ($\Phi_{\mathrm{Sub}} = -E_F$). The work function at the organic semiconductor surface can be calculated by

$$\Phi_{\mathrm{OSC}}(L) = \Phi_{\mathrm{Sub}} - \phi(L). \tag{4}$$

Unfortunately, a direct extraction of the DOS distributions from work-function data is not possible and therefore an *a priori* assumption about its functional form is indispensable. At first, we attempt to reconstruct the work-function curves by assuming a single Gaussian-shaped $g_{\mathrm{HOMO}}(E)$. Close reproduction the work-function data of undoped P3HT on copper, and our previous analysis of the hole mobilities in F_4TCNQ-doped P3HT layers[15] suggest to set the total density of states N to 7×10^{26} m^{-3} and the width parameter σ to 78 meV. In the work-function calculations of the doped and undoped samples, the center of the HOMO DOS distribution E_{HOMO} varies from −4.75 to −4.83 eV. For a proper description of the undoped-P3HT work-function data, a minor injection from aluminum into the tail of the P3HT LUMO distribution has been taken into account in these calculations and in the following [see Fig. 5(b)].

While the calculated work functions for layers with different thicknesses on copper (not shown) are in satisfactory agreement with the experimental data, there are distinct discrepancies for the doped P3HT layers on aluminum (dashed lines in Fig. 5). Most strikingly, the assumption of a simple Gaussian DOS shape is not in line with the long tail of the work-function curves towards saturation, which indicates that a proper description must account for doping-induced states at the low-energy tail of the DOS distribution.

The broadening of the DOS distribution due to ionized dopants has been repeatedly suggested.[23,24,45–48] Arkhipov *et al.* discussed a model that accounts for the Coulomb interaction of the doping-induced charge carriers with the left-behind ionized dopants.[23,24] In this model, the superposition of the original DOS distribution and the Coulomb wells of the ionized dopants is simplified by considering the site nearest to a dopant ion as a trap. The resulting HOMO DOS reads

$$g_{\mathrm{HOMO}}(E) = \frac{N - N_d}{N} g_i(E) + \frac{N_d}{N} g_i\left[E - \frac{e^2}{4\pi\epsilon_0\epsilon_r a} - U_m(N_d)\right], \tag{5}$$

where N is the total site density in an undoped sample, N_d is the density of left-behind ionized (acceptor) dopants (assumed to be equal to the mobile-hole density), and $g_i(E)$ is a Gaussian-shaped DOS distribution centered at E_{HOMO} with a width of σ. The density of ionized dopants causes a reduction of the intrinsic (undoped) DOS (first term) and a subsequent formation of an equal amount of trap states shifted by the energy of the Coulomb interaction (second term). Since the DOS distribution of the undoped material is Gaussian, the distribution of the trap states is chosen to be Gaussian accordingly. Thereby, a represents the typical distance between a dopant ion and the trapped charge carrier. Physically, a should correspond to the distance between the dopant ion and an adjacent site of the semiconductor. The interaction energy is corrected for the overlap of the Coulomb potentials of neighboring dopant ions at high doping ratios by the nontrivial value of $U_m(N_d)$. For simplicity, the width parameter σ is assumed to be equal for both overlapping Gauss functions g_i. Within our previous numerical computation of hopping mobilities, Eq. (5) proved to be eligible to reproduce the doping ratio dependence of the hole mobility in F_4TCNQ-doped P3HT layers.[15] In addition, note that a Gaussian-shaped distribution of subband gap states was reported for F_4TCNQ-doped *N*,*N*'-diphenyl-*N*,*N*'-bis(1-naphthyl)-1,10-biphenyl-4,4"-diamine (α-NPD) as inferred from Kelvin probe force measurements on organic field-effect transistors.[48]

Using the DOS function from Eq. (5) and the parameters in Table III, a good agreement between the calculated and the experimental work functions is reached [see solid lines in Fig. 5(a)]. The according DOS distributions are plotted in Fig. 5(b). Most remarkably, the calculated curves feature the

TABLE III. Parameters of the DOS distributions according to Arkhipov's model, which have been used for the calculation of surface potentials in Fig. 5.[a]

Doping ratio	N_d[b] (m^{-3})	E_{HOMO}[c] (eV)
Undoped	1.16×10^{21}	−4.83
1:5000	5.5×10^{22}	−4.89
1:2000	1.5×10^{23}	−4.89
1:200	5×10^{23}	−4.94

[a]Total site density $N = 7 \times 10^{26}$ m^3, DOS width parameter $\sigma_{HOMO} =$ 78 meV, anion-trapped hole pair distance $a = 0.57$ nm.
[b]Ionized dopant density (equal to the free-hole density).
[c]Center of the bulk Gaussian distribution.

characteristic long tails before the work function saturates. Note that, for simplicity, we have fixed the values of a and σ to 0.57 nm and 78 meV, respectively, assuming that the morphology of the P3HT layer remains unchanged up to a doping ratio of 1:200, which is in line with the observations of Duong *et al.*.[49] A further improved agreement between experimental and calculated data might be achieved by relaxing these constraints or, in particular, by choosing a broader shape for the trap state distribution, being closer to the exponential-like line shape commonly observed in undoped small-molecule organic semiconductor films.[50–52] Above all, our calculations substantiate that a proper description of the gradual approach of the work function towards the bulk limit of F_4TCNQ-doped P3HT on aluminum must generally take into account that additional sites in the polymer HOMO are created via the introduction of ionized acceptor molecules. The accuracy of this approach is supported by the good agreement between the density of these sites determined from the fits at larger thicknesses and the value for the ionized acceptor concentration extracted from the initial parabolic shape at smaller film thickness. In conformity with the interpretation of the absorption data, we do not see a significant amount of LUMO states that could stem from the formation of hybrid charge transfer complexes. If such species were formed between F_4TCNQ and P3HT in the vicinity of the aluminum bottom electrode, we should observe a rather sudden increase of the work function from Φ_{Al} to the level of those LUMO states according to the density of applied F_4TCNQ acceptor molecules.

Free-hole densities (equivalent to the densities of ionized F_4TCNQ molecules that yield mobile holes) derived from the simulations are given in Table III and plotted as a function of the doping ratio in Fig. 6. We observe that the charge density in the depletion zone is only approximately 5% of the present F_4TCNQ molecules. These values complement well the free-hole densities which we have independently determined from our previous capacitance-voltage (C-V) measurements on layers in a metal-insulator-semiconductor (MIS) geometry (see Fig. 6).[15] Note that the coincidence of the free-hole densities from Kelvin probe and C-V measurements on different sample geometries including various metal electrodes substantiates that these densities are characteristic for the bulk of the doped layers. Since we have shown above that almost every F_4TCNQ is ionized, this implies that only every twentieth ionization event creates a mobile hole that can diffuse to the polymer/Al interface, and that can thus contribute to the Fermi level alignment in the samples on aluminum.

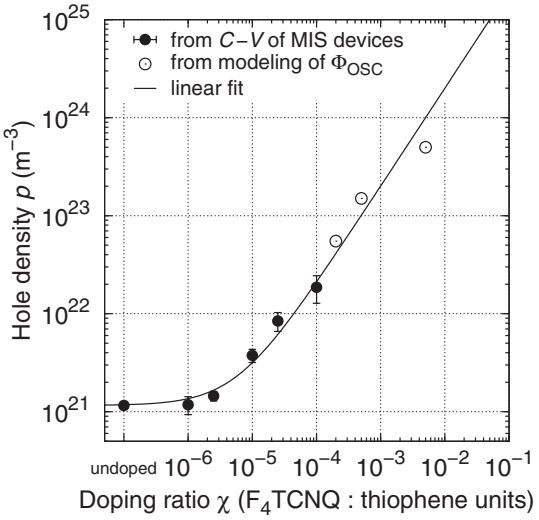

FIG. 6. Free-hole densities as determined by C-V measurements of layers in MIS geometry (see our previous work, Ref. 15) and by numerical modeling of the thickness dependence of the work function of F_4TCNQ-doped P3HT layers on metal substrates. The line corresponds to the linear function $p = 2.0 \times 10^{26}$ $m^{-3}\chi + 1.2 \times 10^{21}$ m^{-3}.

The observation that approximately 95% of the hole-F_4TCNQ anion pairs are bound may be explained by the low permittivity of hydrocarbon-based semiconductors. Assuming that a purely thermal activation process causes free charge carrier formation via charge-pair dissociation requires an activation energy of 77 meV at a temperature of 300 K, which is much lower than the typical exciton binding energy of 0.2–0.5 eV in organic semiconductors.[1] A recent simulation of Mityashin *et al.* indicates that the splitting of these charge pairs is favored by dissociation pathways within the energetic landscape of transport sites which might resolve this discrepancy.[53] According to Mityashin and co-workers, however, these pathways are due to the electrostatic interaction of neighboring charge pairs, which implies a doping ratio dependent dissociation efficiency and, in particular, that almost no dissociation occurs at low doping ratios. This is in clear contrast to our observation that the dissociation efficiency is constantly 5% in a broad range of doping concentrations, including very low doping ratios.

C. Electrical conductivity and free-hole mobility

The electrical conductivities of undoped and F_4TCNQ-doped P3HT layers are shown in Fig. 7. Part of the data stem from our previous analysis of the admittance spectra of MIS devices.[15] We consolidate this data with current-voltage (I-V) measurements of hole-only devices. The respective I-V characteristics show a symmetric and linear behavior around 0 V and up to $|V| \approx 1$ V. At high doping ratios, the hole-only conductivities connect well to the previous data. The undoped and weakly doped samples suffer from an increased conductivity, which is probably due to the degradation of the polymer sample during the more-than-one-year delay between the I-V and the previous admittance measurements. To support this interpretation, we repeated the admittance measurement of a freshly prepared undoped P3HT layer in the

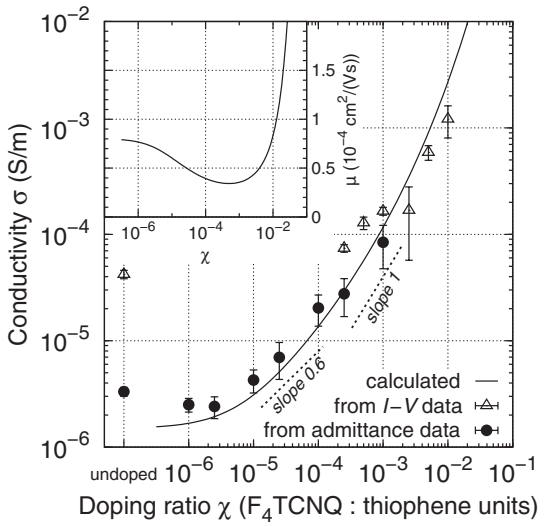

FIG. 7. Conductivities as determined by admittance measurements of layers in MIS geometry (solid symbols)[15] and *I*-*V* measurements of hole-only devices (open symbols). The line is the predicted conductivity based on the mobility model by Arkhipov *et al.*[23,54] and the hole densities from Fig. 6. The inset shows the calculated mobility values.

MIS geometry, and this experiment yielded increased values of the free-hole density and bulk conductivity as compared to the data published previously.

The measured conductivities increase monotoneously and nonlinearly with increasing doping ratio. This implies, in conjunction with a strictly linear increase of the free-hole density upon doping, a rather complicated relationship between the doping ratio and the hole mobility. In particular, we find a sublinear increase of the conductivity at low to moderate doping ratios ($\chi < 10^{-4}$), which means that the mobility decreases in this regime. At higher doping ratios, the conductivity increase is superlinear and, thus, linked with an increase of the free-hole mobility.

Our updated calculations of mobility and conductivity using the mobility model for doped organic semiconductors of Arkhipov *et al.*[23,54] agree excellently with the extended experimental data in the full range of doping ratios (see Fig. 7). Note that we have used similar parameters as in our previous work (see Table IV) and the same DOS distributions as in the above simulation of the work function curves (i.e., the same values for N, σ, and a).

Following the model of Arkhipov and co-workers, we explain the mobility decrease at low to moderate doping ratios with the broadening of the DOS distribution by the attracting Coulomb potentials of the ionized F_4TCNQ molecules [see Fig. 5(b)]. The occurrence of these Coulombic traps counteracts the fill-up of the low-mobility tail of the DOS distribution upon doping. At the low-to-moderate doping regime, this can lead to a reduction of the mobility as seen here. At higher doping ratios, the Coulomb potentials of individual ionized F_4TCNQ dopants overlap such that the effective barrier for the release of trapped holes is lowered. This is accounted for by the term $U_m(N_d)$ in Eq. (5). As a consequence, the mobility becomes increasingly controlled by the fill-up of the DOS distribution in the strong doping regime and, hence, increases.

TABLE IV. Parameters used in the calculations of the free-hole mobility and conductivity in Fig. 7.

Total density of states N	7×10^{26} m^{-3}
DOS width parameter σ	78 meV
Anion-trapped hole pair distance a	0.57 nm
Inverse hole localization radius γ	2.9 nm^{-1}
Attempt-to-hop frequency ν_0	3×10^{12} s^{-1}
Electric field F	2×10^{4} V m^{-1}
Temperature T	300 K

IV. SUMMARY

In summary, we derived a conclusive picture of the ionized-dopant and free-charge carrier formation in P3HT doped with F_4TCNQ. In this system, charge transfer is very efficient and leads to a full onefold ionization of both the donor and acceptor moieties. Thereby the majority of the F_4TCNQ dopants undergoes charge transfer, ruling out significant formation of isolated domains of neutral F_4TCNQ. However, most of the charge carrier pairs remain strongly bound and are not available for electrical conduction. Dissociation, which occurs for only 5% of these pairs, might be favored by dissociation pathways through the energetic distribution of transport sites.

As a consequence of charge carrier pair dissociation, doped layers exhibit an increased density of mobile holes. The corresponding electrons remain localized at the F_4TCNQ dopants, which are dispersed in the P3HT matrix. Due to the low permittivity, the Coloumb potentials of the ionized F_4TCNQ molecules have a rather long range and therefore affect the energetic and charge transport properties of the layer. We have shown that the HOMO-derived density-of-states distribution of P3HT is broadened upon doping with F_4TCNQ and that this broadening serves to explain the complex conductivity-doping ratio relationship. In particular, the presence of F_4TCNQ anions leads to a decrease of the hole mobility at low to moderate doping ratios.

Finally, we would like to point out that the integer charge transfer mechanism of P3HT and F_4TCNQ may not be anticipated for conjugated organic donors and acceptors in general. Intermolecular electronic interactions depend critically on the overlap of the relevant wave functions and are governed by the minimization of energy. Therefore partial charge transfer, i.e., the formation of hybrid charge transfer complexes, may occur for other donor-acceptor pairs as suggested in literature. The possible variety of doping mechanisms has to be considered when investigating organic semiconductor doping-related phenomena.

ACKNOWLEDGMENTS

Thanks are due to Peter Brückner for the surface potential measurements, Dr. Jan Behrends (Freie Universität Berlin) and Prof. Alberto Salleo (Stanford University) for stimulating discussions, and Prof. Ullrich Scherf (Universität Wuppertal) for providing the P3HT sample. This work has been financially supported by the German Ministry of Education and Research (NeMO FKZ 13N10622, PVcomB FKZ 03IS2151D).

*neher@uni-potsdam.de

[1] K. Walzer, B. Maennig, M. Pfeiffer, and K. Leo, Chem. Rev. **107**, 1233 (2007).
[2] W. Y. Gao and A. Kahn, Appl. Phys. Lett. **79**, 4040 (2001).
[3] M. Pfeiffer, A. Beyer, T. Fritz, and K. Leo, Appl. Phys. Lett. **73**, 3202 (1998).
[4] W. Y. Gao and A. Kahn, J. Appl. Phys. **94**, 359 (2003).
[5] B. Maennig, M. Pfeiffer, A. Nollau, X. Zhou, K. Leo, and P. Simon, Phys. Rev. B **64**, 195208 (2001).
[6] H. Kleemann, B. Lussem, and K. Leo, J. Appl. Phys. **111**, 123722 (2012).
[7] E. F. Aziz, A. Vollmer, S. Eisebitt, W. Eberhardt, P. Pingel, D. Neher, and N. Koch, Adv. Mater. **19**, 3257 (2007).
[8] J. Hwang and A. Kahn, J. Appl. Phys. **97**, 103705 (2005).
[9] E. Lim, B. J. Jung, M. Chikamatsu, R. Azumi, Y. Yoshida, K. Yase, L. M. Do, and H. K. Shim, J. Mater. Chem. **17**, 1416 (2007).
[10] L. Ma, W. H. Lee, Y. D. Park, J. S. Kim, H. S. Lee, and K. Choa, Appl. Phys. Lett. **92**, 063310 (2008).
[11] J. Sun, B. J. Jung, T. Lee, L. Berger, J. Huang, Y. Liu, D. H. Reich, and H. E. Katz, ACS Appl. Mater. Interfaces **1**, 412 (2009).
[12] K. H. Yim, G. L. Whiting, C. E. Murphy, J. J. M. Halls, J. H. Burroughes, R. H. Friend, and J. S. Kim, Adv. Mater. **20**, 3319 (2008).
[13] Y. Zhang, B. de Boer, and P. W. M. Blom, Adv. Funct. Mater. **19**, 1901 (2009).
[14] Y. Zhang and P. W. M. Blom, Appl. Phys. Lett. **97**, 083303 (2010).
[15] P. Pingel, R. Schwarzl, and D. Neher, Appl. Phys. Lett. **100**, 143303 (2012).
[16] P. Pingel, L. Y. Zhu, K. S. Park, J. O. Vogel, S. Janietz, E. G. Kim, J. P. Rabe, J. L. Brédas, and N. Koch, J. Phys. Chem. Lett. **1**, 2037 (2010).
[17] S. G. Chen, P. Stradins, and B. A. Gregg, J. Phys. Chem. B **109**, 13451 (2005).
[18] J.-H. Lee, H.-M. Kim, K.-B. Kim, R. Kabe, P. Anzenbacher, Jr., and J.-J. Kim, Appl. Phys. Lett. **98**, 173303 (2011).
[19] M. L. Tietze, L. Burtone, M. Riede, B. Lussem, and K. Leo, Phys. Rev. B **86**, 035320 (2012).
[20] B. A. Gregg, S. G. Chen, and R. A. Cormier, Chem. Mater. **16**, 4586 (2004).
[21] I. Salzmann, G. Heimel, S. Duhm, M. Oehzelt, P. Pingel, B. M. George, A. Schnegg, K. Lips, R.-P. Blum, A. Vollmer, and N. Koch, Phys. Rev. Lett. **108**, 035502 (2012).
[22] L. Zhu, E.-G. Kim, Y. P. Yi, and J. L. Brédas, Chem. Mater. **23**, 5149 (2011).
[23] V. I. Arkhipov, E. V. Emelianova, P. Heremans, and H. Bässler, Phys. Rev. B **72**, 235202 (2005).
[24] V. I. Arkhipov, P. Heremans, E. V. Emelianova, and H. Bässler, Phys. Rev. B **71**, 045214 (2005).
[25] A. Zen, M. Saphiannikova, D. Neher, J. Grenzer, S. Grigorian, U. Pietsch, U. Asawapirom, S. Janietz, U. Scherf, I. Lieberwirth, and G. Wegner, Macromolecules **39**, 2162 (2006).
[26] P. Pingel, A. Zen, R. D. Abellon, F. C. Grozema, L. D. A. Siebbeles, and D. Neher, Adv. Funct. Mater. **20**, 2286 (2010).
[27] A. Zen, J. Pflaum, S. Hirschmann, W. Zhuang, F. Jaiser, U. Asawapirom, J. P. Rabe, U. Scherf, and D. Neher, Adv. Funct. Mater. **14**, 757 (2004).
[28] M. M. Beerbom, B. Lagel, A. J. Cascio, B. V. Doran, and R. Schlaf, J. Electron Spectrosc. Relat. Phenom. **152**, 12 (2006).
[29] P. J. Brown, H. Sirringhaus, M. Harrison, M. Shkunov, and R. H. Friend, Phys. Rev. B **63**, 125204 (2001).
[30] R. Österbacka, C. P. An, X. M. Jiang, and Z. V. Vardeny, Science **287**, 839 (2000).
[31] J. B. Torrance, J. J. Mayerle, K. Bechgaard, B. D. Silverman, and Y. Tomkiewicz, Phys. Rev. B **22**, 4960 (1980).
[32] D. A. Dixon, J. C. Calabrese, and J. S. Miller, J. Phys. Chem. **93**, 2284 (1989).
[33] C. G. Shuttle, B. O'Regan, A. M. Ballantyne, J. Nelson, D. D. C. Bradley, and J. R. Durrant, Phys. Rev. B **78**, 113201 (2008).
[34] J. M. Guo, H. Ohkita, H. Benten, and S. Ito, J. Am. Chem. Soc. **132**, 6154 (2010).
[35] I. A. Howard, R. Mauer, M. Meister, and F. Laquai, J. Am. Chem. Soc. **132**, 14866 (2010).
[36] D. Herrmann, S. Niesar, C. Scharsich, A. Köhler, M. Stutzmann, and E. Riedle, J. Am. Chem. Soc. **133**, 18220 (2011).
[37] See Supplemental Material at http://link.aps.org/supplemental/10.1103/PhysRevB.87.115209 for a discussion of the P3HT polaron and F_4TCNQ anion reference spectra, example reconstructions of the NIR absorption spectra of F_4TCNQ-doped P3HT in chloroform at various solution concentrations, and I-V characteristics of F_4TCNQ-doped P3HT hole-only devices.
[38] O. D. Parashchuk, A. Y. Sosorev, V. V. Bruevich, and D. Y. Paraschuk, JETP Lett. **91**, 351 (2010).
[39] T. J. Prosa, M. J. Winokur, J. Moulton, P. Smith, and A. J. Heeger, Macromolecules **25**, 4364 (1992).
[40] Y. A. Zhang and P. W. M. Blom, Org. Electron. **11**, 1261 (2010).
[41] C. B. Duke, W. R. Salaneck, T. J. Fabish, J. J. Ritsko, H. R. Thomas, and A. Paton, Phys. Rev. B **18**, 5717 (1978).
[42] C. B. Duke and T. J. Fabish, Phys. Rev. Lett. **37**, 1075 (1976).
[43] I. Lange, J. C. Blakesley, J. Frisch, A. Vollmer, N. Koch, and D. Neher, Phys. Rev. Lett. **106**, 216402 (2011).
[44] H. Ishii, N. Hayashi, E. Ito, Y. Washizu, K. Sugi, Y. Kimura, M. Niwano, Y. Ouchi, and K. Seki, Phys. Status Solidi A **201**, 1075 (2004).
[45] Y. L. Shen, K. Diest, M. H. Wong, B. R. Hsieh, D. H. Dunlap, and G. G. Malliaras, Phys. Rev. B **68**, 081204 (2003).
[46] A. Dieckmann, H. Bässler, and P. M. Borsenberger, J. Chem. Phys. **99**, 8136 (1993).
[47] G. Garcia-Belmonte, E. V. Vakarin, J. Bisquert, and J. P. Badiali, Electrochim. Acta **55**, 6123 (2010).
[48] O. Tal, Y. Rosenwaks, Y. Preezant, N. Tessler, C. K. Chan, and A. Kahn, Phys. Rev. Lett. **95**, 256405 (2005).
[49] D. T. Duong, C. C. Wang, E. Antono, M. F. Toney, and A. Salleo, Org. Electron. (2013), doi:10.1016/j.orgel.2013.02.028.
[50] T. Sueyoshi, H. Fukagawa, M. Ono, S. Kera, and N. Ueno, Appl. Phys. Lett. **95**, 183303 (2009).
[51] W. L. Kalb, S. Haas, C. Krellner, T. Mathis, and B. Batlogg, Phys. Rev. B **81**, 155315 (2010).
[52] S. Olthof, S. Mehraeen, S. K. Mohapatra, S. Barlow, V. Coropceanu, J.-L. Brédas, S. R. Marder, and A. Kahn, Phys. Rev. Lett. **109**, 176601 (2012).
[53] A. Mityashin, Y. Olivier, T. Van Regemorter, C. Rolin, S. Verlaak, N. G. Martinelli, D. Beljonne, J. Cornil, J. Genoe, and P. Heremans, Adv. Mater. **24**, 1535 (2012).
[54] V. I. Arkhipov, P. Heremans, E. V. Emelianova, G. J. Adriaenssens, and H. Bässler, Appl. Phys. Lett. **82**, 3245 (2003).

Supporting Information to "Comprehensive picture of p-doping P3HT with the molecular acceptor F_4TCNQ"

P. Pingel and D. Neher

Soft Matter Physics, Institute of Physics and Astronomy, University of Potsdam, Karl-Liebknecht-Str. 24-25, D–14476 Potsdam, Germany

I. OPTICAL ABSORPTION SPECTROSCOPY

A. Reference spectra

In order to evaluate the optical spectra of F_4TCNQ-doped P3HT layers and solutions, proper reference spectra of the neat charged compounds are indispensable. The P3HT polaron reference spectrum was prepared by exposing the P3HT powder to I_2 vapor. The doped polymer was then dissolved in chloroform. The spectrum of this solution, plotted in Fig. 3b of the article, serves as a reference of the relative absorption of P3HT polarons in F_4TCNQ-P3HT blends.

In order to determine the absolute amount of F_4TCNQ anions in our samples, we use the extinction coefficient spectra of neutral F_4TCNQ and ionized F_4TCNQ bound in a charge transfer salt which we have taken from Dixon et al. (Ref. 1 in this Supporting Information). For integrity of our analysis, we compare these spectra with our own measurements. Close accordance is exhibited between the published spectrum of a crystal of neutral F_4TCNQ and our measurement of 0.01 g/l F_4TCNQ dissolved in chloroform (CF) in terms of the shape of the spectra and the absolute value of the extinction coefficient (thick solid and dashed lines in Fig. 1a, respectively). Preparation of a neat reference sample for obtaining the F_4TCNQ anion absorption is unfortunately not straightforward. We have prepared a solution of 0.01 g/l F_4TCNQ in tetrahydrofuran (THF) and added ca. 4 µl of a 1 g/l potassium iodide solution in water (K^+I^-) in order to reduce a significant, but unknown, amount of the F_4TCNQ molecules. Again, excellent accordance of the shapes of the specific F_4TCNQ anion absorption in the NIR (between 1 and 2 eV) is exhibited between our measured spectrum and the literature data (thick solid and dashed lines in Fig. 1b, respectively). As concluded from these comparisons, we can use the spectra published in Ref. 1 as absolute references in order to measure the content of neutral F_4TCNQ and F_4TCNQ anions in our blends.

Note that the algebraic decomposition analysis cannot be directly performed on the spectra of F_4TCNQ-P3HT layers, because the NIR absorption of the F_4TCNQ anions is affected by the polymer matrix in terms of a broadening of the absorption bands and strong tails. This can be seen in Fig. 1b, thin dashed lines, for a sample that incorporates F_4TCNQ anions in an inert matrix of poly(methyl methacrylate) (PMMA). Therefore, in order to evaluate the number of P3HT-F_4TCNQ charge transfer pairs in the doped layers, we proceed as de-

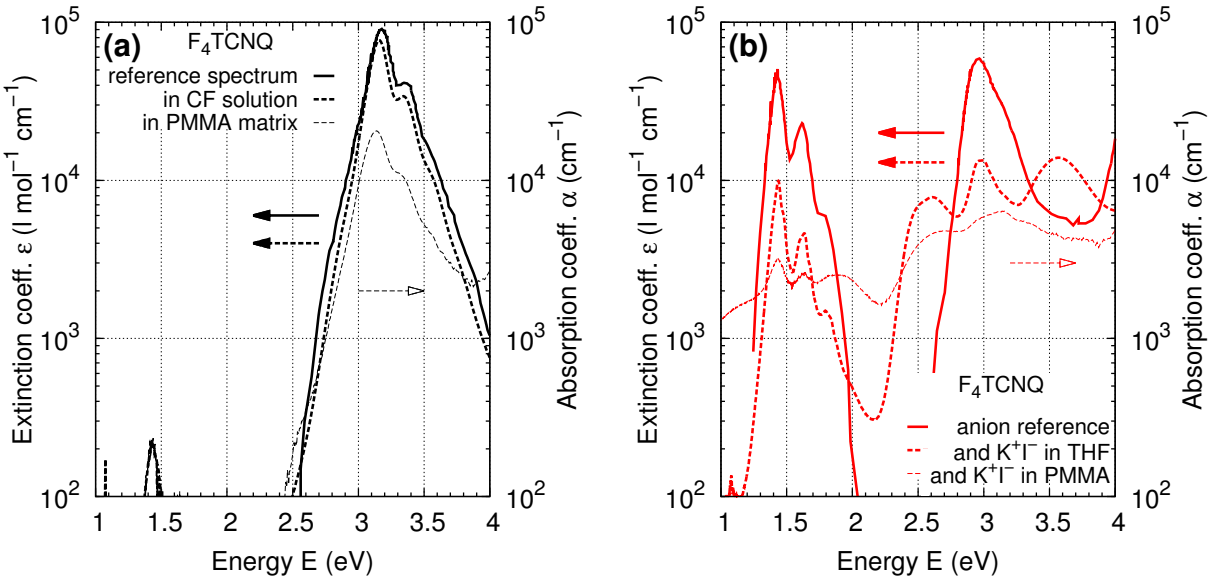

FIG. 1. Reference[1] and experimental extinction and absorption coefficient spectra of (a) neutral and (b) singly negatively charged F_4TCNQ. Solutions were prepared at 0.01 g/l in chloroform (a) and tetrahydrofuran (b). Thin film samples were prepared from a blend of one F_4TCNQ molecule per 100 repeat units of poly(methyl methacrylate). F_4TCNQ was reduced by adding a little amount of a water-based potassium iodide solution to the F_4TCNQ-THF solution.

scribed in the article, i.e., we apply the extinction coefficient of the P3HT-F_4TCNQ charge transfer pairs which we have priorly determined in solution.

B. Decomposition of the solution spectra

Absorption spectra of the F_4TCNQ-P3HT blends in chloroform have been algebraically decomposed in the NIR into the F_4TCNQ anion and P3HT polaron parts (Figs. 2-4). Interestingly, the fraction of intentionally applied F_4TCNQ molecules that has been recovered as F_4TCNQ anions in the analysis is a function of the solution concentration. Depending on the initial concentration of the undoped P3HT solution, we recover $50-83\%$ (at 2 g/l), $42-67\%$ (at 0.5 g/l), and $6-16\%$ (at 0.025 g/l) of the F_4TCNQ molecules as anions (see Tables I-III). For the 0.025 g/l-based solutions, we observe the specific absorption bands of neutral F_4TCNQ between 3 and 3.5 eV. A rough analysis of these bands using the reference extinction coefficient spectrum recovers $73-93\%$ of the applied F_4TCNQ as neutral

molecules. Similar observations have been made by Parashchuk et al.[2] for poly(methoxy-5-(20-ethylhexyloxy)-1,4-phenylene-vinylene), MEH-PPV, doped with the organic acceptor 2,4,7-trinitrofluorenone, TNF. The authors inferred that the dopants do not penetrate into the polymer coils in dilute solutions, resulting in only few charge transfer pairs being formed at the surface of these coils. At higher solution concentrations, dopants do enter and charge transfer occurs with interior polymer units as well. It is worth to note that the typical P3HT concentration in solutions which we have used to prepare solid samples is in the range of $0.5 - 30\,\mathrm{g/l}$, which is in a regime where most of the F_4TCNQ dopants underwent charge transfer with P3HT.

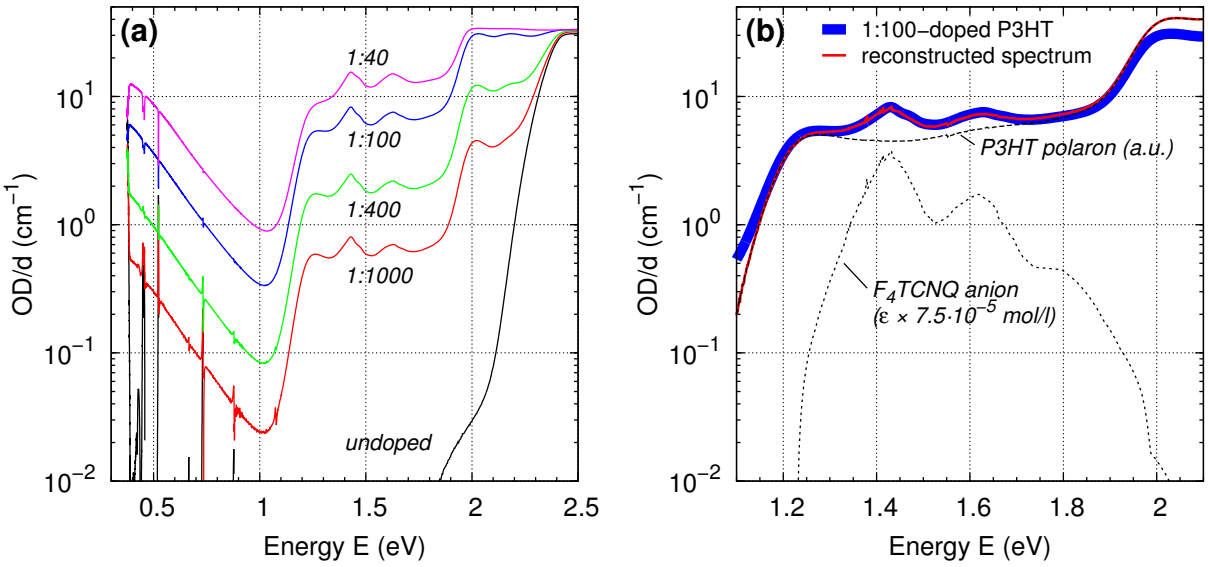

FIG. 2. (a) Absorbance-per-length of undoped and F_4TCNQ-doped P3HT solution in chloroform. The undoped P3HT solution sample had a concentration of 2 g/l. (b) Reconstruction of the P3HT polaron/F_4TCNQ anion absorption of the 1:100-doped P3HT sample from reference spectra. The F_4TCNQ anion spectrum is reprinted with permission from Ref. 1. Copyright 1989 American Chemical Society.

TABLE I. Concentrations of ionized F_4TCNQ found in a blend with P3HT in chloroform at various doping ratios. The undoped P3HT solution sample had a concentration of 2 g/l.

Doping ratio	P3HT repeat units[a] (mol/l)	F_4TCNQ[a] (mol/l)	F_4TCNQ^-[b] (mol/l)	ionized fraction
1:1000	1.19×10^{-5}	1.19×10^{-5}	6.0×10^{-6}	0.50
1:400	1.18×10^{-5}	2.96×10^{-5}	2.0×10^{-5}	0.68
1:100	1.13×10^{-5}	1.13×10^{-4}	7.5×10^{-5}	0.66
1:40	1.03×10^{-5}	2.58×10^{-4}	1.8×10^{-4}	0.70

[a] intentionally applied amount in solution

[b] measured by decomposition of the optical spectra

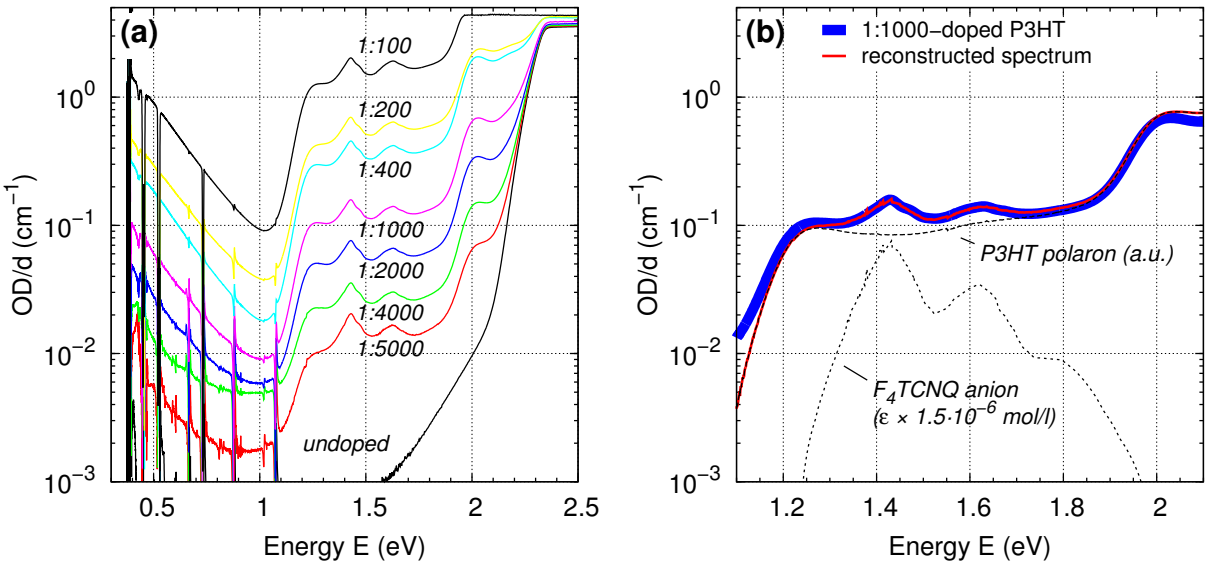

FIG. 3. (a) Absorbance-per-length of undoped and F_4TCNQ-doped P3HT solution in chloroform. The undoped P3HT solution sample had a concentration of 0.5 g/l. (b) Reconstruction of the P3HT polaron/F_4TCNQ anion absorption of the 1:1000-doped P3HT sample from reference spectra.

TABLE II. Concentrations of ionized F_4TCNQ found in a blend with P3HT in chloroform at various doping ratios. The undoped P3HT solution sample had a concentration of 0.5 g/l.

Doping ratio	F_4TCNQ^{-} [a] (mol/l)	F_4TCNQ [b] (mol/l)	ionized fraction
1:5000	2.5×10^{-7}	6.0×10^{-7}	0.42
1:4000	3.5×10^{-7}	7.5×10^{-7}	0.47
1:2000	7.0×10^{-7}	1.5×10^{-6}	0.47
1:1000	1.5×10^{-6}	2.9×10^{-6}	0.52
1:400	5.0×10^{-6}	7.5×10^{-6}	0.67
1:200	7.5×10^{-6}	1.3×10^{-5}	0.58
1:100	2.0×10^{-6}	3.0×10^{-5}	0.66

[a] measured by decomposition of the optical spectra

[b] intentionally applied amount in solution

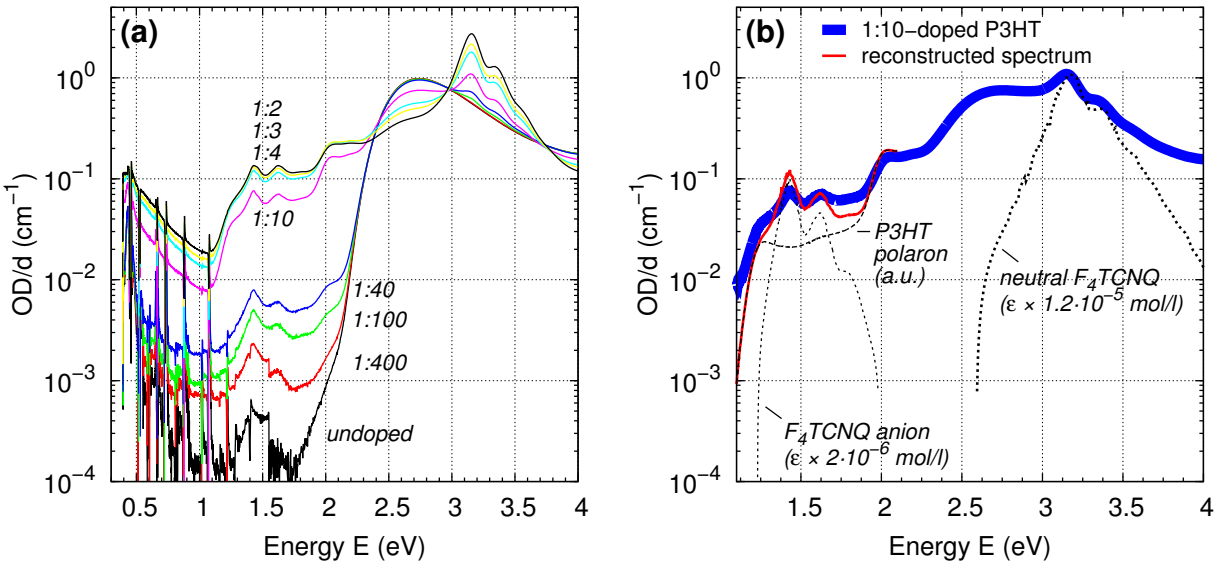

FIG. 4. (a) Absorbance-per-length of undoped and F_4TCNQ-doped P3HT dilute solution in chloroform. The undoped P3HT solution sample had a concentration of 0.025 g/l. (b) Reconstruction of the P3HT polaron/F_4TCNQ anion and neutral F_4TCNQ absorption of the 1:10-doped P3HT sample from reference spectra.

TABLE III. Concentrations of ionized F_4TCNQ found in a blend with P3HT in chloroform at various doping ratios. The undoped P3HT solution sample had a concentration of 0.025 g/l.

Doping ratio	F_4TCNQ^- [a] (mol/l)	F_4TCNQ[a] (mol/l)	F_4TCNQ[b] (mol/l)	ionized fraction	
1:100	1.2×10^{-7}	–	1.5×10^{-6}	0.08	–
1:40	2.0×10^{-7}	–	3.6×10^{-6}	0.06	–
1:10	2.0×10^{-6}	1.2×10^{-5}	1.3×10^{-5}	0.16	0.93
1:4	3.0×10^{-6}	2.0×10^{-5}	2.7×10^{-5}	0.11	0.75
1:3	2.3×10^{-6}	2.4×10^{-5}	3.2×10^{-5}	0.07	0.74
1:2	2.3×10^{-6}	3.0×10^{-5}	4.1×10^{-5}	0.06	0.73

[a] measured by decomposition of the optical spectra

[b] intentionally applied amount in solution

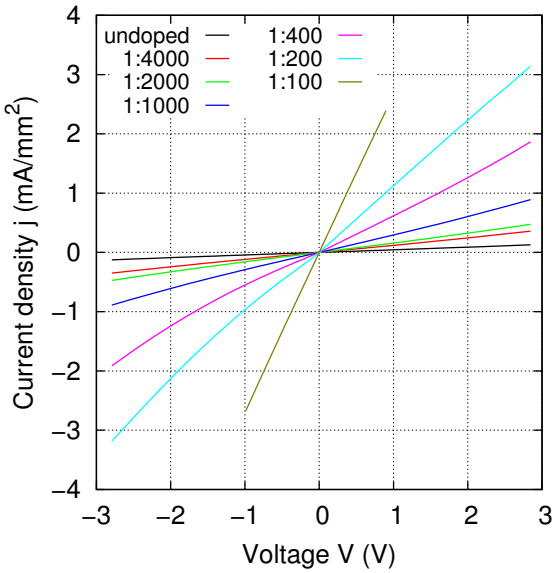

FIG. 5. I-V characteristics of undoped and F_4TCNQ-doped P3HT hole-only devices.

II. HOLE-ONLY I-V CHARACTERISTICS

Hole-only devices of undoped and F_4TCNQ-doped P3HT layers with a PEDOT:PSS bottom electrode and a MoO_3/Al top electrode exhibit symmetric I-V characteristics (Fig. 5). Positive voltages refer to hole injection from the PEDOT:PSS electrode. Conductivities were extracted by using a linear fit within 0 to +1 V.

[1] D. Dixon, J. Calabrese, and J. Miller, J. Phys. Chem. **93**, 2284 (1989).

[2] O. D. Parashchuk, A. Y. Sosorev, V. V. Bruevich, and D. Y. Paraschuk, JETP Lett. **91**, 351 (2010).

Danksagung

Zuerst möchte ich mich ganz herzlich bei Prof. Dr. Dieter Neher bedanken, der mir während der langen Zeit, die ich in der "Physik weicher Materie" forschen durfte, fortwährend Anleitung, Anregungen und auch Freiheit gegeben hat, um die Dinge zu tun, die ich letztlich in dieser Arbeit niedergeschrieben habe. Diese positive Unterstützung, dein Einsatz und deine Ideen haben mich immer zur richtigen Zeit ein Stück weiter gebracht.

Mein Dank gilt auch allen, teils ehemaligen Mitgliedern der PwM sowohl für die fachliche und organisatorische Zusammenarbeit, als auch für die zahlreichen Aktivitäten, die ich mit euch erleben durfte. Etliche Grillfeste, Kochabende und sportliche Unternehmungen zu Land und zu Wasser haben mir immer viel Spaß gemacht und werde ich in guter Erinnerung behalten. Ich bedanke mich bei meinen langjährigen Bürokollegen Sahika und Steve für unsere interessanten Unterhaltungen über türkische Süßigkeiten, Automobiltechnik und so vieles mehr. Marcel, Robert, Frank, Juliane, Ilja, Riccardo, Thomas B., Andreas P., Burkhard, Steffen, Jan, Jona, Fabio, Benjamin, Andreas Hü., Daniel, David, Sina, Sebastian B., Sebastian S., Guanghao, Christoph, James, Patrick Pa., Harry, Debby, Sylvia, Beate, Mahmoud, Sergey, Basu, Thomas U. und Thomas M. haben alle einen Teil zu dieser Arbeit beigetragen, sei es durch fachliche Diskussionen, technische Hilfen oder mentale Unterstützung. Besonderer Dank gilt überdies Sarah, Richard und Peter, die einen Teil der Messungen übernommen haben und mit denen zusammen ich viel lernen konnte. Elke, Dagmar und Andreas Ho. danke ich dafür, dass sie fleißig mit dem Papierkram gefochten und Nachschub organisiert haben, wann immer etwas fehlte.

Einige Untersuchungen aus dieser Arbeit wurden von oder mit der Hilfe von Kollegen aus externen Instituten durchgeführt. Für die freundliche und gute Zusammenarbeit möchte ich daher Dr. Thomas Fischer (Fraunhofer IAP Golm), Dr. Sergei Kühn (MBI Berlin) und Dr. Jan Behrends (FU Berlin) herzlich danken. Prof. Dr. Norbert Koch (HU Berlin) gilt mein großer Dank nicht nur dafür, dass er mich am Beginn meiner Doktorandenzeit finanziell unterstützt hat, sondern auch für die Zusammenarbeit darüber hinaus, gemeinsam mit Dr. Ingo Salzmann. Einige Polymere, die ich für diese Arbeit verwendet habe, wurden von Dr. Sybille Allard, Prof. Dr. Ullrich Scherf (beide Uni

Wuppertal) und Prof. Dr. Hans-Heinrich Hörhold (Uni Jena) bereit gestellt, wofür ich mich bedanken möchte.

Mein ganz besonderer Dank gilt nicht zuletzt Lisa, die mir über die Jahre lieben Zuspruch und Vertrauen schenkt und dadurch nicht nur Anteil an dieser Doktorarbeit hat, sondern mein Leben reicher und die Zeit schöner macht.

Erklärung

Ich erkläre hiermit, dass ich diese Arbeit selbstständig verfasst und keine anderen als die angegebenen Hilfsmittel benutzt habe. Diese Arbeit wurde an keiner anderen Hochschule eingereicht.

Potsdam, den 26.06.13

Patrick Pingel